SCUOLA DI DOTTORATO
UNIVERSITÀ DEGLI STUDI DI MILANO-BICOCCA

Dipartimento di

Scienze dei Materiali

PhD program in Materials Science and Nanotechnology Ciclo XXXIV

Extended defects in heteroepitaxial structures on silicon by Molecular Dynamics simulations: applications to SiGe and cubic SiC

Surname Barbisan Name Luca

Registration number 726289

Supervisor: Prof. Francesco Montalenti

Coordinator: Prof. Marco Bernasconi

ACADEMIC YEAR 2020/2021

UNIVERSITÀ DEGLI STUDI DI MILANO BICOCCA

PH.D. IN

MATERIALS SCIENCE AND NANOTECHNOLOGY

EXTENDED DEFECTS IN HETEROEPITAXIAL STRUCTURES ON SILICON BY MOLECULAR DYNAMICS SIMULATIONS: APPLICATIONS TO SiGe AND CUBIC SiC

Tutor:

PROF. FRANCESCO MONTALENTI

Coordinator:

PROF. MARCO BERNASCONI

PhD Thesis:

LUCA BARBISAN

Registration number: 726289

XXXIV CYCLE

Phd Thesis in Materials Science and Nanotechnology

in

MoSE GROUP

DIPARTIMENTO DI SCIENZE DEI MATERIALI

28 OCTOBER 2021

Contents

List of Figures

List of Tables

List of Abbreviations

fcc	**f**ace **c**entered **c**ubic
SF	**S**tacking **F**ault
TEM	**T**ransmission **E**lectron **M**icroscopy
ISF	**I**ntrinsic **S**tacking **F**ault
ESF	**E**xtrinsic **S**tacking **F**ault
2ESF	double **E**xtrinsic **S**tacking **F**ault
APB	**A**nti-**P**hase **B**oundary
MD	**M**olecular **D**ynamics
LAMMPS	**L**arge-scale **A**tomic/**M**olecular **M**assively **P**arallel **S**imulator
PBC	**P**eriodic **B**oundary **C**onditions
TEM	**T**ransmission **E**lecron **M**icroscopy
SD	**S**teepest **D**escent
CG	**C**onjugated **G**radient
OVITO	**O**pen **Vi**sualization **To**ol
DXA	**D**islocation analysis **A**lgoritm
CNA	**C**ommon **N**eighbor **A**nalysis
WS	**W**igner **S**eitz
MLs	**M**ono**L**ayers
ID	**ID**entifier
ABOP	**A**nalytical **B**ond **O**rder **P**otential
DFT	**D**ensity **F**unctional **T**heory
GAP	**G**aussian **A**pproximation **P**otential
PD	**P**artial **D**islocation
HPD	**H**exagonal **P**artial **D**islocation loops
LDOS	**L**ocal **D**ensity **O**f **S**tates

VB	**V**alence **B**and
CB	**C**onduction **B**and
ML	**M**irror-**L**ike glide plane
PIV	**P**ermutation **I**nvariant **V**ector

Introduction

Silicon has dominated semiconductor technology for almost half a century. Even if the first transistor was made using germanium and other semiconductors show better electronic properties in terms of higher carrier mobility, higher saturation velocity, and larger energy gap. It is the material used to build almost the 97% of all semiconductor-based electronic devices. The reason is straightforward; it is the most economical technology to make integrated circuits. Silicon domain can be assessed into a series of properties of the material that make it the ideal candidate for the fabrication of electronic chips. The chemistry of Si and its native oxides allows for the realization of deposition processes and selective etching with uniques uniformity and yield. Combining these two process technologies on wafers with dimensions constantly growing, it has been possible to fabricate integrated circuits with constantly increasing number of transistors on a single chip. The first that analyzed this trend was Gordon Moore in 1965, and he suggested that the trend was due to a constant exercise in cost reduction.[1] The manufacturing cost for a square millimeter of Si remained constant at about 1$ for many decades, while the number of transistors and other elements has grown exponentially with time. The number of transistors for units of area that can be placed on a semiconductor wafer depends on the capacity of the wafer to dissipate such thermal energy. Materials with elevated thermal conducibility and melting temperature, like silicon, are the ideal ones. The low leakage currents that can be achieved with Si oxide and Si nitrate (its native composite with air) and the elevated thermal conducibility allowed a transistor density higher than with other semiconductors. Even if Si still dominates the main branch of semiconductor technology, there are areas where the low mobility, the low saturation velocity, and the indirect bandgap permitted other semiconductors to develop.

Being the raw material cost much higher than Si one, some techniques have been developed to reduce such costs. A way to maintain the thermal advantage of a silicon substrate and reduce the raw material cost of semiconductors that are not Si consists of using a thin crystalline semiconductor film grown on top of a thick Si crystalline substrate (hetero-epitaxy). Hetero-epitaxy guarantees lower costs maintaining a thermally efficient substrate, but on the other side implies that the semiconductor has to be grown on a substrate with a different lattice parameter. In this case, we can define the lattice misfit between the two crystals:

$$f = (a_{\text{sub}} + a_{\text{epi}}) / a_{\text{sub}} \tag{1}$$

where a_{sub} and a_{epi} are the lattice parameters of the substrate and of the deposited material (often called *epilayer*), respectively. The presence of a misfit implies the existence of an epitaxial strain in the film.

Today's more diffused epitaxial technologies are the epi-grow of group III-V and II-VI alloys (especially for radio frequency amplification and laser technologies) and the epitaxy of group IV semiconductors like the SiC and SiGe alloys and the pure Ge. Group IV semiconductors have the non-negligible advantage of having cheaper fabrication costs than the formers. They could guarantee better performances in terms of electronic properties than Si. Still, the main obstacle in realizing such devices stems from the fact that the lattice mismatch induces the formation of detrimental defects, for the electronic and structural properties of the film, during the epitaxial growth. Such defects hinder the possibility of an industrial, extensive application of group IV semiconductors other than Si. Typically, the generated defects are grain boundaries, misfit dislocations, stacking faults, and other extended defects.

A strong academic and industrial interest exists in the comprehension of defects in epitaxial systems. Many experimental observations have been made about these topics. Still, a complete understanding of how extended defects evolve in epitaxial group IV semiconductor films is lacking. In particular, two systems present at the same time exciting application perspectives and hard theoretical modeling challenges: silicon germanium and cubic silicon carbide. They indeed are attractive semiconductors that can be easily

integrated into the actual silicon-based architecture. Their epitaxy on Si has been studied for years, but defect densities are still too high in those systems. The impossibility of achieving low defect densities in both materials can be found in the existence of many open problems that have to be solved. The two systems are attractive from the point of view of theoretical modeling because they are prototypical systems of plastic relaxation in very different strain conditions. In Ge, misfit dislocations are generated to relax the compressive epitaxial strain; in cubic SiC, partial dislocations and stacking faults appear as a consequence of a very high tensile misfit. The dynamics of the main detrimental defects in these materials, i.e., dislocations and stacking faults, are a complex argument and require studies that can go beyond the experimental practical limits. Indeed atomic mechanisms can play an essential role in defect dynamics, and one of the main problems stems from the empirical difficulty of understanding the temporal and spatial evolution of these defects at the atomic scale. For such a reason, simulations and molecular dynamics calculations can play a significant role in understanding and predicting extended defects behaviors without the necessity of performing thousands of ad hoc experiments.

In this Thesis, we will deal with the problem of modeling extended defects evolution via molecular dynamics simulations. We will tackle some of the open problems about defect evolution in both the materials under consideration. Our results provided enough information to shed light on the specific problems of the formation and evolution of multiple stacking faults in cubic SiC and the formation of ordered arrays of Lomer dislocation in Ge grown on Si. Details will be given in the main text and the conclusions of the manuscript. In the first part of this manuscript, we will discuss the theoretical background regarding extended defects in epitaxial systems. We will first introduce the leading theory used to describe elastic deformations in solids, the *Linear Elasticity Theory*. The instruments to deal with the concepts of strain, stress, elastic constants, and so on will be introduced. The mathematical formalism there introduced will give us the necessary information to comprehend the key factors governing the defects behavior in deformed solids. This part will also provide the technical background about the most critical extended defect: the dislocations. We will introduce the formalism of Dislocation Theory, initially as a general overview and after with a particular focus on the materials under consideration. We will also provide a specific discussion about why we selected silicon carbide and

germanium as prototypical cases to study the modeling of extended defects in epitaxial systems on silicon.

The approach used in the modeling is the classical molecular dynamics that will be discussed as well. The second part of this Thesis will be indeed focused on presenting molecular dynamics crucial aspects. This part of the work will describe the models used to study extended defects. Key terms that have to be introduced when talking about molecular dynamics will be presented. We will discuss how we model defect evolution. We will do that in terms of what kind of simulation we set up, how we set them up, and how we can analyze the results.

In the third part, we will introduce the results obtained using this computational approach. This part will be subdivided into two chapters. The two chapters will be focused separately on the two semiconductors that we have chosen to consider. Our findings are very different for the two subjects of our investigation. In the first one of the two chapters, we will present our results about extended defects modeling in epitaxial 3C-SiC.

This chapter represents the more significant part of the work done for this Thesis. As a first point, we present our investigation about which potential function should be used to model defect evolution in 3C-SiC. The defects that are found in 3C-SiC are for the most stacking faults, which we found to be governed in their development by the partial dislocation that bound them.

Those dislocations resulted in being of foremost importance in the formation of the aggregates of stacking faults that are experimentally observed. Providing an explanation for the appearance of this kind of defect (called multiple stacking faults), we understood the role of the changes in the strain sign during the typical 3C-SiC growing processes.

Analyzing an experimentally observed mechanism of stacking fault reduction, we suggested experimental recommendations about the role of strain that can help in lowering stacking fault densities.

Last, we identified which defect in 3C-SiC can be charged with being the "killer defect" in the epitaxial film (the defects responsible for the appearance of leakage currents in 3C-SiC devices). Before our investigations, indeed, the connection between stacking faults and leakage currents that affected 3C-SiC devices was uncertain.

Germanium films grown on Si (001) substate will represent the last part of the result

section. Germanium, being a well-studied semiconductor in epitaxy systems, is the perfect candidate for studying the modeling of dislocations via molecular dynamics. We will first show an approach able to model the critical aspects of strain relaxation processes in epitaxial germanium films. After that, we will use the information gained to focus on aspects of dislocation evolution in this system that still need to be addressed. We focused on the role of an essential mechanism in dislocation evolution, the climb of misfit dislocation. Technical problems of the modelization of such issue will be present, and our solution will be presented as well. We also provided important information on the actual evolution happening in epitaxially grown Ge films at low temperatures and high deposition rates that were still lacking.

In the end, we will drown the conclusions.

Outline

In the following, we outline how we have organized the present manuscript.

In Chapter 1, we present the main concepts of the Linear Elasticity Theory and Dislocations. A brief introduction to the elastic properties of the crystalline solids is given. Also, the definition of dislocations is given, presenting the main properties determined by the atomistic nature of dislocations and by the influence of the crystal lattice on these defects.

In Chapter 2, the technical background necessary to comprehend dislocation modeling via molecular dynamics will be presented. We will describe how classical molecular simulations are performed and how we can use this technique to model defect evolution. Information on the methods used for the visualization and the analysis of the simulations will be provided as well.

In Chapter 3, results from the study achieved so far are drown. In this chapter, we focus on the results about the former of the two materials that we considered in this Thesis, the cubic phase of the silicon carbide. Here we address the evolution of stacking faults via molecular dynamics simulation, with particular attention to the partial dislocations surrounding the stacking faults. The potential function that should be used to perform simulations, the role of partial dislocation on the stability of dislocation complexes, the dynamics of individual and multiple stacking faults, the processes leading to SF annihilation, and an analysis of what is believed to be one of the most detrimental defects in 3C-SiC will be presented in the various sections of this chapter.

In Chapter 4, the second material, the germanium, is chosen as the subject of our investigations. This chapter investigates two essential aspects of dislocation modeling that could not be easily explored in the SiC epitaxial system. The strain relaxation via the expansion of a misfit dislocation loop and the processes able to allow misfit dislocation climb.

Finally, the principal results and the perspectives emerging from this work are summarized in the Conclusions.

Chapter 1

Theoretical background

Extended defects and material properties are usually studied in the field of linear elasticity theory. One of the critical pieces of literature in this field is represented by the book written by Hirth and Lothe.[2] Many of the key concepts and terms used in this Thesis will be introduced in the following section.

1.1 Linear elasticity theory

When atoms are displaced from their ideal position, an internal deformation exists inside a crystal. This is the case of the deposition of thin films onto a different material substrate (hetero-epitaxy). In hetero-epitaxy, the atoms of the grown substrate have to adapt to the lattice parameter of the underlying substrate. The concepts of deformation and displacement fields are commonly introduced to describe epitaxy.

1.1.1 Displacements and strain tensor

Let's consider a crystal made of a continuum medium in which atomic positions are described by vectors, in a Cartesian reference system, $\vec{x} = (x', y', z')$. New positions can be described by a displacement field $\vec{u}(x)$:

$$\vec{X} = \vec{x} + \vec{u}(x) \tag{1.1}$$

Once the displacement field has been defined is possible to define the symmetric tensor of infinitesimal deformations, i.e., the *strain tensor*:

$$\epsilon_{ij} = \frac{1}{2}\left(\frac{\partial u_i}{\partial x_j} + \frac{\partial u_j}{\partial x_i}\right) \tag{1.2}$$

To understand the relationship between displacements and strain, let's consider the simple case of a bidimensional square lattice as shown in Figure 1.1: Assume that atoms in a relaxed crystal are a set of springs in their equilibrium position fixed in a single point (i.e., the atom near the origin in 1.1). Uniform dilation Δx of the springs by a corresponds to a displacement = a for the atoms bounding the first spring; equal to $2a$ for the next one, equal to $3a$ for the successive and so on. Clearly, this displacement field is not uniform but linear.

Strain tensor is defined under the hypothesis of infinitesimal deformations. Such a hypothesis can be justified considering how the distance between two points changes during deformation. Assuming two points infinitesimally nearby, being dx_i the $i-th$ component of the vector of the distance between the two points before the deformation, after one has $dx'_\mathrm{i} = dx_\mathrm{i} + du_\mathrm{i}$. The distance between the two points before and after the deformation is given by:

$$dr = \sqrt{\sum_\mathrm{i} dx_\mathrm{i}} \qquad dr' = \sqrt{\sum_\mathrm{i} dx'_\mathrm{i}} = \sqrt{\sum_\mathrm{i} dx_\mathrm{i} + du_\mathrm{i}} \tag{1.3}$$

Considering that $du_\mathrm{i} = \dfrac{\partial u_\mathrm{i}}{\partial x_\mathrm{j}}\, dx_\mathrm{j}$ one obtains:

$$(dr')^2 - (dr)^2 = 2\,\varepsilon_\mathrm{ij}\, dx_\mathrm{i}\, dx_\mathrm{j} \tag{1.4}$$

with

$$\varepsilon_\mathrm{ij} = \frac{1}{2}\left(\frac{\partial u_\mathrm{i}}{\partial x_\mathrm{j}} + \frac{\partial u_\mathrm{j}}{\partial x_\mathrm{i}} - \frac{\partial u_\mathrm{i}}{\partial x_\mathrm{j}}\frac{\partial u_\mathrm{j}}{\partial x_\mathrm{i}}\right) \tag{1.5}$$

Equation 1.5 represents the generalized strain tensor for large displacements, as obtained from the variation of an element of length following a deformation. It's easy to demonstrate that, under the hypothesis of small deformation, the quadratic terms in 1.5 can be neglected, obtaining the expression 1.2.

1.1.2 Stress Tensor

Another tensor of fundamental importance in Linear Elastic Theory is the *stress tensor*. Deformation can be induced by the presence of an external force or load. The stress tensor σ_ij is defined as the force per unit of area on the $i-th$ face along the $j-th$ direction. The

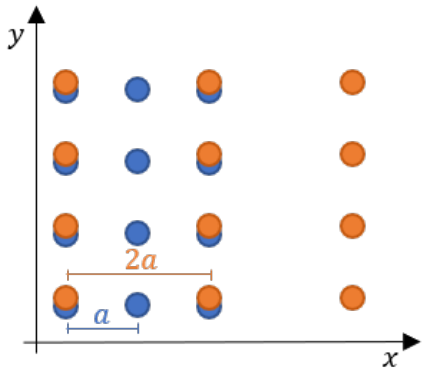

(a) A bidimensional square lattice before and after a uniform dilation of 100% along x, corresponding to $\varepsilon_{xx} = cost$

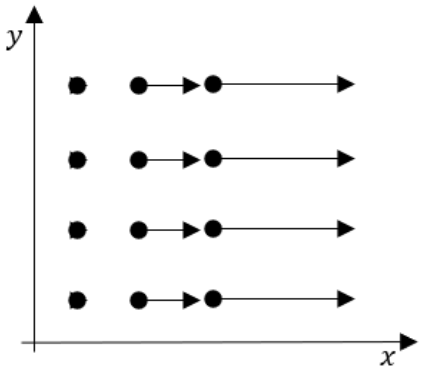

(b) Displacement field u for a uniform dilation of 100% along x, corresponding to $\varepsilon_{xx} = cost$

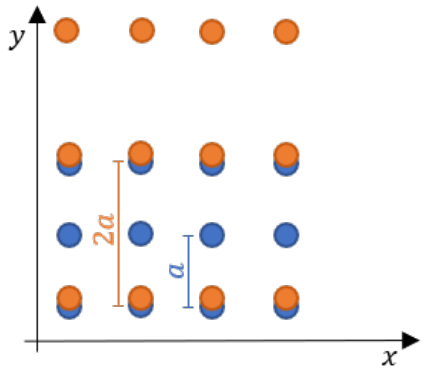

(c) A bidimensional square lattice before and after a uniform dilation of 100% along y, corresponding to $\varepsilon_{yy} = cost$

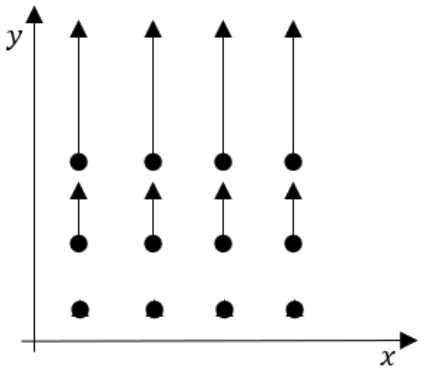

(d) Displacement field u for a uniform dilation of 100% along y, corresponding to $\varepsilon_{yy} = cost$

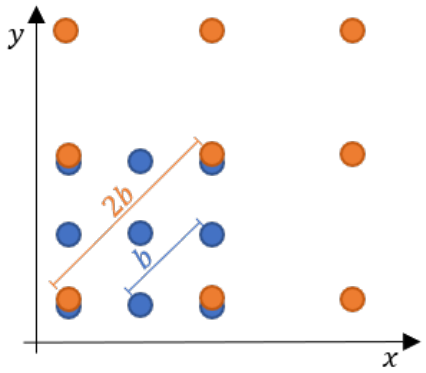

(e) A bidimensional square lattice before and after a diagonal uniform dilation of 100%, corresponding to $\varepsilon_{xy} = cost$

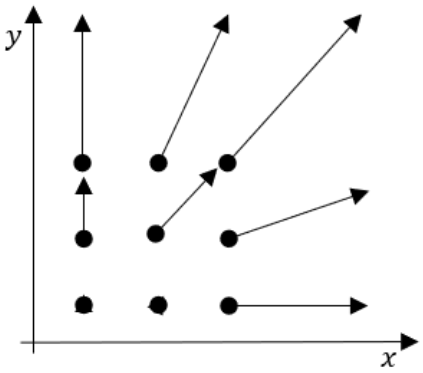

(f) Displacement field u for a diagonal uniform dilation of 100%, corresponding to $\varepsilon_{xy} = cost$

Figure 1.1: Relationship between deformation, displacements and strain.

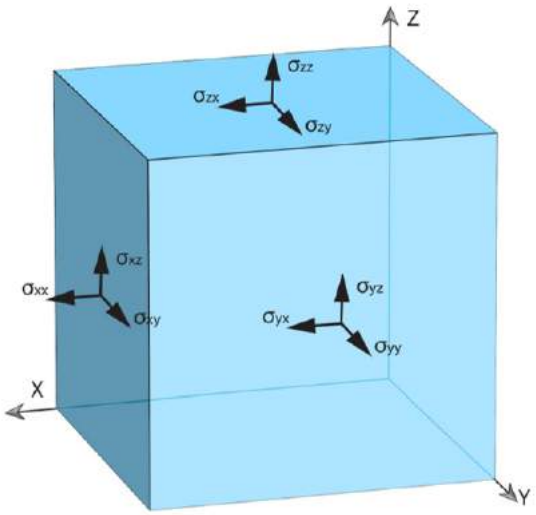

Figure 1.2: Stress tensor components σ_{ij}.

traction T_j represents the force per unit of area acting on a surface with normal vector $\hat{n}$ along the $j-th$ direction. The traction is related to the stress tensor by the relation:

$$\sigma_{ij}\, n_i = T_j \tag{1.6}$$

where $n_i = \hat{n} \cdot e_i$ and $\{e_i \;\; i = 1,2,3\}$ is a set of orthonormal vectors of the coordination system. At the equilibrium, the resultant of the forces acting on a system is zero. Given a solid body and the forces acting on it, the traction T_i acting on the surface, and the volume forces acting per unit of volume, at the equilibrium, the resultant can be written in the form:

$$\int_V f_i \, dV + \int_S T_i \, dS = 0 \tag{1.7}$$

Using the definition of T_i becomes

$$\int_V f_i \, dV + \int_S \sigma_{ij}\, n_i \, dS = 0 \tag{1.8}$$

By using the divergence theorem one obtains

$$\int_S \sigma_{ij}\, n_i \, dS = \int_V \frac{\partial \sigma_{ij}}{\partial x_i} \, dV \tag{1.9}$$

Thus the equation 1.8 becomes:

$$\int_{\mathrm{V}} (f_{\mathrm{i}} + \frac{\partial \sigma_{\mathrm{ij}}}{\partial x_{\mathrm{i}}})\, dV = 0 \tag{1.10}$$

The equilibrium equation is valid for an arbitrary volume, thus it's valid also for an infinitesimally small volume (should be valid punctually). The equation at the equilibrium is obtained imposing that the function to be integrated is equal to zero:

$$f_{\mathrm{i}} + \frac{\partial \sigma_{\mathrm{ij}}}{\partial x_{\mathrm{i}}} = 0 \tag{1.11}$$

It can be demonstrated that the strain tensor it's always symmetric and that its symmetry does not depend on the equilibrium conditions. Due to its intrinsic symmetries, it is made of only six independent entries.

1.1.3 Hooke's law and elastic constants

Linear elasticity is a simplification of the more general nonlinear elasticity theory. The fundamental assumption of linear elasticity is that the response of a system to an external force is linear. In mathematical terms, it can be written as a linear relationship between stress and strain:

$$\sigma_{\mathrm{ij}} = C_{\mathrm{ijnm}}\, \varepsilon_{\mathrm{nm}} \tag{1.12}$$

Where C_{ijnm} is the stifness tensor, a 4-order tensor which is made, in the most general case, by $3 \times 3 \times 3 \times 3 = 81$ entries. The equation 1.12 is a generalization in three dimensions of the mono-dimensional Hooke's law. Equation 1.12 can be inverted to define the compliance tensor S_{nmij}:

$$\varepsilon_{\mathrm{nm}} = S_{\mathrm{nmij}}\, \sigma_{\mathrm{ij}} \tag{1.13}$$

From now on the Voigt convention will be used for convenience. Considering that tensors $\bar{\bar{\varepsilon}}$ e $\bar{\bar{\sigma}}$ are symmetric, only six independent elements are present. In the Voigt notation, Stress and strain are represented as vectors with six components, which are the six independent entries, and $\bar{\bar{C}}$ is a 6×6 matrix. Thus the equation 1.12 becomes:

$$\begin{bmatrix} \sigma_{xx} \\ \sigma_{yy} \\ \sigma_{zz} \\ \sigma_{xy} \\ \sigma_{yz} \\ \sigma_{xz} \end{bmatrix} = \begin{bmatrix} C_{11} & C_{12} & \cdots & C_{16} \\ C_{21} & C_{22} & \cdots & C_{26} \\ \vdots & \vdots & \ddots & \vdots \\ C_{61} & C_{62} & \cdots & C_{66} \end{bmatrix} \begin{bmatrix} \varepsilon_{xx} \\ \varepsilon_{yy} \\ \varepsilon_{zz} \\ \varepsilon_{xy} \\ \varepsilon_{yz} \\ \varepsilon_{xz} \end{bmatrix} \tag{1.14}$$

Equation 1.14 has general validity and remains correct for symmetric systems and anisotropic systems. Given a crystal with cubic symmetry, it's possible to further reduce the number of elastic constants C_{ij} from 36 to only three independent entries. For a cubic crystal, the stiffness tensor can be written as:

$$C = \begin{bmatrix} C_{11} & C_{12} & C_{12} & 0 & 0 & 0 \\ C_{12} & C_{11} & C_{12} & 0 & 0 & 0 \\ C_{12} & C_{12} & C_{11} & 0 & 0 & 0 \\ 0 & 0 & 0 & C_{44} & 0 & 0 \\ 0 & 0 & 0 & 0 & C_{44} & 0 \\ 0 & 0 & 0 & 0 & 0 & C_{44} \end{bmatrix} \tag{1.15}$$

And the compliance tensor as:

$$S = \begin{bmatrix} S_{11} & S_{12} & S_{12} & 0 & 0 & 0 \\ S_{12} & S_{11} & S_{12} & 0 & 0 & 0 \\ S_{12} & S_{12} & S_{11} & 0 & 0 & 0 \\ 0 & 0 & 0 & S_{44} & 0 & 0 \\ 0 & 0 & 0 & 0 & S_{44} & 0 \\ 0 & 0 & 0 & 0 & 0 & S_{44} \end{bmatrix} \tag{1.16}$$

In the case of a cubic lattice also the following relationships stand:

$$\begin{aligned} C_{44} &= C_{11} - C_{12} \\ S_{44} &= S_{11} - S_{12} \end{aligned} \tag{1.17}$$

Thus the number of independent elements can be further reduced to two. Furthermore the components of the stiffness tensor are related to the compliance tensor by the following:

$$\begin{aligned} C_{11} &= \frac{1}{2}\left[\frac{1}{S_{11}+2S_{12}} + \frac{1}{S_{11}-2S_{12}}\right] \\ C_{12} &= \frac{1}{2}\left[\frac{1}{S_{11}+2S_{12}} - \frac{1}{S_{11}-2S_{12}}\right] \end{aligned} \tag{1.18}$$

And, inverting the equations 1.18:

$$\begin{aligned} S_{11} &= \frac{C_{11}+C_{12}}{(C_{11}-C_{12})(C_{11}+2C_{12})} \\ S_{12} &= \frac{C_{12}}{(C_{11}-C_{12})(C_{11}+2C_{12})} \end{aligned} \tag{1.19}$$

1.1.4 Poisson ratio, Young and bulk moduli and Lamè constants

Other two quantities are of main importance; these material specific constants are:

- The *Poisson ratio* ν that represents the ratio between the perpendicular expansion and the contraction in the direction of an external load;
- The *Young modulus* **E**, defined as the ratio between the uniaxial stress and the strain, in the limits of validity of Hooke's law.

The values of Poisson ratio and Young modulus, ν ed **E**, are reported in table 1.1, for silicon, germanium and silicon carbide. The value of the Poisson ratio reported for silicon is the mean value of those along the different crystallographic directions.

The components of compliance tensor can be expressed in terms of the elastic constants just defined as:

$$\begin{aligned} S_{11} &= \frac{1}{\mathbf{E}} \\ S_{12} &= -\frac{\nu}{\mathbf{E}} \end{aligned} \tag{1.20}$$

Table 1.1: Poisson ratio and Young modulus for Si, Ge and SiC.

Material	ν	E [Pa]
Si	0.27[i]	1.31×10^{11}
Ge	0.26	1.03×10^{11}
SiC	0.14	3.90×10^{11}

[i] Mean value of the Poisson ratio along the different crystallographic directions.

Often other constants are introduced in the use of elasticity theory, they are:

$$\begin{aligned} \mu &= \frac{\mathbf{E}}{2(1+\nu)} \\ \lambda &= \frac{\nu \mathbf{E}}{(1+\nu)(1-2\nu)} \\ K &= \lambda + \frac{2}{3}\mu \end{aligned} \tag{1.21}$$

Where μ (often called *shear modulus*) and λ are the second and the first *Lamè constants* while K is the *Bulk modulus*.

From these constants one can redefine the elasticity tensors C ed S in a simple and compact form:

$$\begin{aligned} C_{11} &= K + \frac{4}{3}\mu \\ C_{12} &= K - \frac{2}{3}\mu \\ S_{11} &= \frac{\mu + 3K}{9\mu K} \\ S_{12} &= \frac{2\mu - 3K}{18\mu K} \end{aligned} \tag{1.22}$$

In the same way the stress components can be rewritten using Lamè constants:

$$\begin{aligned} \sigma_{xx} &= 2\mu\varepsilon_{xx} + \lambda(\varepsilon_{xx} + \varepsilon_{yy} + \varepsilon_{zz}) \\ \sigma_{yy} &= 2\mu\varepsilon_{yy} + \lambda(\varepsilon_{xx} + \varepsilon_{yy} + \varepsilon_{zz}) \\ \sigma_{zz} &= 2\mu\varepsilon_{zz} + \lambda(\varepsilon_{xx} + \varepsilon_{yy} + \varepsilon_{zz}) \end{aligned} \tag{1.23a}$$

$$\begin{aligned}\sigma_{xy} &= 2\mu\varepsilon_{xy}\\ \sigma_{yz} &= 2\mu\varepsilon_{yz}\\ \sigma_{xz} &= 2\mu\varepsilon_{xz}\end{aligned} \tag{1.23b}$$

1.1.5 Elastic Energy

For a continuum medium, the stress tensor can be obtained from an elastic energy density function $U(\varepsilon_{ij})$, which is necessarily an exact differential.

$$\sigma_{ij} = \frac{\partial U}{\partial \varepsilon_{ij}} \tag{1.24}$$

Under the hypothesis of linearity, remembering the definition of the stiffness tensor 1.12, by substitution, one obtains that:

$$C_{ijnm} = \frac{\partial^2 U}{\partial \varepsilon_{ij}\partial \varepsilon_{nm}} \tag{1.25}$$

Integrating the equation 1.25 the expression for the density of elastic energy is obtained. The elastic energy for a system is obtained by integrating U on the whole volume

$$U = \frac{1}{2}\varepsilon_{ij}C_{ijnm}\varepsilon_{nm} = \frac{1}{2}\sigma_{nm}\varepsilon_{nm} \tag{1.26}$$

It can be expressed in an explicit form using the Lamè constants:

$$\begin{aligned}U = \frac{1}{2\mu}\left[\frac{\lambda+\mu}{3\lambda+2\mu}(\sigma_{xx}^2+\sigma_{yy}^2+\sigma_{zz}^2)+(\sigma_{xy}^2+\sigma_{yz}^2+\sigma_{xz}^2)\right]+\cdots\\ \cdots-\frac{1}{2\mu}\left[\frac{\lambda}{3\lambda+2\mu}(\sigma_{xx}\sigma_{yy}+\sigma_{xx}\sigma_{zz}+\sigma_{yy}\sigma_{zz})\right]\end{aligned} \tag{1.27}$$

1.1.6 Epitaxial Stress

In the introduction has been anticipated that the presence of a lattice mismatch characterizes epitaxial systems. Such a mismatch is the primary source of elastic stress in these systems. The lattice mismatch produces an in-plane biaxial strain parallel to the growing plane (in most cases, the plane is the (001)). The lattice mismatch depends on the lattice parameter of the film and the substrate. The mismatch value for silicon carbide films grown on silicon is $\approx 20\%$. The mismatch for silicon-germanium alloys depends on the

percentage of germanium in the SiGe alloy. Considering an isotropic system made by an alloy of silicon germanium, grown at the lattice parameter of the silicon substrate in the direction $\hat{n} \parallel \hat{y}$, the strain is equal to:

$$\varepsilon = \frac{a_{\mathrm{Si}} - a_{\mathrm{x}}}{a_{\mathrm{x}}} = 0.0399\, x \tag{1.28}$$

Where a_{x} is the lattice parameter of the epitaxial layer, x is the Ge percentage in the alloy, and a_{Si} is the lattice parameter of the silicon substrate.

The free surface of the film implies that:

$$\sigma \cdot \hat{n} = \sigma_{\mathrm{xy}} + \sigma_{\mathrm{yy}} + \sigma_{\mathrm{zy}} = 0 \tag{1.29}$$

Such a condition always stems at the free surface. In the presence of homogenous stress, like in the case of epitaxial systems, this condition has to be extended to the whole film to maintain the stress field. From the definition of biaxial stress, $\sigma_{\mathrm{xy}} = \sigma_{\mathrm{zy}} = 0$, it results that condition 1.29 becomes:

$$\sigma_{\mathrm{yy}} = 0 \tag{1.30}$$

For what concerns the strain, only diagonal terms are present:

$$\begin{aligned} \varepsilon_{\mathrm{xx}} &= \varepsilon_{\mathrm{zz}} = \varepsilon \\ \varepsilon_{\mathrm{yy}} &= f(\varepsilon) \\ \varepsilon_{\mathrm{ij}} &= 0 \quad se\ \ i \neq j \end{aligned} \tag{1.31}$$

In general, it's important to always remember that, in order to define the strain in direction normal to the growth direction, one has to consider the system 1.15 and the condition 1.30:

$$\begin{aligned} \sigma_{\mathrm{xx}} &= C_{11}\,\varepsilon_{\mathrm{xx}} + C_{12}\,\varepsilon_{\mathrm{yy}} C_{12}\,\varepsilon_{\mathrm{zz}} \\ 0 \ &= C_{12}\,\varepsilon_{\mathrm{xx}} + C_{12}\,\varepsilon_{\mathrm{yy}} C_{12}\,\varepsilon_{\mathrm{zz}} \\ \sigma_{\mathrm{zz}} &= C_{12}\,\varepsilon_{\mathrm{xx}} + C_{12}\,\varepsilon_{\mathrm{yy}} C_{11}\,\varepsilon_{\mathrm{zz}} \end{aligned} \tag{1.32}$$

From which is possible to obtain an expression for ε_{yy}:

$$\varepsilon_{yy} = -\frac{C_{12}}{C_{11}}(\varepsilon_{xx} + \varepsilon_{zz}) \tag{1.33}$$

Knowing all the components of the strain tensor of equation 1.26 is now possible to calculate the energy density of a film that undergoes a biaxial strain:

$$U = \frac{1}{2}\begin{pmatrix} C_{11}\varepsilon + C_{12}\varepsilon - \dfrac{2C_{12}^2}{C_{11}}\varepsilon \\ 0 \\ C_{11}\varepsilon + C_{12}\varepsilon - \dfrac{2C_{12}^2}{C_{11}}\varepsilon \end{pmatrix}^t \begin{pmatrix} \varepsilon \\ -\dfrac{C_{12}}{C_{11}}\varepsilon \\ \varepsilon \end{pmatrix} = Y\varepsilon^2 \tag{1.34}$$

con

$$Y = \left(C_{11} + C_{12} - 2\frac{C_{12}^2}{C_{11}}\right) \tag{1.35}$$

Y is the Young mosulus under biaxial strain, that, in the isotropic case, using ν and E, has the following form:

$$Y = \frac{2E(1+\nu)}{(1-\nu)} \tag{1.36}$$

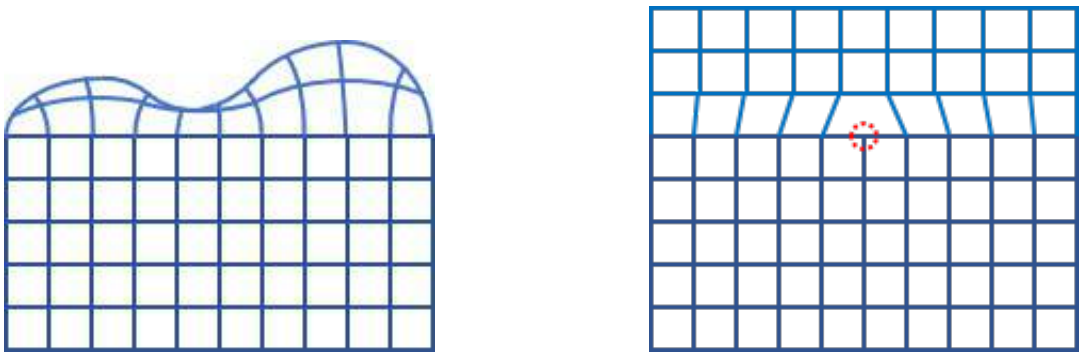

(a) Elastic relaxation ***(b)*** Plastic relaxation

Figure 1.3: Illustration of the two possible way to relax an epitaxial structure formed by a substrate (dark blue) and an epitaxial film (light blue) with square lattice.

The biaxial strain can influence the layer morphology during layer growth. In the first steps of a grow process, the film surface grows flat, but the accumulated misfit elastic energy grows as the thickness increases. The epitaxial layer can relax this energy in two

distinct ways: either trough the nucleation of island on the growing surface (*elastic relaxation*),[3–7] or trough the formation of dislocation at the interface with the substrate (*plastic relaxation*).[8–12] See Figure 1.3 for a comparison.

For most application flat films are required hence the latter relaxation mechanism is preferable.[13] In this Thesis we will consider only plastic relaxation in epitaxy. Therefore, in the next section, we will present in details the key concepts about dislocation; their characteristics, their evolution, and their formation.

1.2 Dislocations

Dislocations are line defects and, even if their presence is observed microscopically, to describe them is mandatory to refer to a crystalline lattice.[14]

1.2.1 Dislocation in crystals

Each dislocation can be classified using two entities which are the *Burgers vector* and *dislocation line*. The two main classes of dislocations are *edge* dislocations and *screw* dislocations.

Edge dislocation

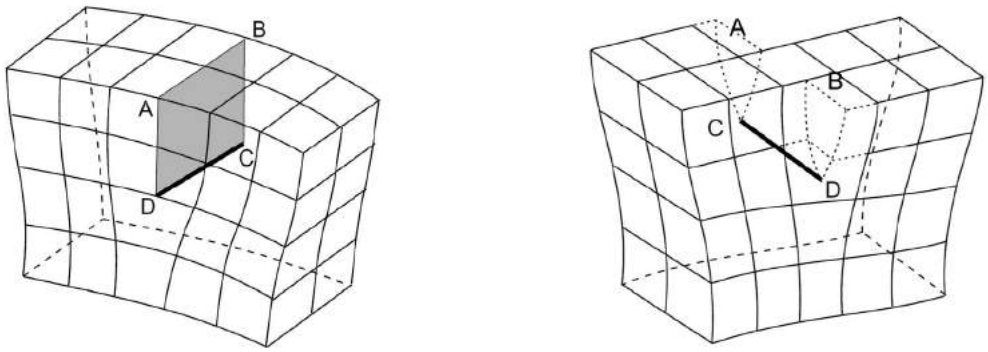

(a) model of a positive edge dislocation "DC" obtained by the insertion of an extra half plane of atoms in "ABCD".

(b) Model of a counterclockwise screw dislocation "DC" model obtained shifting "ABCD" sides in the "AB" direction in an opposite way.

Figure 1.4: Illustration of edge and screw dislocations for a simple cubic lattice.

An edge dislocation is a line extended defect. In a simple cubic lattice, it can be obtained by introducing an extra half-plane of atoms inside a crystal as displayed in figure 1.4 (**a**). To obtain such a dislocation, all the interatomic bonds that intersect the ABCD surface are broken. The two halves are separated so that the extra plane of atoms can be inserted in between. The faces of the two halves are now separated by a quantity equal to a single lattice step. After this procedure, the relative position of atoms with their surroundings is altered only relatively, except for particles close to the segment CD which is called dislocation line and it's denoted by the vector $\vec{\xi}$. Inter atomic bond distortion and bending will decrease gradually with the increase of the distance from the dislocation line.

Screw Dislocation

A screw dislocation can be realized by shifting the two halves introduced in the preceding section along the new direction AB in an opposite way. An example of a screw dislocation is showed in Figure 1.4 (**b**). In the present case, after the shifting equal to the lattice parameter of the two faces along AB, broken bonds that cross the ABCD surface are replaced by new bonds.

Generally talking, in dealing with dislocation, it's helpful to introduce some concepts. One of the most important ones is the concept of the Burgers circuit and consequently that of Burgers vector.[15] In a crystal lattice, the Burgers circuit is any closed path from atom to atom that surrounds dislocations. Therefore it's a sequence of "steps" which define a circuit, as the one shown in Figure 1.5 (**a**). By repeating the same sequence in the ideal crystal, where no dislocations are present, one obtains a circuit that is no more a closed path, as shown in Figure 1.5 (**b**). The vector necessary to close the latter circuit is called Burgers vector $\vec{b}$.[2]

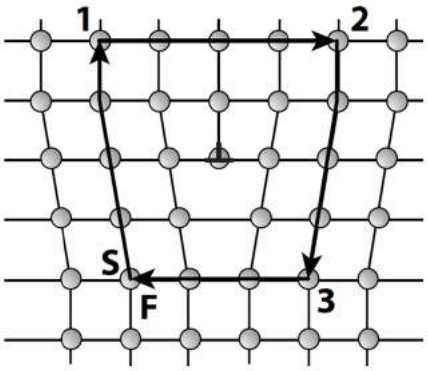

(a) Burgers circuit in a crystal with a dislocation line $\vec{\xi}$. Dislocation line is normal to the view direction.

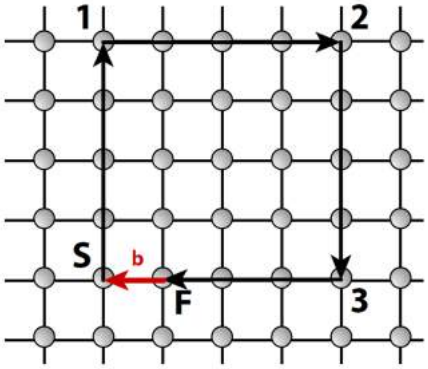

(b) Burgers circuit referred to the ideal perfect crystal.

Figure 1.5: Burgers circuit in a crystal with and without a dislocation. The circuits starts in *S* and ends in *F*. In the perfect crystal an additional vector equal to $\vec{b}$ is necessary to close the circuit.

Two convention have to be introduced to build a Burgers circuit: first of all, aligning the view in the direction of the dislocation line, the circuit must be directed clockwise; secondly, the Burgers vector must be directed in such a way that it goes from the starting

point to the final point of the Burgers circuit (in the perfect crystal). With these conventions, it can be demonstrated that inverting the direction of the dislocation line also the direction of the Burgers vector is inverted. A formal definition of $\vec{b}$ is given by the line integral along a closed path C in the clockwise direction with respect to the dislocation line $\vec{\xi}$, of the elastic displacement $\vec{u}$ around the dislocation:[2]

$$\vec{b} = \oint_C \frac{\partial \vec{u}}{\partial l} dl \tag{1.37}$$

Now it's possible to define the glide plane as the one generated by the two vectors $\vec{b}$ and $\vec{\xi}$, identified by the normal vector $\hat{n}$ given by the vector product $\vec{b} \times \vec{\xi}$.

Two fundamental observations arise from the definitions given above:

- Edge dislocations have their Burgers vector orthogonal to the dislocation line.
- Screw dislocations have their Burgers vector parallel or anti-parallel to the dislocation line.

This is valid for ideal dislocations which are either edge or screw, but more in general, dislocations can form an arbitrarily angle with their Burger vector. Therefore, a generic dislocation has a screw component which is given by:

$$\vec{b}_{\text{screw}} = \vec{\xi} * (\vec{b} \cdot \vec{\xi}) \tag{1.38a}$$

and an edge component given by:

$$\vec{b}_{\text{edge}} = \vec{\xi} \times (\vec{b} \times \vec{\xi}) \tag{1.38b}$$

1.2.2 Stress fields of a dislocation

In section 1.1.6 the stress field induced by epitaxial growth was introduced. Dislocation lines can generate stress their selves. Linear elasticity theory can be applied to describe strain and stress field generated by a dislocation excluding only a small region around the dislocation line. In the surroundings of the dislocation line, indeed, the displacements from equilibrium positions are too big that Hooke's law 1.12 is no more valid.[2] To start, it's simpler to begin introducing the case of a dislocation line in an infinite bulk.

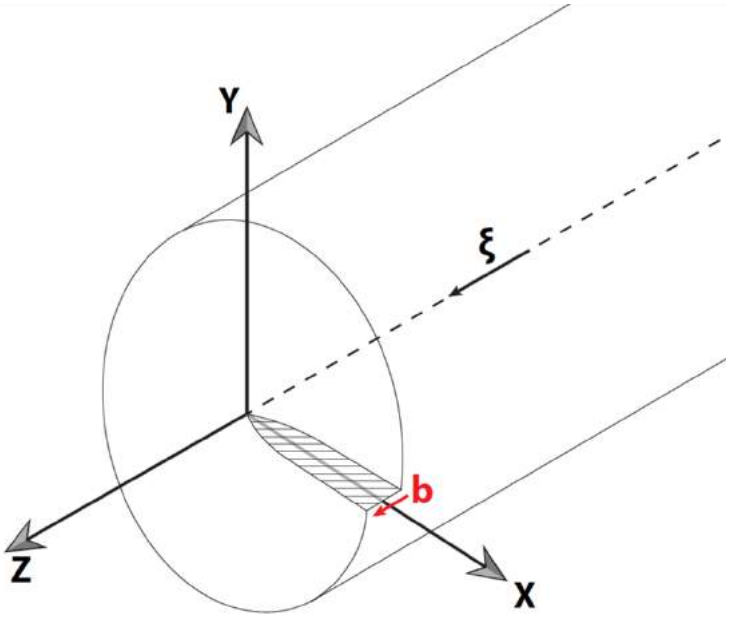

Figure 1.6: Stress field for a screw dislocation with dislocation line $\vec{\xi}$.

Stress field of a screw dislocation

A screw dislocation can be represented as in Figure 1.6. Let's consider a cylinder, and let's R be its radius and L its length. The cylinder axis is the dislocation line $\vec{\xi}$, as in Figure 1.6. A screw dislocation can be obtained from a perfect crystal by applying a shear displacement along z direction with slipping plane xz. The slipping plane is often called *"glide plane"* or *"slip plane"*. An operation of calculation of the Burgers vector $\vec{b}$ along a close circuit that surrounds the dislocation line would show that the considered dislocation is characterized by having a positive Burgers vector. It's evident in Figure 1.6 that the displacements u_x e u_y are both null, an that the displacement u_z has a discontinuity in $y = 0, x > 0$ defined as follow:

$$\lim_{\eta \to 0} \left[u_x(x,-\eta) - u_z(x,\eta) \right] = b_z \quad \eta > 0 \tag{1.39}$$

In the case of an isotropic medium, u_z can be written conveniently in cylindrical coordinates*:

$$u_{r,\theta} = b\frac{\theta}{2\pi} = \frac{b}{2\pi}\arctan\frac{y}{x} \tag{1.40}$$

*The function $f(x) = \arctan(x) : \mathbb{R} \to [-\frac{\pi}{2}; \frac{\pi}{2}]$ returns the angle between $-\frac{\pi}{2}$ e $\frac{\pi}{2}$ while the θ angle is in the interval $[0, 2\pi]$. The correct function that should be used is the two values function $f(x,y) = \arctan 2(x,y) : \mathbb{R}^2 \to [-\pi; \pi]$

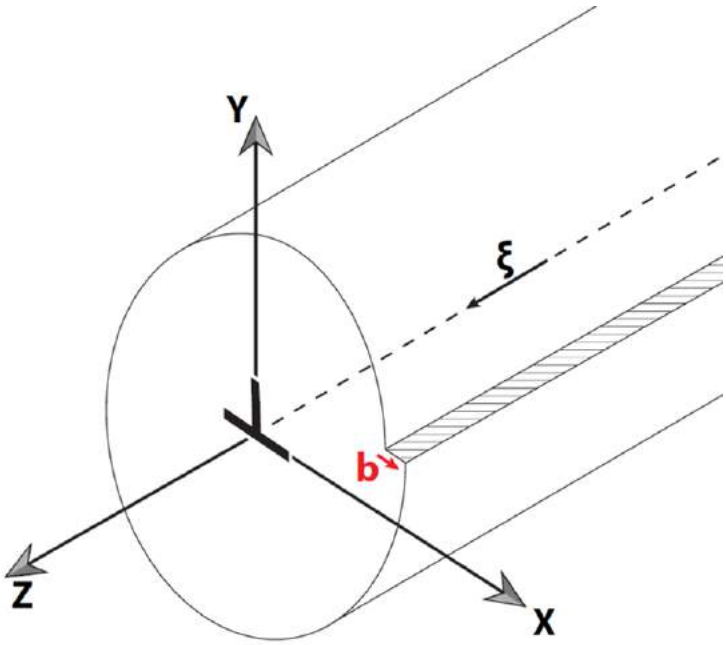

Figure 1.7: Stress field for an edge dislocation with dislocation line $\vec{\xi}$.

Being satisfied the elasticity equation 1.12 it's possible to calculate all the entries of the stress tensor from the displacement field:

$$\begin{aligned}
&\sigma_{xx} = \sigma_{yy} = \sigma_{zz} = 0 \\
&\sigma_{xy} = 0 \\
&\sigma_{xz} = -\frac{\mu b}{2\pi}\frac{y}{x^2+y^2} \\
&\sigma_{yz} = -\frac{\mu b}{2\pi}\frac{x}{x^2+y^2}
\end{aligned} \tag{1.41}$$

Stress field for an edge dislocation

Also, an edge dislocation can be described as the deformation of a cylinder made of an isotropic medium. An edge dislocation is characterized by having a perpendicular Burgers vector $\vec{b}$ and dislocation line $\vec{\xi}$. Let's consider a dislocation line as shown in Figure 1.7. It is parallel to the direction z and coincides with the cylinder axis, while the Burgers vector is directed along the direction x. In this case there aren't any strain nor any displacement in the z direction, and the deformation is called "plane strain". The components of the

stress field are given by the equations:

$$\sigma_{xx} = -\frac{\mu b}{2\pi(1-\nu)} \frac{y(3x^2+y^2)}{(x^2+y^2)^2} \tag{1.42}$$

$$\sigma_{yy} = -\frac{\mu b}{2\pi(1-\nu)} \frac{y(x^2-y^2)}{(x^2+y^2)^2} \tag{1.43}$$

$$\sigma_{zz} = -\frac{\mu b \nu}{2\pi(1-\nu)} \frac{y}{(x^2+y^2)} = \nu(\sigma_{xx}+\sigma_{yy}) \tag{1.44}$$

$$\sigma_{xy} = -\frac{\mu b}{2\pi(1-\nu)} \frac{x(x^2-y^2)}{(x^2+y^2)^2} \tag{1.45}$$

$$\sigma_{yz} = 0 \tag{1.46}$$

$$\sigma_{xz} = 0 \tag{1.47}$$

A complete derivation of these expressions can be found *Theory of Dislocations.*[2] These simple analytical solutions present an intrinsic singularity along the dislocation line that can lead to divergence when calculating energy and force. A non-singular formulation of stress fields has been studied by Cai, Arsenlis, Weinberger, and Bulatov in.[16]

From the relations between stress and strain 1.23 and from the definition of strain 1.2 one can obtain the displacement field for an edge dislocation by integration:

$$\begin{aligned} u_x &= \frac{b}{2\pi}\left[\arctan\frac{y}{x} + \frac{xy}{2(1-\nu)(x^2+y^2)}\right] \\ u_y &= \frac{b}{2\pi}\left[\frac{1-2\nu}{4(1-\nu)}\, ln(x^2+y^2) + \frac{x^2-y^2}{4(1-\nu)(x^2+y^2)}\right] \end{aligned} \tag{1.48}$$

A deformation like the one in Figure 1.7 has a discontinuity in the displacements u_x in $x > 0$, and in particular on the x axis with $\eta > 0$ we have:

$$\begin{aligned} \lim_{x\to-\infty} \Delta u_x &= u_x(x,\eta) - u_x(x,-\eta) = 0 \\ \lim_{x\to\infty} \Delta u_x &= u_x(x,\eta) - u_x(x,-\eta) = b \end{aligned} \tag{1.49}$$

The solutions 1.48 of the displacement field have a discontinuity in the origin, where the dislocation is placed. Still, this is not a problem when dealing with a discrete lattice. Indeed (unlike in the case of a continuum medium), the displacements are well defined in every point of the lattice (having care not to place the dislocation on an atomic position).

Function $\Delta u_x(x,0)$ trend is showed in Figure 1.8 (**b**). Points in the tensile half-plane

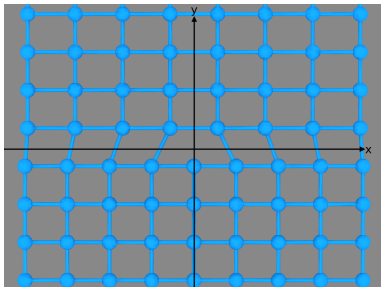

(a) An edge dislocation for simple cubic lattice.

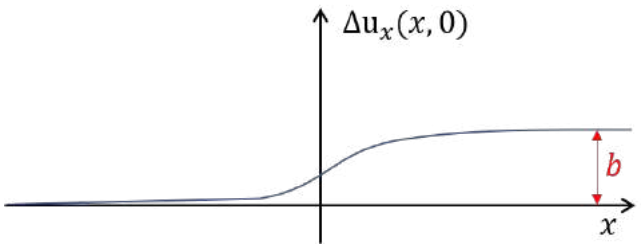

(b) Jump of the function $\Delta u_x(x,0)$ for an edge dislocation.

Figure 1.8: Jump of the function $\Delta u_x(x,0)$ for an edge dislocation.

(above) accumulated an increasing amount of disparity $d(\Delta u_x)$ with respect to the points of the other half-plane until the accumulated displacement is equal to b. In an atomistic system, that is translated in the insertion of an increasing amount of disparity between atomic positions until the crystalline structure is re-obtained again (see Figure 1.8 (**a**)).

Hence, we have that in the vicinity of the x axis, with $\eta > 0$:

$$\int_{-\infty}^{\infty} d(\Delta u_x) = \lim_{\eta \to 0^+} \int_{-\infty}^{\infty} d\left(u_x(x,\eta) - u_x(x,-\eta)\right) = b \tag{1.50}$$

And from the strain definition, still with $\eta > 0$,

$$\int_{-\infty}^{\infty} \left(\frac{\partial u_x(x,\eta)}{\partial x} - \frac{\partial u_x(x,-\eta)}{\partial x} \right) dx = \int_{-\infty}^{\infty} \left(\varepsilon_{xx}(x,\eta) - \varepsilon_{xx}(x,-\eta) \right) dx = b \tag{1.51}$$

It can be verified easily that the strain field derived from 1.47, satisfy the condition 1.51. It should be noted that this condition is satisfied in a different way depending on the formalism that has been used to express the stress and strain field. The stress, in the case of dislocation with an extra half-plane in $y < 0$ and Burgers vector directed along the positive direction of x axis, as in Figure 1.8 (**a**), we always have that for $\eta > 0$, $\eta \to 0^+$:

$$\begin{aligned} \int_{-\infty}^{\infty} \varepsilon_{xx}(x,\eta)\, dx &= \frac{b}{2} \\ \int_{-\infty}^{\infty} \varepsilon_{xx}(x,-\eta)\, dx &= -\frac{b}{2} \\ \implies \int_{-\infty}^{\infty} \left(\varepsilon_{xx}(x,\eta) - \varepsilon_{xx}(x,-\eta) \right) dx &= b \end{aligned} \tag{1.52}$$

In simple terms, the condition 1.51 indicates that each dislocation expands the tensile region by a factor equal to $\vec{b}$ with respect to the compressive region.

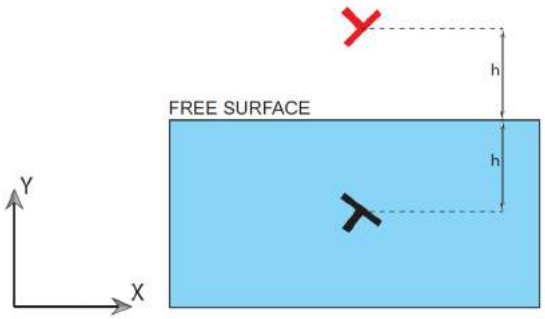

Figure 1.9: Construction of an image dislocation.

1.2.3 Free surface effects

The role of surfaces is of primary importance. Indeed, infinite straight dislocation lines cannot exist in a perfect bulk crystal: the elastic energy of a single dislocation in bulk diverges because of its long-range strain and stress fields. Dislocations must start and end on another defect or a surface, forming loops or semi-loops. Beyond that, heteroepitaxial structures have a limited thickness of few hundreds of nm typically. For all these regions and many more, the role of the free surface is not negligible.

Let's consider a dislocation placed in the origin of a cartesian reference system and a free surface with normal vector $\hat{n}$ parallel to y axis. Let's assume that the thickness of the film is h, the boundary condition set by the existence of the free surface is the equation 1.29 and hence we have:

$$\sigma \cdot \hat{n} = 0 \quad at \quad y = h \tag{1.53}$$

Molecular dynamics, which will be used in this Thesis to model dislocation evolution, automatically reproduce the condition 1.53. Indeed the equilibration of the system makes the system evolve toward a final configuration that has at the free surface, at equilibrium $\sigma \cdot \hat{n} = 0$.

It's also possible to obtain a configuration that has $\sigma \cdot \hat{n} = 0$ by considering a displacement field made by a dislocation and its virtual image above the surface.

1.2.4 Image dislocation

It's possible to analytically satisfy the condition 1.53 using a construction very similar to the method of image charges used in electrostatic. In analogy with the electrostatic

method, here we use a mirror image of the dislocation above the free surface. This method is also called "dislocation dipole." While the electric charge in a point x_0 is defined by a scalar quantity q, a dislocation is defined by a vector $\vec{b}$. Therefore the image dislocation is a dislocation placed in a mirror-symmetric point with respect to the surface, and its Burgers vector is inverted $-\vec{b}$. With reference to Figure 1.9: the dislocation is placed in the point $(x_0^{\text{disl}}, y_0^{\text{disl}})$, the free surface, with normal vector $\hat{n}$, is placed at the height $y = h$ and the image dislocation is placed in the point $(x_0^{\text{disl}}, y_0^{\text{disl}} + 2h)$. The Burgers vector of the image dislocation is:

$$\vec{b}_{\text{imm}} = -\vec{b}_{\text{disl}} \tag{1.54}$$

The condition 1.53 for this system becomes:

$$\sigma \cdot \hat{n} = \sigma_{\text{xy}} + \sigma_{\text{yy}} + \sigma_{\text{yz}} = 0 \tag{1.55}$$

In the case of more complex dislocation geometries, the image method is not enough to obtain the condition1.29 and a further correction term has to be added.[17]

1.3 Dislocations in diamond/zinc-blende crystals

Silicon, germanium, and cubic silicon carbide have a diamond/zinc-blende crystalline structure (zinc-blende in the case of the cubic SiC). In these crystalline structures the smallest vectors that connect two atomic positions inside the lattice are those belonging to the class $\frac{1}{2}\langle 110\rangle$ and $\langle 100\rangle$. Being the smallest possible vectors makes them the preferred ones for the formations of dislocation because they introduce deformation with lower energy (as will be discussed later, this energy is proportional to $\vec{b}^2$).

The dislocation elastic energy is proportional to the square modulus of its Burgers vector,[2] therefore the elastic energy of dislocations of the family $\frac{1}{2}\langle 110\rangle$ is only half that of those in $\langle 100\rangle$ family. This is the reason why dislocations $\langle 100\rangle$ are energetically less favorable and less abundant in non strained crystals. Dislocation with Burgers vector along $\langle 110\rangle$ are called "60° dislocations" because the angle between the Burgers vector and the dislocation line is indeed 60°. When the Burgers vector is oriented in a $\langle 110\rangle$ direction and is perpendicular to a dislocation line $\vec{\xi}$ which is in one of the $\langle 110\rangle$ direction is called "Lomer", "edge" or "90°" dislocation for the same reason.

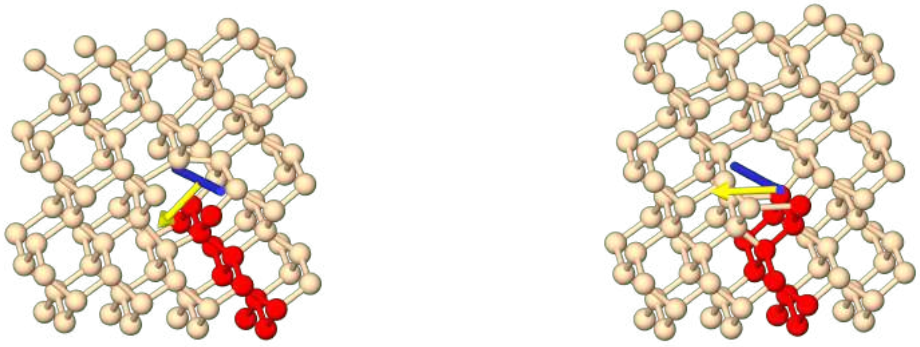

(a) A 60° perfect dislocation. ***(b)*** A 90° perfect dislocation.

Figure 1.10: Perfect dislocations in diamond lattice. A red color highlight the atoms of the extra half-planes. The blue line is the dislocation line $\vec{\xi}$, the yellow arrow is the Burgers vector $\vec{b}$.

A slip (sometimes "glide") system is the set of symmetrically identical slip (glide) planes and associated families of glide directions for which dislocation motion can easily occur. Possible glide systems are conventionally represented using the *Thompson tetrahedron* shown in Figure 1.11. Considering a cell oriented in such a way that the dislocation line coincides with the "CD" direction, we can identify:

- An edge (90°) dislocation with $\vec{b}$ in the AB direction
- A screw dislocation with $\vec{b}$ in the CD direction
- A 60° dislocation with $\vec{b}$ in the AD, AC, BD, BC directions

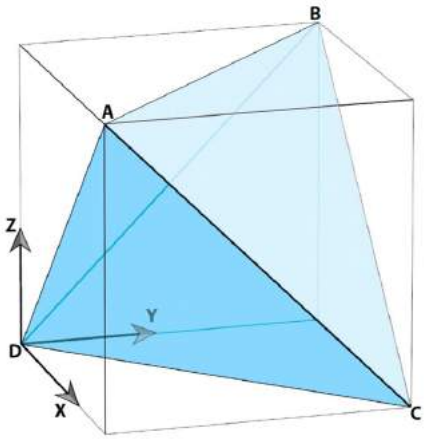

Figure 1.11: One eighth of the unitary cell of the fcc lattice with a Thompson tetrahedron inside it: tetrahedron faces are all the possible glide planes and the edges are all the possible glide directions, i.e. all possible $\vec{b}$ e $\vec{\xi}$.

Given the dislocation line direction, for a 60° dislocation, there exists a total of two glide planes and eight possible Burgers vectors, four of them relax the compressive stress in the epilayer and the other four the tensile stress (considering a growth on (001) substrate). Considering a dislocation line in the [110] direction (CD), the two possible glide planes are (111) (ACD) and (1$\bar{1}$1) (BCD), each of them have a total of four Burgers vectors. They are subdivided as follows:

Glide plane	Burgers vectors:			
(111) (ACD)	[0$\bar{1}$1] (AC)	[101] (AD)	[01$\bar{1}$] (CA)	[$\bar{1}$0$\bar{1}$] (DA)
(1$\bar{1}$1) (BCD)	[10$\bar{1}$] (BC)	[011] (BD)	[$\bar{1}$01] (CB)	[0$\bar{1}\bar{1}$] (DB)

Table 1.2: Glide planes of a 60° dislocation and suitable Burgers vectors. In the parenthesis the Thompson tetrahedron edges.

1.3.1 Glide and shuffle set

The presence of a dislocation inside a solid significantly changes crystalline ordering only in the proximity of the dislocation line. Indeed, at a sufficient distance from the dislocation, the relative position of atoms are those of the perfect crystal, i.e., diamond/zinc-blende structure for silicon, germanium, and cubic silicon carbide. In the vicinity of the dislocation line, the structure is extremely different from the perfect crystal, and possible atomic geometries around the dislocation line are usually called *dislocation core*. In the case of 60° dislocations, the possible geometries were first described by J. Hornstra.[18] They correspond to have the dislocation in the glide and shuffle subset of {111} planes, and therefore they are two for each possible glide plane. The edge component of a 60° dislocation implies the presence of an extra half-plane of atoms in the lattice. The diamond/zinc-blende structure is made by a *face centered cubic* (fcc) lattice with a bi-atomic base, and each {111} plane is made up of a plane of pairs of atoms (a bi-layer). Essentially in the case of the glide set {111} planes appears to be formed of close {111} planes of single atoms (one for each atom of the base), while in the case of the shuffle subset, they appear to be formed of distant {111} planes of single atoms. In the case of 60° dislocation core, two

different configurations are possible depending on where the slipping plane of the dislocation is placed, if the dislocation line lays exactly in between two close {111} planes or in between two distant {111} planes. The two possible configurations are characterized by a different termination of the extra half-plane of atoms. In Figure 1.12 and in Figure 1.14 it is shown how the two possible configuration can be obtained.

Glide core

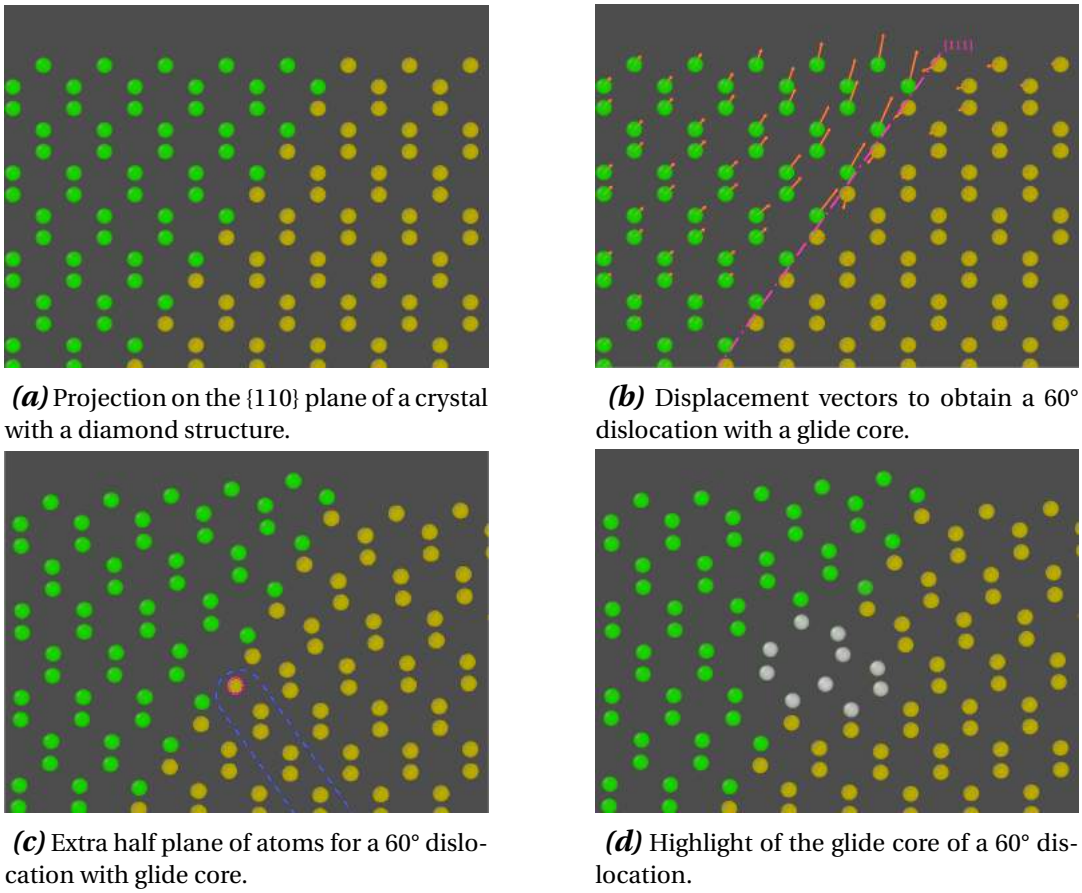

(a) Projection on the {110} plane of a crystal with a diamond structure.

(b) Displacement vectors to obtain a 60° dislocation with a glide core.

(c) Extra half plane of atoms for a 60° dislocation with glide core.

(d) Highlight of the glide core of a 60° dislocation.

Figure 1.12: Projections on the {110} plane of a crystal with diamond structure where a 60° dislocation perpendicular to the sheet has been inserted in the glide subset in such a way that a glide core is produced. The dashed purple line shows the cutting plane between two {111} close planes. Note the extra plane of atoms that terminates with a single atom in (c).

Figure 1.12 (**a**) shows the projection of a perfect crystal on the {110} plane. In Figure 1.12 (**b**) orange arrows show how the two halves of the crystal delimited by the plane {111}, that is between two close atomic planes (in the {111} projection), are displaced. After the shifting, a double row of atoms (which in 3-D is a double plane) terminates in correspondence of the {111} plane. In the presented case, the dislocation has a glide core. In the

plane view, it is characterized by a 7-ring and a 5-ring highlighted in Figure 1.12 (**d**).

The glide core is characterized by a structure where all the atoms are tetra-coordinated. For this reason, the energy of a 60° dislocation glide core is lower than the one of a shuffle 60° dislocation. Even though the absence of dangling bonds limits its motion. Figure 1.13 shows the core structure of 60° dislocation in three dimensions and the absence of under-coordinated atoms.

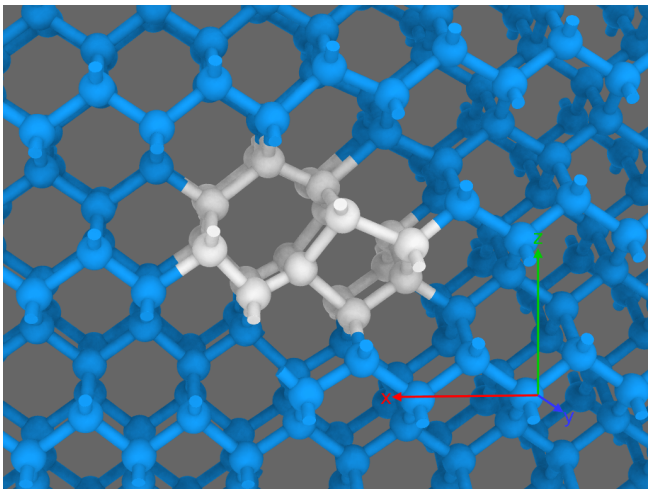

Figure 1.13: Glide core of a 60° dislocation.

Shuffle core

Figure 1.14 shows that, to have a shuffle core, the two halves of the crystal are delimited by the {111} plane that is in between two distant atomic planes. After the displacement, a double row of atoms terminates in correspondence of the {111} plane with a pair of particles (Figure 1.14 (**c**)). The shuffle core is characterized by a single 8-ring highlighted in panel (**d**).

In the case of the shuffle core, there is an under-coordinate atom, with a *dangling bond*, this allows shuffle dislocations to have higher mobility with respect to glide core dislocations. Notably, shuffle core dislocations tend not to split as described in section 1.3.2 because stacking fault (SF) in the shuffle set has very high energy. In Figure 1.15 it's possible to notice the under-coordination of the last atom of the extra half-plane (circled in red in Figure 1.14 (**c**)).

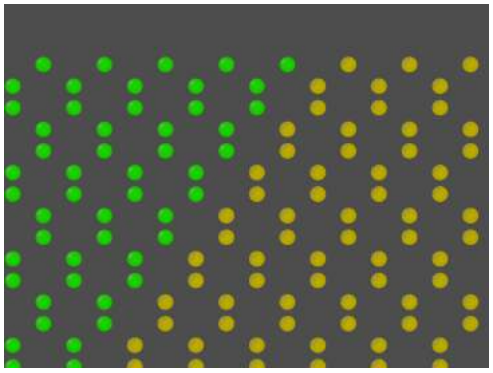

(a) Projection on the {110} plane of a crystal with a diamond structure.

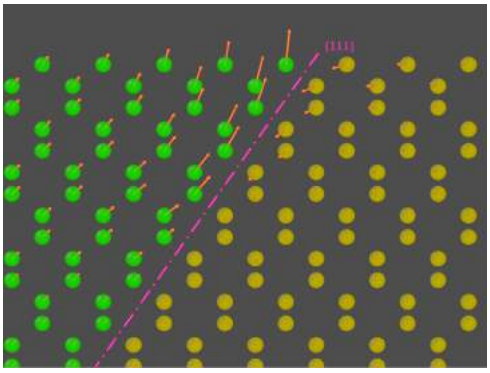

(b) Displacement vectors to obtain a 60° dislocation with a shuffle core.

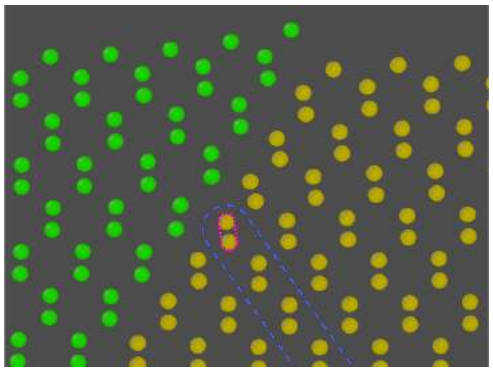

(c) Extra half plane of atoms for a 60° dislocation with shuffle core.

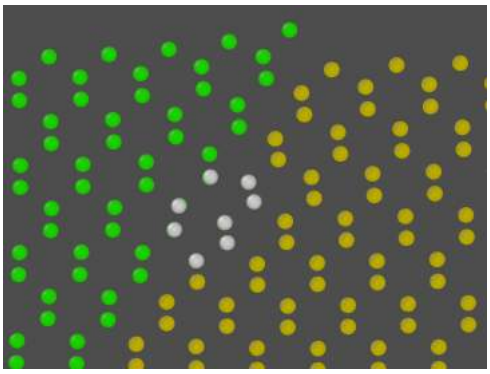

(d) Highlight of the shuffle core of a 60° dislocation.

Figure 1.14: Projections on the {110} plane of a crystal with diamond structure where a 60° dislocation perpendicular to the sheet has been inserted in the shuffle subset in such a way that a shuffle core is produced. The dashed purple line shows the cutting plane between two {111} distant planes. Note the extra plane of atoms that terminates with a pair atoms in (c).

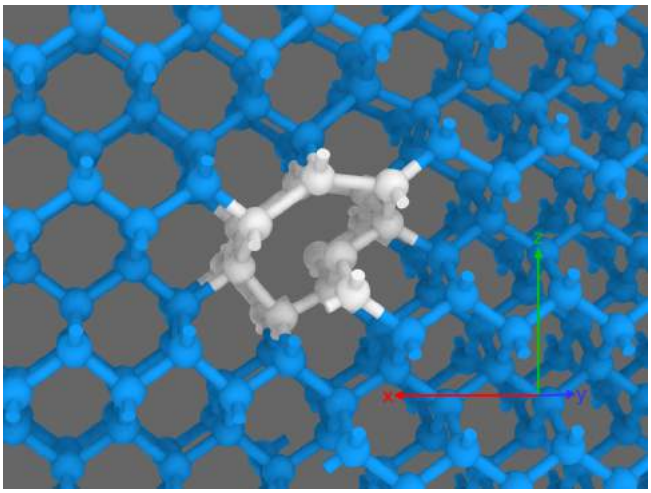

Figure 1.15: Shuffle core of a 60° dislocation.

1.3.2 Partial dislocations and stacking Faults

As anticipated in the preceding section, the self energy of a dislocation line is proportional to the square of the Burgers vector of the dislocation. Thus any dislocation with a Burgers vector $\vec{b}$ would find energetically favourable to split up into two dislocations $\vec{b}_1$ and $\vec{b}_2$, provided that $\vec{b}^2 > \vec{b}_1^2 + \vec{b}_2^2$. This is the case, for example when $\vec{b}_1 = \vec{b}_2 = \frac{1}{2}\vec{b}$. Therefore it's energetically favourable to spit up a dislocation into dislocations whose Burgers vector is as small as the structure of the lattice permits. Frank first formulated a general rule[19] that states that, if $\vec{b}$, $\vec{b}_1$ and $\vec{b}_2$ are permissible Burgers vectors in a particular crystal lattice, a dislocation with the Burgers vector $\vec{b}$ will split up into dislocations $\vec{b}_1$ and $\vec{b}_2$ if:

$$\vec{b}^2 > \vec{b}_1^2 + \vec{b}_2^2 \tag{1.56a}$$

and will not split if:

$$\vec{b}^2 < \vec{b}_1^2 + \vec{b}_2^2 \tag{1.56b}$$

Suppose we restrict ourselves to *perfect dislocations* in diamond/zinc-blende structure, the smallest Burgers vector possible, points toward the various possible ⟨110⟩ directions. The length of these Burgers vectors is the distance from the center of one atom to the center of the next atom along any of these directions. The term perfect dislocation means a dislocation that leaves the atoms in a position equivalent to those occupied originally as it moves past along its slip plane. If a is the lattice parameter of the lattice, the length of the smallest Burgers vector possible to a perfect dislocation is $a/\sqrt{2}$. This Burgers vector can be written:

$$b = \frac{a}{2}[110] \tag{1.57}$$

Dislocations of the type $\frac{a}{2}[110]$ that lie on (111) planes may lower their energy by combining among themselves (for example, forming a Lomer dislocation) or by splitting up into several new dislocations.

The most important reaction involving perfect and partial dislocations is the *dissocation* of a perfect dislocation into two *Shockley partial dislocations*. A perfect dislocation with Burgers vector of $\frac{a}{2}[110]$ can split into Shockley dislocations with the following Burgers vector:

$$\frac{a}{2}[\bar{1}01] \rightarrow \frac{a}{6}[\bar{2}11] + \frac{a}{6}[\bar{1}\bar{1}2] \tag{1.58}$$

Such dissociation will be shown in Chapter 3 in Figure 3.2. A perfect dislocation (in blue) which is surrounded by a perfectly reconstructed crystal (light blue atoms) split up into two Shockley partial dislocations (in green). Between the two partial dislocations, orange atoms show the presence of a stacking fault. A stacking fault appears because the two vectors $\frac{a}{6}[\bar{2}11]$ and $\frac{a}{6}[\bar{1}\bar{1}2]$ connect two atomic position in the diamond lattice but belonging two sites of two different fcc lattices that made up the diamond structure. A fault is now introduced in the ordering of the atomic layers as will be described later in Section 1.4.

1.3.3 Dislocation motion

When a solid crystalline material undergoes external force, dislocations already present in the crystal or nucleated consequentially to growth processes move throughout the crystal until a free surface is reached where the macroscopic deformation is observed.

Dislocation motion follows two complementary ways: by glide motion and by climb motion.

The glide motion is achieved making slipping the dislocation line in the plane, which is determined by the Burgers vector $\vec{b}$ and the dislocation line $\vec{\xi}$, which is named as anticipated before *glide plane*. The motion along the glide plane is called *conservative motion* because only swapping the atomic bonds is needed to achieve motion.

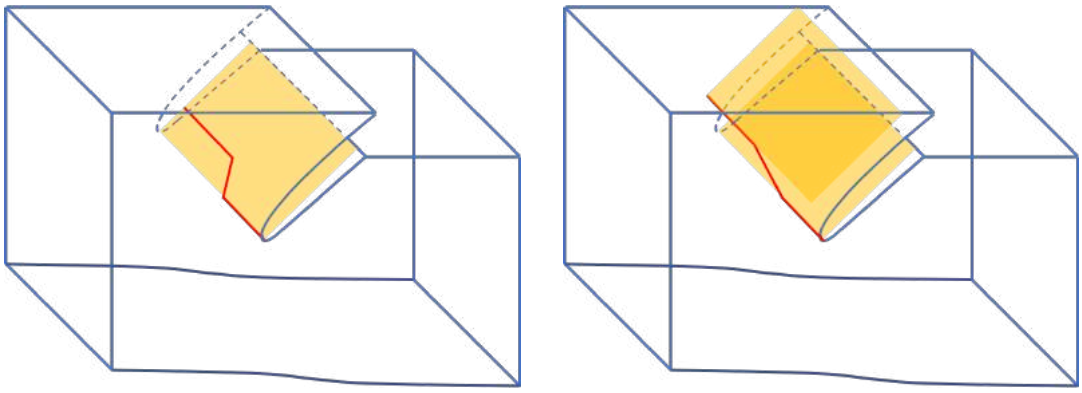

(a) 60° dislocation kink ***(b)*** 60° dislocation jog

Figure 1.16: 60° dislocation kinks and jogs.

At high temperatures, when high mobility of atoms is possible, and an out of equilibrium concentration of point defects is present, the dislocation can also migrate outside its slip plane, thanks to a climbing process. Instead, at low temperatures, only the glide motion is active. Because several atoms need to be added or removed to make a dislocation climb, such a motion is often called "*non-conservative motion*." Let's consider a straight dislocation line moved along its glide plane, as shown in Figure 1.16 (**a**); we can observe that a *kink* connects two dislocation line straight segments. Indeed, the glide motion is characterized by the formation of two symmetric kinks, followed by the migration in two opposite directions. The migration of the kinks leads to an enlargement of the dislocation line on the new position. Because vectors belonging to the family ⟨110⟩ are transnational vectors for the lattice, the glide motion of a perfect dislocation leaves behind a perfect crystal. Notably, partial dislocation glides by the formation of kinks, but they leave behind a fault in the atomic stacking. Partial dislocation can create a stacking fault when they migrate through a perfect crystal or remove it. The Burgers vector of the dislocation determines the belonging to one of these two categories. That influences the motion of partial dislocation. Indeed, they will not be able to cross stacking faults if they are of the former class and cannot move outside faulted regions if they belong to the latter. Partial dislocations are further subdivided into trailing and leading dislocations by means of their velocity. Leading partial dislocations are faster than trailing ones, and a stacking fault is encompassed in between them. Depending on the strain sign, the stacking fault encompassed by the two partials is longer or shorter because the trailing and leading dislocation are inverted.

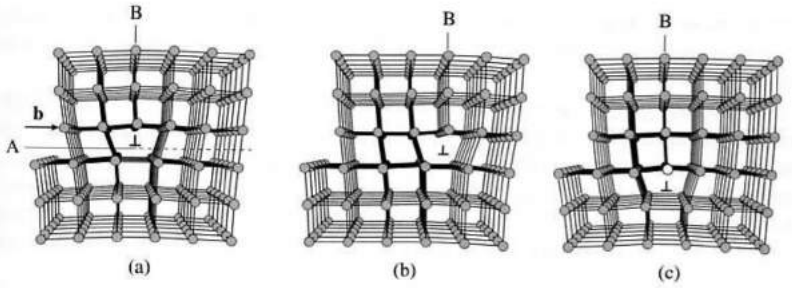

Figure 1.17: An edge dislocation in a simple cubic crystal. When it moves on its glide plane by one lattice spacing (b) no atoms need to be inserted or removed. When it moves perpendicular to its glide plane (c) a row of atoms (white spheres) needs to be inserted.[20]

The analogous of kinks are *jogs* in the climb motion. They allow one to connect dislocation segments belongings to different parallel glide planes, as shown in Figure 1.16 (**b**). The climb motion is activated mainly because of the dislocation - point defects interaction. These point defects are vacancies and interstitial atoms.[2,21] The direction of the climb motion is determined by the point defects that are present. Indeed, let's consider the Figure 1.17 (**b**) an edge dislocation in a cubic lattice can climb up if the row of white atoms is inserted as in Figure 1.17 (**c**) (in this case, white atoms are a row of interstitials). Instead, if we start from a configuration where white atoms are present (Figure 1.17 (**c**)), and we remove them, the dislocation climbs upward (Figure 1.17 (**b**))(in this case, white atoms are a row of vacancies).

As shown in Figure 1.17 (**a**), for the simple cubic crystal for simplicity, the glide does require any change in the number of atoms to be obtained. Only a change in the bonding of the atoms happens, whereas in the case of the climb, a line of vacancies or interstitial is necessary to achieve motion. Often glide and climb are introduced as conservative and non-conservative motion because of that.

Peach e Koehler Force

The interaction of dislocations with an external stress field has been studied by Peach and Koehler from the physical and mathematical points of view in Ref. [22]. Let's consider a dislocation at $\vec{r}$ being $\vec{b}$ its Burgers vector. The dislocation is immersed in a stress field described by the tensor σ. The dislocation has, therefore, interaction energy W. Note that the stress field does not consider the stress field induced by the dislocation itself but only the external contribution. Given an infinitesimal translation, $d\vec{s}$ in an arbitrary direction moves the dislocation to a new position $\vec{r}'$ where it possesses an interaction energy W', the energy variation is hence:

$$\Delta E = W - W' \tag{1.59}$$

As described in Section 1.2.2 it is possible to construct a cylinder centered in $\vec{r}$ with axis $d\vec{s}$ extended up to the crystal surfaces. The dislocation is obtained by cutting the crystal on the cylinder surfaces and shifting the atoms of the solid inside the cylinder by $\vec{b}$. The interaction energy W at $\vec{r}$ with the stress σ can be calculated by estimating the work done on the cylinder surface, during the displacement, by the stress σ. Similarly, the interaction

energy W' can be obtained considering the cylinder at $\vec{r}'$. As a consequence, the negative work made by σ on the cylinder portion of the surface that has $\vec{r}$ and $\vec{r}'$ as the base is $\Delta E = W - W'$. Now consider that an element $d\vec{s} \times d\vec{l}$ of the cylinder surface that has a normal vector pointing outside the cylinder. The force acting on this element of area is $\sigma \cdot (d\vec{s} \times d\vec{l})$ and the work done by the force is $\vec{b} \cdot \left[\sigma \cdot (d\vec{s} \times d\vec{l})\right]$. By integrating the work on the entire cylinder surface, we obtain the total work:

$$-\Delta W = \int_l \vec{b} \cdot \left[\sigma \cdot (d\vec{s} \times d\vec{l})\right] \tag{1.60a}$$

the force acting on the dislocation along the direction $d\vec{s}$ is therefore:

$$-\frac{\partial W}{\partial s} = \int_l \vec{b} \cdot \left[\sigma \cdot (d\vec{l} \times \hat{\lambda})\right] \tag{1.60b}$$

where $d\vec{s} = \hat{\lambda} ds$, $d\vec{l} = \hat{v} dl$ with $\hat{\lambda}$ and $\hat{v}$ unitary vectors. Because σ it's symmetric, it's possible to write:

$$\vec{F}_\alpha = -\int_l \left[(\vec{b} \cdot \sigma) \cdot (\hat{\lambda} \times \hat{v})\right] dl \tag{1.60c}$$

The integration is on all elements dl, therefore the function to be integrated can be interpreted as the α-th component of the force acting on the dislocation line and hence we can write:

$$d\vec{F}_\alpha = -\hat{\lambda} \cdot \left[\hat{v} \times (\vec{b} \cdot \sigma)\right] \tag{1.60d}$$

As a consequence, the resulting force $d\vec{F}$ inside a stress field σ acting on an element $\hat{v} dl$ of a dislocation with Burgers vector $\vec{b}$ is given by:

$$d\vec{F} = -\hat{v} \times (\vec{b} \cdot \sigma) dl \tag{1.60e}$$

This is a very general formula. The local stress field, acting on the dislocation, can be generated from other dislocations, form the interaction with free surfaces, form the epitaxial mismatch, or in general from any defect that produces a stress field. The total stress is then given by the linear superposition of all these contributions. For a straight dislocation line, the Peach and Koehler force is the following:

$$\vec{F}_{\mathrm{PK}} = (\sigma \cdot \vec{b}) \times \vec{\xi} \tag{1.61}$$

where $\vec{\xi}$ is the dislocation line. The Peach and Koehler force is always directed perpendicularly to the dislocation line, as guaranteed by the vector product with $\vec{\xi}$.

1.3.4 Cross-slip

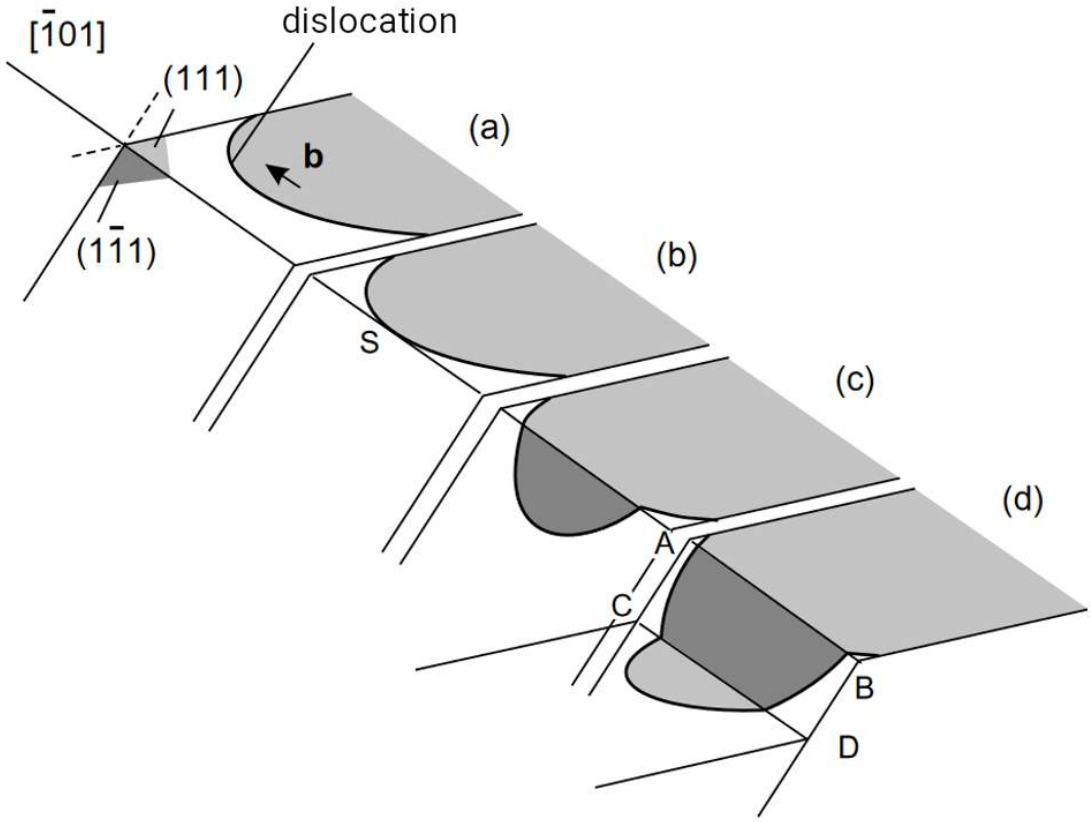

Figure 1.18: Snapshots of the so called *cross slip* (a), (b), (c). The direction $[1\bar{1}1]$ is common to both (111) and $(1\bar{1}1)$ plane. The dislocation segment in S it's free to glide in both planes because has a screw character. The cross slip produces a non planar slip surface. A double cross slip is shown in (d).

As a general rule, dislocation segments tend to move on specific crystallographic planes. In crystals that have a zinc-blende/diamond lattice, most of the dislocations move on planes belonging to the {111} family. Dislocation segments with a screw character can go from one {111} plane to another plane of the same family provided that the Burgers vector $\vec{b}$ belongs to the new plane. This process, know as *cross slip* is shown in Figure 1.18. In Figure 1.18 a dislocation line with Burgers vector $\vec{b} = \frac{1}{2}[\bar{1}01]$ glides to the left on the (111) plane under the action of an applied shear stress. The only other plane containing this Burgers vector is the $(1\bar{1}1)$ plane. Suppose that while the dislocation is gliding, a local change in the stress that makes the dislocation move is encountered. Suppose now

that the motion is easier along the $(1\bar{1}1)$ plane instead of (111) plane. In opposition with edge and mixed dislocations (that have an unique glide plane), a pure screw segment is free to move on $(1\bar{1}1)$ and (111) planes and therefore cross slip can happen at *S* (see Figure 1.18 (**b**)). Thereafter the dislocation is on the $(1\bar{1}1)$ plane (Figure 1.18 (**c**)). A *double cross slip* is shown in Figure 1.18 (**d**). Dislocation cross slip is experimentally observed by transmission electron microscopy (TEM).[23]

1.3.5 Formation mechanism of misfit dislocations

As anticipated before, SiGe or Ge epilayers grown on silicon (001) substrates undergo a strong compression in the (001) plane.† During the layer by layer growth, misfit dislocations form at Si/Ge (SiGe) interface aligned in the [110] and $[1\bar{1}0]$ direction with the extra half-plane of atoms pointing toward the substrate.

Depending on the character of the dislocation, we have different efficiency in the relaxing of hetero-epitaxial strain. Screw dislocations do not have any extra plane of atoms, and therefore they do not take part directly in the film relaxing. Instead, all those dislocations that have an edge component do. The effectiveness of the strain relaxation depends on the orientation of the Burgers vector: a 60° dislocation or a 90° dislocation better relaxes the epilayer as bigger the Burgers vector is in its perpendicular component ($\vec{b}$ component perpendicular to dislocation line). As a consequence, the 90° dislocation is two times more efficient in relaxing than 60° dislocation because the projection of the Burgers vector of a 60° dislocation on the growth plane is half that those of a 90° one.

In a bulk material, without defects, dislocation are closed lines (loops) where the Burgers vector is conserved. Instead, in the case of a finite crystal, dislocation can terminate at a free surface, forming the so-called semi-loops. One of the main mechanisms proposed for the nucleation of dislocations is the formation of 60° dislocation loops at the free surface.[24] Misfit dislocation can nucleate as loops/semi loops only in their glide planes, and 90° misfit dislocation is thought to form as a reaction of two complementary 60° because their glide plane is (001), i.e., the substrate/film interface.[25–28] After the nucleation,

†In the following discussion, we will introduce dislocation loops and semi-loops to explain the formation of dislocations. We will not consider cubic silicon carbide because the epitaxial strain is especially high in this latter case due to a tensile lattice mismatch of ≈ 20% and dislocations form in a few atomic layers concept of the loop itself, in this case, is non-trivial. Even though, in 3C SiC, when most of the strain has been relaxed, dislocation loops can play a role.

the hetero-epitaxial strain of the film acts on each segment of the dislocation loop, making it expanding until it reaches the interface of the film with the silicon substrate. The loop, which in effect is a semi-loop, can be seen as a composition of three main segments: a *misfit segment* deposited at the film/substrate interface and two *threading arm* connecting the defect at the interface with the free surface. The misfit segment has the characteristics of a 60° dislocation because, as already stated, it is the most energetically favorable dislocation to nucleate and can relax the epitaxial strain having an edge component. Differently, threading arms are screw dislocations, where the dislocation line is directed in the same direction of the Burgers vector. Being screw segments, they don't relax the film, but they deteriorate the crystalline structure; still, they have an essential role in extending misfit segments and, therefore, in the relaxation process. It should be noted that a dislocation semi-loop is nucleated so that the slipping part is in its interior. In the semi-loop opening, an atomic step is formed, and detrimental defects are formed at the intersection of the steps with the threading arms. Those defects form the so-called *etch pits* when the free surface is treated with etching processes.

1.4 Stacking order in diamond/zinc-blende structure and polytypism

Many tetrahedrally bonded materials that have a diamond/zinc-blende structure can also show a different structure. This is typical of materials such as the SiC, the GaAs and others. This characteristic is called polytypism. It is common to identify each polytype (crystallographic phase) by considering the crystal as an assembly of tetrahedra.[29] A tetrahedron arises out of the tetrahedral bonding of these materials, as shown in the top of Figure 1.19 (for SiC). Note that one of the bonds is parallel to the c-axis in Figure 1.19. In any of the structures of tetrahedrally bonded materials, such as Si, Ge, diamond, GaAs, ZnS, etc., tetrahedra are joined to each other at their corners. Because the c-axis is taken to coincide with one of the Si-C bonds, the triangular base of the tetrahedron opposite to this bond is normal to the c-axis and defines a c-plane. Each c-plane can be formed either by a tetrahedron (a) or (b) oriented as shown in top left of Figure 1.19. Indeed, rotating the tetrahedron by 180° around the c-axis produces a different variant (a "twin" variant).

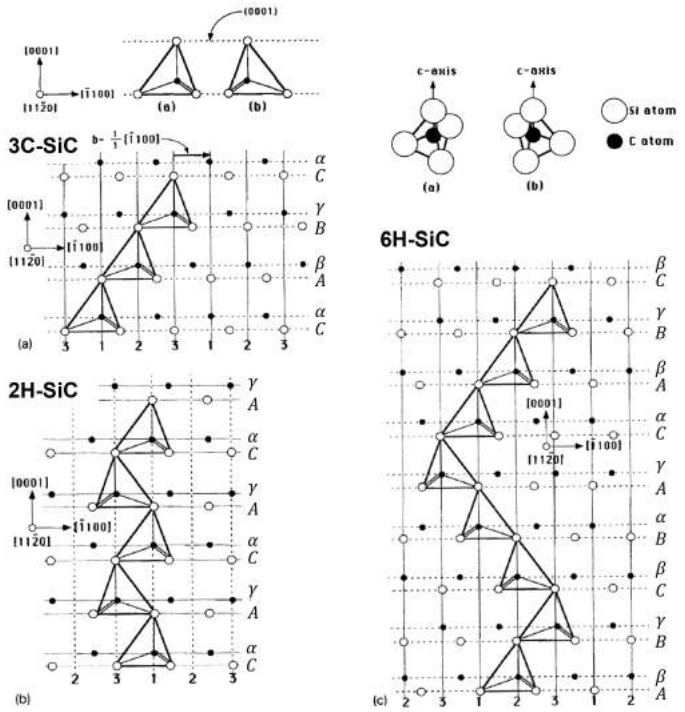

Figure 1.19: Stacking order for tetrahedrally bonded materials. In the top row the tetrahedra that compose a stacking sequence are shown with the c-axis aligned vertically. The material considered in this sketch is SiC. The stacking sequencies are shown for (a) 3C- (zinc-blende), (b) 2H- (wurtzite), and (c) 6H-SiC.

Note that the edges of the triangle base in a SiC tetrahedron are along the (1120) directions. Just as for a sphere in a close-packed assembly, a tetrahedron in an assembly of corner-sharing tetrahedra can occupy one of the three sites on a c-plane; we shall indicate these three sites as T_1, T_2, and T_3, respectively. For the twinned variants the sites are T_1', T_2' and T_3'. Thus, a layer of tetrahedra can be denoted as a T_1, T_2, T_3, T_1', T_2', or a T_3' layer. Hence, the projection of a SiC tetrahedron and its twinned variant on a {1120} plane will appear in the form of acentric triangles. Each of the tetrahedra is associated with a set of widely spaced double sheets of carbon and silicon atoms. In each set, a sheet of silicon atoms is located parallel to and above the sheet of carbon atoms. Following the Ramsdell notation,[30] the silicon and carbon planes in a double sheet are denoted by Roman (A, B, C) and Greek (α, β, γ) letters (or vice versa). Thus, a T_1 tetrahedron can be associated with an αA widely spaced double sheet of atoms passing through the centroid and the vertex of the tetrahedron, respectively. Similarly the T_2 and T_3 tetrahedra are associated with βB and γC double sheets of atoms (Figure 1.19). The variant of a tetrahedron, i.e. whether it is T or T', is determined by its preceding double sheet in the cycle ...αAβBγC... Thus the

αA double sheet is associated with a sheet of T_1 tetrahedra if the double sheet preceding it is the preceding set of letters, i.e. it is in the sequence γCαA. On the other hand, the αA double sheet is associated with a sheet of T_1' tetrahedra if the double sheet preceding it is the preceding set of letters (anti-cyclic order of letters), i.e. it is in the sequence βBαA.[29] The various stacking sequence for 3C- (zinc-blende) 2H-, and 6H- SiC are shown in Figure 1.19 (**a**) - (**c**).

1.4.1 Single Stacking Fault

A single plane stacking fault (or Intrinsic Stacking Fault (ISF)) is an extended defects that appears in diamond/zinc-blende structure when the conventional ordering of the crystal ...αAβBγCαAβBγC... is inverted in a single set of widely spaced double sheet of atoms. E.g., ...αAβBγCαA$\boldsymbol{\gamma}$**C**αAβBγC... (planes with an anti-cyclic sequence are highlighted by bold symbols). It corresponds to a twinning of the tetrahedra of a single c-plane, i.e., a single 2H layer.

1.4.2 Double Stacking Fault

A double plane stacking fault (or Extrinsic Stacking Fault (ESF)) is an extended defects that appears in diamond/zinc-blende structure when the conventional ordering of the crystal ...αAβBγCαAβBγC... is inverted for two consecutive sets of widely spaced double sheets of atoms. E.g., ...αAβBγCαA$\boldsymbol{\gamma}$**C**$\boldsymbol{\beta}$**B**γCαA... (planes with an anti-cyclic sequence are highlighted by bold symbols). It corresponds to a twinning of the tetrahedra of two c-planes, i.e., single 3C layer twinned along its c-plane.

1.4.3 Twin - Triple Stacking Fault

A Twin is a triple plane stacking fault (or double Extrinsic Stacking Fault (2ESF)). It is an extended defects that appears in diamond/zinc-blende structure when the conventional ordering ...αAβBγCαAβBγC... is inverted for three consecutive sets of widely spaced double sheets of atoms. E.g., ...αAβBγCαA$\boldsymbol{\gamma}$**C**$\boldsymbol{\beta}$**B**$\boldsymbol{\alpha}$**A**βB... (planes with an anti-cyclic sequence are highlighted by bold symbols).

1.4.4 Anti Phase Boundary

An Anti Phase Boundary is a the extended defect that can appear at the border between two crystalline regions that have the same structure, i.e., in our case the diamond/zinc-blende structure, but have a different stacking order. It is the case, e.g., for SiC when two separated regions of a growing crystal start with a different initial-specie layer because of an atomic step on (001) substrates, or because a twinning in the sequence of layers on (111) substrates.[31] Indeed, a mono-atomic step on a the Si (001) surface makes the two regions divided by the step start with a carbon atom. On one side the carbon atom is on top of the widely spaced layer, whereas on the other side it is below. The two regions continue with a perfect structure, but their staking is made up by a sequence which differs on the specie which is on top. For a growth on a (111) substrate, let's consider the two stacking sequences:

$$\overbrace{\alpha \mathrm{A} \beta \mathrm{B} \gamma \mathrm{C}}^{\text{substrate}} \overbrace{\alpha \mathrm{A} \beta \mathrm{B} \gamma \mathrm{C}}^{\text{film}} \tag{1.62a}$$

and,

$$\overbrace{\alpha \mathrm{A} \beta \mathrm{B} \gamma \mathrm{C}}^{\text{substrate}} \overbrace{\mathrm{A} \alpha \mathrm{B} \beta \mathrm{C} \gamma}^{\text{film}} \tag{1.62b}$$

the two sequences start with a carbon (greek letter) or a silicon atom (roman letter). On a Si (111) substrate both the sequences are possible, an therefore two separated region of a SiC film can have a different ordering at their border an Anti-Phase boundary can appear also in absence of any step.[32]

1.5 Materials: Ge and 3C-SiC on Si(001)

The materials that we consider in this Thesis are silicon carbide and germanium. Their epitaxy on Si substrate represents the ideal test case for extended defect modeling via classical molecular dynamics simulations. We have chosen Ge and 3C-SiC as prototypical materials because they cover two separate parts of the defect behavior spectrum in an epitaxial system. The details that characterize each one of these two materials will be discussed in the following two subsections.

1.5.1 3C-SiC on Si (001)

Silicon carbide is a group IV semiconductor. The strong covalent bonding between the C and Si atoms characterize this material. It presents a tetrahedral structure formed by a stoichiometric alloy of Si and C atoms. Each Si atom forms four bonds with its four C first neighbors, but different lattice arrangements are possible beyond the first coordination sphere. SiC is indeed known to present a vast number of allotropes. Such property is also known as polytypism. The ability to have many possible crystallographic structures interested us because the evolution of extended defects can determine the mechanism behind the transition between different SiC phases. In this Thesis, we will focus on the cubic (3C) phase of SiC, being it the natural output of SiC growth on Si substrate. The 3C-SiC has attracted the attention of the scientific community for many exciting properties that it possesses. Many of them are determined by the high symmetry of the zinc-blende lattice of the 3C phase. A reduced phonon scattering, the highest carrier mobility of SiC, and outstanding thermal stability are only some of them.[33–35] Polytypism has important consequences on crystallographic defects' appearance. The different phases of SiC have stability which depends on the temperature, as demonstrated in Ref. [36]. Therefore, we can expect to observe the generation of defects that introduce hexagonal inclusion inside the cubic one at specific temperatures. These defects are the stacking faults. They generate and propagate by the motion of another critical class of defects, the partial dislocations.

Other crystallographic defects frequently appears in 3C (or β-SiC growth on Si (001). Between them the most commonly observed extended defects there are twins and Anti Phase Boundaries (APBs). Because most of the APBs can be eliminate through well-known experimental procedures, we will not focus on them in this Thesis. The presence of a considerable strain also characterizes the epitaxy of 3C-SiC on Si substrate. A $\approx$ 20% misfit exists between the SiC and the silicon lattice parameter. Being the strain tensile, it prescribes the formation of partial dislocations and the dissociation of perfect dislocations. For all the reasons stated above, the modeling of defects in 3C-SiC necessitates being improved. It will be considered first, and most of this Thesis will try to give new insight into 3C-SiC extended defect modeling via molecular dynamics.

1.5.2 Ge on Si (001)

Germanium is, for many aspects, on the completely opposite side of the defect behavior spectrum. First, it possesses a diamond lattice structure. It is completely miscible with Si (whereas SiC is stochiometric). It does not present a polytypism, APBs and twins. Furthermore, epitaxial Ge on Si(001) is characterized by the presence of a compressive strain, which intensity is around 4%. The compressive strain implies that the observation of stacking faults in Ge is much rarer than in SiC, and most of the defects in the material are perfect 60° or 90° dislocations. Ge is an excellent candidate to study strain release mechanisms via the motion of extended defects. It represents a perfect case to investigate the modeling of perfect dislocation glide and climb via classical molecular dynamics simulations.

Chapter 2

Modelling of extended defects in solids

2.1 Classical molecular dynamics

Classical molecular dynamics (MD) is a computational technique used to calculate equilibrium and transport properties of multi-body systems. In this context, the word *"classic"* means that the motion of particles obeys the laws of classical mechanics. Such an approximation is an excellent one for a large set of materials.[37] To understand when quantum mechanical effects must be taken into account, the *quantum volume* is often considered. The quantum volume is a measure of the extension of the wave-function of a particle/atom/molecule; it is defined by considering the *de Broglie length*:

$$\lambda_{\mathrm{dB}} = \frac{h}{p} \tag{2.1}$$

that, in the case of thermal vibration is equal to:

$$\lambda_{\mathrm{T}} = \frac{h}{\sqrt{2\pi m K_{\mathrm{b}} T}} \tag{2.2}$$

hence, the quantum volume is defined as the quantity:

$$V_{\mathrm{Q}} \equiv \lambda_{\mathrm{T}}^3 \tag{2.3}$$

If the quantum volumes of the particles overlap in a given system, we have that an overlap of the wave functions exists and the effects of the symmetrization/anti-symmetrization of

the total wave function (arising from the concept of indistinguishable particles) must be considered.

Typically, quantum mechanical effects can be neglected if high density, small masses (atoms and molecules like He, H_2, D_2) and very low temperature are not present.

Molecular dynamics simulations are very similar to real experiments. Indeed, when preparing an experiment, one usually proceeds as follows:

- The material of interest is prepared.
- A sample of the material under investigation is connected to a measuring apparatus (for example, a thermometer, a barometer, etc...).
- The properties of the material under investigation are measured for a certain time period.
- If the measure is susceptible to statistical error, the more the measure is long, the more it will be accurate.

In molecular dynamics, we proceed in the same way. First, the sample is prepared: a system made up of N particles is selected, and Newton's equations of motion are solved until the system properties do not change anymore in time (equilibration of the system). After equilibration, a measure of the properties that we want to obtain is done. In practice, most of the common errors that can be done in a computer simulation are similar to those that can be done in a real experiment.

To measure an observable in a molecular dynamics simulation, it is necessary to be able to express such a quantity as a function of the position and momentum of the system particles. For example, a convenient definition of the temperature in a multi-body classical system can be obtained from the equipartition of the energy on all degrees of freedom that enter as a power of two in the system Hamiltonian. In particular, the mean kinetic energy for each degree of freedom is:

$$\left\langle \frac{1}{2} m\, v_{\mathrm{a}}^2 \right\rangle = \frac{1}{2} K_{\mathrm{b}} T \tag{2.4}$$

In a simulation, the equation 2.4 is used as an operative definition of the temperature. In practice, one should measure the kinetic energy of the whole system and divide it by the

number of degrees of freedom $N_f (= 3N-3$ for a system of N particles with fixed momentum*). When the total kinetic energy fluctuates, so does the instantaneous temperature:

$$T(t) = \sum_{\mathrm{i}=1}^{N} \frac{m_{\mathrm{i}} v_{\mathrm{i}}^2(t)}{K_{\mathrm{b}} N_{\mathrm{f}}} \tag{2.5}$$

The relative fluctuations of the temperature will be of the order of magnitude of $1/\sqrt{N_f}$. Considering N_f of the order magnitude of 10^2-10^3, statistical fluctuations are of the order of 5-10%. In this case, to have an accurate estimation of the temperature is mandatory to mediate it on many oscillations.

In this Thesis, we studied a variety of systems in different conditions using the Large-scale Atomic/Molecular Massively Parallel Simulator (LAMMPS).[38] LAMMPS is a classical molecular dynamics code for materials modeling. LAMMPS has the possibility to be used with different potentials for solid-state materials (metals, semiconductors) and others. We will use it to model atoms as a parallel particle simulator at the atomic scale with a focus on extended defects at this scale. The use of LAMMPS is preferable to the use of other engines because it easily enables one to run it on single processors or in parallel using message-passing techniques and spatial decomposition of the simulation domain. Many of its models have internal versions that provide accelerated performance on CPUs, GPUs, and Intel Xeon Phis. The code is designed to be easy to modify or extend with new functionality.[38]

2.1.1 Simulations set up

To make any simulation start, independently from the program used, it is necessary to assign positions and velocities to each atom. The atomic positions of the particles have to be compatible with the crystalline structure that is under investigation. In this work, we always started from a configuration which is the diamond/zinc-blende lattice, i.e., an *fcc* lattice with a bi-atomic base. The positions on the diamond/zinc-blende lattice are a good starting point for an MD simulation, but in the case of most of the extended defects, it results to be necessary to actually start our simulation from configurations that

*In truth, if the temperature is defined in the micro-canonical ensemble by $\frac{1}{K_{\mathrm{b}} T} = \frac{\partial \log \Omega}{\partial E}$, with Ω the number of states, we obtain that, for a d-dimensional system composed by N atoms with fixed momentum, $K_{\mathrm{b}} T$ is equal to $\frac{2E}{d(N-1)-2}$.

are different from the ideal crystal. Indeed, extended defects appear in real systems after nucleation processes that are very tricky. In semiconductors, they are rare processes that happen with a frequency such that no MD simulation is big/long enough to observe it in a reasonable time. It is therefore easier to create specific configurations with already some defects inside.

Once the positions have been initialized; it's necessary to establish the velocity for each particle. This is done randomly assigning the velocities following a certain velocity distribution that can be uniform, Gaussian, or even more complex. Let's suppose for the sake of simplicity that a uniform distribution is used. In the ideal case of infinite particles, the velocity distribution would be centered around 0. This is not guaranteed for a finite number of particles whose velocities have been extracted randomly from the distribution. Hence, the velocity distribution in such a system is centered around a non-zero value; therefore, the system has a mean translation velocity $\langle \vec{v}_\mathrm{m} \rangle \neq 0$, and the whole system would move. To avoid such an inconvenience is enough to remove $\vec{v}_\mathrm{m}$ to all the velocities in such a way as to zero the total linear momentum of the system. An analogous procedure is employed to zero the total angular momentum $\vec{L}$. In LAMMPS, this is done by specific commands at the beginning of a simulation.

At the thermal equilibrium the following relation must stem:

$$\langle v_\alpha^2 \rangle = \frac{K_\mathrm{b} T}{m} \tag{2.6}$$

where v_α is the α-th component of the velocity of a given particle. This relation can be used to define an instantaneous temperature $T(t)$ at the time t:

$$K_\mathrm{b} T(t) \equiv \sum_{\mathrm{i}=1}^{N} \frac{m v_{\alpha,\mathrm{i}}^2(t)}{N_\mathrm{f}} \tag{2.7}$$

Clearly, it is possible to adjust the instantaneous temperature $T(t)$ in such a way that it corresponds to a desired temperature T scaling the velocities by a factor $(T/T(t))^{1/2}$. This first set of the velocity is not very critical because the temperature will change in the course of the equilibration. Other techniques are used to maintain a specific temperature and pressure of interest. They will be described in section 2.1.4.

As will be discussed later, in most of the simulation algorithms, the velocity of a particle is not used to solve the equations of motion. Instead, the particle positions at the actual time step x and the position at the preceding one x_{old} are combined with the knowledge of the force f acting on the particles to establish the positions at the next timestep. When a simulation is started for the first time, such a procedure is forced, generating fictitious preceding positions. Indeed without any particular consideration on what laws of the mechanics are involved, the position x_{old} of a particle i is approximated to be :

$$x_{\text{old}}(i) = x(i) - v(i) \cdot dt \tag{2.8}$$

Clearly, it is possible to establish a more rigorous preceding set of particle positions, but these are only the initial step of a simulation, and therefore this procedure is not so critical.

2.1.2 Force calculation

In this section, we will discuss the part of a MD program that takes the most of the time in the computation: the calculation of the forces acting on each particle. Let's consider the simple case of a pair interaction. To compute the force acting on each particle, it is necessary to consider the contribution given by the interaction of the particle with all the surroundings. Only considering the interaction of the particle with the other closest one or the closest virtual image of another particle [†], for a system made by N particles, is necessary the calculation of $N \times (N-1)/2$ pairs of distances. That means that, without particular precautions, the time required for the force calculation scale as N^2.

Let's consider how force calculations are made. As a first operation, the distances for each couple of atoms i and j are computed, if the calculated distance is higher than a specific cutoff value r_c, then, between particle i and particle j, there will not be any interaction. Otherwise, if a particle is close enough to interact, the interaction strength is calculated by computing the force acting on the two particles as well as the contribution to the potential energy. Considering only the force component along the x direction we

[†] In the case of a cell with periodic boundary conditions, for each particle, the distance from a given particle is not unique because multiple virtual images exist of the same particle, as will be discussed in the section 2.1.2.

have, in the case of a simple pair interaction:

$$f_{\mathrm{x}}(r) = -\frac{\partial V(r)}{\partial x} \tag{2.9}$$

The forces that act on a single particle are calculated by adding all the contributes given by the particles not further away than a fixed *cutoff radius* so, in truth, it is only the time spent for distance calculation that scales as N^2 not the calculation of forces. A technique that is used to reduce a lot the simulation time is the so-called *Verlet cages* method. This and many other tricks to reduce simulation time are implemented in LAMMPS.

Neighbors list and Verlet Cages

The Verlet cages method allows reducing the number of calculations to compute the forces of the system by a factor $\approx N$. Let's suppose to assign an index ID to each atom. At the first calculation of the force, it is necessary to compute the distance of each atom i from all other atoms. At this point, atoms within the cutoff radius are selected, and the interactions are computed. Those atoms are usually called the *neighbors*. It is now possible to list on a table which are the neighbors of the atom i. In such a way, in principle, at the next force computation, it will not be necessary to compute the distance between each atom i and all the other but only that between it and its neighbors. By iterating the operation of neighbors identification for all the atoms, creating a neighbors list, the number of the operations needed for the dynamics cycle would scale down from $\propto N^2$ to only $\propto N$. There is a non-negligible inconvenient; this method does not take into account in any way that some atom which is not in the neighbor's list of an atom i, at a time t could, by moving, become closer to the atom i than the cutoff radius at a time t'. Because this atom is not in the neighbor's list of the atom i when calculating the forces acting on i at the next step, that atom would be ignored, leading to an error in the computation of the interactions. Such an atom that has migrated unobserved to atom i will be named *ghost atom* in the following.

A simple solution exists for such an inconvenient, the so-called Verlet cages. At the first cycle, the neighbor's list is created as described above, but are considered to be neighbors of atom i those atoms that are at a distance lower than r_v equal to the cutoff distance r_c

plus a small margin r_{skin}. The neighbor's list now contains more atoms than those that actually interact with atom i. This margin contains some atoms that are under strict surveillance, indeed at each step also the distance of those atoms is computed in such a way that if they come closer than the cutoff radius, they are taken into account for the interaction. Now, let's consider the atoms that can become ghost atoms; they are at least at a distance higher than r_{skin} from the inner boundary r_c, which is the limit of the interaction. To never commit errors in the interaction calculation is sufficient to verify that no atom has moved more than the watch distance $r_{\text{max}} = r_{\text{skin}}$ since the last time the neighbor's list has been constructed.[‡] If that has happened is only sufficient to compute the neighbors again and, therefore, the distance of the atom i from all other atoms in the simulation. In truth, to take into account the reciprocal motion of atoms is appropriate to set as watch distance $r_{\text{max}} = {}^1/_2\, r_{\text{skin}}$.

Periodic Boundary conditions

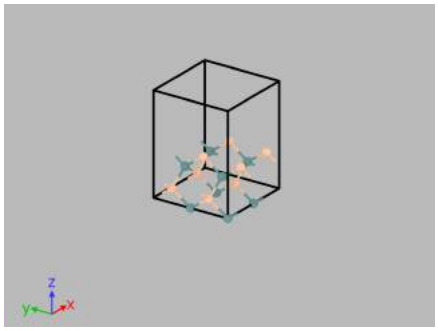

(a) Elementary cell of the zinc-blende.

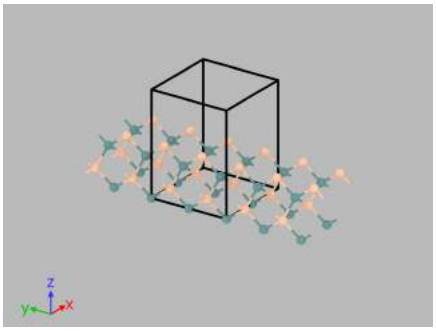

(b) Virtual images: PBCs along y.

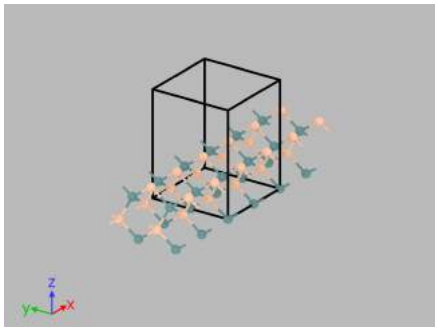

(c) Virtual images: PBCs along x.

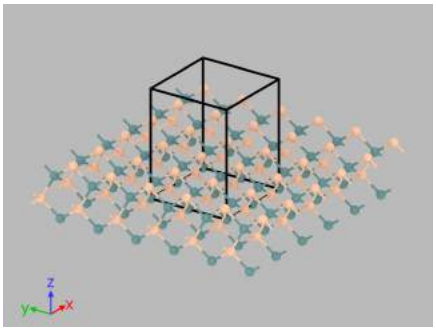

(d) Virtual images: PBCs along x, y.

Figure 2.1: Elementary cell of the zinc-blende lattice with virtual images determined by periodic boundary conditions.

[‡]Therefore any time that the neighbors are computed it is necessary to save the reference positions of atoms to compute the maximum displacement

Often the systems under investigation are composed of an enormous number of atoms. In effect, the order of magnitude is that of a mole, i.e., $N_A = 6.022 \times 10^{23}$. It's difficult to imagine that it will ever be possible to simulate such a high number of atoms or molecules. Systems composed by a limited number of atoms [§] have a surface/volume ratio that is completely different from that of a bulk solid. The size of the systems that can be simulated in their totality extends up to tenth or hundreds of nm.

In this sense, it is possible to introduce *Periodic Boundary Conditions* (PBCs) that make the system infinitely extended in specific directions. Let's consider for simplicity the uni-dimensional case, i.e., a row of N atoms that extend for a length L_x on the x axis. The atoms at the left and right boundary result in being under-coordinated and are, in all the senses, superficial atoms. Instead, if we imagine bending and connecting the atoms at the edges to form a ring, we have that none of the atoms is under-coordinated. In order to obtain such a condition at the boundary is possible to redefine the distance in the x direction, $\tilde{d_x}$, as the minimum between the Euclidean distance d_x and the virtual distance $d_x - L_x$. In a mathematical form:

$$\tilde{d_x} = d_x - L_x \cdot \left\lfloor \frac{d_x}{L_x} \right\rfloor \tag{2.10}$$

where $\lfloor x \rfloor$ is the integer part of x. In three dimensions the operations to make the system periodic are the same, i.e. is necessary to redefine the distance in all three directions. In topology the created system is the three-dimensional boundary of a four-dimensional torus. In Figure 2.1 a conventional cell of the zinc-blende lattice is shown together with its periodic images as determined by the imposition of periodic boundary conditions in x and y directions.

2.1.3 Series expansion of the potential

Given a system composed of N atoms, in general, the total potential energy can be written as series expansion of n-bodies potentials:

$$U = \sum_i V_1(r_i) + \sum_{i \neq j} V_2(r_i, r_j) + \sum_{i \neq j \neq k} V_3(r_i, r_j, r_k) + \cdots \tag{2.11}$$

[§] A record of 110 billion atoms were simulated setting up a record[39] which is negligible with respect to a mole.

where $r_1, r_2, \cdots, r_n$ indicate atomic positions. The first term V_1 is a single-particle potential related to any external potential acting on the whole solid, V_2 is the two-body term, V_3 the three-body, and so on. Stopping the expansion at V_2 as in the preceding section is sufficient for the description atomic interaction that depend only from the distances $\left|r_j - r_i\right|$, that's the case for ionic bonds and noble gasses interactions, where we have a *Van der Waals interaction*. When studying an atomic system of covalent solids, pair potentials are not enough. Indeed covalent bonds are characterized by the superposition of valence electron orbitals, which do not depend only on atomic distances but also on the bond direction. For these systems, it is necessary to consider also the three-body term V_3, which not only takes into account the atomic distances but also takes into account also the angles formed by triplets of atoms r_i, r_j, r_k. A detailed analysis of the potential function for each material that has been investigated in this Thesis will be discussed later in this chapter.

2.1.4 Motion equations time-integration

Once the forces have been computed for all the particles, it is possible to integrate Newton's equations of motion. A variety of algorithms have been realized with the aim of efficiently integrating them. We will discuss some of them in detail.

Verlet algorithm

One of the simplest but also one of the best algorithms used to integrate Newton's equations of motion is the *Verlet* one. Such algorithm can be obtained directly by making a Taylor series expansion of the position of a particle at the time t,

$$r(t+\Delta t) = r(t) + v(t)\Delta t + \frac{1}{2}\frac{f(t)}{m}\Delta t^2 + \frac{1}{3!}\dddot{r}(t)\Delta t^3 + \mathcal{O}(\Delta t^4) \tag{2.12a}$$

e similmente,

$$r(t-\Delta t) = r(t) - v(t)\Delta t + \frac{1}{2}\frac{f(t)}{m}\Delta t^2 - \frac{1}{3!}\dddot{r}(t)\Delta t^3 + \mathcal{O}(\Delta t^4) \tag{2.12b}$$

Adding the two equations, the following is obtained:

$$r(t+\Delta t) + r(t-\Delta t) = 2\,r(t) + \frac{f(t)}{m}\Delta t^2 + \mathcal{O}\Delta t^4 \tag{2.12c}$$

in another way:

$$r(t+\Delta t) = 2\,r(t) - r(t-\Delta t) + \frac{f(t)}{m}\Delta t^2 + \mathcal{O}\Delta t^4 \tag{2.12d}$$

The estimation of the new position contains an error which order of magnitude is Δt^4, where Δt indicates the timestep used in the molecular dynamics calculations. From equation 2.12d it is evident that the Verlet Algorithm doesn't use the velocity of a particle explicitly to calculate the new position. The velocity, however, can be derived from the knowledge of the trajectory, using:

$$r(t+\Delta t) - r(t-\Delta t) = 2\,v(t)\,\Delta t + \mathcal{O}(\Delta t^3) \tag{2.13a}$$

moving $v(t)$ to the left and by dividing by Δt,

$$v(t) = \frac{r(t+\Delta t) - r(t-\Delta t)}{2\Delta t} + \mathcal{O}(\Delta t^2) \tag{2.13b}$$

This expression of the velocity is accurate with a precision which is of the order of Δt^2. However, a more accurate algorithm for the calculation of the velocity exists (they are usually important for the calculation of kinetic energy), still compatible with the Verlet algorithm (equation 2.12d).

Once the new positions have been computed, the old ones at the time $t-\Delta t$ can be discarded. Now the current positions become the old ones, and the ones just computed become the current ones. At this point, the system properties such as energy and temperature can be calculated. It should be noticed that a molecular dynamics code that operates in this way should preserve the energy of the system because the simulation generates system trajectories consistent with the micro-canonical ensemble. A molecular dynamics simulation is considered to be valid when the relative error in the conservation of energy is below 10^{-5}. In the micro-canonical ensemble, the number of particles, the volume, and the energy are constant; it is usually indicated as the (NVE) ensemble. Instead, in

real experiments is the temperature that is controlled rather than the energy. The correct ensemble used to describe the real experimental conditions is the canonical one. A variety of methods exist to maintain the temperature constant in a molecular dynamics simulation. The most popular ones are the *velocity rescale*, the *Andersen thermostat*, the *Nosé Hoover thermostat*, the *Berendsen thermostat* and the *Langevin* dynamics. The point of these techniques is to have the canonical distribution: it means to fix the mean value of the temperature of the system under consideration while allowing fluctuations of the temperature with a typical canonical distribution at the same time.

Nosè Hoover thermostat

In the approach proposed by *Nosé* an Hamiltonian with an extra degree of freedom is introduced, s, which is the thermal bath:

$$\mathscr{H}(P,R,p_s,s) = \sum_{\mathrm{i}} \frac{\vec{p}_{\mathrm{i}}^2}{2ms^2} + \frac{1}{2}\sum_{\substack{\mathrm{i,j} \\ \mathrm{i}\neq\mathrm{j}}} V(\vec{r}_{\mathrm{i}} - \vec{r}_{\mathrm{j}}) + \frac{p_s^2}{2Q} + gK_{\mathrm{b}}Tln(s) \tag{2.14}$$

where g is the number of independent degrees of freedom of the system, R and P are all the coordinates in the phase space $\vec{r}_{\mathrm{i}}$ and $\vec{p}_{\mathrm{i}}$ and Q is an imaginary mass. The R and P coordinates and the time t in this Hamiltonian are *virtual*. They are related to the real coordinates by:

$$\begin{aligned} R' &= R \\ P' &= \frac{P}{s} \\ t' &= \int^{\mathrm{t}} \frac{1}{s} d\tau \end{aligned} \tag{2.15}$$

Where the superscript $'$ indicates the real coordinates. It should be noted that the average in the Hamiltonian, introduced for $g = 3N$ coincides with the average of the canonical ensemble. The principle behind equations 2.15 is that the time and the momentum are scaled by a factor s, as described by equations 2.15, in such a way that a thermal-regulation exists, as compatible with the presence of a thermal bath.

2.1.5 Geometrical optimization: minimization

A procedure always implemented in most molecular dynamics simulations is a geometrical optimization of the atomic configurations by a minimization of the potential energy of the system. To have a good simulation is very important that atoms, at the beginning of the simulation, should be placed in such a way that the system is close to a relative minimum of the potential energy. That's is needed because, if this stands, the potential will behave as a harmonic potential, and because of the *equipartition theorem*, the system will exchange half of its kinetic (thermal) energy into harmonic potential energy. Using this trick, the choice of the distribution of starting velocities will not be so much important because, after an initial equilibration, the system will evolve, gaining a velocity distribution analogous to the Maxwell-Boltzmann distribution. Also, starting from non-minimum configurations can lead to bad dynamics. For example, if in the starting configuration two atoms are overlapping, the force between them is gargantuan, and integrating the motion, it's possible that the timestep result to be too large (even if it was chosen in a reasonable way) and is therefore possible that the next computed position is again to close to other atoms (indeed in between two positions there is no intermediate calculation of the forces) causing a chain reaction. In order to avoid such situations, the starting atomic positions are modified, exploring multiple configurations to discover those that are close to a *local minimum* of the potential. Many different methods can be used to minimize atomic configurations; between them, the *Steepest Descent* and the *Conjugated Gradient* method are the most notorious ones. The use of these techniques is of extreme importance even if the atomic positions in the crystal are artificially modified.

Steepest Descent Method

The *Steepest Descent* (SD) method consists in making the entire system move in the configurational phase-space alongside the direction which is opposed to the energy gradient. To obtain this, each atom is moved by a little step in the direction of the force calculated on it. The system will reach a local minimum when the energy gradient tends to zero. Therefore a SD code should impose that the maximum values of the energy and of all force components are below a determined threshold. The algorithm operates as is sketched as follows.

1. Being known the atomic positions $\vec{x}_i$ the total energy U_{old} and the force acting $\vec{f}_i$ on each atom are computed using the considered potential.

2. The atomic positions are updated following:

$$\vec{x}_i = \vec{x}_i + c\vec{f}_i \tag{2.16}$$

   where c is a factor of an order of magnitude of $10^{-2}/10^{-3}$ which allows to displace the atoms by a small distance.

3. If the total energy U_{new} of the new configuration is less than U_{old}, the procedure is repeated with the new coordinates; otherwise, the c factor is divided by two, and the coordinates before the displacement are re-considered.

Conjugated Gradient method

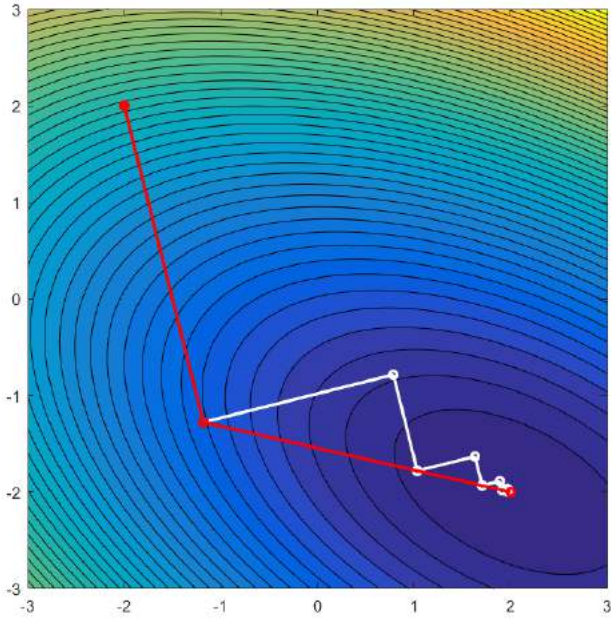

Figure 2.2: Comparison between the Steepest Descent (in white) and the Conjugate Gradient (in red) methods. The color-bar represents a potential energy along with its contour lines.

The *Conjugated Gradient* (CG) method is very similar to the SD one, but it differs from it because, at each iteration, the energy gradient is combined with the information of the preceding iteration to set up a new exploration direction of the configuration which is that

perpendicular (conjugated) to the preceding exploration direction. Such an algorithm is faster than the SD one that still is more reliable in some situations. In Figure 2.2 a comparison between the two methods is shown.

2.2 Analysis of atomic configurations

One of the most interesting aspects of MD is that it is possible to follow single atoms trajectories during the simulation. This is possible by making the MD program print atomic position at each step to a file. One simple example is the diffusion of adatoms on a surface, which result not of particular difficulty. On the contrary, extended and in general, all defects are not so easy to be identified and visualized in their motion and evolution, being them a defect of the lattice, not a group of atoms. For example, it is not possible to follow the motion of a dislocation by following the motion of a group of atoms. Indeed the dislocation is a defect of the crystal, and when it glides, the motion is given by a change in the bonding of atoms of the dislocation core, not by the motion of atoms as described in section 1.3.3.

To deep explore the phenomena and the physical processes that happen inside materials with defects, the right instruments need to be used. In this Thesis, to analyze atomic configurations and to obtain the relevant properties of the solids, multiple algorithms have been used. Most of them were instructions for the Open Visualisation Tool (*OVITO*), a specific software for the analysis of atomistic simulation, with a great focus on the analysis of crystalline structure with crystallographic defects. The software has been developed by Stukowski at the *Technische Universität* of Darmstadt.[40] The action of the main analysis algorithm used for this Thesis will now be described in detail.

2.2.1 Displacements

In Chapter 1 the displacement field was introduced, form equation 1.1 one can easily obtain that the displacement field is given by

$$\vec{u}(x) = \vec{X} - \vec{x} \tag{2.17}$$

where $\vec{X}$ are the displaced positions and $\vec{x}$ are the original position before the deformation. Given a configuration, to compute the displacement of each atom is enough to subtract from the actual position $\vec{X}_{\mathrm{i}}$ the reference position $\vec{x}_{\mathrm{i}}$. It is therefore of fundamental importance that the MD program prints to a file the reference atomic positions together with a unique identifier for each atom, the atom *ID*

To use the concepts of linear elasticity theory in the study of extended defects via MD, one should translate the displacements field into the other mathematical entities of the linear elasticity theory.

2.2.2 Elastic Strain

To compute the elastic strain, we used the OVITO "`Elastic strain calculation`" instruction. This instruction tells OVITO to analyze the local distortion of a crystalline lattice.[41] The gradient of the elastic deformation is the tensor $\bar{\bar{F}}_{\mathrm{el}}$, it is related to the gradient of the elastic displacement $\vec{u}_{\mathrm{el}}$ as follows:

$$\bar{\bar{F}}_{\mathrm{el}} = \nabla u_{\mathrm{el}} + Id \tag{2.18}$$

$\bar{\bar{F}}_{\mathrm{el}}$ transforms the vector of the positions of a strain free, ideal lattice into the vector of the physical positions at the instant of the simulation that is under consideration, as follows:

$$\Delta\vec{x} = \bar{\bar{F}}_{\mathrm{el}} \cdot \Delta\vec{X} \tag{2.19}$$

where $\Delta\vec{X}$ is a column vector of the ideal lattice and $\Delta\vec{x}$ is the corresponding vector in the elastically deformed crystal. The calculation of the elastic strain does not require any reference configuration; it only requires that the ideal unitary cell of the crystal is set, in such a way that it can be used as a base to build an ad-hoc reference configuration. The elastic deformation is obtained from the comparison of the actual atomic position with those of the virtual reference. OVITO also allows the computation of the atomic strain (which is not purely elastic) through the modifier "`atomic strain`." It determines the total deformation for each atom from the displacement of its relative neighbors with respect to a given reference configuration.

The elastic strain tensor can be computed only for those atoms for which it is possible to locally map the neighbors in the ideal lattice. In practice, this is the case of atoms placed in a structure similar to that of the ideal lattice. OVITO identifies those atoms in an intermediate step using common neighbor analysis and crystalline structure analysis methods. Atoms in a strongly deformed environment, like, for example, the atoms of the dislocation core, on a surface and at grain boundaries, are excluded from the computation. To these atoms, a zero elastic strain value is assigned.

A elastic strain tensor can be calculated from the gradient of the elastic deformation tensor, calculated for each atom. Two options are possible:

Strain tensor in spatial frame

A first option is to chose the instruction "`Strain tensor in spatial frame`", in this case the *Eulerian-Almansi finite strain tensor* is computed, it is defined:

$$\varepsilon = \frac{1}{2}\left[Id - (\bar{\bar{F}}_{\mathrm{el}})^{-t}(\bar{\bar{F}}_{\mathrm{el}})^{-1}\right] \tag{2.20}$$

This elastic strain tensor describes the elastic deformation in the coordinates reference system of the simulation. For example, the $\varepsilon_{\mathrm{xx}}$ components are the axial strain alongside the x axis of the reference system of the simulation. One advantage of this choice is that it does not suffer from any of the ambiguities described in the following.

Strain tensor in lattice frame

Instead, if the "`Strain tensor in lattice frame`" convention is considered, the *elastic Green-Lagrangian strain tensor*, defined as:

$$\epsilon = \frac{1}{2}\left[(\bar{\bar{F}}_{\mathrm{el}})^{t}(\bar{\bar{F}}_{\mathrm{el}}) - Id\right] \tag{2.21}$$

Such elastic strain tensor describes the elastic deformation in the coordinate reference system of the lattice. The ϵ_{xx} component is the axial strain alongside a $\langle 100 \rangle$ direction of the crystal. In OVITO, the direction is identified automatically, arbitrarily choosing one of the directions of the family $\langle 100 \rangle$. Because in cubic crystals, the [100], [010], and [001] directions are exchangeable, that raises ambiguity.

2.2.3 Dislocation Analysis (DXA)

Dislocations are defects of the crystalline structure; their visualization in an atomistic system is not trivial, in particular for non-straight dislocations. OVITO provides specific routines for the identification of such defects: the `"Dislocation Analisis (DXA)"` modifier. This routine implements the so-called *Dislocation Extraction Algorithm (DXA)*, a computational method developed by the OVITO author, Stukowski. The method used to extract dislocations is described in article.[42] The actual implementation in OVITO follows the newer and more general approach in the successive article.[43] The *DXA* algorithm transforms the original atomic representation into another representation made up of line networks. Thereafter, it determines the Burgers vector of each dislocation segment, and it identifies the dislocation line interactions. The algorithm is able to recognize partial dislocations and some secondary dislocation of grain boundaries (the so-called *twinning dislocations* in *fcc* crystals).

DXA Algorithm

The fundamental concept behind DXA is the construction of the Burgers Circuit,[15] which is the usual method proposed in the fifties to discriminate the dislocations from other crystallographic defects and to determine their Burger vector. The formulation is that proposed in Section 1.2.1, the Burgers circuit C is a path in the dislocated crystal that consists in a sequence of step Δx from atom to atom, Figure 1.5 has been reported here to ease the reading.

The Burgers vector $\vec{b}$ is the failing of the tentative of closing the circuit after having transferred it in the perfect crystal. Instead, if $\vec{b} = 0$, the Burgers circuit does not enclose any defect with dislocation character, de-facto ignoring the possibility that the Burgers circuit is enclosing more than one dislocations that have Burgers vectors that sum up to zero.

The automatic identification and analysis of extended defects inside the crystalline lattice, an efficient strategy to build the Burgers circuit, has been implemented in OVITO. In DXA algorithm, the problem is solved by making a Delaunay tessellation of the dislocated crystal (Figure 2.4 (**a**)). The edges of such tessellation define the ensemble of the atomic step that will form the Burgers circuit. First, before going on and building any

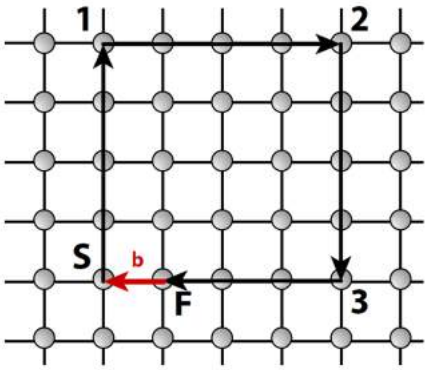

(a) Burgers circuit referred to the perfect crystal.

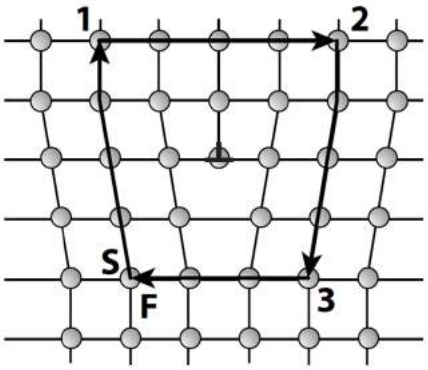

(b) Burgers vector in a real crystal with a dislocation line $\vec{\xi}$. The dislocation line is normal to the page plane.

Figure 2.3: Burgers circuit in a crystal with and without a dislocation. It starts from point S and end in F. In the perfect crystal an additional vector equal to $\vec{b}$ is necessary to close the circuit..[40]

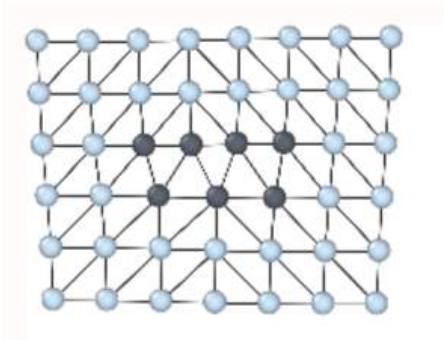

(a) Delaunay tessellation of an imaginary dislocated crystal. Defect core atoms as identified by a structure identification are shown in a darker hue.

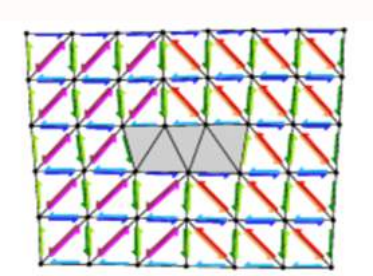

(b) Colored arrows indicate the mapping of tessellation edges to corresponding ideal lattice. Bad tessellation elements, for which the mapping to the perfect reference lattice cannot be determined, have been marked with a gray filling.

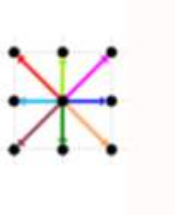

(c) Color legend for the eight different ideal lattice vectors appearing in (b)

Figure 2.4: Delaunay tessellation of a dislocated crystal.[40]

Burgers circuit, the algorithm tries to map each edge of the Delaunay tessellation in a point of the ideal lattice that can correspond to it (Figure 2.4 (**b**)). The latter operation is done thanks to the "`Common Neighbor Analisis (CNA)`" method. The CNA method

identifies which atom forms a perfect crystalline lattice elastically strained.

Inside the dislocation's core, the atomic ordering strongly deviates from that of a perfect crystal. Hence, the CNA will identify the core atoms as non-crystalline atoms. All the tessellation edges which are adjacent to these atoms will be labeled as *"bad" tessellation edges* by the DXA algorithm, and they will be excluded from the building of the Burgers circuit. On the contrary, *good tessellation regions* will be all the regions of the dislocated crystal where the mapping to the perfect crystal is not ambiguous. In effect, the DXA subdivides the crystal in "good" and "bad" regions with this spirit in mind, as shown in Figure 2.4 (**b**).

A this point, the only step remaining is the problem of how efficiently to build trial Burgers circuits to find and classify dislocations. The total number of all the possible closed circuits in a three-dimensional crystal is prohibitive; it's of main importance to considerably reduce the search space. The solution is clearly given by the definition just introduced of good and bad regions of the crystal. It defines a boundary surface between the two regions. In a three-dimensional system, this boundary is called *interface mesh* and is made up of those triangular faces of the Delaunay tessellation that are faces of a "good" tetrahedron on one side and of a "bad" one on the other side.

The interface mesh, shown in Figure 2.5, is a bi-dimensional manifold that surrounds all the crystal defects (including some point defects, grain boundaries, and free surfaces). Building sequential trial Burgers circuits on this surface made up of triangles is enough

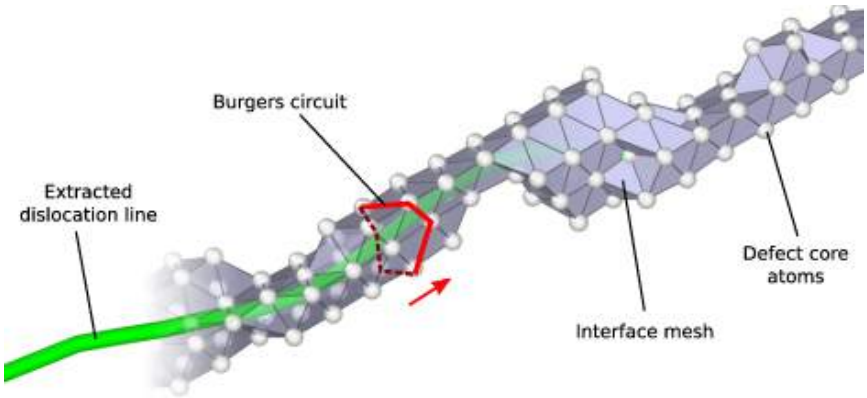

Figure 2.5: Illustration of the dislocation line extraction phase of the DXA. After the built of the interface mesh, that surrounds the defect core atoms, the algorithm uses a Burgers circuit on the interface to extract the dislocation line. While the Burgers circuit advances step by step, triangle by triangle, a continuous dislocation line is produced as a representation of the extended defect.[40]

to discover all the dislocation with a non-zero Burgers vector. The DXA generates trial circuits on the interface mesh, which are a sequence of edges of the Delaunay tessellation. The Burgers vector for each circuit is calculated as defined by equation 1.37 on page 15, summing the corresponding vectors in the ideal crystal determined at the first step of the DXA algorithm.

The DXA algorithm enumerates all the possible circuits on the interface mesh in ascending order by their length until a non-zero-Burgers-vector circuit is encountered. This trial circuit is thereafter used as a seed to find the rest of the dislocation line. It is done making the circuit advancing on the interface mesh, unveiling the dislocation line as shown in Figure 2.5. A mono-dimensional line representation is generated by calculating the center of each circuit while it advances alongside the manifold. While the circuit advances alongside the dislocation segments, it's possible that it locally expands to follow larger core sections, for example, in the presence of kinks and jogs. To avoid the extraction of dislocation lines from segments that have already been extracted or from interfaces, an upper limit can be specified using the parameter `Circuit stretchability` which specifies the maximum length of the circuit.

2.2.4 Vacancy and point defects identification

The identification of point defects is useful to study climbing mechanisms. That is possible in OVITO using the *Wigner-Seitz defect analysis* (WS) function.

This OVITO instruction is able to identify point defects in crystalline structures using the so-called Wigner-Seitz cell method. It makes it possible to count vacancies and interstitials in a virtual cell or to track their motion inside a crystalline lattice.

In Figure 2.6 it's possible to follow the subsequent description of WS method. The WS method requires two frames of the atomistic system as input: the reference configuration (e.g. Figure 2.6 (**a**)) and the displaced configuration (e.g. Figure 2.6 (**b**)). The first one defines where atoms would be located in a defect-free state of the crystal. In the first configuration, every site is occupied by exactly one atom. The configuration that we want to analyze is the "displaced" configuration. By direct experience, we found that, for visualization purposes, it's useful to make an affine transformation of the displaced simulation cell in such a way that it perfectly matches the reference configuration (as in Figure 2.6 (**b**),

(**c**). Similar results can be obtained using setting the OVITO parameter "`Affine mapping`" to on, but in the case of simulations in which only one direction changes, our approach resulted to work better.

To describe how the identification process works in OVITO, we follow a simple terminology: reference configuration atoms will be denoted as atomic sites (or simply sites), while atoms from the displaced configuration will be called simply atoms. The reference configuration specifies where atoms are supposed to be; if an atom is located on or close to a site, we can say that the site is occupied by the atom as shown in Figure 2.6 (**d**).

The WS cell method determines atoms-sites occupation and create a property called "`occupancy`" (Figure 2.6 (**e**), (**f**)). Using this method, every atom will be assigned to one site. Sites may be occupied by no atom, one atom, or more than one atom. We call these sites vacancy, normally occupied and interstitial sites, respectively.

The partitioning of the reference configuration is done by creating many Wigner-Seitz cells as the number of atoms in the configuration. Each atomic site defines the center of a Wigner-Seitz cell (or equivalently, a Voronoi cell). Any atom that is located within the Voronoi cell of a site belongs to that site.

Mathematically, the Wigner-Seitz (Voronoi cell) is the region of the space made up by the points that are closer to the point at the center of the site than to any of the other sites. Points exactly on the borderline between two Wigner-Seitz cells have exactly the same distance from the two site centers.

Actually, to determine in which cell a given atom is located, it is enough to determine what is the closest site and the WS algorithm never has to construct the geometric shapes of the WS cells.

The number of atoms in the two configurations doesn't need to be the same. But when they are, the number of vacancies and the number of interstitials will match. That's because, in this case, the sum over all occupancy numbers is equal to the number of sites in the reference.

2.3 Creation of atomic configurations

In the study of defects via molecular dynamics, the starting atomic configurations need to be prepared in advance. Specific details of how simulations starting configurations are

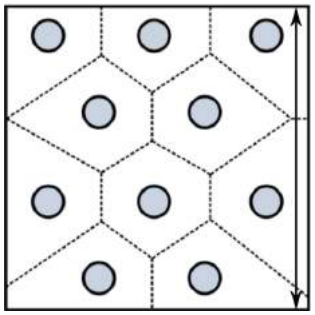

(a) Wigner-Seitz partitioning of the reference configuration.

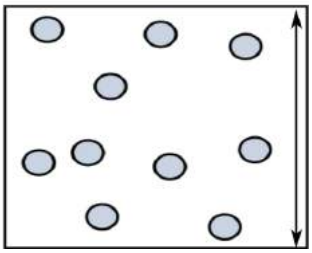

(b) Displaced configuration.

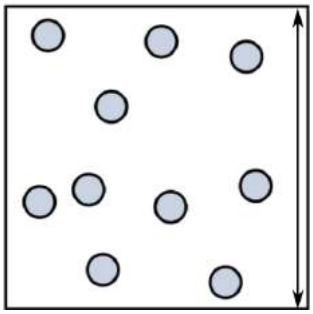

(c) Affine transformation of displaced configuration.

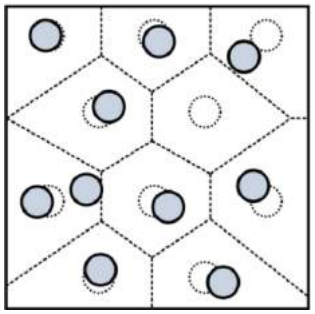

(d) Assignment of each atom to one site.

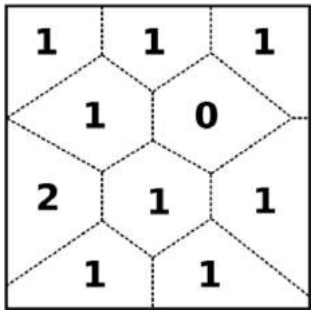

(e) Site occupancy.

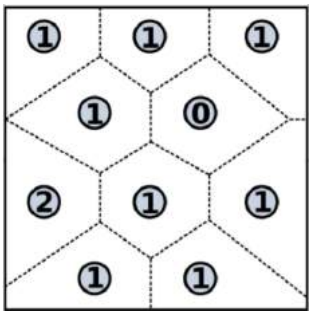

(f) Atom occupancy.

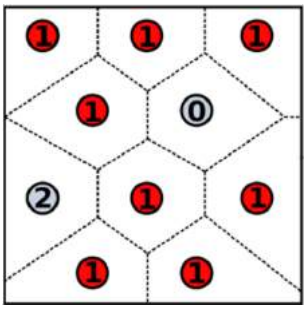

(g) Selection of atoms with occupancy equal to one.

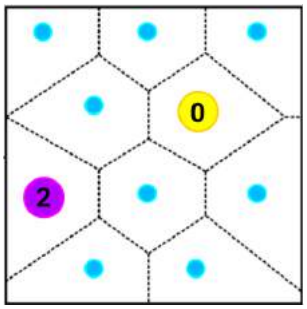

(h) Visualization of vacancies (yellow), interstitials (purple) and other atoms (light blue).

Figure 2.6: Point defects identification using Wigner Seitz analysis.[40]

prepared will be discussed punctually for each result/simulation presented in the next chapters of this Thesis. A brief description of the general procedures used will be given here below.

2.3.1 Supercell approach

The region that contains all the atoms of a simulation is usually called simulation *box*. The shape of this region typically is a rectangular prism which edges are big enough to contain all the atoms that one wants to simulate. As anticipated in Section 2.1.2, it is not possible

to simulate the complete extension of a real solid, and PBCs are used. To simulate thin epitaxially grown thin films on Si substrates, PBCs are applied. Most of the simulations in this Thesis were performed using the slab approach, and PBCs were applied in the two directions perpendicular to the deposition plane normal direction.[44] The height of the film is typically small and few nms are enough to represent a relevant part of the epitaxial film without making the computational cost too high. The substrates on which the thin films are grown have variable thickness, but a trick allows to simulate only a limited number of substrate atoms, reducing the computational time. It consists of the simulation of only a few tenths of monolayers (MLs) of atom substrates. To make sure that few MLs of atoms behave like a thick substrate, the few bottom layers of substrate atoms are kept fixed to ideal bulk positions.

Reference system

The cell is created by placing atoms with the species of the material under investigation in the positions determined by the chosen lattice and its orientation. The lattice can be arbitrarily oriented with respect to the simulation cell axes. Thin films which we investigated in this Thesis are usually grown on the [001] surface of Si; therefore, the lattice is conveniently oriented in such a way that one of the ⟨100⟩ directions is aligned alongside one of the simulation cell reference system axes. In our case, we have chosen to align the [001] direction alongside the z box axis. It is helpful to orient the other two crystallographic directions in such a way that the x and y axes of the box are alongside the ⟨011⟩ directions. In this way the dislocation line directions in the diamond/zinc-blende lattice $\vec{\xi} = [1 \pm 10]$ are parallel to one of the box axes.

In the simulation box the crystallographic directions must form a right-handed triad and are aligned as follow:

- x axis parallel to the $[1\bar{1}0]$ direction
- y axis parallel to the [110] direction
- z axis parallel to the [001] direction

The Burgers vector in the new reference system are given by:

$$\frac{a}{2}\begin{bmatrix} b_x \\ b_y \\ b_z \end{bmatrix} = \frac{\alpha}{\sqrt{2}}\begin{bmatrix} 1 \\ -1 \\ 0 \end{bmatrix} + \frac{\beta}{\sqrt{2}}\begin{bmatrix} 1 \\ 1 \\ 0 \end{bmatrix} + \gamma\begin{bmatrix} 0 \\ 0 \\ 1 \end{bmatrix} \tag{2.22}$$

Where a is the lattice parameter, b_x, b_y and b_z are the components of the Burgers vector in the canonical reference system, while α, β and γ are the $\vec{b}$ components in the new reference system. The components of the Burgers vector in the rotated reference system is given by the system of equations:

$$\begin{cases} \alpha = \sqrt{2}\,\dfrac{a}{2}\left(b_x - \frac{1}{2}(b_x + b_y)\right) \\ \beta = \sqrt{2}\,\dfrac{a}{2}\left(\frac{1}{2}(b_x + b_y)\right) \\ \gamma = \dfrac{a}{2}\,b_z \end{cases} \tag{2.23}$$

2.3.2 Tilted cell

It's possible to simulate non-orthogonal boxes. This possibility is helpful when one wants to take advantage of special orientation of box axes. For example, consider a generic $\langle 111 \rangle$ direction (which is the direction of misfit dislocation glide planes and stacking faults planes), if the box has the usual orthogonal shape aligned with the axes aligned respectively alongside the $[\bar{1}10]$, $[110]$ and $[001]$ directions, none of the $\langle 111 \rangle$ direction is aligned with one of the axes. That's a problem if one is interested in the study of infinitely long threading arms or SFs which are aligned with $\langle 111 \rangle$ but wants to have the z cell axis aligned with the conventional $[001]$ direction. Tilting the cell edges also allows to create small cells with PBCs along all three directions that don't have internal stress due to non-zero Burgers vector defect at their interior.[20] Due to PBCs, the simulated system is not influenced by the tilting of the periodic face.

2.3.3 Straight dislocation lines insertion

The output of the supercell box creation is a text file containing all the positions and the properties of the atoms of the system under investigation. The atomic positions are the

perfect, ordered ones of the diamond/zinc-blende lattice. To simulate extended defects such as dislocations and SFs, it's necessary to manually introduce them in the crystal.

A straight dislocation line is inserted in the crystal applying the corresponding displacement field. A dislocation aligned alongside the $\vec{\xi}$ direction, with an arbitrary Burgers vector $\vec{b}$, can be inserted in a virtual crystal using the displacement fields of the linear elasticity theory described by Equations 1.48 and 1.40 on page 18. Once the directions of the dislocation line $\vec{\xi}$ and of the Burgers vector $\vec{b}$ specific instructions tell OVITO to operate as follow:

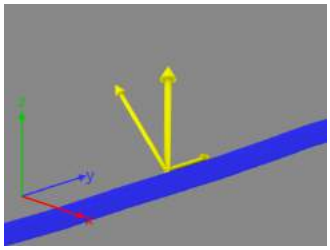

Figure 2.7: Burgers vector decomposition into the two components $\vec{b}_{\parallel}$ and $\vec{b}_{\perp}$.

1. The Burgers vector is decomposed into two components, one parallel to $\vec{\xi}$ one perpendicular.

$$\vec{b}_{\parallel} = \vec{b} \cdot \vec{\xi} \tag{2.24a}$$

$$\vec{b}_{\perp} = \vec{b} - \vec{b}_{\parallel} \tag{2.24b}$$

   The angle between $\vec{b}$ and $\vec{\xi}$ is given by:

$$\theta = \arccos\left[\frac{(\vec{b} \cdot \vec{\xi})}{\|\vec{\xi}\| \|\vec{b}\|}\right] \tag{2.24c}$$

   In Figure 2.7 an example of the decomposition of a 60° dislocation is shown. The Burgers vector is $\vec{b}$ equal to $a/2\,[011]$, where a is the lattice parameter of the crystal.

2. An affine transformation of all the positions of atoms is done:

   - All the atomic positions are translated by a vector equal to $-\vec{p}_{dis} = -(x_0^{\text{dis}}, 0, z_0^{\text{dis}})$ in such a way that the origin of the reference system of the simulation cell corresponds with the point where the dislocation core have to be inserted, i.e. the dislocation field origin.

$$\vec{p}^{\,1} = \vec{p} - \vec{p}_{\text{dis}} \tag{2.25}$$

- A rotation transformation is applied. The transformation corresponds to the rotation of the whole crystal in such a way that the x direction of the reference system is aligned as the $\vec{b}_\perp$ vector and the z direction is aligned with the dislocation line direction.

  The rotation matrix is simply given by the matrix that has as first column the perpendicular component of the Burgers vector $\vec{B}_\perp$, as third column the dislocation line direction $\vec{\xi}$, and as second column the vector determined by the right-hand rule and is equal to the glide plane normal $\vec{G}$. Note that the three vectors need to be normalized and written with the reference system of the simulation cell. To avoid problems it is convenient to change the reference system to the canonical one before the rotation of the system, i.e. $x = [100]$, $y = [010]$ and $z = [001]$.

$$\mathbf{R}_\theta = \begin{bmatrix} B_{\perp \mathrm{x}} & G_\mathrm{x} & \xi_\mathrm{x} \\ B_{\perp \mathrm{y}} & G_\mathrm{y} & \xi_\mathrm{y} \\ B_{\perp \mathrm{z}} & G_\mathrm{z} & \xi_\mathrm{z} \end{bmatrix} \tag{2.26}$$

  The new positions $\vec{p}^{\mathrm{II}}$ are given by:

$$\vec{p}^{\mathrm{II}} = \vec{p}^{\mathrm{I}} \cdot \mathbf{R}_\theta \tag{2.27}$$

  In this way, the vector $\vec{b}_\perp$ and the dislocation line $\vec{\xi}$ are aligned with the x and z directions. The y direction now indicates the position of the extra half-plane.

3. Now the Hirth and Lothe Equations 1.40 and 1.48 that describe the displacement field are applied. The $\vec{b}_\parallel$ parallel component determines the screw displacement, whereas the $\vec{b}_\perp$ component determines the edge displacement. We have that the displaced positions $\vec{p}^{\mathrm{II'}}$ are given by:

$$\vec{p}^{\mathrm{II'}} = \vec{p}^{\mathrm{II}} + \vec{u} \tag{2.28a}$$

For each atom i:

$$\begin{cases} x_{\mathrm{i}}^{\mathrm{II'}} &= x_{\mathrm{i}}^{\mathrm{II}} + u_{\mathrm{x}}(x_{\mathrm{i}}, y_{\mathrm{i}}, z_{\mathrm{i}}) \\ y_{\mathrm{i}}^{\mathrm{II'}} &= y_{\mathrm{i}}^{\mathrm{II}} + u_{\mathrm{y}}(x_{\mathrm{i}}, y_{\mathrm{i}}, z_{\mathrm{i}}) \\ z_{\mathrm{i}}^{\mathrm{II'}} &= z_{\mathrm{i}}^{\mathrm{II}} + u_{\mathrm{z}}(x_{\mathrm{i}}, y_{\mathrm{i}}, z_{\mathrm{i}}) \end{cases} \tag{2.28b}$$

where

$$u_{\mathrm{x}}(x,y,z) = \frac{b_{\perp}}{2\pi}\left(\arctan2(y,x) + \frac{x\,y}{2(1-\nu)(x^2+y^2)}\right) \tag{2.28c}$$

$$u_{\mathrm{y}}(x,y,z) = -\frac{b_{\perp}}{2\pi}\left(\frac{(1-2\nu)log(x^2+y^2)}{4(1-\nu)} + \frac{x^2-y^2}{4(1-\nu)(x^2+y^2)}\right) \tag{2.28d}$$

$$u_{\mathrm{z}}(x,y,z) = \frac{b_{\parallel}}{2\pi}\arctan2(y,x) \tag{2.28e}$$

4. Thereafter, the inverse affine transformations are applied. It means to apply a rotation of θ around the y axis in the opposite sense and to subsequently apply a translation of $\vec{p}_{\mathrm{dis}} = (x_0^{\mathrm{dis}}, 0, z_0^{\mathrm{dis}})$ in such a way that the positions are in the original reference system.

$$\vec{p}^{\,\mathrm{I'}} = \vec{p}^{\,\mathrm{II'}} \cdot \mathbf{R}_{\bar{\theta}} \tag{2.29}$$

$$\vec{p}\,' = \vec{p}^{\,\mathrm{I'}} + \vec{p}_{\mathrm{dis}} \tag{2.30}$$

2.3.4 Dislocation loops insertion

A dislocation loop is a non-straight, close dislocation line. The line surrounds a circular region that is co-planar to the glide plane. Any Burgers circuit that intersects this area will have a corresponding Burgers vector $\vec{b} \neq 0$. Any other Burgers circuit that doesn't pass through this region will have $\vec{b} = 0$.

To obtain the displacement field which generates such a system, we operated in a similar way as in the case of straight dislocation lines.

Circular dislocation loops

1. Initially a dislocation line direction is set, even it the loop is a closed line. It is needed for debugging purposes, and by considering as $\vec{\xi}$ the segment of the loop

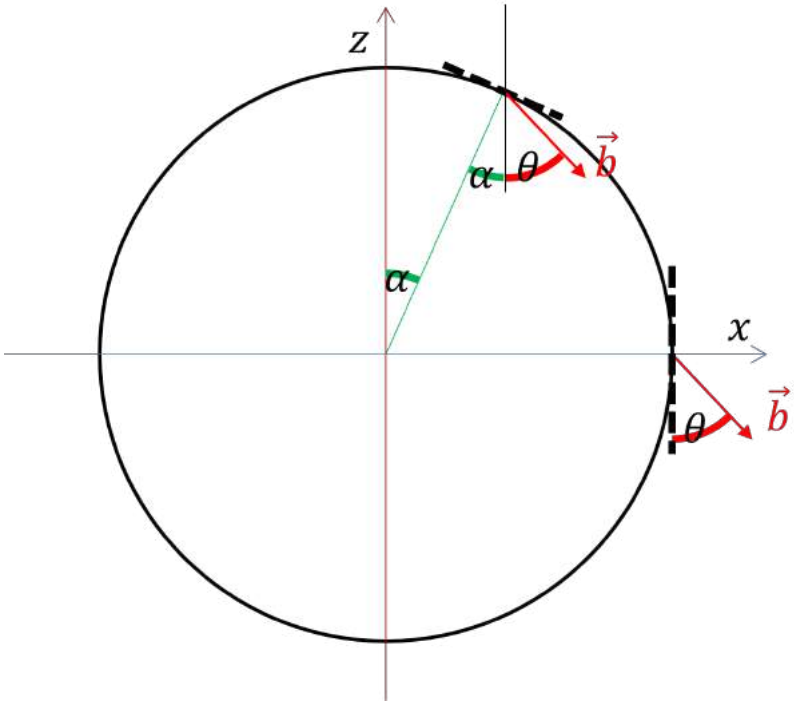

Figure 2.8: Burgers vector decomposition into the two components $\vec{b}_{\parallel}$ and $\vec{b}_{\perp}$ in the case of a dislocation loop.

corresponding to a convenient dislocation line (e.g. the misfit segment) it's easier to label the loop by the angle θ between this direction and the Burgers vector (as it would be in the case of a straight dislocation line). The angle θ between $\vec{b}$ and $\vec{\xi}$ is given by:

$$\theta = \arccos\left[\frac{(\vec{b}\cdot\vec{\xi})}{\|\vec{\xi}\|\|\vec{b}\|}\right] \tag{2.31}$$

2. An affine transformation of all the positions of atoms is done:

   - All the atomic positions are translated by a vector equal to $-\vec{p}_c = -(x_0^c, 0, z_0^c)$ in such a way that the origin of the reference system of the simulation cell corresponds with the center of the dislocation loop.

$$\vec{p}^{\,\mathrm{I}} = \vec{p} - \vec{p}_{\mathrm{c}} \tag{2.32}$$

   - A rotation transformation is applied. The transformation corresponds to the rotation of the whole crystal in such a way that the x direction of the reference system is aligned as the $\vec{b}_{\perp}$ vector and the z direction is aligned with the set dislocation line direction, in this way the xz plane is now parallel to the glide

plane. The rotation matrix is simply given by the matrix that has as first column the perpendicular component of the Burgers vector $\vec{B}_\perp$, as third column the dislocation line direction $\vec{\xi}$, and as second column the vector determined by the right hand rule and is equal to the glide plane normal $\vec{G}$ as in the preceding section.

$$\mathbf{R}_{\vec{\mathrm{b}}} = \begin{bmatrix} B_{\perp \mathrm{x}} & G_{\mathrm{x}} & \xi_{\mathrm{x}} \\ B_{\perp \mathrm{y}} & G_{\mathrm{y}} & \xi_{\mathrm{y}} \\ B_{\perp \mathrm{z}} & G_{\mathrm{z}} & \xi_{\mathrm{z}} \end{bmatrix} \tag{2.33a}$$

The new positions $\vec{p}^{\mathrm{II}}$ are given by:

$$\vec{p}^{\mathrm{II}} = \vec{p}^{\mathrm{I}} \cdot \mathbf{R}_{\vec{\mathrm{b}}} \tag{2.33b}$$

3. Differently from the straight dislocation line, now other two transformation are made.

   - For each atom is computed the angle α between the straight line connecting the atom to the center of the loop and the x axis. It lays in the xz plane which is also the glide plane of the loop. It is given simply by:

   $$\alpha(i) = \arctan2(z^{\mathrm{II}}, x^{\mathrm{II}}) \tag{2.34}$$

   - The Burgers vector is decomposed into a component parallel to the closest dislocation line segment of the loop and into a perpendicular one. In Figure 2.8 a sketch is shown to illustrate the geometrical relationship that are used for the decomposition. The dashed line is the direction set as the dislocation line direction.

   $$\vec{b}_\parallel(i) = \vec{b}_\parallel \cdot cos(\alpha(i) + \theta) \tag{2.35a}$$

   $$\vec{b}_\perp(i) = \vec{b}_\perp \cdot sin(\alpha(i) + \theta) \tag{2.35b}$$

   - The positions are translated in an angle dependent manner:

   $$\vec{p}^{\mathrm{III}} = \vec{p}^{\mathrm{II}} - \vec{p}_{\mathrm{loop}}(i) \tag{2.36a}$$

where $\vec{p}_{loop}(i)$ is the closest point of a circular shaped line with radius R to the atom i:

$$\vec{p}_{loop}(i) = (R \cdot sin(\alpha(i), 0, R \cdot cos(\alpha(i)) \tag{2.36b}$$

- The position of each atom is transformed again by placing it in a reference system where the x axis is aligned with $\vec{b}_{\perp}(i)$, the z axis with $\vec{b}_{\parallel}(i)$, and the y axis is not changed. The rotation matrix $\mathbf{R}_{\alpha}$(i) is different for each atom i and is given by:

$$\mathbf{R}_{\alpha}(i) = \begin{bmatrix} sin(\alpha(i)) & 0 & -cos(\alpha(i)) \\ 0 & 1 & 0 \\ cos(\alpha(i)) & 0 & sin(\alpha(i)) \end{bmatrix} \tag{2.37}$$

4. Now the Hirth and Lothe Equations 1.40 and 1.48 are applied as for straight lines. Indeed for each atom, the atomic position has been changed in such a way that we can use the displacement field of a straight dislocation line which is, in reality, a small portion of the segment of the loop perpendicular to the line connecting the atom to the center of the loop. The $\vec{b}_{\parallel}$ parallel component determines the screw displacement, whereas the $\vec{b}_{\perp}$ component determines the edge displacement. We have that the displaced positions $\vec{p}^{\text{III'}}$ are given by:

$$\vec{p}^{\text{III'}} = \vec{p}^{\text{III}} + \vec{u} \tag{2.38a}$$

For each atom i:

$$\begin{cases} x_{\text{i}}^{\text{III'}} & = x_{\text{i}}^{\text{III}} + u_{\text{x}}(x_{\text{i}}, y_{\text{i}}, z_{\text{i}}) \\ y_{\text{i}}^{\text{III'}} & = y_{\text{i}}^{\text{III}} + u_{\text{y}}(x_{\text{i}}, y_{\text{i}}, z_{\text{i}}) \\ z_{\text{i}}^{\text{III'}} & = z_{\text{i}}^{\text{III}} + u_{\text{z}}(x_{\text{i}}, y_{\text{i}}, z_{\text{i}}) \end{cases} \tag{2.38b}$$

where again,

$$u_x(x,y,z) = \frac{b_\perp}{2\pi}\left(\arctan2(y,x) + \frac{x\,y}{2(1-\nu)(x^2+y^2)}\right) \tag{2.38c}$$

$$u_y(x,y,z) = -\frac{b_\perp}{2\pi}\left(\frac{(1-2\nu)\,log(x^2+y^2)}{4(1-\nu)} + \frac{x^2-y^2}{4(1-\nu)(x^2+y^2)}\right) \tag{2.38d}$$

$$u_z(x,y,z) = \frac{b_\parallel}{2\pi}\arctan2(y,x) \tag{2.38e}$$

5. Thereafter the inverse affine transformations are applied. It means to apply a rotation of θ around the y axis in the opposite sense and to subsequently apply a translation of $\vec{p}_{dis} = (x_0^{dis}, 0, z_0^{dis})$ in such a way that the positions are in the original reference system.

Hexagonal shaped dislocation loops

Polygonal shaped loops can be generated using the procedure anticipated in the preceding section simply changing the definition of $\alpha(i)$in and $\vec{p}_{loop}(i)$ in Equations 2.34 and 2.36b. For example an Hexagonal shaped loop can be obtained with:

$$\alpha(i) = -\frac{\pi}{6} + \frac{\pi}{3}\cdot \text{round}\left(\frac{\pi/6 + \arctan2(z^{II}, x^{II})}{\pi/3}\right) \tag{2.39a}$$

$$\vec{p}_{\text{hex}}(i) = (R\cdot sin(\alpha(i), 0, R\cdot cos(\alpha(i)) \tag{2.39b}$$

2.4 Interatomic potentials for SiGe

They exist many three-body potentials used for the modeling of crystalline covalent solids such as silicon and its alloys with germanium with tetrahedral structure, between them the most notorious one made by *Stillinger and Weber (1985)*[45] and the one made by *Tersoff (1988).*[46]

2.4.1 Tersoff potential

The potential formulated by Tersoff in[46] and subsequently updated in[47] is a potential based on a two- and a three-body term in the calculation of the potential energy. The potential energy is obtained from:

$$E = \frac{1}{2}\sum_{\mathrm{i}}\sum_{\mathrm{j}\neq\mathrm{i}} V_{\mathrm{ij}} \tag{2.40}$$

where the potential V_{ij}, is the Tersoff potential which has the following expression:

$$V_{\mathrm{ij}} = f_C(r_{\mathrm{ij}})\left[f_R(r_{\mathrm{ij}}) + b_{\mathrm{ij}} f_A(r_{\mathrm{ij}})\right] \tag{2.41a}$$

The two terms $f_R(r_{\mathrm{ij}})$ and $f_A(r_{\mathrm{ij}})$ in equation 2.41a represent a repulsive term and an attractive term respectively with a dependency on the interatomic distance r_{ij} only. Differently, $f_C(r_{\mathrm{ij}})$ is a cutoff function that zeros the interaction beyond a determined distance $R+D$, usually called cutoff radius (more precisely, this distance is such that each atom interacts only with its first four neighbors, in a perfect diamond/zinc-blende lattice). This function is nothing more than a sinusoidal junction function between $R-D$ and $R+D$ inserted in such a way that the continuity of the potential is preserved.

$$\begin{aligned} f_R(r) &= A\,e^{-\lambda_1 r} \\ f_A(r) &= -B\,e^{-\lambda_2 r} \\ f_C(r) &= \begin{cases} 1 & \text{if } r < R-D \\ \frac{1}{2} - \frac{1}{2}\sin\left(\pi\frac{r-R}{D}\right) & \text{if } R-D < r < R+D \\ 0 & \text{if } r > R+D \end{cases} \end{aligned} \tag{2.41b}$$

In the expression of the Tersoff potential 2.41a the three functions f_R, f_A and f_C contain only distance-depending terms; as shown in the equations 2.41b[¶], hence they represent a pair interaction. The term that contains the three-body interaction is b_{ij}, it is usually called in the literature as *Bond Order* and takes into account the interaction with a third atom $k \neq i, j$. The term b_{ij} has the functional formulation described by the equations 2.41c. The bond order term makes less intense the attraction term, as well as the bond, between an atom i, and another atom j when the number of neighbors n_{i} of atom i-th increases. Moreover, bonds are favored or unfavored depending on the function $g(\theta_{\mathrm{ijk}})$ which depends on the bond direction. Indeed, θ_{ijk} represents the angle formed by the

[¶]For simplicity, we have chosen to omit the $i\,j$ subscript form all the parameters and also the distance r_{ij}

bonds ij and ik.

$$\begin{aligned} b_{ij} &= (1+\beta^{n_i}\zeta_{ij}^{n_i})^{-\frac{1}{2n_i}} \\ \zeta_{ij} &= \sum_{k\neq i,j} f_C(r_{ik})\,\omega_{ik}\,g(\theta_{ijk})\,e^{[\lambda_3^m(r_{ij}-r_{ik})^m]} \\ g(\theta_{ijk}) &= \gamma_{ijk}\left(1+\frac{c_i^2}{d_i^2}-\frac{c_i^2}{\left[d_i^2+(\cos\theta_{ijk}-\cos\theta_0)^2\right]}\right) \end{aligned} \tag{2.41c}$$

The parameter on which the potential depends on are:

$$A \quad B \quad \lambda_1 \quad \lambda_2 \quad \lambda_3 \quad R \quad D \quad \beta \quad c \quad d \quad m \quad \gamma \quad \cos\theta_0 \tag{2.42}$$

2.4.2 Stillinger and Weber potential

Stillinger and Weber originally proposed their model with a certain parametrization for Si only. Later, Stillinger and Weber were able to re-parametrize the SW model for Ge and fit their theoretical phonon-dispersion relationship to the experimental one.[45] The 3-body Stillinger-Weber potential for the energy E of a system of atoms is given by

$$E=\sum_i\sum_{j>i}\phi_2(r_{ij})+\sum_i\sum_{j\neq i}\sum_{k>j}\phi_3(r_{ij},r_{ik},\theta_{ijk}) \tag{2.43a}$$

where ϕ_2 is a two-body term and ϕ_3 is a three-body term, r_{ij} and r_{ik} are the distances between the atom i and the atom j and between the atom i and the atom k, respectively, and θ_{ijk} is the angle between the two distances. The summations in the formula are over all neighbors j and k of atom i within a cutoff distance a. Fortunately, almost all parameters were found to be identical to those of Si. Each atom in the system has four degrees of freedom: The first is a discrete variable (or pseudo-spin)S; given by the nature of the atom. We choose the notation so that $S_i = +1$ for a Si atom, and $S_i = -1$ for a Ge atom. The three other degrees of freedom correspond to the three coordinates of the atom r_i. The spatial dependence of the two-body interaction is introduced through the function ϕ_2 which has the following explicit form:

$$\phi_2(r_{ij})=A_{ij}\epsilon_{ij}\left[B_{ij}(\frac{\sigma_{ij}}{r_{ij}})^{p_{ij}}-(\frac{\sigma_{ij}}{r_{ij}})^{q_{ij}}\right]\exp\left(\frac{\sigma_{ij}}{r_{ij}-a_{ij}\sigma_{ij}}\right) \tag{2.43b}$$

It is interesting to note that $\phi_2(r)$ is a function of there-scaled bond lengthy only, and

therefore is the same for both Si and Ge. Another interesting feature of $\phi_2(r)$ is that, at $r = a$, it vanishes without any discontinuities in its derivatives. the same cutoff advantage can be extended to the three-body interactions ϕ_3. Specifically, the three-body interaction have the form‖:

$$\phi_3(r_j, r_k, \theta_{jk}) = \lambda_{jk}\epsilon_{jk}\left[\cos\theta_{jk} - \cos\theta_{0jk}\right]^2 \exp\left(\frac{\gamma_j\sigma_j}{r_j - a_j\sigma_j}\right)\exp\left(\frac{\gamma_k\sigma_k}{r_k - a_k\sigma_k}\right) \tag{2.43c}$$

The parameter on which the potential depends on are:

$$A \quad B \quad \varepsilon \quad \sigma \quad a \quad \lambda \quad \gamma \quad p \quad q \quad \cos\theta_0 \tag{2.43d}$$

2.5 Interatomic potentials for 3C-SiC

As for silicon and germanium, many three-body potentials are used for the modeling of crystalline silicon-carbide, between them, there is the one already presented in Section 2.4.1 made by Tersoff[46]**, the one made by Erhart and Albe[48] and the *Vashishta potential*.[49] Their mathematical details will be presented in the following sections; a detailed analysis of their applicability will be discussed in Chapter 3 in Section 3.1.

2.5.1 Tersoff potential

The Tersoff potential used to model silicon and its alloys with germanium, it is capable of modeling 3C-SiC. There is no change in its mathematical form; the only change is in the parameter used for the calculations. Notably, as already anticipated in 1.5, while germanium is completely miscible in a silicon structure, SiC is not. Therefore one should remember that, even if the potential allows the simulation of any alloy of SiC, only a stoichiometric SiC has a reasonable physical significance. Even though, such flexibility enables the study of a wide range of SiC configurations, where for example, a lot of carbon-carbon or silicon-silicon bonds are present. Due to its mathematical form (which is the same as Section 2.4.1), the potential is not able to reproduce any difference in energy depending on the SiC polytype, i.e., no difference in energy between 3C-SiC, 2H-SiC, 4H-SiC and 6H-SiC exists as well as no stacking fault energy.

‖Note that the subscript ij has be replaced by j, the subscript ik by k and the subscript ijk by jk.

**Tersoff potential admit atomic species which are the silicon, the germanium and the carbon.

2.5.2 Erhart-Albert analytical bond order potential

Erhart-Albert *Analytical Bond Order Potential* (ABOP) is a potential for atomic-scale simulations developed for the study of processes that involve transitions between widely different atomic configurations. It has been realized for pure Si, pure C and SiC using a fitting approach which follows a scheme that was previously applied to GaAs and GaN.[50,51] Bond-order potentials[52] are approximations of the moment expansion within the tight-binding framework and close relatives to the embedded atom method.[50,53] The functional form used in LAMMPS is the same as Tersoff potential with different parametrization.

2.5.3 Vashishta potential

The Vashishta potential computes the combined 2-body and 3-body family of potentials developed in the group of Priya Vashishta and collaborators. By combining repulsive, screened charge-dipole, and dispersion interactions with bond-angle energy based on the Stillinger-Weber potential, this potential has been used to describe a variety of inorganic compounds.[49]

The potential for the energy U of a system of atoms is

$$\Phi = \sum_{i}^{N}\sum_{j>i}^{N}\Phi_{ij}^{(2)}(r_{ij}) + \sum_{i}^{N}\sum_{j\neq i}^{N}\sum_{k>j,k\neq i}^{N}\Phi_{ijk}^{(3)}(r_{ij}, r_{ik}, \theta_{ijk}) \tag{2.44a}$$

where N is the number of atoms, ri the position of the i-th atom. The chemical bonds in SiC like III–V semiconductors have both small ionic and strong covalent features. When SiC is formed, a small amount of charge is transferred between Si and C atoms, resulting in a Coulomb interaction between the ions. Atoms also interact by charge-induced dipole and dipole-dipole (van der Waals) interactions, arising from the electronic polarizability of the ions. At short range, atoms repel each other. The two-body term Φ of the effective interaction potential representing all these two-body interactions is given by:

$$\Phi_{ij}^{(2)}(r) = \frac{H_{ij}}{r^{\eta_{ij}}} + \frac{Z_i Z_j}{r}\exp(-r/\lambda_{1,ij}) - \frac{D_{ij}}{r^4}\exp(-r/\lambda_{4,ij}) - \frac{W_{ij}}{r^6} \tag{2.44b}$$

where H_{ij} is the strength of the short-range steric repulsion, $r = r^{\eta_{ij}}$ the exponents of the

steric repulsion term, Z_{i} is the effective charge, D_{ij} is the strength of the charge–dipole attraction, W_{ij} is the *van der Waals* interaction strength, and λ_1, λ_4 are the screening lengths for Coulomb and charge–dipole terms, respectively. The summation over two-body terms is over all neighbors j within a cutoff distance r_c, i.e. $r < r_{\mathrm{c,ij}}$. The two-body terms are shifted and tilted by a linear function so that the energy and force are both zero at r_c.

The three-body terms of the potential have a spatial and an angular dependence defined by:

$$\Phi^3_{\mathrm{ijk}} = \Gamma(r_{\mathrm{ij}}, r_{\mathrm{ik}}) \cdot \Lambda(\theta_{\mathrm{ijk}}) \tag{2.44c}$$

where:

$$\Gamma(r_{\mathrm{ij}}, r_{\mathrm{ik}}) = B_{\mathrm{jk}} \cdot \exp\left(\frac{\gamma_{\mathrm{ij}}}{r_{\mathrm{ij}} - r_{0,\mathrm{ij}}}\right) \exp\left(\frac{\gamma_{\mathrm{ik}}}{r_{\mathrm{ik}} - r_{0,\mathrm{ik}}}\right) \tag{2.44d}$$

$$\Lambda(\theta_{\mathrm{ijk}}) = \frac{\left[\cos\theta_{\mathrm{ijk}} - \cos\theta_{0\mathrm{ijk}}\right]^2}{1 + C_{\mathrm{ijk}}\left[\cos\theta_{\mathrm{ijk}} - \cos\theta_{0\mathrm{ijk}}\right]^2} \tag{2.44e}$$

which gives[††]:

$$\Phi^{(3)}_{\mathrm{jk}}(r_{\mathrm{j}}, r_{\mathrm{k}}, \theta_{\mathrm{jk}}) = B_{\mathrm{jk}} \frac{\left[\cos\theta_{\mathrm{jk}} - \cos\theta_{0\mathrm{jk}}\right]^2}{1 + C_{\mathrm{jk}}\left[\cos\theta_{\mathrm{jk}} - \cos\theta_{0\mathrm{jk}}\right]^2} \times \exp\left(\frac{\gamma_{\mathrm{j}}}{r_{\mathrm{j}} - r_{0,\mathrm{j}}}\right) \exp\left(\frac{\gamma_{\mathrm{k}}}{r_{\mathrm{k}} - r_{0,\mathrm{k}}}\right) \tag{2.44f}$$

B_{ijk} is the strength of the three-body interaction, θ_{ijk} is the angle formed by r_{ij} and r_{ik}, and $\theta_{0,\mathrm{ijk}}$ is the covalent bond angle. The summation over three-body terms is over all neighbors j and k within a cut-off distance r_0, where the exponential screening function becomes zero, i.e. $r_{\mathrm{ij}} < r_{0,\mathrm{ij}}$, $r_{\mathrm{ik}} < r_{0,\mathrm{ik}}$

The parameter on which the potential depends on are:

$$H \quad \eta \quad Z_{\mathrm{i}} \quad Z_{\mathrm{j}} \quad \lambda_1 \quad D \quad \lambda_4 \quad W \quad r_c \quad B \quad \gamma \quad r_0 \quad C \quad \cos\theta_0 \tag{2.44g}$$

2.6 Interatomic potentials for Si

Silicon is one of the most intensely investigated semiconductors. Such a strong interest in silicon is motivated by its great technological importance. It is also the ideal covalent solid because theoretical concepts about covalent bonding can be tested. The nature of

[††]Note that the subscript ij has be replaced by j, the subscript ik by k and the subscript ijk by jk to show the whole formula.

Si bonding often makes the description of them difficult: the electrons in covalent bonds can only be described properly by quantum theory, while many interesting phenomena involve large numbers of atoms (in the range $\approx 10^3 - 10^9$), which quantum-mechanical approaches cannot handle.[54] Between all empirical model for inter-atomic interactions, the Stillinger and Weber,[45] the Tersoff potentials,[46,47,55] and the one proposed by Justo et al.,[56] are the most widely used. Still, their transferability to a wide class of structures remains in question. Techniques based on machine-learning ideas for interpolating the potential energy surface without explicitly describing electrons have recently shown great promise, but accurately and efficiently fitting the physically relevant space of configurations remains a challenging goal.[57] Bartok et al., presented a Gaussian approximation potential for silicon that achieves this,[59] reproducing *Density-Functional-Theory* (DFT) reference results for a range of many observable properties, including crystal, liquid, and amorphous bulk phases, as well as point, line, and plane defects.[58] They demonstrated that their potential enables calculations such as finite-temperature phase-boundary lines, self-diffusivity in the liquid, formation of the amorphous by slow quench, and dynamic brittle fracture, all of which are very expensive with a first-principles method.

2.6.1 Gap potential for Si

The *Gaussian Approximation Potential* (GAP) proposed by Bartok et al.[58] has many advantages with respect to standard semi-empirical potentials such as the Tersoff potential or the Stillinger and Weber one. It has been fitted via a machine learning approach to reproduce a wide class of ab-initio results. The time required for the ab-initio calculations (DFT) framework can be limiting, especially when the number of atoms involved is high. At this, the use of GAP to reproduce the same experiments can drastically reduce the time required for the calculations. The results obtained by Bartok et al. that interest us the most are (1) the ability to reproduce the different cohesive energies of different structures in the phase diagram of Si, (2) the surface energies of a wide class of Si surface alongside different orientations, (3) the phonon dispersion curves, and (4) defects energies, structures. An excellent agreement with DFT-based calculation for all this class of structures was achieved. The spatial and time scales achievable using GAP for Si are reduced in comparison with classical semi-empirical potentials but not so as it would be with an ab-initio approach.

Chapter 3

Results: Stacking faults evolution in 3C-SiC on Si(001)

The strong bonding between Si and C atoms makes SiC a group IV semiconductor with unique chemical and physical properties. It is a wide bandgap semiconductor (2.3 - 3.3 eV, depending on the crystal phase). It possesses strong thermal stability (sublimation temperatures up to 2800 °C), high thermal conductivity, about three times higher than that of Si (3.2 - 4.9 $W cm^{-1} K^{-1}$), a breakdown field ten times higher than that for Si (30×10^5 $V cm^{-1}$), large carrier saturation velocity (2×10^7 $cm\,s^{-1}$, hardness (Knoop hardness of 2480 $kg mm^{-2}$), and chemical inertness.[33–35] The hexagonal phases of this interesting semiconductor are increasingly used for electronic devices. It can be used for applications where elevated temperatures, high power, and frequencies, harsh environments are present.[60] First neighbors, in SiC, have a tetrahedral structure, but silicon and carbon atoms may occupy different lattice positions at further neighbors, giving rise to multiple crystal structures.[36,61,62] Between them, the most common SiC polytypes are the hexagonal (6H and 4H phases) and the cubic (3C phase) one, with a stability hierarchy depending on temperature, as understood in a recent paper.[36] The deposition on Si substrates has as natural output the 3C-SiC cubic phase and displays several interesting features. The zinc-blende structure's higher symmetry gives it excellent electrical properties, such as a reduced phonon scattering and the highest electron mobility and saturated drift velocity, compared to the other SiC polytypes. Furthermore, 3C-SiC can be a valid substrate for the epitaxial growth of boron nitride and gallium nitride thin films.[63,64]

The growth of a large area bulk 3C-SiC material is still under development: 3C-SiC

epi-layers on hexagonal SiC substrates (4H and 6H) are possible. Unfortunately, hexagonal SiC commercially available wafers are much smaller than the Si ones, and their crystal quality is also not sufficiently good. Indeed, they contain a large number of extended defects that may propagate in the 3C-SiC epilayers.[65] An important alternative is growing 3C silicon carbide by heteroepitaxy on Si (001) and Si (111) substrates. It could enable direct integration onto the Si technology and thus offer an advantage over hexagonal SiC polytypes. Nevertheless, there are structural differences between the substrate and epilayers. They hinder the possibility of obtaining crystalline 3C-SiC on Si substrates with high quality, reducing the great potential of this material for electronics and power electronics. In particular, a $\approx$ 20% misfit strain between the epilayer and the substrate arises due to the difference between the atomic spacing of cubic silicon carbide with respect to silicon (their lattice parameters are 4.53 Å and 5.43 Å, respectively, at room temperature). Moreover, there is a difference in their thermal expansion coefficients of ($\approx$ 8%) that causes the presence of a thermal strain in the epilayer. Thus, at all the growth stages, extended defects nucleate close to the SiC/Si interface and propagate into the films, as driven by the misfit strain relaxation.[32,66] Between all classes of defects, the most relevant ones are *dislocations*, *twins*, *stacking faults*, and *anti phase boundaries*. Such defects have detrimental effects on device performance. In particular lower breakdown electric fields are possible, and leakage currents are present. Several publications have experimentally shown their correlation with twins and stacking faults in the epitaxial 3C-SiC films.[67–72] Anti phase boundaries are often observed in 3C-SiC and are very detrimental for device performances and fabrication.[73] Nevertheless, most of the problems related to APBs can be avoided using misoriented substrates. Indeed, on Si(001) substrates, APBs appear only in presence of a mono-atomic step on the Si substrate.[31] Such a step can be easily eliminated by the having a miscutted Si substrate. Although at the moment, many consider the Si substrates as the most convenient choice for 3C-SiC epitaxy, the high-quality growth is still a significant challenge for researchers.

3.1 Study of stacking fault evolution via different potentials in 3C-SiC

One should never forget that the potentials used for classical MD simulations are empirical, and hence they should not be regarded as universally reliable or quantitatively precise. Therefore it is often required to test different potentials for investigating a specific phenomenon. A number of different potentials have been developed for MD simulations of SiC materials.[46–49,55] In the Literature, they have been applied to study the fundamental SiC characteristics successfully. The range of conditions where these potential have been applied ranges from SiC structural phase transformations under pressure,[74] to the behavior of SiC ceramics under shock loading,[75,76] and to the study of the plasticity of single crystal 3C–SiC during *nanometric cutting*.[77,78] In particular, many publications have focused on the MD simulation of the formation and evolution of extended defects in 3C–SiC induced by mechanical impact.[75–78] In these studies, defect networks with high amounts of dislocations and SFs are considered on average, in their ensemble, ignoring the evolution of the atomic detail at the level of the dislocation cores and the details of individual dislocation interaction. For the mentioned kind of problems, the potential proposed by Vashishta et al.,[49] has demonstrated its superior efficiency over other MD potentials, thanks to its ability to reproduce the generalized SFs energy and mechanical characteristics of 3C–SiC accurately. However, in epitaxially grown 3C–SiC on Si substrates, one should not ignore the interaction of individual *partial dislocations* (PDs) and the formation of local atomic configurations of dislocation complexes. Clear examples were given in a series of papers of us in References.[79–81]

As a first step, we did an independent test of the applicability of classical potentials to meet the requirements to tackle these issues by MD simulations. A comparison between Vashishta and the other MD potentials in describing individual defects and processes at atomic scale has been reported by us in Reference.[82] We performed a comparative MD simulation study of the evolution of systems consisting of 60° perfect and 30° and 90° Shockley partial dislocations as well as SFs in 3C–SiC material with three potentials, namely Tersoff,[46,47,55] analytical bond order,[48] and Vashishta potential.[49] In this section of the Thesis, we report the detailed analysis of the capabilities offered by each potential and their restrictions in application to describe the structures and dynamics of

extended defects in 3C–SiC. Based on the study published in the article[82] we suggest an MD simulation approach in terms of the potentials to be used to model various types of extended defects, including dislocations and SFs as well as their complexes, in cubic silicon carbide epi-layers.

MD simulations that will be presented in the next subsections have been performed in the canonical ensemble (NVT), using a Nose–Hoover thermostat regime at temperatures ranging from 1200 to 2000 K. These simulation temperatures have been chosen as satisfying the following conditions:

- to be not close enough to the actual temperatures of 3C–SiC layer deposition(≈1300 °C-1600 °C).
- to be sufficiently high to allow one to observe defect evolution in reasonable simulation times, a condition which (see below) was achieved in the upper limit of the explored temperature range.
- to be well below the 3C–SiC melting temperature predicted by each of the potentials (≈3250 K for Vashishta potential,,[49] and ≈3800 K for Tersoff potential and ABOP,[83] respectively) to avoid the possible influence of the pre-melting lattice disorder on the defect dynamics.

The value of the time step was set to 0.3 fs. It was determined as the largest one that maintained sufficient energy conservation in micro-canonical simulation runs at the highest temperature. The simulation cell used to perform the analyses on the behavior of the MD potentials for cubic SiC were box-shaped simulation cell bounded by the planes with orientations $[1\bar{1}\bar{2}]$, $[1\bar{1}1]$, and [110] in the directions of the axes X, Y, and Z, respectively. With such an orientation, the glide plane of the dislocation lies in the X direction, and the dislocation line is oriented along the Z one, allowing the simulation of periodic arrays of dislocation. Periodic boundary conditions were applied in all three directions. Before any simulation of the cell annealing, the presented configurations have been allowed to relax using the energy minimization procedure with the Polak–Ribiere conjugate gradient algorithm, with stopping tolerance for energy and force equal to 10^{-6} eV and 10^{-8} eV Å^{-1}, respectively. We inserted the dislocations into the simulation cells by displacing all the atoms in a perfectly crystalline cell using the approach described in Section 2.3.3.

To preserve the integrity of the simulation cell, perfect or partial dislocations with opposite Burgers vectors have to be inserted in pairs into the same (111) plane with some in-plane separation between them. Indeed, the insertion of a single dislocation would lead to the appearance of an atomic step on the simulation cell boundary plane induced by atom shifting.

Dislocations with opposite Burgers vectors considered together are usually referred to as dislocation dipoles. We probed various separation distances and simulation cell sizes to find the optimum values of these quantities with respect to the reliability of modeling predictions on the one hand and simulation speed on the other hand. In particular, for each trial simulation run, the cell dimensions from the preceding run have been doubled in alternation with doubling the distance between the inserted dislocations. We chose the simulation cell size and the distance between the dislocations so that doubling these quantities made no effect on the dislocation behavior during probe MD simulations. Based on this study, a cell with 24576 atoms in total, sized as $24 \cdot \frac{\sqrt{6}}{6} 4a \times 4 \cdot \frac{\sqrt{3}}{3} 6a \times 4 \cdot \frac{\sqrt{2}}{2} 2a$, with a distance between the dislocations equal to $18 \cdot \frac{\sqrt{6}}{2} a$ (where a is the potential dependent lattice constant of 3C–SiC material) have been chosen for the demonstration of simulation results.

3.1.1 Properties of 3C–SiC with MD potentials

Before studying the evolution of extended defects in 3C–SiC by MD simulations with the potentials described above, the latter have been comparatively tested with respect to their predictions of some of the basic 3C–SiC characteristics. In particular, for each potential, we have determined the lattice parameter a and the cohesive energy E_{coh}, calculated applying the LAMMPS energy minimization procedure at each value of a.

Table 3.1 shows the values of the lattice constant and cohesive energy of 3C–SiC calculated using three MD potentials and compared to respective experimentally determined values. All three potentials demonstrate satisfactory predictive power for these quantities. There are almost no discrepancies between the experimental and calculated results for ABOP and Vashishta potential,* while Tersoff potential shows a small underestimation of the value of 3C–SiC lattice constant by about 1.9% and overestimation of the cohesive energy value by approximately 1.4%, respectively. To better demonstrate the predictive

*Indeed those quantities are in the chosen ones in the potentials fitting.

Table 3.1: Calculated and experimental values of selected physical quantities of 3C–SiC phase

	Tersoff	ABOP	Vashishta	Exp.
	3C–SiC			
Lattice constant (Å)	4.2796	4.3593	4.3582	4.3596[84]
Cohesive energy (eV/atom)	6.4338	6.3392	6.3401	6.34[85]
	2H–SiC			
Equivalent cubic lattice const. (Å)	4.2796	4.3593	4.3341	
a* (Å)	3.0261	3.0825	3.0647	3.0763[86]
c* (Å)	4.9417	5.0337	5.0046	5.0480[86]
Cohesive energy (eV/atom)	6.4338	6.3392	6.3209	
	Stacking Faults			
Intrinsic SF (meVÅ^{-2})	0	0	12.1	2.1[87]

power of all three potentials, we have also determined the values of the lattice constants of the hexagonal 2H–SiC phase, as well as its cohesive energy. We calculated the lattice constants for the hexagonal phase over the equivalent cubic lattice constant a as follows:

$$a^* = \frac{a}{\sqrt{2}}, \quad c^* = \frac{2a}{\sqrt{3}} \tag{3.1}$$

Because Tersoff potential and ABOP compute the interaction only inside the first coordination sphere, the results presented in Table 3.1 provide the exact same result for the 3C and 2H–SiC phases. On the other hand, Vashishta potential takes into account interaction well beyond the first coordination sphere. Hence the equivalent lattice constant and cohesive energy is different, and, in particular, they are smaller for 2H–SiC compared to those of the 3C–SiC phase. As in the case of the cubic phase, ABOP and Vashishta potentials demonstrate much better agreement of calculated values with respective experimental data. In addition, the specific energy of a single SF has been calculated with each MD potentials. In the cubic crystal lattice, intrinsic SF is formed by removing a double plane from the ABC plane sequence along the [111] direction, thus creating an inclusion with hexagonal wurtzite configuration in the zinc-blende structure the 3C–SiC phase. Intrinsic SFs are closely related to partial dislocations as the boundaries between the former and the surrounding perfect crystal in the SF plane.[88] The values of the SF energy in 3C–SiC have been calculated, subtracting the potential energy of the stacking faulted configuration from that of the corresponding perfect cubic lattice. The energy cost per unit area

of a single SF calculated with Vashishta potential is equal to 12.09 $meV\text{Å}^{-2}$. This value is overestimated as compared to the respective energy of 2.51 $meV\text{Å}^{-2}$ provided by the DFT calculations,[36] and 2.12 $meV\text{Å}^{-2}$ obtained from experimental results.[87,89] Despite this discrepancy, no better estimation can be obtained with existing empirical MD potentials. Note that values of the SF energy determined both by DFT and using Vashishta potential are of the same sign and will influence the energy of the 3C–SiC system with the extension or shrinking of the SF in the same way. In particular, positive energy contribution will affect the evolution of the systems containing SFs during MD simulations, with Vashishta potential tending to decrease the SF extension. In their turn, both Tersoff potential and ABOP, being limited to the first coordination sphere, make no difference between the hexagonal wurtzite and cubic zinc-blende SiC configurations, therefore, predicting zero value of the SF energy.

3.1.2 Stability of dislocation core reconstructions with MD potentials

In the literature,[88,90] peculiar reconstructions of the cores of 30° and 90° partial dislocations in 3C–SiC have been reported, obtained by density functional theory (DFT) calculations.

We analyze the capability of three used MD potentials to maintain the atomic configurations of the reconstructed dislocation cores. Using a DFT approach, as described in Ref. [36], we produced the 30° partial dislocations 2×1 core reconstruction and the single period reconstruction of the 90°partial. The resulting core configurations fully agree with those obtained in References[88,90] and are shown in Figure 3.1 (**a**) and (**e**) for the 30° and 90° partial dislocations, respectively. We took the DFT reconstructed dislocations and then minimized the cell energy through a standard minimization algorithm with the MD potentials. As can be seen from Figures 3.1 (**b**)–(**d**),(**f**)–(**h**), the core reconstructions are maintained by only Tersoff potential and ABOP, while transformations of the cores of partial dislocations occur after energy minimization with Vashishta potential (see Figures 3.1(**d**) and (**h**)). For the single period reconstructed 90° PD, we observe a slight displacement of the SF plane so that Si-Si and C-C atomic distances in the core become equal. The Vashishta potential mathematical formulation is the reason for such behavior. Indeed the repulsion between the atomic species of the same types drives them to separate

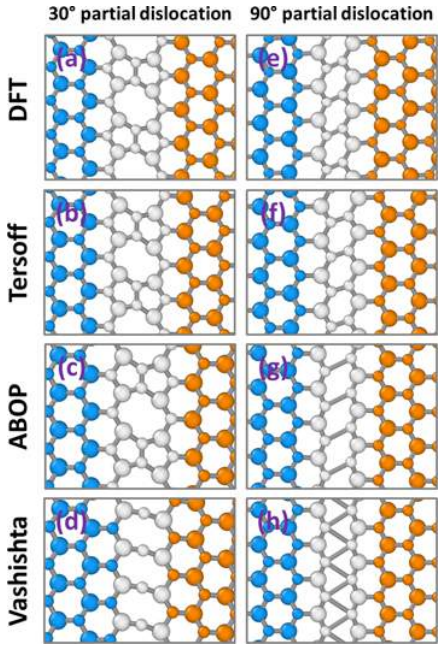

Figure 3.1: Top view of the atomic configurations of the cores of 30° (**a**)–(**d**) and 90° (**e**)–(**h**) Shockley partial dislocations obtained by DFT calculations (**a**), (**e**) as well as after energy minimization procedure with Tersoff potential (**b**), (**f**), ABOP (**c**), (**g**), and Vashishta potential (**d**), (**h**), respectively. Larger spheres represent Si atoms, while smaller ones correspond to C atoms, respectively. Blue color corresponds to the atoms in cubic diamond lattice. The atoms in the stacking faults (hexagonal diamond lattice) are shown in orange color. White color corresponds to the atoms within the dislocation cores that do not match any of the two mentioned perfect crystal lattice configurations.

each other.

3.1.3 Dissociation of 60° perfect glide dislocations

This subsection considers the predictions of all three MD potentials described above regarding the known phenomenon of *dissociation of a 60°* perfect glide dislocation. The processes addressed here can be referred to as described in Ref. [82] "local" processes being primarily determined by local atomic configurations and rearrangements of bonds.

We inserted 60° dislocation dipoles according to the procedure described in Section 2.3.3 using the atom displacements calculated as described there. The origin of the displacement field belongs to the $(1\bar{1}1)$ plane that is the correct one to have a glide 60° dislocation. In Figure 3.2(**a**) we show the simulation cell with the inserted 60° glide dislocation dipole before any MD operation. On the left, we have the so-called carbon terminated dislocations and on the right silicon terminated ones.[90] For each MD potential considered we report in Figures 3.2(**b**),(**c**) the images of the structure of 60° dislocations after energy

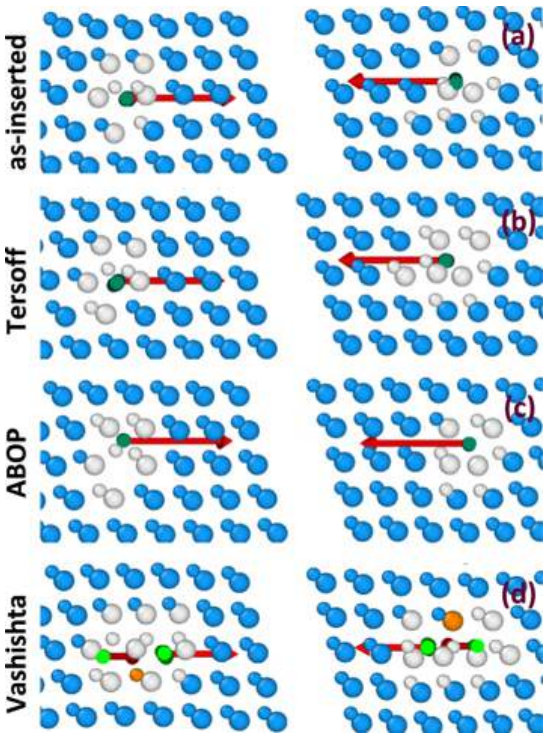

Figure 3.2: Snapshots of the left and right parts of the 3C–SiC simulation cell after insertion of a pair of 60° perfect dislocations (a) and after energy minimization procedure with Tersoff potential (b), ABOP (c), and Vashishta potential (d), respectively. Larger spheres represent Si atoms, while smaller ones correspond to C atoms, respectively. Flat dots indicate the projections of the dislocation lines of 60° perfect or 30° and 90° partial dislocations. Arrows show the dislocation Burgers vectors. Blue color corresponds to the atoms in cubic diamond lattice. The particles in the stacking faults (hexagonal diamond lattice) are shown in orange color. White color corresponds to the atoms within the dislocation cores that do not match any of the two mentioned perfect crystal lattice configurations.

minimization. Experimental observations[91,92] report the dissociation of 60° perfect dislocations into 30°-90° pairs.

We observed the dissociation with a pure minimization procedure using Vashishta potential (see Figure 3.2(**d**)). On the contrary, Tersoff potential and ABOP maintain the initial perfect structure of both C- and Si-terminated 60° dislocations (see Figure 3.2(**b**) and (**c**), respectively). The energy minimization not leading to a dissociation of the 60° dislocation can be related to the energetic barrier, which these two potentials cannot overcome. We still need to understand the capability of the latter two MD potential to model 60° dissociation and if it is energetically favorable. So we proceeded as follows. We computed the energy of not-dissociated 60° and the energy of pairs of 30° and 90° PDs at a different distance one from the other. Then we compared them in Figure 3.3.

We calculated the energy corresponding to each configuration as follows. We take note

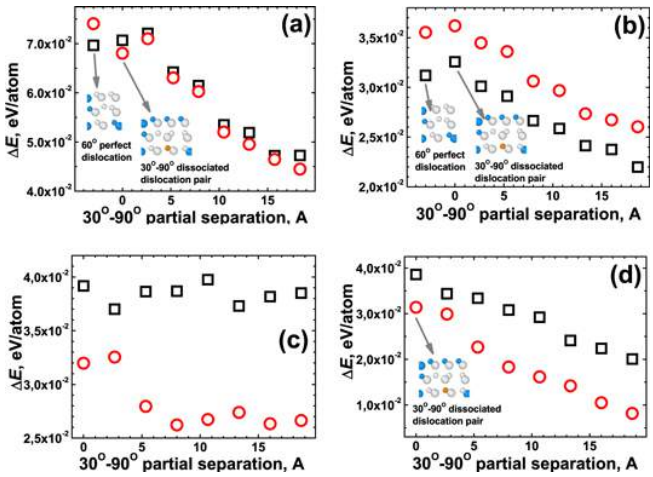

Figure 3.3: Potential energy per atom versus separation of the pairs of 30° and 90° Shockley partial dislocations representing the dissociated states of perfect 60° dislocations terminated by carbon (squares) and silicon (circles) atoms, calculated with Tersoff (a), ABOP (b) and Vashishta (c), (d) potentials. In the case of Vashishta potential, the results with (c) and without (d) account of the energy of stacking faults formed between the 30° and 90° dislocations are presented. Insets in the graphs show the perfect 60° or dissociated 30°–90° dislocation configurations.

of the total energy of the simulation cell, and then we subtract the total energy of the corresponding, completely defect-free configuration. The obtained energy difference ΔE takes into account the core energy of 60°, 30°, and 90° dislocation cores and the interaction energy acting between them. In the case of the Vashishta potential, also the SF energy is accounted for. In the case of Tersoff potential and ABOP, the first point corresponds to the perfect configuration of a 60° dislocation of the glide subset. The first point on the left in Figures 3.3(**a**) and (**b**) corresponds to a glide 60° perfect dislocation.[†] There is an energy advantage of having a dissociated pair of 30° and 90° PDs instead of a perfect 60° dislocation for Tersoff potential and ABOP. As the distance between the two dissociated PDs increases, the value of ΔE decreases. Such tendency is due to the repulsive force between the dissociated pair's 30° and 90° dislocations.[93] We also note that C- and Si-terminated 30° and 90° PDs have almost equal energy. In contrast, ABOP prescribes lower energy for carbon terminated pairs than silicon terminated ones. Vashishta potential is treated as a separate case because it prescribes a non-zero SF energy, and no stable 60° configuration can be built and minimized (see Figure3.2(**d**)). What we observe indeed is that an increase of the distance between partials leads to small energy changes, especially in the

[†]The actual 60° glide perfect dislocation configuration was possible only in the case of Tersoff potential and ABOP

case of carbon terminated dislocations, as shown by the graphs in Figure3.3(**c**). We identified in the positive energy of SF the cause of this tendency. Indeed, a more extended SF will have higher energy, compensating for the energy gain separating the dissociated pairs. By subtracting the SF energy from the energy values corresponding to the data presented in Figure3.3(**c**), it's possible to compensate for such effect. Indeed a similar trend to that obtained with other potentials is observed (see Figure3.3(**d**)).

3.1.4 Simulation of the evolution of perfect and partial dislocation dipoles

In this section, we test three considered MD potentials to assess their predictions regarding the evolution of dislocation dipoles. We consider the cases of perfect 60° – 60° pairs, partial 30° – 30°, and 90° – 90° with opposite Burgers vectors, studying them when subjected to annealing at high temperature. The MD potential used in each simulation determines the dislocation's evolution. Tersoff potential performed poorly in the simulation of 60°dislocation dipoles. Indeed, in a simulation time of six ns at a temperature of 2000 K, we observed only local perturbations of the dislocation structures but no actual motion. We observed such behavior for 60° dislocations and also for a pair of dissociated 30° and 90° PDs when they are in contact with each other (analogous to the structure shown in Figure 3.2(d). In their turn, ABOP or Vashishta potential succeeded in the simulation of 60° perfect dislocations motion.

Figure 3.4 shows a series of snapshots of the evolution of 60° perfect dislocations in 3C–SiC via MD using the Vashishta potential at an annealing temperature of 2000 K. The inserted 60° dislocation dipole dissociate into two pairs of 30° and 90° PDs in the initial minimization of the energy (see Figure 3.4(a)). The two dislocations attract because of their opposite deformation fields, and the annealing at 2000 K makes the two pairs of dissociated PDs move one toward the other. The 90° and 30° PDs separate one from the other because of a difference in their mobility. Being the 90° ones the faster, the SFs between the two PDs become longer (Figure 3.4(b)). The two opposite 90° PDs eventually merge in the prolonged annealing. It causes the annihilation of the 90° dislocations. What remains is a single SF connecting the two 30° partials. In the end also the two 30° PDs met, leading to complete annihilation of the inserted defects and the restoration of perfect lattice structure (Figures 3.4(c)–(e)). The evolution pattern obtained using ABOP is equivalent to

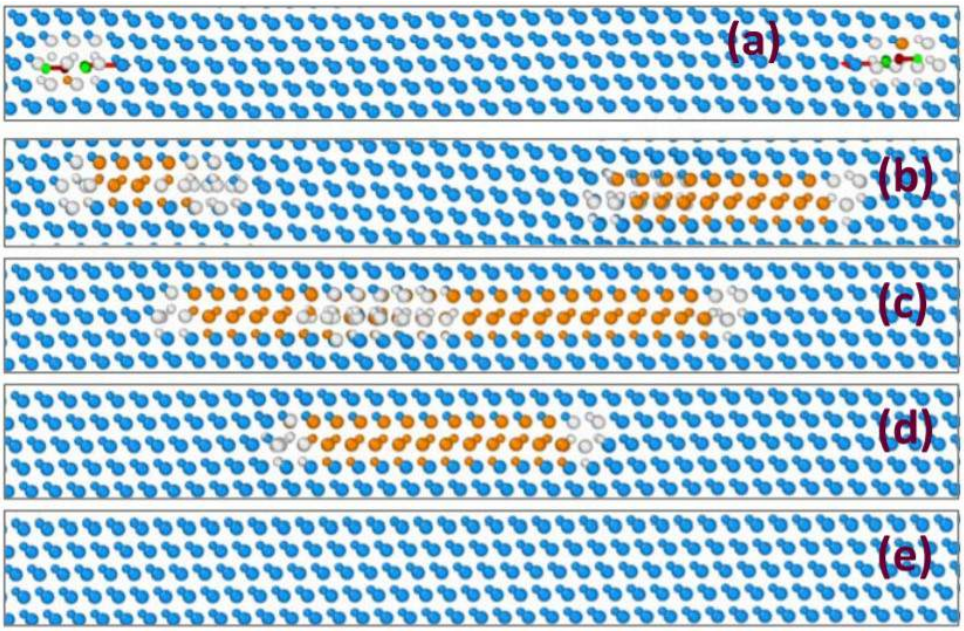

Figure 3.4: evolution of 60° perfect dislocations in 3C–SiC at 2000 K simulated with Vashishta potential after energy minimization (a) and after 6 (b), 11.4 (c), 18 (d), and 24 (e) picoseconds of simulated time. Blue color corresponds to the atoms in cubic diamond lattice. The atoms in the stacking faults (hexagonal diamond lattice) are shown in orange color. White color corresponds to the atoms within the dislocation cores that do not match any of the two mentioned perfect crystal lattice configurations.

that depicted in Figure 3.4. The main difference between the two is the time scale which is several orders of magnitude larger than Vashishta potential. We can attribute this to few aspects. First, the system needs time to overcome the energy barrier for dissociating the initial perfect 60° dislocation with ABOP. Second, we also found the dislocation motion much slower with ABOP than with Vashista potential. We studied the different predicted velocities of PDs by each potential, considering only 30° and 90° PDs pairs separately here below.

PDs velocities

In a simulation cell with PBCs, we must insert a dipole of dislocations to preserve the integrity of the crystal. By chance, it represented an advantage in the study of the velocities of PDs. Indeed, with a single simulation cell, where we inserted a dipole of 30° PDs or a dipole of 90°, we always have two different terminating species at each core.

In Figure 3.5 we show the snapshots of an MD simulation of the evolution of a dipole of 30° PDs annealed at 2000K. The two PDs attract due to their opposite deformation fields, and they move one toward the other until they meet and annihilate (Figures3.5(b)–(e)).

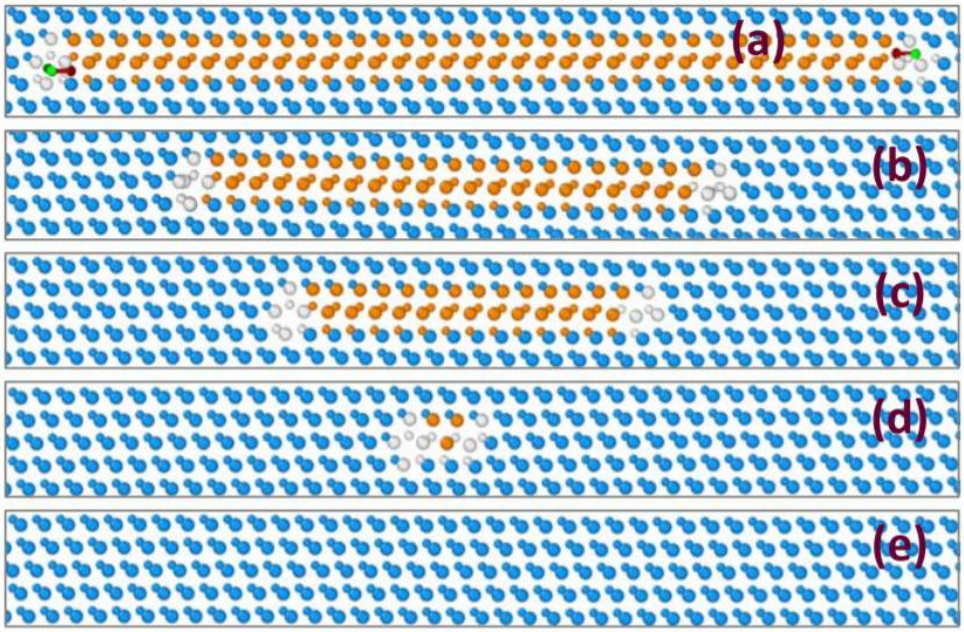

Figure 3.5: Evolution of 30° partial dislocations in 3C–SiC at 2000 K simulated with Vashishta potential after 0 (a), 6 (b), 12 (c), 18 (d), and 19.5 (e) picoseconds of simulated time. Blue color corresponds to the atoms in cubic diamond lattice. The atoms in the stacking faults (hexagonal diamond lattice) are shown in orange color. White color corresponds to the atoms within the dislocation cores that do not match any of the two mentioned perfect crystal lattice configurations.

All the potential considered could produce an evolution of the dipole for both 30° and 90° PDs. Still, a remarkable difference in the timescale for each process exists. We characterized the PD velocities in terms of the migration distances and respective times in which was observed. Results are summarized and presented in Table 3.2.

The data in Table 3.2 can be summed up as follows: Between PDs with the termination of the same species (carbon or silicon), the 90° ones are faster than the 30° ones. With the Vashishta potential, 90° PDs are about an order of magnitude faster than the other two potentials. Note that using the Tersoff potential, we did not observe any movement of the Si-core 90° dislocation until its carbon counterpart annihilated it. Vashishta potential prescribes almost equal velocity for 90° and 30°. On the contrary, Tersoff and ABOP have 90° PDs one and two orders of magnitude faster than 30° PDs. Therefore performing MD simulations with these two potentials will lead to a wide separation of the dislocations originating from a dissociated 60°, with a long SF in between. Finally, both Vashishta potential and ABOP agree to predict a higher motion velocity for the Si-terminated PDs. Tersoff potential reveals the contrary behavior.

Table 3.2: Times and migration distances of partial dislocations characterizing their motion velocities calculated with three MD potentials at 2000 K.

Simulated time	Potential	Dislocation type	Distance[i]
7.5 ps	Vashishta	90 °C-terminated	18.6819 Å
		90° Si-terminated	37.3638 Å
		30 °C-terminated	16.013 Å
		30° Si-terminated	18.6819 Å
75 ps	Tersoff	90 °C-terminated	26.2071 Å
		90° Si-terminated	0 Å
75 ps	ABOP	90 °C-terminated	10.6781 Å
		90° Si-terminated	13.3476 Å
750 ps	Tersoff	30 °C-terminated	10.4828 Å
		30° Si-terminated	7.86213 Å
6 ns	ABOP	30 °C-terminated	2.66952 Å
		30° Si-terminated	10.6781 Å

[i] The migration distances of dislocations are calculated over the lattice parameter a with the step l equal to the shortest distance between the same-type atoms in the ⟨112⟩ direction, $l = a\frac{\sqrt{6}}{4}$

3.1.5 Applicability of MD potentials in 3C-SiC

In the preceding subsections, we demonstrated that molecular dynamics (MD) simulations with analytical bond order (ABOP) and Vashishta potentials represent two complementary approaches that should be considered synergically. If one is interested in the long/large scale evolution of SFs and PDs in 3C-SiC, the Vashishta potential is preferable. Still, its mathematical form does not allow for the correct modeling of same-specie interactions such as Si-Si and C-C bonds. So, one interested in local details of the core structure of PDs that involve such bonds should perform MD simulations with ABOP instead. In conclusion, the best solution is a synergic use of both potentials: the large-scale dynamics should be investigated initially with the Vashishta potential. After that, the stability of the defective structure should be analyzed using ABOP.

3.2 Stability of dislocation complexes in 3C-SiC

An ideal testing framework for the employ of ABOP and Vashishta potential is represented by the study of multiple stacking faults structure and stability. With the term stability, we are referring to the capability of the boundary of multiple SFs to remain as a whole and not dissociate, as described in the work of Sarikov et al.[79] The most frequent, electrically active defects in 3C-SiC are the stacking faults,[94,95] and double and triple ones are particularly abundant.[96]

Each SF is strictly related to the defect (either a 30° or a 90° PD) that surrounds it at the border with bulk crystal. For this reason, it is of primary importance to identify which configurations of partial bounding dislocations are possible. Note that multiple SFs are bounded by a number of PDs equal to the number of planes of the SF.

In experimental observations via high-resolution transmission electron microscopy (HRTEM),[97–100] complexes of dislocation formed by two and three partial dislocations have been observed. The identification of which PD combinations (and the relative structure), between all possible ones, are possible can be helpful to improve the electrical characteristics of 3C-SiC by eliminating detrimental defects. In Ref. [79], we employed synergically the ABOP and Vashishta potential to study the dynamics of 30° and 90° PDs as bounding defects of double and triple stacking faults in 3C-SiC. This section will discuss the role of the reciprocal orientation of the Burgers vector of the PDs terminating multiplanes SFs complexes and what their interaction leads to.

MD simulations have been performed using LAMMPS code. Simulations were in the (NVT) ensemble. The time step used in the simulations was 0.3 fs.

At the beginning of the run, the initial velocities were set up at a corresponding temperature of 300K. After that, the temperature was increased linearly from 300 to 1800 K during 1.5 ps of simulated time. PBCs were applied in all three boundaries of the simulation cell. This time, the cell contained 65'280 atoms and was sized as $30 \cdot \frac{\sqrt{6}}{6} 4a \times 17 \cdot \frac{\sqrt{3}}{3} 6a \times 2 \cdot \frac{\sqrt{2}}{2} 2a$, where a is the 3C-SiC lattice constant. It slightly dependent on the MD potential used. We established the dimensions of the simulation cell by increasing them until the increase did not affect the observed behavior. The analysis of the defect structures was performed using OVITO. Partial dislocations were inserted so that their SF is on the $(1\bar{1}1)$ planes with dislocation lines aligned in the Z direction. Dislocations were inserted

as described before, (see Section 3.1 and 2.3.3).

We inserted each SF bounded by two identical PDs with opposite Burgers vector so that the total Burgers vector is zero. Hence, along each $(1\bar{1}1)$ plane, we can have either 30° or 90° pairs bounding each SF. In Figure 3.6 we report the atomic layout obtained for each dislocation, together with a sketch of the dislocation line and the Burgers vector of the PD. Note that the PDs are terminated by a different atomic species (Si or C) on each side of the SF. Also, note that Si-terminated 90° and C-terminated 30° dislocations are on the left side of Figure 3.6, whereas C-terminated 90° and Si terminated 30° are on the right. We inserted dislocation dipoles into two or three consecutive $(1\bar{1}1)$ planes with all possible orders of PDs. Then we studied the influence of the mutual orientations of the Burgers vectors of each combination of PDs to assess their interaction and the stability of double or triple dislocation complexes.

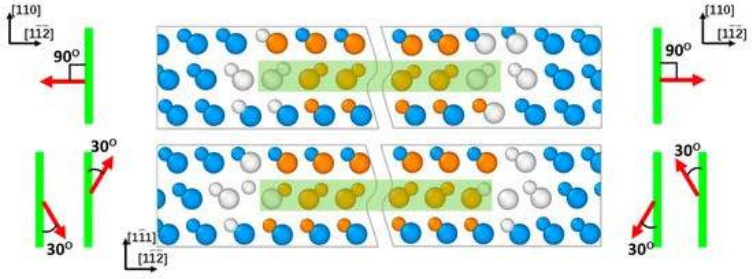

Figure 3.6: Atomic configurations of the dislocation dipoles consisting of Si- and C-terminated 90° (top panel) and C- and Si-terminated 30° (bottom panel) Shockley partial dislocations viewed in the direction [110]. Left and right panels show schematic representations of the dislocation Burgers vectors with respect to the dislocation lines viewed perpendicular to the $(1\bar{1}1)$ plane. Highlighted are the stacking faults formed between the partial dislocations in the dipoles. Vertical lines in the left and right panels correspond to the dislocation lines, and the arrows indicate possible directions of the dislocation Burgers vectors, respectively.

In the following subsections, we present the results of molecular dynamics simulations of the interaction of partial dislocations (PDs) terminating stacking faults. We will show that certain combinations of their Burgers vectors are more stable than others.

The results shown are only for combinations of the partial dislocations that were shown in the right panel of Figure 3.6, i.e., Si-terminated 30° and C-terminated 90° PDs. We obtained the same qualitative results considering the interactions between the Si-terminated 90° and C-terminated 30° PDs.

3.2.1 Stability of Extrinsic Stacking Faults and Partial Dislocation Complexes

Using the approach described, we start our discussion from the double dislocation complexes comprising two partial dislocations located in consecutive $(1\bar{1}1)$ planes. Depending on the mutual orientations of the dislocation Burgers vectors, these complexes may be stable and form spontaneously as a result of PDs interaction, or unstable as will be seen in more detail below. Figure 3.7 shows MD simulation snapshots of the evolution of two 90° partial dislocations with equal Burgers vectors initially forming a double dislocation complex. The structure is very unstable and, as shown in the snapshots in Figure 3.7 **b–d**, it dissociates back into individual 90° dislocations. Once they have dissociated, they move one away from the other, driven by their mutual repulsion. This behavior can also be expected for all double SFs made up of two identical Burgers vectors. Indeed, complexes formed by two identical 30° PDs dissociate in a very similar way with the difference that 30° partials move much slower than 90° PDs once they re-appear as individual defects.[82]

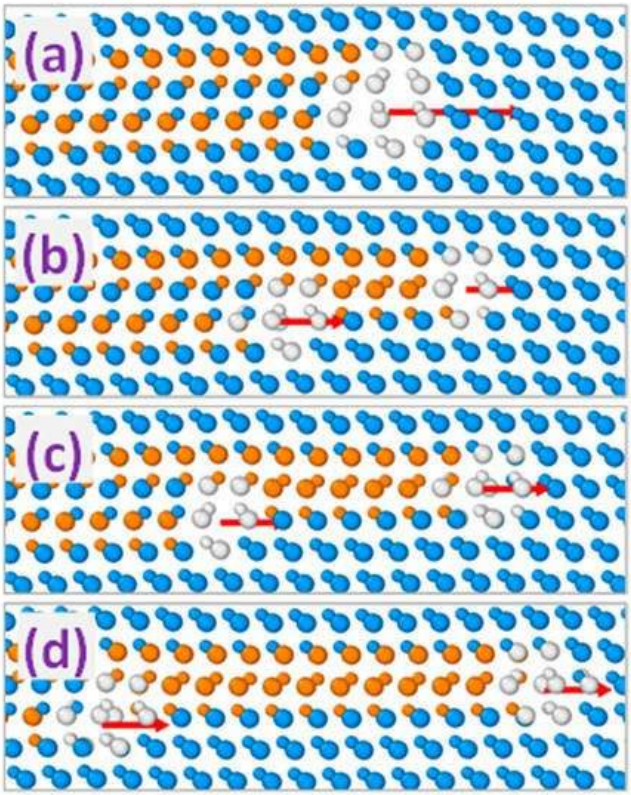

Figure 3.7: MD simulated evolution of the dislocation complex formed by a pair of 90° Shockley partial dislocations with equally oriented Burgers vectors. Simulated time: (a): 0, (b): 10, (c): 20, and (d): 50 ps, respectively. Arrows indicate the directions of the Burgers vectors of complex (a) and single dislocations (b–d).

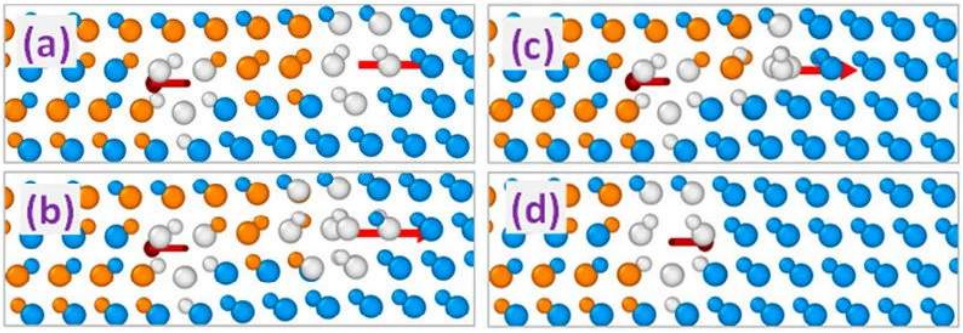

Figure 3.8: MD simulated evolution of the interaction of 30° and 90° partial dislocations forming the 30° extrinsic partial dislocation. Simulated time: (a): 0, (b): 20, (c): 50, and (d): 100 ps, respectively. Arrows indicate the directions of the Burgers vectors of the partial dislocations (a–c) and the dislocation complex (d).

Stable complexes that can terminate double SFs must be searched between the combinations of 30° and 90° PDs that are not made up by two identical dislocations. They can be either two 30° PDs with opposite screw components (projections of the Burgers vectors on the dislocation lines) or a 90° and a 30° PD. For these configurations, the interaction between the deformation fields is attractive. Indeed, in Figure 3.8 the 30° and 90° case is reported. Note that this time the two defects, initially separated, move one toward the other. They join and form a double plane dislocation complex. Figure 3.9 show possible double planes dislocation complexes. It also shows how the Burgers vectors of the single dislocations combine together when a unique defect is formed.

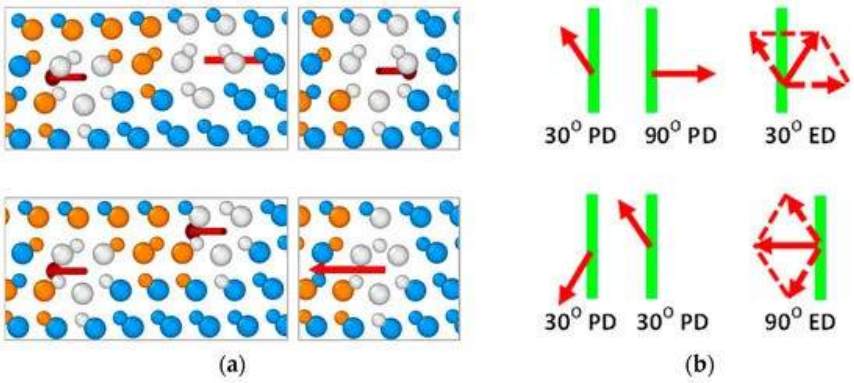

Figure 3.9: (a) MD simulation snapshots and (b) schematic top views of the formation of stable 30° (top images) and 90° (bottom images) extrinsic partial dislocations in 3C-SiC. Arrows indicate the directions of the dislocation and dislocation complexes Burgers vectors. Vertical lines in part (b) correspond to the dislocation lines.

When a 30° PD form a double plane complex with a 90° PD, the resulting Burgers vector is equivalent to that of a 30° PD that points away from the SF[‡] (see top panel of Figure

[‡]while individual 30° PDs have their Burgers vectors that point toward the SF in this glide plane.

3.9). When two 30° PDs with opposite screw components merge to form the boundary of a double SF (or extrinsic stacking fault (ESF)), the resulting Burgers vector is equivalent to that of 90° PD but points toward the SF (see bottom panel of Figure 3.9). The PD complexes that terminate double SFs (or ESF) will be referred to as 30° and 90° extrinsic partial dislocations. In MD simulations at 1800K, we found 30° and 90° ESF to be stable in the sense that no change in their structure was observed in a simulation time of 2ns. We also noted that no motion of any of the ESFs was observed, but this can be due to significantly reduced mobility and an external strain's absence.

3.2.2 Triple Stacking Faults and Partial Dislocation Complexes

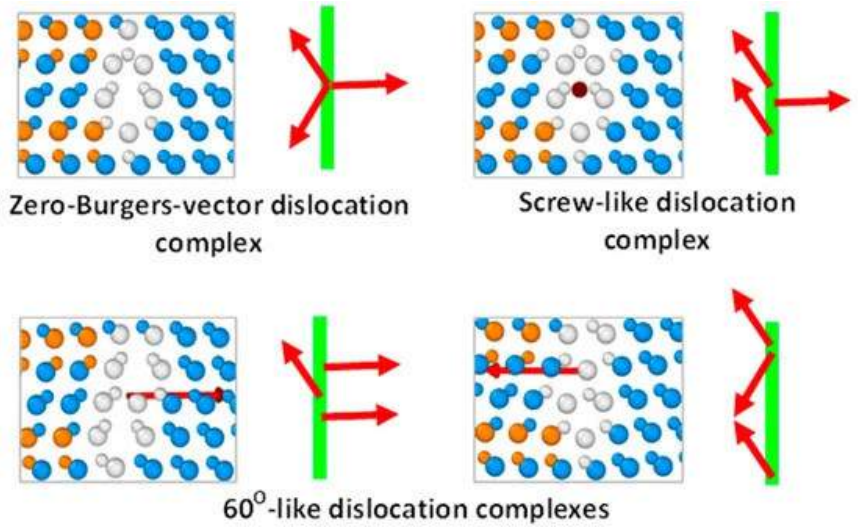

Figure 3.10: Examples of the atomic configurations of triple PD complexes in 3C-SiC viewed in the [110] direction together with schematic representations of dislocation Burgers vectors with respect to the dislocation lines viewed perpendicular to the $[1\bar{1}1]$ plane. Zero-Burgers-vector complex is stable, while other complexes experience dissociation into double PD complex and single partial dislocation during annealing. Arrows indicate the directions of the Burgers vectors of the complexes as well as complex composing partial dislocations. Vertical lines correspond to the dislocation lines.

Adding a third SF allows us to study which defect can bound triple SF. Let's consider PD complexes consisting of three partial dislocations. We can consider any combination of the Burgers vectors presented in Figure 3.6. Still, most of them are not interesting. Indeed complexes made up of three identical PDs are expected to dissociate as for the complex made up of two identical 90° PDs. The configurations that at least have two different PDs constituting them are shown in Figure 3.10. We identified three sets of configurations: a triple complex with zero total Burgers vector, two triple-defect complexes with the Burgers

vector of a perfect 60° dislocation, and a triple defect complex with the Burgers vector aligned with the dislocation line, i.e., a screw dislocation. Note that the structure of the zero total Burgers vector complex of defects and the screw-like Burgers vector complex of defects are indistinguishable when observed in cross-sections. The MD simulations of these four defects indicated that only the defect with zero total Burgers vector is stable and doesn't dissociate. As before, we performed our simulation at 1800K, and after 2ns of simulation time, only the defect composed by three different PDs remained a single complex of defects. Notably, as in the case of the ESF, no motion of the triple defects was observed in 2ns of simulated time. On the contrary, all the triple PD complexes with non-zero total Burgers vectors are unstable. Indeed in our MD simulations, the evolution observed leads to a separation of the triple dislocation complex. During the annealing, the defect dissociated into a single partial dislocation and an ESF; a 90° or a 30° extrinsic partial dislocations depending on the starting triple defect.

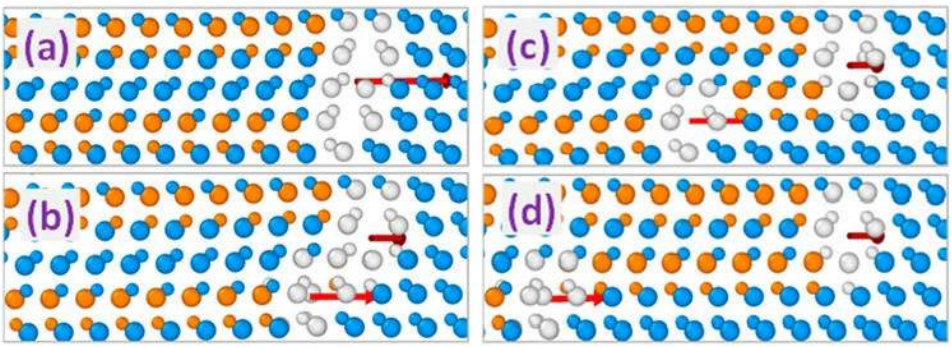

Figure 3.11: MD simulated evolution of the 60°-like triple dislocation complex formed by 90°-30°-90° partial dislocation sequence. Simulated time: (a): 0, (b): 30, (c): 60, and (d): 100 ps, respectively. Arrows indicate the directions of the Burgers vectors of the triple dislocation complex (a) as well as double dislocation complex and 90° partial dislocation (b–d).

In Figure 3.11, we show the structure of the 60°-like dislocation complex, which is made by 90° + 30° + 90° PDs in sequence. The complex dissociates and produces a stable 30° extrinsic SF and a 90° partial, moving apart.

3.2.3 Conclusions on Stability

Figure 3.12 shows color maps of the the volumetric strain (ε_{xyz}), and the elastic energy density (E_{def}) for two configurations of PDs. A clear connection exists between the two properties and the fact that PDs attract and repel each other. It is seen that individual PDs

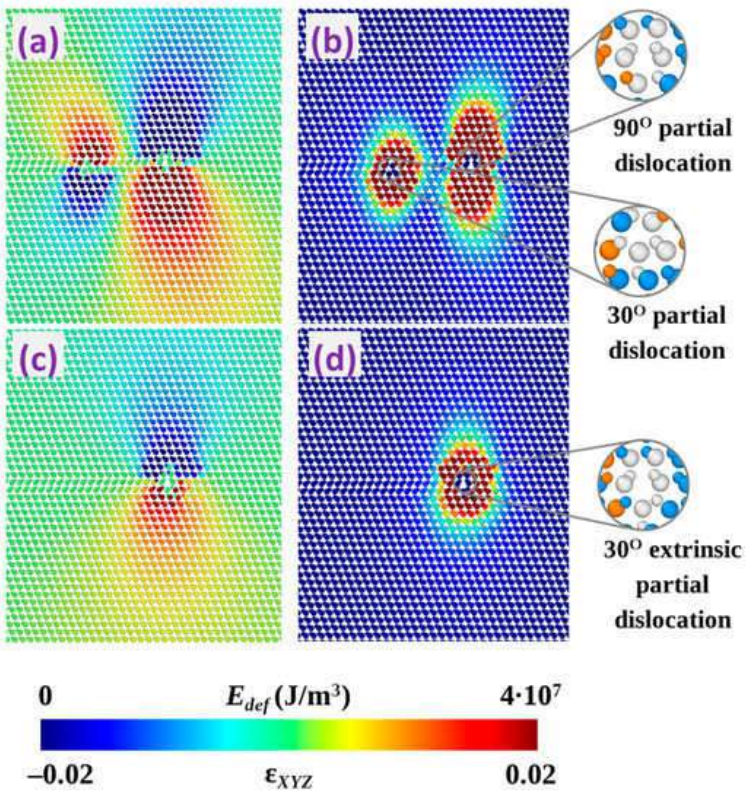

Figure 3.12: Distribution of volumetric strain (a), (c) and elastic energy density (b), (d) in 3C-SiC cell introduced by separated 30° and 90° partial dislocations located in consecutive [1$\bar{1}$1] lattice planes (a), (b) and 30° extrinsic partial dislocation formed as a result of their interaction (c), (d).

induce a value of ε_{xyz} that is opposite in its sign in the considered case (see Figure 3.12**a**). After the joining of the two PDs the deformation is much less intense (see Figure 3.12 **c**, **d**). We notice that the highest stability is obtained for the triple dislocation complex with a zero Burgers vector.

The defect complexes that resulted in being stable were ESF formed by 90° and 30° PDs and Σ3 formed by the combination of PDs that gives a total Burgers vector equal to zero. As stated before, we do not observe the further motion of the PDs when they join in a double or triple complex in our MD simulations at 1800 K in 2 ns. Hence, the mobility is reduced at least some orders of magnitude with respect to individual partial dislocations. Because of the reduced mobility, ESFs and zero Burgers vector triple SFs are expected in epitaxial 3C-SiC films. The zero-Burgers-vector complexes are reasonably expected to be the most abundant ones, given the smallest distortion introduced by them. Indeed experimental observations confirm our interpretation.[97–100] Notably, zero-Burgers-vector dislocation complexes with the structures shown in the top part of Figure 3.10 have been observed in

HRTEM images and were demonstrated to form at the interfaces of the 6H-SiC inclusions in cubic silicon carbide.[100]

3.3 Nature and Shape of Stacking Faults in 3C-SiC on Si(001)

In the preceding section, we identified which defects can terminate SFs. In this way, we have identified the defects that can be found at the boundary between SFs and the perfect crystal. Still, we have not identified the shape of SFs and, particularly, of multi-plane SFs in epitaxial 3C-SiC. The knowledge of the shapes assumed by SFs and why they assume specific shapes can help fight detrimental defects. We expect growing techniques and their optimization to benefit from a clear understanding of the dynamics of SFs (and their bounding defects) during deposition. An interesting phenomenon that is not entirely understood in the literature is the self vanishing of SFs,[101] as the authors call it. The phenomenon is peculiar because it prescribes the reduction of the SFs linear density only for SFs aligned along one of the ⟨110⟩. Namely, they observe that at the 3C-SiC surface SFs that expose a line of Si atoms are much more abundant than those that expose (or terminate with) C atoms. We assess the not complete understanding of this phenomenon to the lack of proper modeling of three-dimensional SFs evolution in epitaxial 3C-SiC layers. In a recent paper, to fill the gap, we exploit classical molecular dynamics (MD) to simulate the evolution of large-area SFs under the typical strain conditions encountered at different stages of 3C-SiC growth.[102] We modeled the evolution of single plane SFs, even if we know from the previous section that experiments demonstrate an abundance of SFs grouped in two or three adjacent {111} planes, whereas single SFs are less frequent.[96] Indeed, a successive nucleation mechanism has been proposed to explain such evidence.[81] It consists of the nucleation of a partial dislocation (PD) loop at the stage of Si carbonization to release the tensile misfit strain, followed by nucleation of two additional loops in adjacent planes during the subsequent 3C-SiC deposition stage. We will discuss the details of the mechanism in the next section of this Thesis. Still, the main point is that the boundary of double extrinsic SFs is stabilized by a triple dislocation defect formed due to the interaction between the PDs terminating the SFs. In Ref. [81] this defect has been identified to be detrimental, introducing leakage current in 3C-SiC.[81]

In the presence of high-stress concentrations, e.g., in indentation,[103,104] dislocations and SFs can nucleate in the simulation cell during MD simulations. Still, in the strain conditions typical of epitaxial 3C-SiC, extended defect nucleation would require a very long time scale, not achievable in a classical MD simulation. A common strategy to overpass

this problem is to artificially introduce PD loops, skip the defects phase's nucleation, and study the evolution after the nucleation. We followed this approach. Please note that, in this section and in the following, the positioning of the nucleated defects is used to study certain aspects of SFs and partial dislocations evolution. Therefore the distance of the defects from the free surface and the interface, as well as the film thickness, is chosen to better suit the study of a specific aspect or mechanism. It is also worth noting that the nucleation mechanism itself is not so important as long as the final result of the nucleation is a SF which is bounded by PDs which evolution can be studied efficiently considering PD loops.

In this Section, we show how we used the obtained results to interpret the experimental evidence, strengthening the general understanding of defect evolution in 3C-SiC. In particular, we first clarify the mechanism resulting in the experimentally observed different extensions and terminations of SFs at the surface.[102] We performed MD simulations with Vashishta potential at 1400K (typical experimental temperature during 3C-SiC growth), and we showed that the SFs assume one of two shapes (Δ or V one), depending on the SF plane. The shape is determined by the evolution at different velocities of the boundary of the SF. Some segments (the Si- terminating ones) propagate much faster than others (the C- terminating ones). The resulting shape is inverted for the glide plane that intersects the (001) surface along the [110] or the [1$\bar{1}$0] direction. Hence the observation of a different SF line extension at the free surface is the consequence of the SF shape beneath the surface. As we will explain later, such evolution and, therefore, the shape of each SF is determined in the initial phases of the growth when a tensile strain is present. Indeed, considering the theoretical work of Scalise et al.[81] we know that multiple (and in particular triple) SFs can be easily generated in a second phase of the growth when an inversion in the strain sign is experienced in the epi-layer. Here we analyzed the possibility of successive nucleation of PD loops when pre-existing SFs are present. We analyze their shape and provide details of the bounding defect structure. The possibility of forming multi-plane loop complexes is interpreted in terms of reducing the elastic energy in the epi-layer. As expected from the previous section, we obtain the maximum energy decrease when we have a triple stacking fault with common boundaries and zero total Burgers vector. We

used LAMMPS[38] as the MD engine and Vashishta as the potential function.[49] Simulations were run in the canonical (NVT) ensemble, using a Nose-Hoover thermostat.[105] We analyzed atomic configurations with OVITO software.[40] Simulation cells have been prepared as orthogonal boxes with orientations: $\boldsymbol{u} = a/2[1\bar{1}0]$, $\boldsymbol{v} = a/2[110]$, and $\boldsymbol{w} = a[100]$. PBCs were applied in the $\boldsymbol{u}$ and $\boldsymbol{v}$ directions. We do not explicitly introduce a Si substrate because of Vashishta mathematical formulation which is not able to handle Si-Si bonds, and we simply freeze the bottom three layers of the simulation not to have two free surfaces. The simulation cell extension is remarkable, and it was made up of 3'456'000 atoms in a box with sizes $38.8 \times 38.8 \times 26.0$ nm^3.

Dislocation loops were inserted in the form of hexagonal partial dislocation loops (HPD) by shifting each atom by the displacement field vectors calculated by dislocation modeling in the framework of the linear elasticity theory as described in Section 2.3.4.

The integration time step was set to 1 fs. It guaranteed relative energy conservation of 10^{-5} in micro-canonical simulations. We scaled the simulation box dimensions to account for thermal dilation of the 3C-SiC.

3.3.1 Strain condition in 3C-SiC during typical growth on Si (001)

The growing conditions experienced by epitaxial 3C-SiC can actually change drastically during the growth, and hence the evolution of SFs is determined by such strain conditions. In many growing approaches, they use a carbonization process to reduce the 3C-SiC misfit with Si.[106] The tensile misfit of $\approx 20\%$ between SiC and Si generates a tensile strain that accumulates in the film. SFs develops typically in the tensile condition being the tensile strain a known source of PDs. In particular, 90° PDs are expected to nucleate to resolve the tensile stress. Indeed, in 3C-SiC, the only partial dislocation defects that can relax the tensile stress are loops with Burgers vector of the family $\langle 112 \rangle$. A drastic change happens when a reconstruction of the 3C-SiC/Si interface is formed. The formation of an ordered array of edge dislocations just above the Si substrate allows matching five SiC unit cells to four Si cells.[92] An easy calculation shows that if we match five SiC cells at the lattice distance of four Si cells, we have a slightly compressed 3C-SiC layer at the growth temperature. In the subsequent deposition, this change in the strain sign determines a change in the class of defects that can generate, and in particular partial dislocations with Burgers

vector of the two families ⟨121⟩ (30° PDs) and ⟨211⟩ (30° PDs, opposite screw component) can appear.[81] In the following two subsections, we will discuss the two strain conditions separately. In the first one, we will correlate the experimentally observed shape of SFs with that observed in our simulation for individual SFs expanding in tensile strain conditions. In the second, we present how the change in the strain sign can generate multi-plane SFs with a shape that is the one determined by individual loops in the first stage of the growth.

3.3.2 Evolution of SF at the initial stage of the deposition

We studied the evolution of a general case SF by considering a hexagonal partial dislocation loop. This choice arises from the fact that SFs lie in {111} planes, and dislocations in zinc-blende lattice tend to be aligned along <110> directions. Hence, even if we insert PDs as a circular loop, the bounding PDs terminating them will try to align along the six preferential equivalents <110> directions in each plane. Therefore we started our simulation with SFs, which are surrounded by a hexagonal-shaped loop as shown in Figure 3.13 (**a**).

Figure 3.13 shows four snapshots of the evolution of two HPD loops via MD. The two SFs expand driven by an external applied bi-axial tensile strain $\varepsilon_{xx} = \varepsilon_{yy} = 4\%$. We have chosen the value of the tensile strain to be much smaller than the experimental one ($\approx 20\%$) because such strain is not compatible with MD simulation of dislocation loop evolution. Strain higher than 5% produced pronounced crystal disorder making it impossible to determine SFs evolution straightforwardly. It should also be noted that local reconstruction of the 3C-SiC at the Si interface will have a wide range of different intensities in the strain. Hence the tensile strain is not a know fixed value. For all these reasons, the value of the tensile strain must be considered as a parameter. A 4% strain allowed us to achieve essential aspects of a simulation: it was high enough to obtain a relevant evolution in a reasonable time. It was not too high to produce crystal disordering, which could hinder SFs dynamics. On the left cell shown in Figure 3.13 we illustrate snapshots of the evolution of an HPD loop that lies in a (111) plane. On the right cell (blue), we show the evolution of an HPD loop lying in a $(1\bar{1}1)$. The simulations are identical, except for the glide plane where the HPD loop is located. As anticipated before, in this first section, we focus on the initial stages of the 3C-SiC growth. We have that only PDs whose Burgers vector belongs to the family ⟨112⟩ can nucleate in tensile conditions. We will refer to HPDs

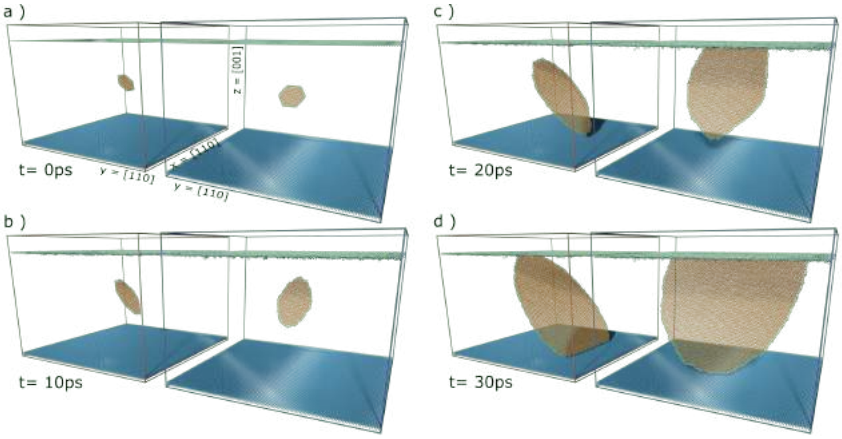

Figure 3.13: Classical molecular dynamics simulations snapshots of the evolution of hexagonal partial dislocation loops. Simulations were performed under bi-axial tensile strain at 1400K, computing the atomic interactions using Vashishta potential. Periodic boundary conditions are applied in x and y directions. Two simulations are analyzed in parallel. On the left (red cell) the evolution of an HPD loop that lies in a (111) plane is presented. The right panels (blue cell) show the evolution of an HPD loop lying in a $(1\bar{1}1)$ plane. Only stacking faulted atoms (orange), fixed atoms (dark blue) and surface atoms (light blue) are shown for clarity. Dislocation lines, obtained with OVITO DXA algorithm are displayed as green lines bounding the SFs. Four snapshots correspond to: initial configurations (a), atomic configurations after 10 ps (b), 20 ps (c) and 30 ps (d) of simulation time.

as 90° HPDs being a 90° angle between the loop Burgers vector and the segment of the loop parallel to the [110] or $[1\bar{1}1]$ direction. A geometrical analysis (see for reference panels (**a**) and (**f**) of Figure 3.14) easily illustrates that each dislocation loop comprises three segments terminated by silicon and three other segments terminated by carbon atoms. Each segment also has a different character in terms of the angle with the HPD Burgers vector. Each loop has two segments with a 90° character and four with a 30° character. If we now consider the zinc-blende lattice, shown in Figure 3.14 (**k**) and (**l**), (111) and $(1\bar{1}1)$ planes are not equivalent in the order of which atom is above the other inside a glide set of planes in 3C-SiC (dashed colored lines). As a consequence dislocation loops along (111) and $(1\bar{1}1)$ have inverted termination of their bounding PDs.

Considering the geometrical analysis of Figure 3.14 it is easy to interpret MD simulation results. We indeed observe the two loops expanding in a very different manner. The relative velocities of the PD segments model the loop evolution; 90 ° PDs will move faster, 30° PDs will move slower.[82,90] The dislocation loop suddenly reshape into a diamond loop (Figure 3.13 panel (**b**)), having the 90° PD segments higher velocity than 30° ones. The 90° segments bend until they are completely aligned as the other 30° PD segments. Because the loop has only 30° PD segments now, the only difference in the gliding velocity of the PD

segments is given by the termination of the PDs. As expected in many experiments,[107–109] we find silicon terminating dislocations to be faster than carbon ones. Si terminating segments move faster, reaching the free surface or the 3C-SiC/Si interface first. The rest of the loop expands much slower, and hence the SF has the shape of the slower segments. It results in a triangular shape with the apex toward the surface if the C- terminating PDs are in the upper half of the loop, while toward the Si substrate if the C- terminating PDs are in the lower half of the loop. SFs will expose a line of C atoms at the free surface in the former case and a line of Si atoms in the latter.

We can summarize the result by considering all the four possible glide planes. SFs that expose a line of Si atoms along the [110] direction are those in the $(1\bar{1}1)$ and $(1\bar{1}\bar{1})$ planes; SFs that expose a line of C atoms along the $[1\bar{1}0]$ direction are those in the (111) and $(11\bar{1})$ planes. They have a V-shape and a Δ-shape, respectively. One could argue that such an evolution can happen in the first stages of the growth, hence only for few layers. Still, clear experimental evidence exists that subsequent deposition of 3C-SiC decreases the length of C-terminated SFs and increases the length of Si-terminated SFs.[68] This is due to the C atoms having opposite polarity with respect to the surrounding Si-terminated surface. The Δ and V conformations of SFs are expected to be maintained during the growth of successive 3C-SiC layers.

The evolution via MD described above can be also summarized as shown by the sketches of Figure 3.14 (**a**)-(**e**) and (**f**)-(**j**). The evolution expected for HPD in the (111) and $(11\bar{1})$ glide planes is shown in Panels (**a**)-(**e**); the evolution for HPD in the $(1\bar{1}1)$ and $(1\bar{1}\bar{1})$ planes is shown in panels (**f**)-(**j**). Our results are in agreement with the experimental evidence of a plane-dependent SF shape.[101] The final SF shapes obtained by MD simulations correlate with the experimental evidence via optical microscopy investigations of a plane-dependent SF shape.[101] The authors evidenced in the case of 3C-SiC layers grown on undulated Si substrates the presence of almost only the Si-SFs (see the evolution expected for SFs in $(1\bar{1}1)$ and $(1\bar{1}\bar{1})$ planes). Moreover, in Ref. [101] cross-sectional transmission electron microscopy imaging in the perpendicular (110) and $(\bar{1}10)$ showed only the stacking faults in $(1\bar{1}1)$ and $(1\bar{1}\bar{1})$ planes, while the ones in (111) and $(11\bar{1})$ planes were not observed. The authors used the V- and Δ-shape of SFs to justify the higher extension of Si-SFs and

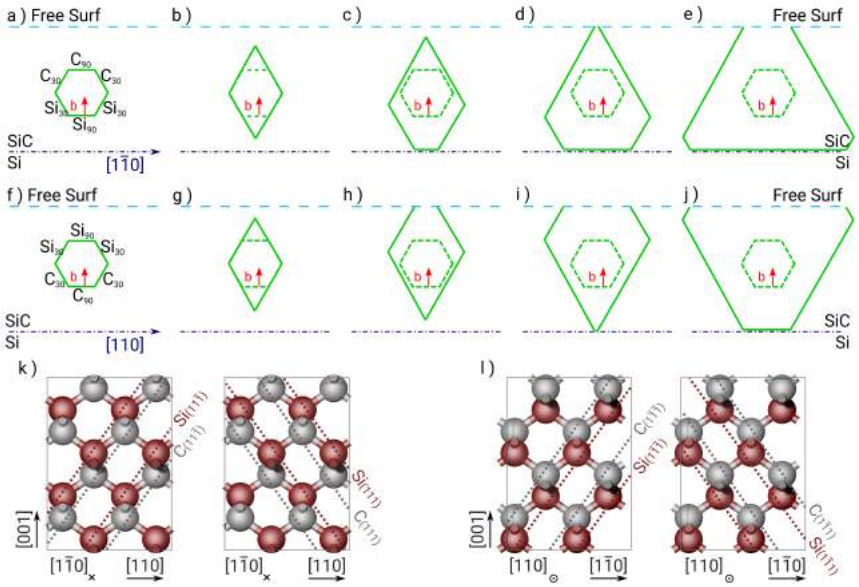

Figure 3.14: Diagram of the evolution of hexagonal partial dislocation loops in different glide planes. The evolution of the loops with Burgers vector <112> under tensile strain conditions is shown. Burgers vectors are displayed as red arrows. In the top row (a - e) the evolution of loops in the (11$\bar{1}$) and (111) glide planes (i.e. glide planes parallel to the [1$\bar{1}$0] direction) is shown. Middle row (f - j) shows the evolution of loops in the (1$\bar{1}$1) and (1$\bar{1}\bar{1}$) glide planes (i.e. glide planes parallel to the [110] direction). In the bottom row (k - l) the reference zinc-blende structure projected in [110] and [1$\bar{1}$0] directions is presented, relevant glide planes are highlighted by dashed lines.

shrinking of C-SFs, respectively. Our result provides a clear explanation for their observation, and an important step on the comprehension of SFs dynamics in 3C-SiC growth has been done.

3.3.3 Formation of triple SFs at the deposition stage

The results of the previous subsection must take into account a noticeable point: SFs rarely appear as individual SFs in 3C-SiC. More frequently, especially in the case of very thick layers, SFs appear to be formed by more than one faulted plane. Still, the shape of the defect complex is that described in the last subsection. Since we have a discrete knowledge of which defects complexes can be stable from Section 3.2, we know that each plane of the multi-plane SF has a different Burgers vector. One can thus suppose that a subsequent nucleation mechanism happens once the epitaxial layer strain is inverted. Such nucleation could lead to the formation of multi-plane SF if the new SFs have an energetic advantage in nucleate on planes adjacent to a pre-existing SF. As a consequence, the formed multi-plane SF will acquire the shape of the former individual SF.

Experimental investigations via cross-sectional TEM images have shown that by counting the relative number of planes making up a SF, one finds a clear trend for different film thicknesses. As the thickness of the film increases, the density of multi-plane SFs increases as well, with triple SFs being the most abundant ones for thick layers. Individual SFs are present only for thin SiC film and almost disappear in thick layers.[96] It exists a strong interest in triple SFs. Indeed they have been identified as a possible cause of leakage currents in 3C-SiC.[81] One should focus in particular on the bounding defects of such multi-plane SFs because neither the SF per se neither the boundaries of individual SFs can introduce significant states in the gap to explain the leakage problem in epitaxial 3C-SiC devices.[81] In the next Section (3.6) we will describe how a successive nucleation mechanism forms a triple SFs and which bonding defects are expected.[81] The proposed mechanism states what was anticipated before: Initially, a SF nucleate and expands to release the misfit tensile strain. After that, two other SFs are formed in the planes adjacent to the pre-existing defect, inducing a triple SF (or a micro-twin). In Ref. [81], the authors proved the proposed mechanism via MD, limiting their investigation to straight partial dislocation lines. It is possible to generalize the proposed mechanism considering PD loops, even though the actual nucleation cannot be studied in classical simulations. Nucleation is a rare event, and we need to skip this process due to the modeling limits via MD. Still, we can infer interesting things about nucleation and triple SF formation by considering the strain fields of PD loops.

We identified which PD segments tend to form common boundaries and which do not by performing static and energetic analyses of different configurations of three-dimensional HPD loops. We geometrically optimized HPD loops configuration via an energy minimization with Vashishta potential. Then we analyzed with OVITO the elastic energy, and we produced a map for each HPD configuration (see Figure 3.15). Our findings provide a working generalization in three-dimension of the mechanism proposed in Ref. [81]. Our results further support our ideas about the formation of triple SFs, which we believe is how the system chooses to relax its elastic energy efficiently.

In the panels of first column (**a**), (**e**) and (**i**) of Figure 3.15 the three possible individual HPD are shown. Around each loop segment, a colored map displays the elastic energy in the vicinity of the dislocation. Since we believe that a key factor in the formation of triple

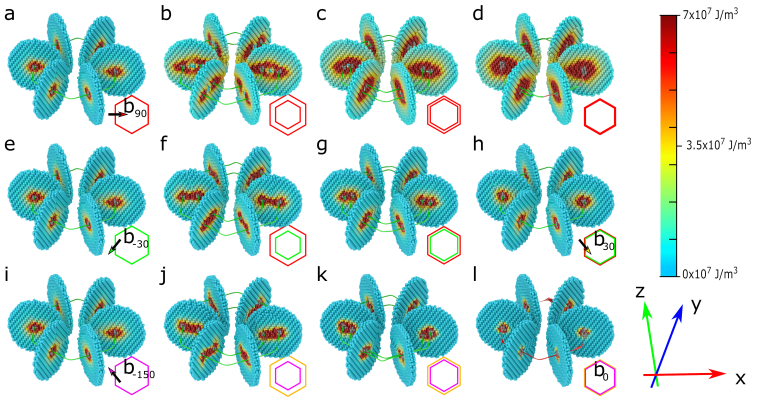

Figure 3.15: Elastic energy map near each segment of HPD loops. First column: maps for single HPD loop with different Burgers vectors, (**a**) elastic energy map along a loop with $\vec{b}_{90} = [1\bar{1}\bar{2}]$; (**e**) along a loop with $\vec{b}_{-30} = [121]$; (**i**) along a loop with $\vec{b}_{-150} = [\bar{2}\bar{1}1]$. Second to fourth column: maps for combinations of HPD loops in adjacent planes, segments of different loops are separated by a distance that varies form 1 nm (second column) to 0 nm (fourth column). For different configurations of HPD loops the difference in loop radii decreases along each row from 2^{nd} to 4^{th} column. (**b**-**d**) elastic energy map for the combination of two loops with $\vec{b}_{90}$; (**f**-**h**) combination of two loops with $\vec{b}_{90}$ and $\vec{b}_{-30}$; (**j**-**l**) combination of three loops with $\vec{b}_{90}$, $\vec{b}_{-30}$ and $\vec{b}_{-150}$, in this case loops with $\vec{b}_{90}$ and $\vec{b}_{-30}$ have the same radius because they correspond to the stable double HPD loop of panel (**h**) with $\vec{b}_{30} = [21\bar{1}]$.

SFs is the loop interaction and not a strain release mechanism, no strain is applied to the presented configurations. The three loops are labelled as follows, $\vec{b}_{90} = [1\bar{1}\bar{2}]$, $\vec{b}_{-30} = [121]$, $\vec{b}_{-150} = [\bar{2}\bar{1}1]$[§]. The defects are aligned with the direction shown by the three arrows on the right of Figure 3.15, $x = [\bar{1}12]$, $y = [110]$ and $z = [1\bar{1}1]$. The HPD loop shown in Figure 3.15 (**a**) can relax the initial tensile strain. The two loops in Figure 3.15 (**e**, **i**) can relax a compressive strain. In Ref. [110] the authors proposed a hypothesis for the formation of multiple SFs. They stated that a multiple SF could originate from PD loops with the same Burgers vector nucleated under tensile strain conditions. We initially follow their hypothesis, and we plot the elastic energy corresponding to two HPD loops with the same Burgers vector in Figure 3.15 (**b**)-(**d**). It is evident that the elastic energy increases as the two loops segments become close to each other. The compressed/dilated regions near each segment are identical, so they superimpose, dramatically increasing the elastic energy (see panel (**d**)). Considering these results, it's evident that forming a multiple SF by identical PD loops in adjacent planes is unfavorable. Even if they nucleate on adjacent planes, their bounding defects will remain separated, and we know that such defects do not introduce detrimental states in 3C-SiC, being them individual 90° PDs.

[§]each HPD loop is identified by referring to its Burgers vector and the angle between the latter and the HPD loop segment parallel to the 3C-SiC/Si interface

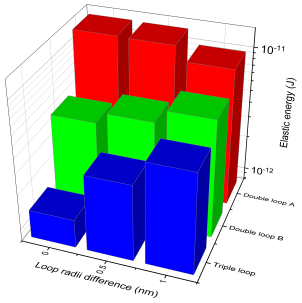

Figure 3.16: Elastic energy of three combinations of HPD loops as a function of the difference between the loop radii: red bars represent the elastic energy of two HPD loops in adjacent planes, both loops having $\vec{b}_{90}$; green bars show the elastic energy of two HPD loops in adjacent planes, one with $\vec{b}_{90}$, the other with $\vec{b}_{-30}$; blue bars correspond to the elastic energy of three HPD loops in adjacent planes, one with $\vec{b}_{90}$, one with $\vec{b}_{-30}$ (with the same radius), one with $\vec{b}_{-150}$.

We hence consider the mechanism proposed in Reference.[81] Once the strain changes after the carbonization step, the nucleation of SFs in the planes adjacent to the first SF is enhanced, but they are generated by defects with a different Burgers vector. So we considered as first loop the same while the second loop has a different Burgers vector, either $\vec{b}_{-30}$ or $\vec{b}_{-150}$ (note that they both relax compressive strain). Figure 3.15 (**f**-**h**) indeed shows that the interaction between loops with $\vec{b}_{90}$ and $\vec{b}_{-30}$ is attractive, and that the elastic energy decreases as the segments of the two loops approach each other.[79] Eventually, the most favorable configuration is the latter when the two loops join. They form a double SF and a bi-plane HPD loop with Burgers vector $\vec{b}_{30} = [21\bar{1}]$. Note that this can be easily justified considering that the compressed/dilated regions near each segment are opposite, so they mutually relax. The compression/dilation is stronger in the equatorial plane of the loop, so the effect is stronger if the two loops are situated in adjacent planes. It justifies nucleation events located preferentially on the adjacent plane. Obviously, triple SFs can be justified similarly by considering the third possible Burgers vector. If we take as starting HPD loop the one formed by $\vec{b}_{90}$ and $\vec{b}_{-30}$ HPD loops (Figure 3.15(**h**)), and we add a third HPD on top, with the last possible Burgers vector, we quickly note that the resulting interaction is similar. This is almost expected because the third HPD loop has a Burgers vector, which is the opposite of the double HPD. The elastic energy decreases as the segments of the two loops become closer (see Figure 3.15 (**j**)-(**l**)), and the reduction is almost complete when the loops overlap entirely. From the crystal's elastic energy point of view, the formation of the triple SF with a sharp boundary and a zero total Burgers vector is completely

justified. Figure 3.16 summarize the results of Figure 3.15. Each bar in the figure is the elastic energy of the whole cell for each one of the configurations shown in panels (**b**)-(**d**), (**f**)-(**h**), (**j**)-(**l**) of Figure 3.15. The elastic energy of the cell where we inserted two HPD loops with the same Burgers vector is represented by red bars ("double loop A" in Figure 3.16). When the loop segments approach, the elastic energy increases. In the other cases, the elastic energy decreases. Green bars ("double loop B" in Figure 3.16) show how the energy decreases in the case of the double loop formed by HPD loops with different Burgers vectors. Finally, blue bars ("triple loop" in Figure 3.16) display how the energy is dramatically reduced in the case of three loops with three different Burgers vectors. We can summarize the process by saying that the most abundant class of SFs are triple ones. Their shape is what we have called a Δ- or a V-shape depending on the SF plane, and its boundary is a dislocation with a zero total Burgers vector. The order of the individual PDs expected is shown in Figure 3.17 as well as an exemplification of the three-dimensional shape. Such a SF is formed in sequence. Initially, a SF is generated in tensile conditions, and it acquires the Δ- or V-shape depending on the SF plane. Once the strain change, a second SF forms in one of the planes adjacent to the original SF. Eventually, a third SF nucleates in the other adjacent plane. The two SFs acquire the former SF's shape and form a microtwin with a common sharps boundary. The defects that generated the two successive SFs must have a Burgers vector different from the former SF and distinct from the other. The last prescription is that their Burgers vector should be those relaxing compressive strain deformations. The structures shown in Figure 3.17 have been obtained by inserting three trapezoidal PD loops in three adjacent glide planes. The obtained configuration has been geometrical optimized using a conjugate gradient algorithm. The potential used was the Vashishta potential. The central SF in both the structures is generated by a defect with Burgers vector belongings to the family $\vec{b}_{90} = \langle 112 \rangle$. The other two SFs that sandwich the middle one is generated by defects that have two different Burgers vectors belonging to the two families $\vec{b}_{-30} = \langle 121 \rangle$ and $\vec{b}_{-150} = \langle 211 \rangle$. The core structure of the bounding, zero total Burgers vector, dislocations are displayed in the circular insets of the Figure 3.17. These configurations are shown in detail because in Ref. [81] some of them have proven to be a leakage currents potential source.

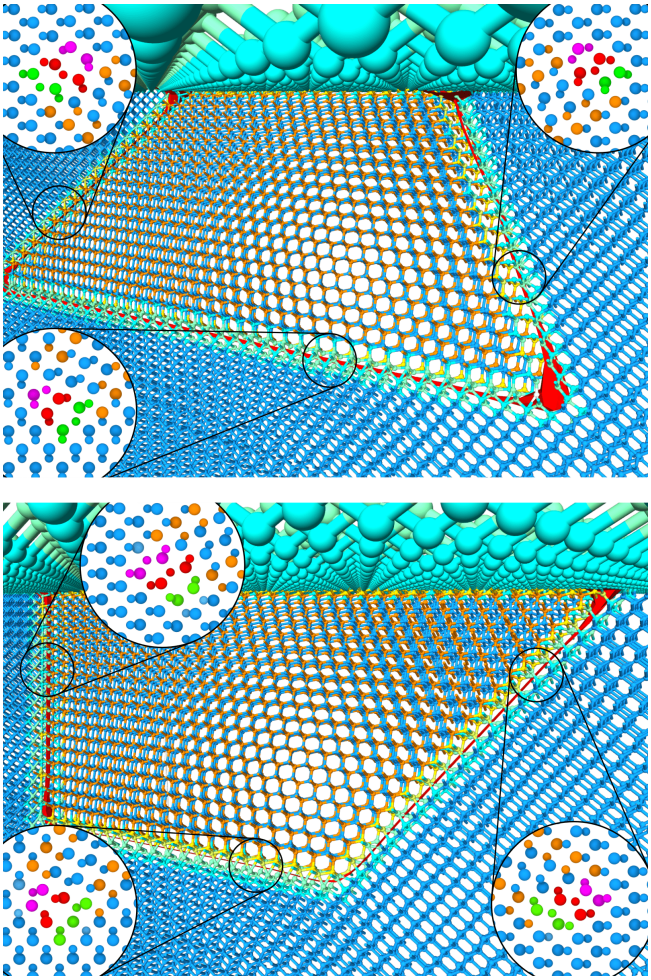

Figure 3.17: Shape and terminations of triple SFs. Top: SF shape in the (111) and (11$\bar{1}$) planes; Bottom: SF shape in the (1$\bar{1}$1) and (1$\bar{1}\bar{1}$) planes. The dislocation line is colored in red. In the circles the core structures projected on the planes perpendicular to the line direction are highlighted. Core atoms are colored to indicate the Burgers vector of the dislocation in the respective plane: each color correspond to a different Burgers vector, with the same nomenclature of Figure 3.15. Blue sticks and atoms correspond to zinc-blende structure, orange ones to wurzite structure. Lighter hues are used in the defect surroundings.

3.4 Mechanism of stacking fault annihilation in 3C-SiC on Si(001)

In the previous sections, we have considered SFs generated by the expansion of 90° partial dislocation loops, evolving under the initial tensile strain. Still, other mechanisms are possible, and probably a combination of many different ones are the cause of SFs in epitaxial 3C-SiC. An alternative path that can explain the presence of SFs is the dissociation of 60° misfit dislocations formed at the 3C-SiC/Si interface during the carbonation step. This phenomenon was ignored in the preceding sections. Still, it can regard another experimentally observed behavior, the annihilation of SFs via the intersection between SFs and junction of their bounding partial dislocations. Indeed if two SFs generate from the 3C-SiC interface and migrate throughout the epi-layer, they can cross and stop before reaching the free surface. In the point of view of increasing 3C-SiC quality, it is of particular interest to understand the mechanism behind this experimental observation.

Unlike other types of extended defects, stacking faults cannot be completely eliminated by mutual annihilation even in very thick 3C-SiC layers due to concurrent stacking fault generation.[111–113] The minimum SF densities achieved so far for 3C-SiC grown on flat Si(001) substrates amount to about $10^4 cm^{-1}$.[96] Specific substrate patterning such as undulation,[114] inverted pyramidal structuring,[115,116] and deep profiling in the form of ridges or pillars,[117,118] was proposed to reduce this value. Nevertheless, 3C-SiC layers with acceptably lower SF concentrations remain a challenging goal.

SF elimination may take place by mutual annihilation mechanism,[113,119] i.e., the propagation of stacking faults lying in opposite {111} planes is suppressed upon their intersection. Two SFs migrating from the 3C-SiC toward the free surface can stop propagating in the film if their bounding PDs met and form the so-called Lomer–Cottrell lock. Alternatively, one can stop its motion if the SF extension's PD is blocked upon encountering a stacking fault on its route.[96,120] This mechanism requires a more profound comprehension of the conditions of 3C-SiC epi-layer growth and the characteristics of stacking faults and terminating them partial dislocations. Based on the obtained results, we characterized the SF annihilation mechanism in key terms: stress in the 3C-SiC layers at different growth stages and mutual arrangement and orientations of the Burgers vectors of SF leading partial dislocations. These results have been published in Ref. [80].

Simulations cell were set as an orthogonal boxes defined by the vectors [$\bar{1}$10], [110] and

[001]. The box encloses 86'400 atoms and has the following size: $281.6 \times 12.4 \times 240.2 Å^3$. It ensured an optimum balance between the computational cost and the accuracy of the description of considered defects. We modeled an infinite 3C-SiC slab as the rest of this Thesis by applying PBCs in the X and Y direction. The bottom three layers were kept immobile as done before. The results were analyzed using OVITO. PDs were inserted with dislocation lines along the Y-axis by shifting all the simulation cell atoms by the displacement vectors calculated as described in Section 2.3.3 in the framework of dislocation theory.[2] The displacements have also been corrected to account for the infinite dislocation arrays created by the periodic boundary condition along the X axis.[2,81,121] MD simulations were performed using the LAMMPS in the canonical ensemble (NVT) using a Nose–Hoover thermostat. The Vashishta potential described the atom interactions in the 3C-SiC phase. The molecular dynamics time step was set to 0.3 fs. Simulations were performed at the thermostat temperature of 1800 K. Thermal dilation of the 3C-SiC layer was accounted for scaling up the cell dimensions by the factor obtained from simulations in the NPT ensemble.

3.4.1 Experimental evidence of stacking faults annihilation

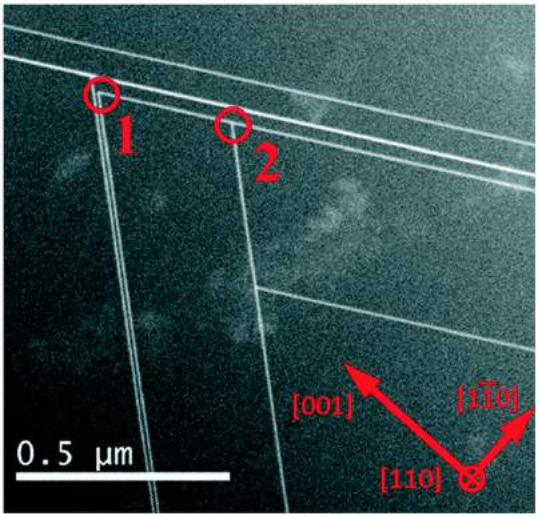

Figure 3.18: Low-magnification TEM image of the 3C-SiC layer epitaxially grown on Si(001) substrate. [001] is the growth direction. Stacking faults appear as the white lines. Marked areas 1 and 2 show the "inverted V" and "λ"-shaped stacking fault intersections.

The phenomena we are discussing in this section are both evident in the low-magnification cross-section TEM image of the epitaxial 3C-SiC layer shown in Figure 3.18. The 3C-SiC

layer is observed in the (110) projection plane. The high density of SFs in the first nanometers from the Si substrate is too high to obtain clear images. Hence, the TEM image has been taken at a distance exceeding $1\mu m$ from the 3C-SiC/Si interface.[112] The SFs in the TEM image are individuated by the white lines tilted by ≈35° from the [001] direction. They form "inverted V" or "λ" patterns. The two patterns are highlighted in the figure by the numbered circles. Circle "1" encloses the "inverted V" pattern, i.e., complete annihilation of the SFs. Circle "2" encompasses the other one, i.e., partial annihilation. The number of planes that made up the SFs of Figure 3.18 can be higher than one. Still, we can determine the evolution of multi-plane SFs considering the evolution of the intrinsic stacking faults composing them.[81]

We recall once again that the evolution of SFs is determined by the motion of PDs surrounding the SF because of the stress present at different stages of layer growth. In the first stages of the growth, a carbonation process converts the upper part of a Si substrate into a thin 3C-SiC film, accomodating the lattice mismatch between the two materials.[96,113] On average, Lomer dislocations form every five 3C-SiC planes at the 3C-SiC/Si substrate interface,[122] and most of the misfit tensile strain is released. Still, some of the strain can remain unreleased because of the difference between the expansion coefficients of SiC and Si.[123,124] This remaining strain is released by 60° perfect dislocations. They can form, but as they appear, they suddenly dissociate into pairs of 90° and 30° PDs with a SF in between.[125] The former PD is at the end of the SF toward the Si substrate, while the latter is at the upper end. The tensile strain pushes the 90° PD into the 3C-SiC/Si interface, where it remains pinned. The trailing 30° PD remains closer to the 3C-SiC layer surface. It can further extend SF in the 3C-SiC film.[120] After the carbonization, the relaxed 3C-SiC layer assumes a slightly compressive strain condition (≈0.45%) because of the different expansion of Si and SiC lattices.[123,124]

30° partials lead the relaxation in compressive strain.[126] The 90° PDs remain pinned at the 3C-SiC, and 30° ones migrate through the 3C-SiC film. They now lead the extension of SFs in the crystal, and when two of such SFs belong to non-parallel planes meet, they can form the "inverted V" or "λ" intersection patterns. It is challenging to observe such

evolution experimentally, but MD simulation can be the right tool to confirm our understanding of the annihilation processes. Indeed it allows us to set up ad experiments to validate our hypothesis with a significant spatial and scale resolution. Still, one should never forget to make a ponderated choice of the most suitable potential function for a particular task. As described in Section 3.1 and published in Ref. [82], we have validated the reliability of PDs dynamics in 3C-SiC layers with Vashishta potential, and we treat the results on the mechanisms of dislocation motion and interaction, obtained, with high confidence. Nevertheless, the results via MD are potential-dependent and will always deviate, to some extent, from real processes.

We prepared the simulations by inserting pairs of 90° and 30° PDs on the two glide planes $(1\bar{1}\bar{1})$ and $(1\bar{1}1)$) with the 90° PDs in the region where atom are fixed. In this way, we account for the pinning of those at the SiC/Si interface.[120] The 30° PDs are instead in the upper region of the cell and are free to move. The strain applied to the simulation box was set to 1.2% instead of the experimental value of ≈0.45%. The slight increase in the strain inserted is a trick to compensate the overestimation of the SF energy of the Vashishta potential with respect to the actual value (12.09 meV Å^{-2} (Ref. [82]) vs. 2.51 meVÅ^{-2} (obtained by DFT calculations[36]). The increase precisely enlarges the Peach–Koehler force acting on the leading dislocations to compensate for the excess of attractive force between the 30° and 90° PDs due to the SF Vashishta overestimation of the SF energy.

3.4.2 Intrinsic Stacking Faults annihilation

Inverted "V" shape junction of SFs

MD results on the formation of an "inverted V" intersection patterns are shown in Figure 3.19. We observe the annihilation of both participating SFs via the joining or their trailing 30° PDs. The two PDs have a Burgers vector with an opposite screw component. The reaction between the two segments is: $\frac{a}{6}[\bar{1}\bar{2}1] + \frac{a}{6}[21\bar{1}] \rightarrow \frac{a}{6}[1\bar{1}0]$ (or, alternatively, $\frac{a}{6}[211] + \frac{a}{6}[\bar{1}\bar{2}\bar{1}] \rightarrow \frac{a}{6}[1\bar{1}0]$). We found that the trailing PDs attract each other and form an inverted V defect even if we prepare the simulation cell so that they should not arrive at the intersection point simultaneously. More precisely, an effective radius of 15nm exists for the attraction of the two dislocations. The 15nm value should be subject to some deviation from the actual value, being potential-dependent.

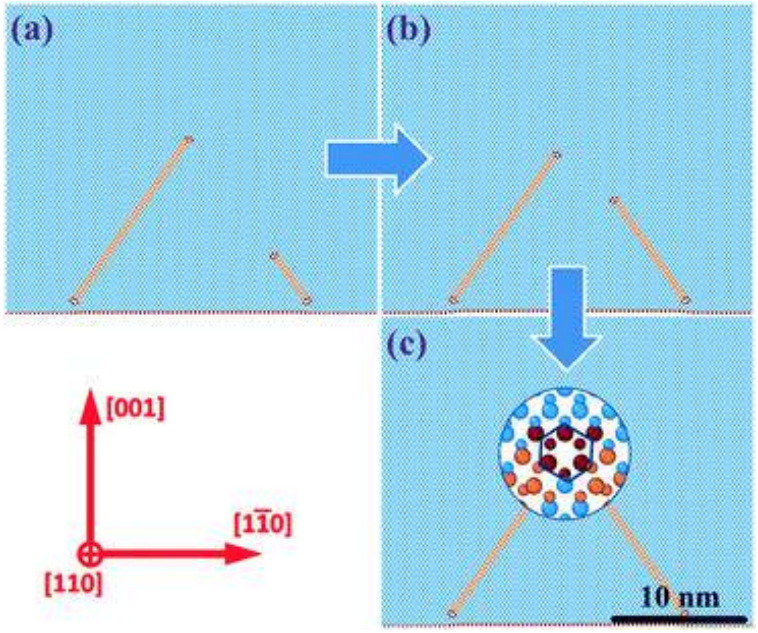

Figure 3.19: MD simulation snapshots of the formation of "inverted V"-shaped intersection of stacking faults in 3C-SiC epi-layers on a Si(001) substrate by the interaction of leading 30° partial dislocations with opposite screw components of Burgers vectors. The simulation time: a - 0, b - 120 ps, and c - 180 ps. Blue atoms correspond to the Si and C atoms in the cubic diamond lattice, orange atoms belong to the stacking faults. Inset in panel (c) shows the atomic configuration of the formed Lomer–Cottrell lock dislocation.

At the intersection of the two SFs, a Lomer–Cottrell lock dislocation forms. The core of the dislocation is indeed characterized by the presence of a six-member ring of atoms (see Figure 3.27 (**c**) and Ref. [120]).

The "λ" shape junction of SFs

We found two pathways for the formation of "λ"-type SF intersections. Each column of Figure 3.20 report one of them. In column number one, panels (a) to (c) show the first case: two SFs propagate in the film on (1$\bar{1}$1) and (1$\bar{1}\bar{1}$) glide planes, but the trailing PDs at the upper extreme of the SFs do not interact enough. The PD, which arrives last at the intersection point, stops upon encountering the stacking fault left behind by the PD who came there first. Similar behavior happens no matter the Burgers vector of the two trailing 30°PDs. Indeed, trailing PDs cannot glide over an existing SF because they would generate a high energy structure. That limits their further motion, not the reciprocal orientation of the Burgers vectors. In Figure 3.20**c** we report the atomic configuration at the SF intersection. The second column, panels (**d**) to (**f**) of Figure 3.20 show the alternative pathway:

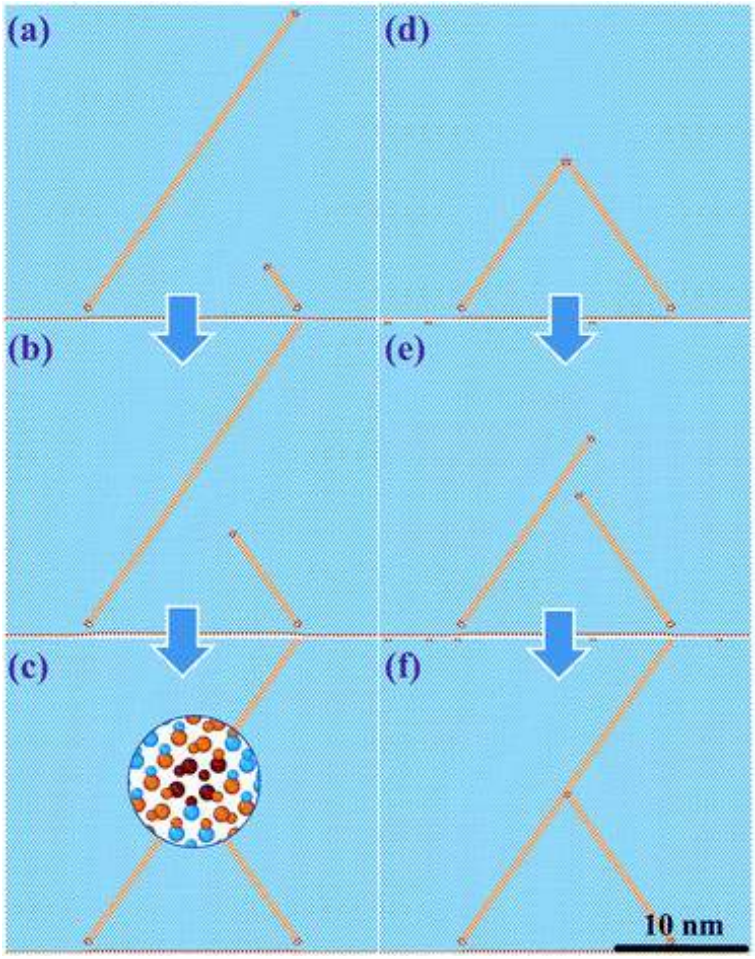

Figure 3.20: MD simulation snapshots of the formation of "λ"-shaped intersections of stacking faults in 3C-SiC epi-layers on a Si(001) substrate in the case of the large distance between the 30° leading dislocations (a-c) and as a result of the interaction of closely spaced 30° dislocations with equal screw components of Burgers vectors (d–f). Simulation time: a - 0, b - 360 ps, c - 540 ps, and d - 0, e - 60 ps, f – 200 ps. Blue atoms correspond to the Si and C atoms in the cubic diamond lattice, orange atoms belong to the stacking faults. Inset in panel (c) shows the atomic configuration of the intersection of 30° partial dislocation with crossing stacking fault, also corresponding to the intersection in panel (f).

Two SFs bounded by trailing 30° PDs with the same screw component of the Burgers vector will not form an inverted V- pattern in any case. They will always create a "λ"-shaped SF intersection. Indeed, even if we introduce the two trailing PDs at the glide plane intersection (see Figure 3.20 (**d**)), they will separate. Once one of them is pushed away, the other will migrate toward the free surface, leaving a SF behind. The SF limits the further motion of the remaining PD, and the "λ" pattern is observed. The structure at the intersection is the same that we showed in the inset of Figure 3.20 (**c**).

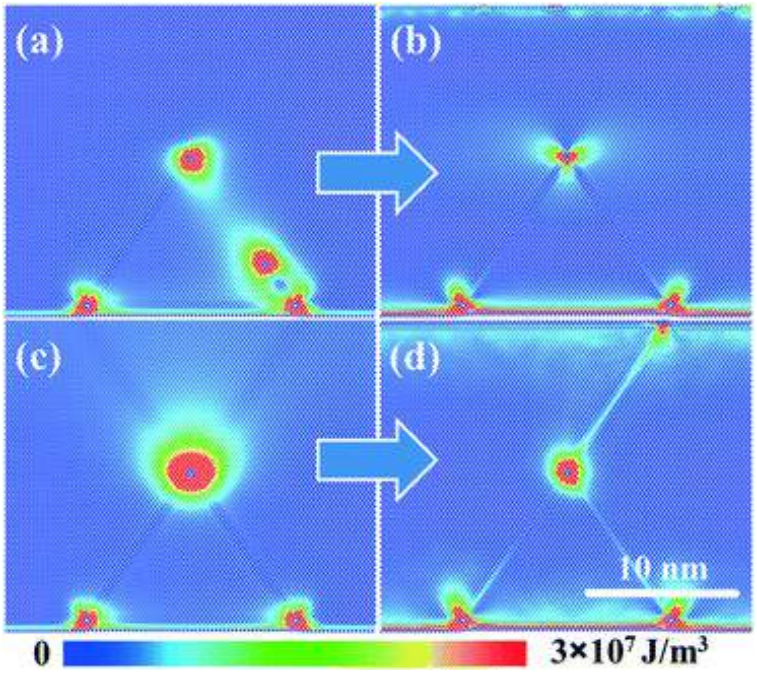

Figure 3.21: Elastic energy maps corresponding to the interaction of closely spaced 30° partial dislocations with opposite (a and b) and equal (c and d) screw components of Burgers vectors in the initial (a and c) and final (b and d) states of evolution.

Discussion on simulation results

MD simulations results can be summarized as follows. The gliding of 30° trailing PDs terminating the SFs determines the formation of SF intersection patterns in 3C-SiC epitaxial layers. The presence of a compressive strain determines the glide of the PDs from the 3C-SiC/Si interface to the free surface. The SF extension, all the way from the interface to the free surface, can be limited by the two pathways identified by our calculations. 30° PDs will stop gliding if they encounter a SF on their path or come close to another 30° PD that possesses a Burgers vector with an opposite screw component. In the former case, shown in Figure 3.20, the 30° dislocation is suppressed from further gliding at the intersection junction because of the disconnection of its slip plane. In the latter, the two defects form the so-called Lomer–Cottrell lock shown in Figure 3.19. The presented results can be viewed in connection with elastic energy maps. The dislocation energy is proportional to the square of its Burgers vector, $\vec{b}^2$,[2,19] hence the formation of a Lomer–Cottrell lock should appear to be more convenient than two individual PDs. The elastic energy maps of the configuration of the Lomer-Cottrell lock formation (shown in Figure 3.19 (**a**) and (**c**) are shown in Figure 3.21 (**a**) and (**b**), respectively). The elastic energy maps confirm the convenience of the Lomer-Cottrel lock over individual PDs.

Via the formation of the Lomer-Cottrell lock, two stacking faults are excluded from the further extension. Therefore, the process is the most efficient in reducing SF concentration in the 3C-SiC layer. On the contrary, the reaction of two 30° PDs with equal screw components of their Burgers vectors is unfavorable, leading to the increase in the elastic energy of the crystal. Indeed the trailing PDs would combine Burgers vectors as $\frac{a}{6}[\bar{1}\bar{2}1] + \frac{a}{6}[\bar{1}\bar{2}\bar{1}] \rightarrow \frac{a}{3}[\bar{1}\bar{2}0]$ (or, alternatively, $\frac{a}{6}[211] + \frac{a}{6}[21\bar{1}] \rightarrow \frac{a}{3}[210]$). Figure 3.21 (**c**) and (**d**) show the energy maps corresponding to the configurations in Figure 3.20 (**d**) and (**f**), respectively. The separation of the mentioned dislocation indeed decreases the elastic energy of the crystal. Still, a process that reduces the number of SFs is possible, but only one of them is excluded from further motion.

Our study provided insight into the annihilation mechanisms of stacking faults observed experimentally in 3C-SiC layers on silicon to reduce SF concentration. It suggests that manipulating the stress in the 3C-SiC layers during deposition may help in SF elimination, e.g., by limiting the propagation of the 30° partial dislocations leading the SFs via optimization of the growth temperature. The generation of new SFs can also be limited by the attenuation of the compressive strain.

3.5 Multiple stacking fault formation via partial dislocation loops evolution

In the previous sections, we have seen that many Burgers vectors characterize the bounding dislocation of single plane (intrinsic SF). They move as prescribed by the Peach and Koehler force depending on the strain sign present in the epi-layer. They can be grouped into two classes, dislocations with Burgers vector that extend SFs in the presence of tensile strain and dislocations with Burgers vector that extend SFs in the presence of compressive strain. For simplicity, we can ignore the possibility that SFs can generate from the dissociation of 60°, and instead, we consider SF as generated by dislocation loops. In such a simplification, the behavior of SF-bounding dislocations is the same; we are just ignoring the dislocation segments pinned at the 3C-SiC interface or that have been expelled from the free surface.

Therefore we decided to tackle the problem of multiple stacking fault formation by studying the evolution of partial dislocation loops via an MD approach. MD allows us to prepare ideal configurations and study them evolving in controlled conditions, and after that, inferring which phenomenon can be considered to explain multiple stacking fault formation. In an ideal scenario, one could perform an extremely long simulation and observe SF nucleating under the effect of external stress. Still, in reality, such events are so rare that no amount of computational power can give us results in a reasonable time. This is true for the values of strain on which we are interested, which are those typical of epitaxial systems. Therefore, we set up simulations where we skipped PD loops' nucleation and started them with dislocation loops already present. MD simulations have been performed using LAMMPS code in the Nose-Hoover thermostat regime at the temperature of 1000 K. The value of the time step has been chosen equal to 1 fs based on the energy conservation of the simulation system in the course of preliminary simulation runs. The simulation cell used to perform the analyses on the behavior of partial dislocation loops were box-shaped simulation cells bounded by the planes with orientations $[1\bar{1}\bar{2}]$, $[1\bar{1}1]$, and [110] in the directions of the axes X, Y, and Z, respectively. With such an orientation, the glide plane of the dislocation loop is aligned along the XY plane, and the segment of the loop that corresponds to the misfit segment is oriented along the Y axis. We call "misfit segments" those segments of the dislocation loops which would be parallel to the 3C-SiC

interface if the loop was in a cell oriented along the conventional $x = [\bar{1}10]$, $y = [110]$, and $z = [001]$ set of reference direction with the free surface on one side of the cell in the z direction and the 3C-SiC interface at the other extreme. Periodic boundary conditions were applied in all three directions. That segment can be one the two straight segments shown in Figure 3.22 (**a**).

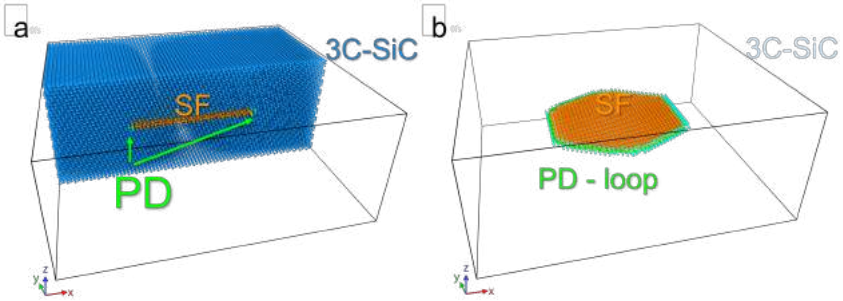

Figure 3.22: Insertion of a SF in a simulation cell. (a) Partial dislocations limiting a SF; (b) An hexagonal shaped loop as inserted in the simulation cell.

This time, the cell contained 259'200 atoms and was sized as $27 \cdot \frac{\sqrt{6}}{6} 4a \times 30 \cdot \frac{\sqrt{2}}{2} 2a \times 5 \cdot \frac{\sqrt{3}}{3} 6a$, where a is the 3C-SiC lattice constant for Vashishta potential. Analysis of the defect structures in the 3C-SiC systems obtained at the various time steps was performed using OVITO. Dislocations loops were inserted as described in Section 2.3.4, as prescribed in the framework of dislocation theory.[2] The dislocation loop so inserted, with an hexagonal shape, is illustrated in Figure 3.22 (**b**).

3.5.1 Intrinsic stacking fault evolution under shear strain

Our investigation focused on the possibility that a pre-existing SF can enhance the nucleation of another dislocation loop on the glide plane adjacent to the defect's glide plane. As a starting point, we need to know the barrier that has to be overcome to nucleate the dislocation loop. There exist some methods to obtain a precise estimation of the barriers for rare events, one of the most used is the Nudged Elastic Band.[127] This method was applied successfully to dislocation nucleation in epitaxial Ge films on Si substrates by Trushin et al. in Ref. [26]. The exact value of the barrier for the nucleation of a dislocation loop is strongly influenced by the potential function used, by the presence of free surfaces or steps. Therefore, we decided not to use such methods, mainly because we are interested in establishing the presence or not of an enhancement of the nucleation. We are not interested in the value of the barrier per se. So we have proceeded as follows: we have

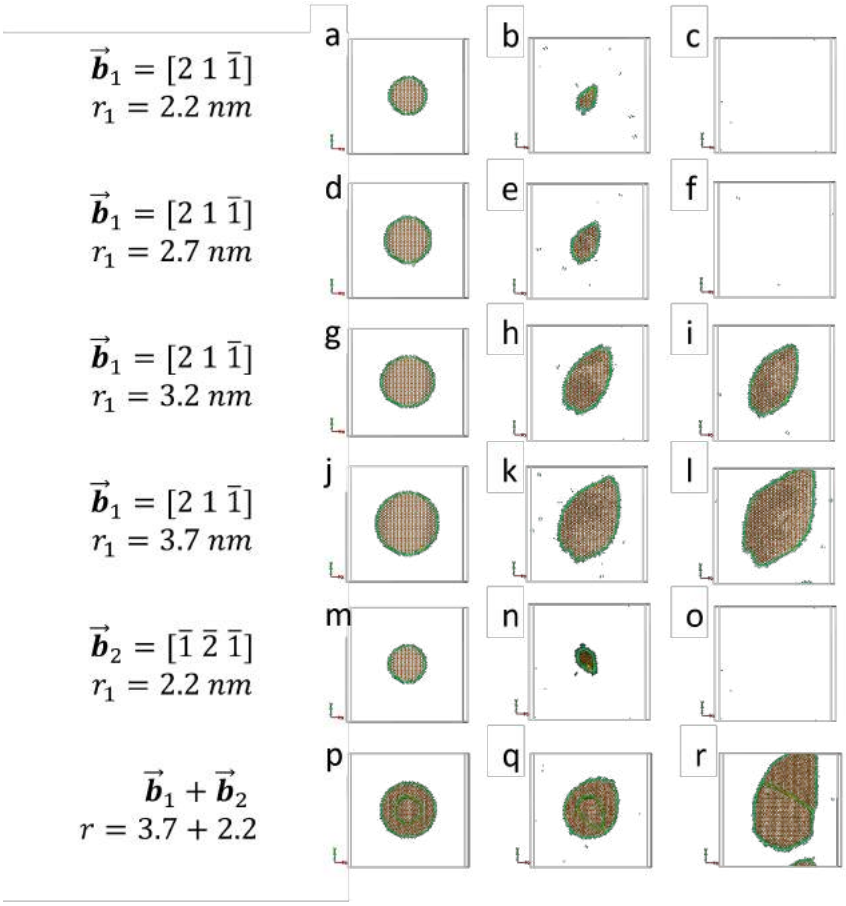

Figure 3.23: Evolution via MD simulation of SF under shear strain. In each row a different radius of the PD loop that surrounds the SFs is simulated. The Burgers vector and the loop radius are written on the left. (a)-(c), (d)-(f): sub-critical loops; (g)-(i), (j)-(l): super-critical loops; (m)-(o): sub-critical loop with a different Burgers vector; (p)-(r): sub-critical loop of frame (m) placed in the glide plane adjacent to a super-critical loop with a different Burgers vector.

created many loops with a different radius, and we have let them evolve under the effect of an externally applied strain. The strain was applied as a shear strain (ε_{xz}), inserted by deforming the simulation cell by tilting the z axis in the x direction. We have set the shear strain to a fixed value $\varepsilon_{xz} = -4\%$. The shear strain can make a dislocation loop open in the same way that the compressive/tensile strain makes it open in the epitaxial system. In this case, the strain acts the same way as the compressive strain present in SiC film after the carbonization process. Hence, it is the right one to study the expansion of SFs surrounded by PDs with Burgers vector that forms an angle of 30° with the misfit segment of the loop. Here below, we will refer to such loops as "30° partial dislocation loops".

A minimum loop radius that can make the dislocation loop open for a determined shear strain value exists. This behavior can be interpreted as determined by two opposite

forces acting on the dislocation loop. On one side, the shear strain pushes each loop segment away from the other to resolve the applied shear strain. On the other side, each loop segment is attracted by its counterpart with opposite line direction on the other side of the dislocation loop. In Figure 3.23 we reported the obtained loop evolution for dislocation loop radii from 2.2nm to 3.7nm. As clearly visible in Figure 3.23 (**a**)-(**c**), (**d**)-(**f**) and (**m**)-(**o**), if the dislocation loop is to small it collapse leaving an almost perfect crystal as a result at the end of the simulation. Instead, if the loop radius is higher than the critical value, the loop expands and the SFs enlarge itself (see Figure 3.23 (**g**)-(**i**) and (**j**)-(**l**)). It is worth noting that the SFs evolution observed is coherent with the experimental observation of SFs expansion in hexagonal SiC.[128] Indeed the initially circular-shaped loop assumes a diamond shape at the end of the simulation. This behavior is due to the boundary dislocation surrounding the SFs, which possesses a different character in terms of terminating the species and the Burgers vector. A simple scheme to better clarify this point is given in Figure 3.24.

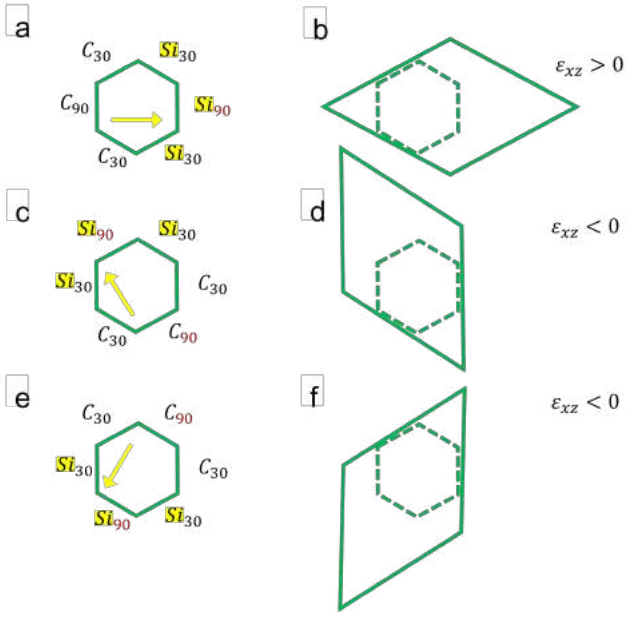

Figure 3.24: Sketch of the termination and the character of PD loop segments for the three possible Burgers vectors (first column) and the expected evolution under a shear strain (second column). (a), (b) $\vec{b}_{90} = \langle 112 \rangle$; (c), (d) $\vec{b}_{30} = \langle 121 \rangle$; (e), (f) $\vec{b}_{150} = \langle 211 \rangle$.

A generic-shape SF has six preferential orientations for the bounding dislocation lines. They are the $\langle 110 \rangle$ directions in its glide plane, in general, a $\{111\}$ plane, and in our simulation the $(1\bar{1}1)$ plane. Let's consider the three possible Burgers vectors of a partial dislocation loop. We will always obtain a diamond shape because we always have a dislocation

segment oriented perpendicularly to the Burgers vector of the loop. Such segment will move faster, in particular the Si- terminating one as we found in our publication,[82] and we described in Section 3.1.

This section focused on 30° partial dislocation loops, but a similar behavior is also observed for 90° PD loops. The main difference is that the strain sign to make a 90° PD loop open is inverted, and, with equal radius, a lower strain is necessary to make the loop open. In truth, the different strain sign and the big difference between the critical loop radii make very difficult to study via MD the possibility of formation of multiple SFs considering together all the three Burgers vector. We recall here that for this reason, in Section 3.3 we performed an analysis of the elastic energy of multiple loops instead of performing the same simulation scheme presented here. We anticipate that we will overcome this problem in the following main section, considering only straight dislocation lines. An interesting simulation of the formation of multiple SFs will be discussed in detail.

3.5.2 Extrinsic stacking fault formation via PD loop evolution

As shown in Figure 3.23 for both the two Burgers vector suitable for the insertion of SF in the considered glide plane, i.e. $\vec{b} = [21\bar{1}]$ and $\vec{b} = [\bar{1}\bar{2}\bar{1}]$, loops with radius below 3nm collapse with the strain which was set in the presented simulations. But the behavior drastically changes if one PD loop is placed on the glide plane just above or below the SF generated by another dislocation loop if the latter has a different Burgers vector. Indeed, consider the loop with Burgers vector $\vec{b} = [\bar{1}\bar{2}\bar{1}]$ in Figure 3.23 (**m**)-(**o**), it collapsed being the only SF in the simulation cell. Instead, if it is placed in the closest glide plane above a super-critical partial dislocation loop with the other Burgers vector ($\vec{b} = [21\bar{1}]$) it opens and a double SF is formed (see Figure 3.23 (**m**)-(**o**)).

In Figure 3.25 we reported relevant simulation frames of this process for the formation of double SFs. The two loops are inserted as HPD loops as in Section 3.3, the bigger one has Burgers vector $\vec{b} = [21\bar{1}]$ and a radius of 3.7nm, the smallest one has Burgers vector $\vec{b} = [\bar{1}\bar{2}\bar{1}]$ and a radius of 2.2nm. Even if the radius of the latter is below the critical value for a single SF opening, the smaller loop expands (in a diamond shape aligned with its Burgers vector as sketched in Figure 3.24). The bounding dislocation of the small loop and the big one met in a few ps of simulation time, as shown in Figure 3.25 (**b**). The joining of two

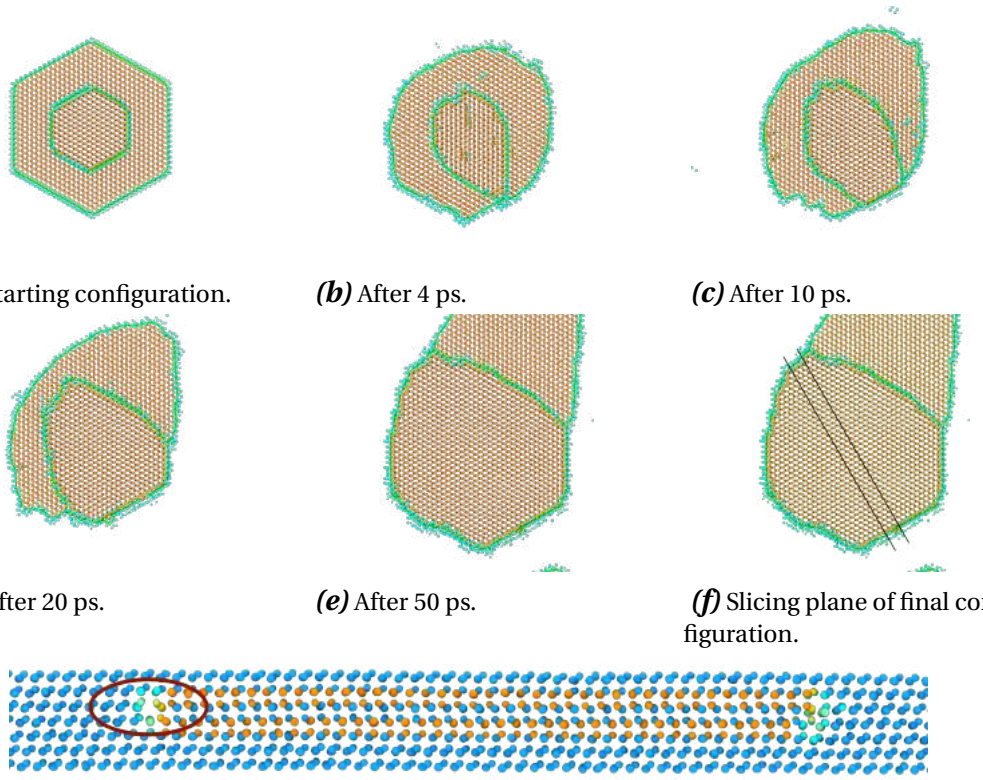

(a) Starting configuration. ***(b)*** After 4 ps. ***(c)*** After 10 ps.

(d) After 20 ps. ***(e)*** After 50 ps. ***(f)*** Slicing plane of final configuration.

(g) Section of the ESF as shown in 3.25 (**f**)

Figure 3.25: Molecular dynamic simulation of the formation of an extrinsic SF. The presence of a HPD loop with a different Burgers vector enhances the opening of a sub-critical HPD loop.

30° dislocations with opposite screw components leads to the formation of a stable defect as described in Section 3.2. Once the two lines meet, they remain together and move as a whole (see Figure 3.25 (**c**) and (**d**)). Progressively the rest of the small loop reaches the bigger one, and a double extrinsic SF is obtained as displayed in Figure 3.25 (**e**). Only a section of the bigger loop remains as a single plane SF, the segment of the bigger loop that is Si-terminated and is perpendicular to the Burgers vector of the loop, being it the fastest segment. The cross-section displayed in Figure 3.25 (**g**) shows the nature of the dislocation that bound the ESF. One can easily find the very stable structure identified in Section 3.2.

3.6 The origin and nature of killer defects in 3C-SiC

So far in this Thesis, we have discussed various aspects of SFs evolution and formation in epitaxial 3C-SiC. Still, they are so numerous that one should find a precise "enemy" for fighting. Once an accurate defect is identified as the most deleterious one, selective approaches can be imagined. Indeed, once we know what causes the problems typical of 3C-SiC, we can either focus on eliminating the defect causing the problem or compensate for the problem themselves. With that in mind, let's consider once again how 3C-SiC is typically grown. The first step is characterized by the so-called carbonization process. It allows the relaxation of the high tensile strain via the formation of arrays of sessile Lomer dislocation at the interface between the 3C-SiC film and the Si substrate. Some stress still remains in the film and can partially be relaxed by the nucleation of PDs. Those dislocations introduce hexagonal phases into the cubic SiC; hence their formation is favored by the polytipism of the material. At the high deposition temperatures (T = 1200-1400 °C), indeed, the inclusion of hexagonal polytypes in 3C-SiC effectively corresponds to the appearance of the multi-plane stacking faults in the cubic lattice.[36,129] several attempts have been made to achieve SF densities reduction.[68,101,117,130–132] Multi-plane SFs have lower formation energies than the single-plane SF,[36] and they are found to be more abundant also experimentally.[92,96,133–135] Even if a clear correlation exists between the high SF density and the presence of detrimental leakage currents,[67–72,101,136] it is an open question what directly causes the leakage currents. Indeed SFs per se does not introduce mid-gap states in the 3C-SiC phase.[137,138] Therefore, we have focused on defects surrounding SFs, considering them valid candidates as killer defects in 3C-SiC, inducing leakage currents. In our recent article[81] we use a multi-scale approach combining classical molecular dynamics (MD) simulations and ab initio calculations to study the formation mechanisms and the electronic properties of complexes of partial dislocations in 3C-SiC epitaxial layers. We will show that the strain conditions in 3C-SiC growth enhance the probability of obtaining three partial dislocations in adjacent planes. They can form triple-plane SFs in agreement with experimental indications.[96] As shown in various points of this Thesis, a strong interaction force exists between PDs, especially when located on adjacent planes. They can form a complex of defects made up by PDs aligned to create multi-plane dislocations. Ab initio calculations demonstrated the appearance of defect states in the middle

of the bandgap of 3C-SiC for many of these stable configurations. The most detrimental ones were those composed of three successive SFs.

This section, which follows our results in Ref. [81] is organized as follows. We will present the discussion of the obtained results in two parts: we first discuss in detail the origin of the dislocation complexes studied by MD simulations. Then we will briefly present the electronic properties, obtained by ab initio calculations, of the partial dislocation complexes. This latter part will be discussed for completeness, but it regards the work done by other group staff members. Details on this part can be found in Ref. [81].

The formation of dislocation complexes was studied via MD simulations. The simulations were performed using the LAMMPS in the canonical ensemble (NVT) using a Nose–Hoover thermostat. The Vashishta potential described the atom interactions in the 3C-SiC phase. The molecular dynamics time step was set to 1 fs. Simulations were performed at the thermostat temperature of 1400 K, which represents the typical growing temperature. Thermal dilation of the 3C-SiC layer was accounted for scaling up the cell dimensions by the factor obtained from simulations in the NPT ensemble. The atomic trajectories were analyzed with OVITO.

The simulation cell is composed of an orthogonal box defined by $\vec{s} = \frac{a}{2}[1\bar{1}0]$, $\vec{v} = \frac{a}{2}[110]$, $\vec{w} = a[001]$. We modeled an infinite 3C-SiC slab as done before by applying PBCs in the X and Y direction. The bottom three layers were kept immobile as usual. The simulation cell is composed of 40'320 atoms arranged in a $21.6 \times 1.23 \times 15.7\text{nm}^3$ box.

We inserted dislocations lines according to the displacement field vectors calculated as discussed in Section 2.3.3. As a first stage, we considered infinitely long and straight dislocation lines. We chose the box dimension in the $\vec{s}$ direction so that a specific strain was present in the cell after the insertion of dislocations. On the other periodic direction the cell was much more narrow to reduce the computational cost. We tested the appropriateness of the box dimension by increasing three times the cell size in this direction, but no difference was found in the motion of dislocations. The number of atomic layers in the vertical direction was 144, which allowed a good description of dislocation dynamics. For all the results presented, we note that we reproduced them also using the ABOP potential. In this case, the temperature has been increased to 2000 K.

3.6.1 Extended defect formation mechanism by MD: single and multiple SFs

This subsection will reveal the critical steps of the formation of dislocation complexes by showing the results of ad hoc MD simulations. The defects that originate will be later considered as possible killer defects in 3C-SiC layers.

3C-SiC is a crystal with a zinc-blende lattice. The primary slip system of the zinc-blende is {111} ⟨110⟩. Hence the most convenient defects are perfect glissile dislocations which are aligned along the ⟨110⟩ direction, and their Burgers vectors are $\vec{b} = a/2\langle 011\rangle$.

In tensile strain conditions, perfect glissile dislocations tend to dissociate into two partial dislocations with Burgers vectors $\vec{b} = a/2\langle 121\rangle$ (Shockley dislocations). The first step of the growth is characterized by the so-called carbonization process. It allows the relaxation of the high tensile strain via the formation of arrays of sessile Lomer dislocation at the interface between the 3C-SiC film and the Si substrate. Some stress still remains in the film and can partially be relaxed by the nucleation of glissile perfect dislocations that can dissociate into 30° and 90° PDs.[92,133] Under tensile strain conditions, the 90° partials lead the relaxation process and are driven towards the 3C-SiC/Si interface.[79] The residual strain can be further released during the subsequent 3C-SiC layer deposition by the motion of the glissile dislocations already present in the layer or by the nucleation of new extended defects at the film surface their propagation into the bulk.[81]

In Figure 3.26 we show the results of MD simulations. The red-colored atoms in Figure 3.26 highlight the core of a 90° partial dislocation inserted deep in the simulation cell. We inserted it there to mimic the resulting 90° PD near the SiC/Si interface that have formed by the dissociation of a perfect 60° as described above. An inset of the figure shows the volumetric strain map corresponding to the configuration shown. Note how the initial tensile strain can be relaxed by the compressive lobe above the 90° PD core. To reproduce the slight compressive strain present in the layer after the five to four reconstruction of the 3C-SiC/Si interface of $\approx 0.45\%$, we set the cell size along the $\vec{s}$ direction to be a precise value. In this way, we have an array of equidistant 90° PDs that introduce a well defined compression in the film above them.

Eventual 30° PDs that have formed by dissociation of perfect 60° at the interface relax the stress by moving toward the free surface.[139] Other 30° PDs can nucleate from the free surface, moving under compressive strain toward the interface. We inserted 30° PDs in

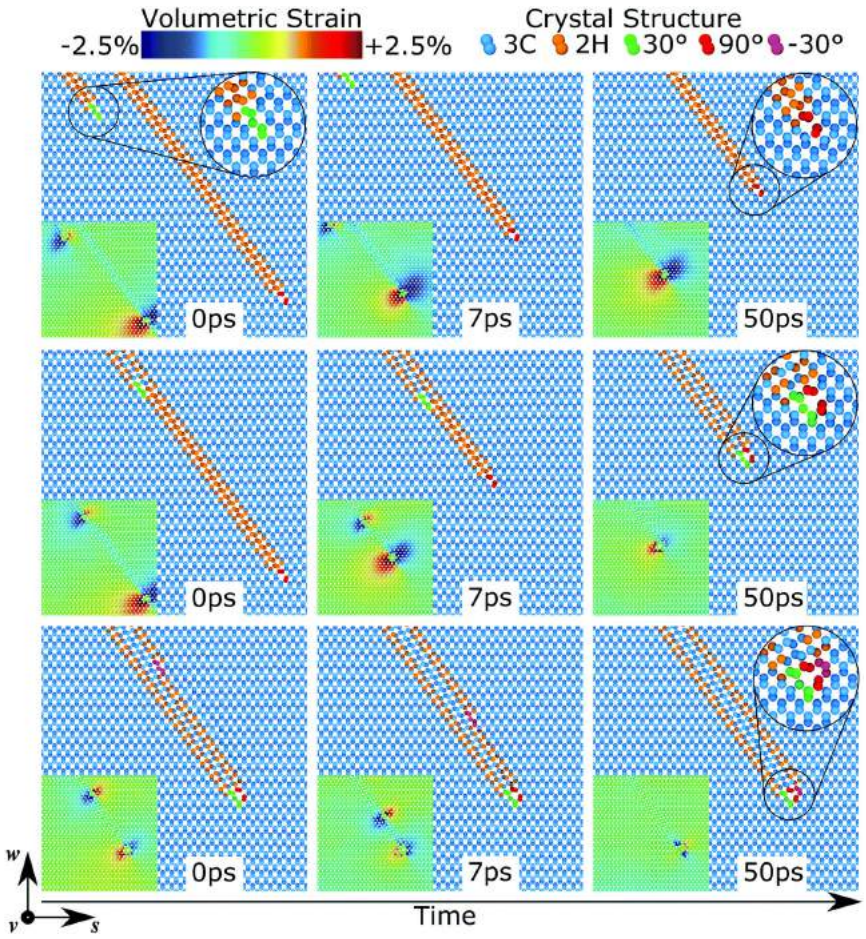

Figure 3.26: MD simulation snapshots of the proposed triple SFs and relative defect termination formation mechanism. First row: the 30° partial dislocation (core atoms in green) is inserted six 111 planes away from the glide plane of a 90° partial glide plane (core atoms in red). Both dislocations are expelled. Second row: the 30° partial dislocation is inserted in the adjacent plane to the 90° glide plane. Dislocations move in opposite directions, join and form a 30° extrinsic partial dislocation. Third row: another 30° partial dislocation (core atoms in fuchsia) is inserted in the plane adjacent to the double SF. It reaches the 30° extrinsic partial and forms the stable triple defect. In the insets volumetric strain maps for each snapshot are reported.

the simulation to model also their evolution. We placed them at a distance of 2.5 nm from the free surface. We chose them to form SFs aligned in the same glide plane of the 90° PD. Green atoms highlight the core atoms of 30° PDs cores in Figure 3.26. In our simulations, 30° PDs are almost always expelled from the film, as reported in the first row of Figure 3.26, except for one case. As shown in the second row of Figure 3.26, when the 30° PD is in the glide plane adjacent to the 90° one, it is not expelled and moves downward. The 90° partial is pulled in the opposite direction. A 30° ESF forms when the two PDs join, and a double SF with a unique boundary appears. Such defect has been experimentally observed 3C-SiC and in other compounds.[140] This behavior is explained by considering the strain fields

shown in the insets. The color maps of the second row of Figure 3.26 show the opposite-in-sign deformation fields of the dislocation overlap as the two defects become closer. The lower formation energy should also enhance the formation of a double SF more than that of individual SFs. At this, the MD potential is not able to prescribe the correct ranking in the formation energy: the *formation energy for multiple SF* is almost identical and with the inverse trend for single, double and triple SFs using the Vashishta potential[¶]. In the third row of Figure 3.26 we start considering the so formed 30° ESF and another 30° PD (which core atoms are colored in fuchsia). The Burgers vector of the latter defects has a screw component that is the opposite of the former. The dislocation is labeled as -30° for this reason in Figure 3.26. The Burgers vector chosen has two important aspects: it releases the compressive strain and can lead to the formation of a zero total Burgers vector complex which was demonstrated to be the stablest configuration.[79] Also in this case, we observe the gliding of the 30° PD only when placed in the glide plane adjacent to the other (double) SF. As we expect, when the new 30° PD glides along the double SF, it moves until it reaches the other two dislocations forming there a complex of three defects with a zero total Burgers vector. Independently from which of the two adjacent planes we chose, the -30° dislocation moves away from the surface. Its motion is only slightly faster when inserted on a glide plane adjacent to the SF bounded by the 90° PD. The formation of double and triple SFs appears to be very similar in evolution. Still, we notice that the latter is very important because it corresponds to an inclusion of a hexagonal 6H-SiC stripe in the 3C-SiC, often defined as a microtwin. The defect terminating the triple SF well corresponds to the experimentally observed $\Sigma 3$ {112} incoherent boundaries,[97–99] and to the defect that appears at the grain boundary between the (3C) cubic and the (6H) hexagonal phase of SiC.[100]

3.6.2 Electronic properties by ab initio calculations

In this Section, we will briefly present the electronic properties, obtained by ab initio calculations, of the partial dislocation complexes. As stated above, this part will be discussed for completeness, but it regards the work done by other group staff members. Still, we found them to be non-negligible in supporting the role of our MD simulations on the

[¶]In preliminary calculations we found: 12.1, 14.2, and 14.2 meV/Å^{-2} respectively

identification of the "killer" defect in epitaxial 3C-SiC. Details on this part can be found in Ref. [81].

Stacking faults

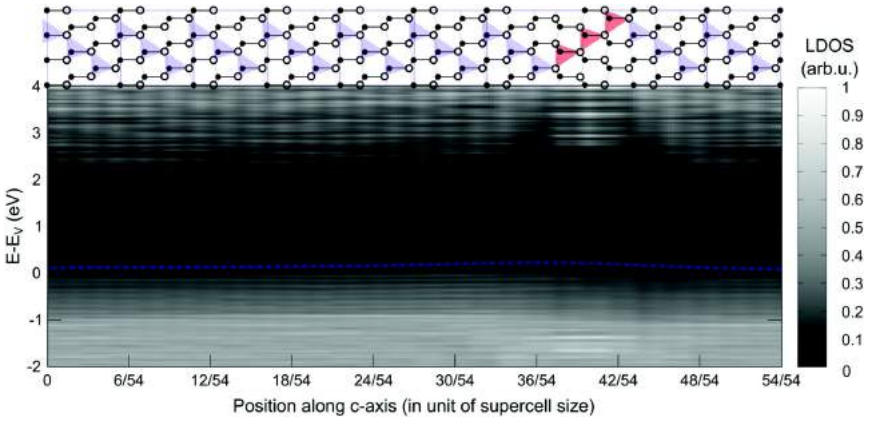

Figure 3.27: Local density of states (LDOS) integrated in slice boxes along the c-axis of the simulated supercell, which is illustrated on top. The red triangles highlight the tetrahedra of the faulted planes as compared to the perfect stacking of the 3C-SiC (blue tetrahedra). The dotted lines highlight the trend of the band edges along the c-axis: a quantum barrier is very evident in the space region where the triple SF is present. Figure from Ref. [81].

The determination of electronic aspects that regards SFs cannot be treated via MD simulations. A superior DFT approach must be used. Many theoretical groups have investigated the changes in the electronic properties caused by the presence of SFs in 3C-SiC. In contrast to what is found for hexagonal SiC phases, in 3C-SiC, the scientific community agrees that SFs do not give rise to electrically active states in the fundamental bandgap of the material.[137,138,141,142]

In Figure 3.27, we report the local density of states (LDOS) obtained by density functional theory (DFT) calculations.[81] The LDOS changes as a function of the position along the c-axis ([111] direction) of a simulated 3C-SiC supercell, which includes a triple SF (highlighted by the red tetrahedra). The bandgap of the 3C-SiC is smaller than those of the 6H phase. Hence the SFs in 3C-SiC do not create quantum wells in the material but quantum barriers. No intra-gap states, which can create the leakage current in 3C-SiC devices, are present in the plot. It confirms the general consensus about SFs per se not creating electrically active defects in 3C-SiC. Therefore, one should include SF termination in the analysis of possible detrimental defects in 3C-SiC.

Terminating single SFs by partial dislocations

We proceeded in the investigation by considering the possible atomistic configurations for the partial dislocations terminating the single, double and triple SFs. The goal is to identify which of them introduce detrimental effects for the electronic properties of the devices. The analyses were made in the DFT framework as described in Ref. [81]. We discarded configurations where dangling bonds were present because it has been proven that unreconstructed configurations of PDs are less favorable than the reconstructed ones.[142] In Figure 3.28 we show the electronic properties of the 90° partial dislocations. The results are very close to those obtained for the 30° partial dislocations (Figure 3.29). The Si-core partial dislocations (on the right) show intra-gap states, the C-core ones (on the left side) do not. Still, these intra-gap states are very close to the valence band edge. In Ref. [81] the authors proved that the states are generated by the Si-Si bonds of the 90° and 30° partial dislocation cores. The ones generated by the 90° partial dislocation are higher in energy and closer to the CB than the Si-core 30° PD states. The longer and thus weaker Si-Si bonds in the 90° partials can explain that evidence.

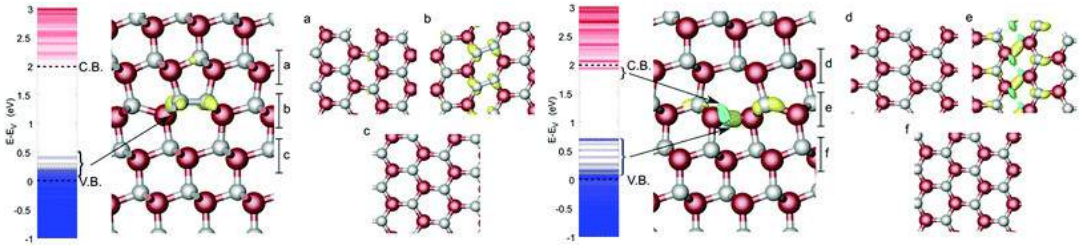

Figure 3.28: Defect states at the C-core (on the left) and at the Si-core (on the right) of the 90° partial dislocation: the Kohn–Sham eigenvalue spectra of the dislocation cores are plotted, with the blue (red) lines indicating occupied (unoccupied) states and the two dashed lines indicating the valence band (VB) and the conduction band (CB) edges in the pristine SiC. The side views of the dislocation cores with the charge densities of the corresponding gap states are also illustrated, including the top views of the $(\bar{1}11)$ glide planes (with a, b, c and d, e, f labels) and the charge densities of the gap states. Red and grey balls indicate Si and C atoms, respectively. The different colors of the charge densities highlight the different integration energy ranges.

Double SF

In the previous subsection, the terminations of SFs have proven to introduce some potential sources of electrically active states in the 3C-SiC bandgap. Still, those states were at energies about 1.5 eV far from the CB minimum in energy. It is hard to attribute them trapping-assisted recombination/tunneling processes that can cause leakage current.[71,143]

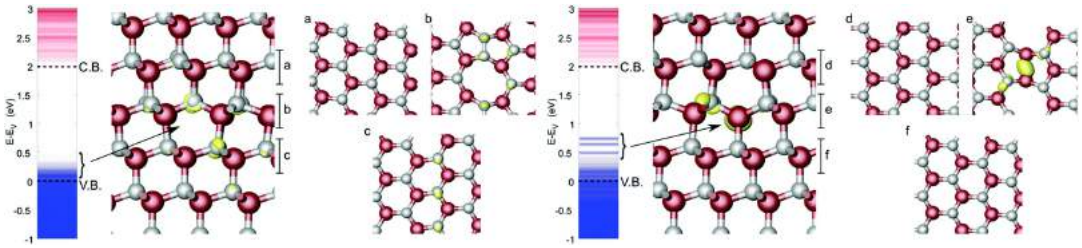

Figure 3.29: Defect states at the C-core (on the left) and at the Si-core (on the right) of the 30° partial dislocation: the Kohn–Sham eigenvalue spectra of the dislocation cores are plotted, with the blue (red) lines indicating occupied (unoccupied) states and the two dashed lines indicating the valence band (VB) and the conduction band (CB) edges in the pristine SiC. The side views of the dislocation cores with the charge densities of the corresponding gap states are also illustrated, including the top views of the ($\bar{1}11$) glide planes (with a, b, c and d, e, f labels) and the charge densities of the gap states. Red and grey balls indicate Si and C atoms, respectively.

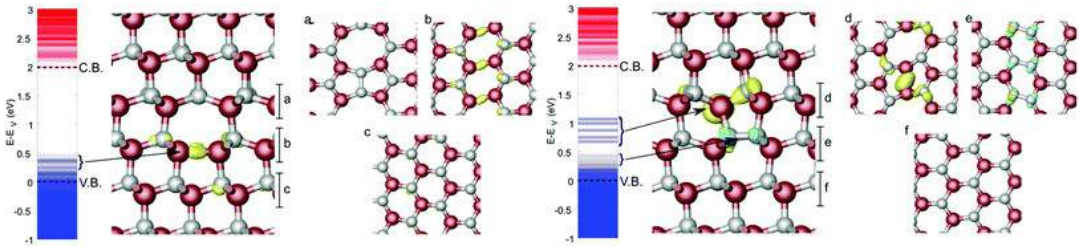

Figure 3.30: Defect states at the double dislocation complexes: structure A, left side, composed of a C-core 30° partial on top of a Si-core 90° partial, while structure B, right side, with a Si-core 30° partial on top of a C-core 90° partial. The Kohn–Sham eigenvalue spectra of the dislocation cores are plotted, with the blue (red) lines indicating occupied (unoccupied) states and the two dashed lines indicating VB and CB edges in the pristine SiC. The side views of the dislocation cores are illustrated and the corresponding top views of the ($\bar{1}11$) glide planes are shown in insets a, b, c and d, e, f. Red and gray balls indicate Si and C atoms, respectively. The different colors of the charge densities highlight the different integration energy ranges.

We can therefore focus our attention on double and triple SFs. Indeed, they are known to be more stable than the single ones,[36] and from the simulation in the first subsection, we know that they can easily be formed during growing procedures (see Figure 3.26). The MD simulation also provided important information about the character and position of the PDs that should be considered as the bounding defects of double SFs. Figure 3.30 shows the two stable structures terminating the double SF (or ESF). The two sides of the figure provide the two possible terminations. On the left side, we have a C-core 30° (see inset (**a**)) on top of a Si-core 90° (see inset (**b**)). On the right side, we have a Si-core 30° PD (see inset (**d**)) above a C-core 90° PD (see inset (**e**)). Few states appear in the band structure corresponding to the configuration on the left, but their position is similar to the Si-core 90° PD case. The charge density plot of Figure 3.30 illustrates that the cause of these states is

also in this case, the Si-Si bond of the 90° partial dislocation. In agreement with the results found for the single SF, nothing is found due to the 30°PD C–C bond.

A completely different situation is found for the configuration on the right. The Si-core 30° PD induces evident deep defect states much higher in energy than in single SF case. The charge density plot of Figure 3.30 for the configuration on the right shows that the Si-core 30° PD introduces into the 3C-SiC bandgap a dispersive band with energy from 0.7 eV to 1.1 eV above the VB edge. The charge density plot also evidences that the C-core 90° partial dislocation does not contribute directly to these states. Still, the C atoms of the dislocation core are bonded to the Si atoms of the Si-core 30° partial dislocation. It can have a role in the rise of the energy of the intra-gap states by making the Si-Si bond even weaker than in the case of a single PD.

Triple SF

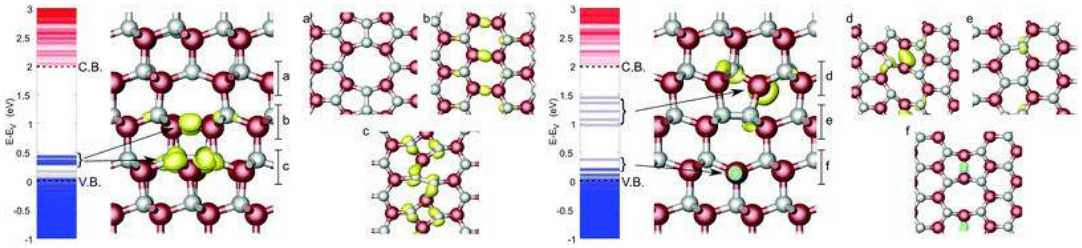

Figure 3.31: Defect states at the triple dislocation complex: configuration A on the left and configuration B on the right. The Kohn–Sham eigenvalue spectra of the dislocation cores are plotted, with the blue (red) lines indicating occupied (unoccupied) states and the two dashed lines indicating VB and CB edges in the pristine SiC. The side views of the dislocation cores with the charge densities of the corresponding gap states are also illustrated, including the top views of the ($\bar{1}11$) glide planes (as in the side view with a, b, c and d, e, f labels) and the charge densities of the gap states. Red and gray balls indicate Si and C atoms, respectively. The different colors of the charge densities highlight the different integration energy ranges.

The most probable shape for a triple SF is formed by three successive planes of SFs, each bounded by a PD with a different Burgers vector. From the analysis performed via MD in the first subsection, we expect to have a 90° PD in the middle and two 30° PDs with an opposite screw component above and below it. Figure 3.31 show the reconstructed structure of the triple bounding defect. Note the terminations, which are opposite for the 30° PDs and the 90° PD. The configuration on the left is very similar to that of the double SF. The band structure is similar: defective states are outside the gap (C-core) or close to the valence band-edge (Si-core). Still, the triple SF termination on the left has another

single 30° C-core PD (see inset (**c**) of Figure 3.31). This latter PD shows a reconstruction that is slightly different from the ones mentioned above. Its defect states are in the same energy range.

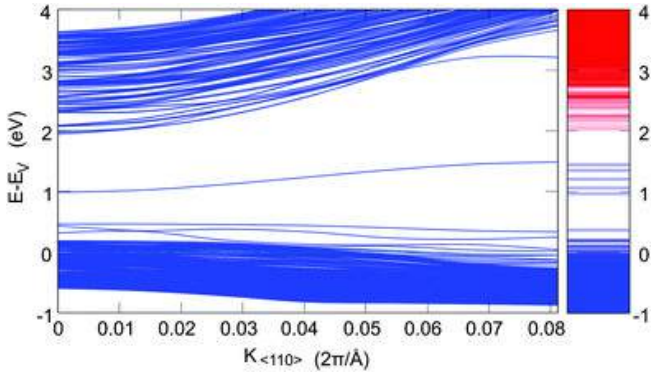

Figure 3.32: Band structure along the ⟨110⟩ direction for the supercell containing the terminations of the triple SF. The deep defect states in the LDOS are clearly due to a single dispersive band.

Dramatic defects states appear in the configuration shown in the right of Figure 3.31. The (top) 30° Si-core PD generates a dispersive band in the SiC bandgap with energy from about 1.0 eV to about 1.5 eV above the VB edge (see inset (**d**)), similar to the double SF case. The defect energy band is almost identical to that of the ESF but shifted upward by about 0.4 eV. The further weakening of the Si-Si bond due to the presence of a third PD can explain this shift. Indeed, the structure analysis performed with OVITO shows an increase in the length of the Si-Si bond from 2.33 Å to 2.39 Å.

Since the Si atoms of the top PD are bonded to the C-core atoms of the 90° PD, while the bottom 30° are almost connected as in the case of the single 30° partial, the bottom 30° PD shows states that are closer to the VB (see inset (**f**)). The observed Si-Si bond length is indeed slightly shorter (2.36 Å, compared to 2.37 Å of the single one). The band structure along the ⟨110⟩ direction for the triple SF supercell of Figure 3.31 is plotted in Figure 3.32. The five energy levels appearing on the right side of Figure 3.31 which resembled different states are in truth a single dispersive branch. The discrete energy levels in Figure 3.30 and 3.31 are an artifact of the limited K-points employed for the calculation of the LDOS.[81]

We conclude by saying that the double and triple SFs illustrated in Figure 3.30 and 3.31 are the most plausible candidates as killer defects in 3C-SiC. The presence of multiple PDs leads to a distortion and weakening of the Si-Si bond of the 90° PD core. It pushes the

energy of this state inside the 3C-SiC bandgap. These defect states are dispersive in the k-space because of the periodicity of the defect along the dislocation line. The state is a 0.5 eV wide defect band placed almost in the middle of the bandgap. Note that Σ3 {112} incoherent boundaries are structurally identical to the triple dislocation complex. It is possible that also such defects introduce similar detrimental states.[97–99,144] From experimental observations,[96] a coexistence of double and triple SFs in 3C-SiC (with a higher population of the latter) is expected. Hence their bounding defect can be reasonably charged with the appearance of leakage currents in 3C-SiC devices.

3.7 Conclusions

In this Chapter, we considered the Silicon Carbide prototypical cases of semiconductor epitaxy on Si presented in this manuscript. We studied extended defects in SiC epitaxial film, grown on silicon substrates in the framework of classical molecular dynamics. The epitaxy of such an important material for the realization of new power devices and automotive represents one of the ideal test cases for extended defect modeling via classical molecular dynamics simulations. The chosen approach, i.e., Classical molecular dynamics simulation, resulted in being appropriate. Indeed, we found the results of such simulation to be reflected by experimental observations. In this Chapter, we focused on some open questions about extended defects in epitaxial SiC on Si (001) and we provided an answer to them. The obtained results gave us essential information that can practically be used to reduce the appearance of those defects in the epitaxial systems. Most of the work presented in this Thesis is represented by the study on extended defects and, in particular stacking faults, in the cubic silicon carbide. We started our analysis by considering the molecular dynamics potential functions that can be used to model stacking fault evolution in 3C-SiC. We provided the technical details about the reliability of the different potentials on the description of defects: The Vashishta potential is, overall, the most reasonable choice as a potential function to model SF evolution in 3C-SiC. Nevertheless, it has some disadvantages over the Analytical Bond Order Potential (ABOP) in describing the fine core structure of dislocation cores and surfaces. The other potential considered, the Tersoff potential, instead, was found not to be a good candidate potential function for the description of SF evolution in 3C-SiC. Then we addressed the lack of theoretical

understanding of the mechanisms regarding stacking fault aggregation into multiplane stacking faults characterized of being composed specially by two or three defected planes. We performed MD simulations at constant temperature and energy minimization simulations that allowed us to understand that only specific configurations of stacking faults are possible. A crucial point in the composition of these structures was found: stable configurations are determined by the partial dislocations that bound each stacking fault with the perfect crystal. Some prescriptions exist on the choice of a candidate partial dislocations that generated the stacking fault. Their Burgers vector should be different for each one of the stacking fault planes. An important implication arises from that: the very abundant multiplane stacking faults are generated by defects that may have formed under very different strain conditions. The latter point determined how we proceeded in the investigation of stacking fault evolution thereon in this Chapter: we reconsidered the growth conditions experienced by the 3C-SiC film. It resulted to be clear that a change in the strain sign is achieved after the first stages of the growth, after the so-called carbonization process. The former high tensile strain becomes a slight compressive strain thanks to the formation of an array of Lomer dislocation at the SiC/Si interface. We, therefore, draw a novel picture of stacking fault evolution and formation: stacking faults are formed in the initial phase, which is tensile. The partial dislocations present are well known because of the strain sign they have to be 90° partial dislocations leading stacking fault extension from the surface to the interface, or either 30° partial ones leading stacking fault expansion from the interface toward the free surface. We hence analyzed the open problem regarding the unexplained experimental observation that leads to stacking fault annihilation while they migrate from the interface toward the free surface. In doing so, we identified the dislocations leading the stacking fault expansion in being 30° partial ones. And then, we identified the annihilation mechanism in being the formation of a Lomer-Cottrell lock at the junction of two crossing stacking faults. The considered change in the strain resulted to be key also in the enhancement in the probability of having double or even more frequently triple stacking faults with a common boundary of partial dislocations. By considering that once again, we were able to explain another open problem in 3C-SiC epitaxy on Si (001): the observed and not completely understood shape of stacking faults. We

found that the Δ and V shape of stacking faults are determined by the evolution of individual stacking faults in the initial tensile strain. They successively transform into multiple stacking faults when a compressive strain arises in the film. As a last result, we presented another important step forward in the comprehension of extended defects and their role in 3C-SiC epitaxy, filling the gap of another crucial open problem for 3C-SiC exploitation: the identification of a defect that can be charged with being the source of leakage currents in 3CSiC-based devices. It resulted (from a synergic approach of molecular dynamics and density functional theory calculations) that the complex of bounding partial dislocations of a triple or double SF can be charged with being the source of leakage currents in 3C-SiC devices.

Chapter 4

Results: Formation of ordered arrays of dislocations in Ge on Si (001)

This Chapter will focus on epitaxially strained Ge on Si (001). Ge on Si is the ideal prototypical case to study dislocation motion because of many aspects. First, a well-known experimental background exists about dislocation in Ge and its alloys with Si grown on Si (001) substrates. Second, the epitaxial strain in the system is compressive and is ≈ 4%, whereas, in the case of SiC, it was tensile and much higher (≈ 4%). The system actually relaxes in a very different way, generating dislocation loops at the free surface instead of, for example, generating an interface reconstruction as in the case of 3C-SiC during the carbonization. At the same time, the strain is sufficiently high to make it possible to investigate dislocation loops evolution in their full extension (threading arms plus misfit segments), as we will show later. Another essential aspect that makes Ge on Si an ideal system to study dislocations is that the epitaxial stress makes the PK force act so that both the glide and the climb motion are enforced. In this Chapter, we will discuss two main sections. In the first section, we will focus on the glide motion of an entire dislocation loop in an epitaxially strained Ge film. In the second section, we will concentrate on giving an answer to an open question that lasted for fifteen years related to the appearance of ordered arrays of misfit dislocations under specific growth conditions. The first section will show how MD Simulations allow studying strain release in epitaxial Ge via misfit dislocation loops expansion. In the second one, we will study straight dislocation lines. In this way, PBCs will be used to reduce the spatial scales necessary for a simulation, thus enabling the study of dislocation line evolution on time scales that range from few hundreds of ps to many several tenths of ns.

4.1 Misfit dislocation loop

One of the most successful theories of dislocation formation in epitaxial germanium films on Si substrates is the nucleation of dislocation loop at the free surface.[145–148] The most believed mechanism prescribes the nucleation at the free surface of a dislocation loop (or, more precisely, a half-loop). The simulation of the nucleation of such defects cannot be modeled in classical MD because the corresponding energy barrier is too high to be overcome in a reasonable time. Indeed, using the Nudged Elastic Band approach, Trushin et al. showed that the nucleation of dislocation loops in Ge films on silicon, using semiempirical potentials, has an energy barrier of ($\approx 40eV$), which is strongly influenced by the presence of defects such as other dislocations or steps on the surface.[26,149] Even considering other defects and step on the surface, the energy barrier was too high to ever overcome at any temperature in a classic MD simulation. Therefore, we will skip the nucleation and model the evolution after that, considering dislocation loops with a radius that makes them super-critical. The Burgers vector of such dislocation loops belongs to the family $\vec{b} = \langle 110 \rangle$, and their glide plane is a $\{111\}$ plane. Possible combinations of glide planes and Burgers vector are composed of four planes on which four Burgers vectors are suitable. Mathematically speaking, each glide plane is the plane that is spanned by one of the eight possible Burgers vectors and either the [110] or the $[1\bar{1}0]$ direction, being the latter one of the two possible misfit segment line direction. Only half of the possible Burgers vectors are effectively able to relax the compressive strain. The other half relaxes the tensile strain. Under the action of the PK force, the dislocation loop gradually extends and, in doing so, it releases the compressive strain in the film. The loop section closer to the Si/Ge interface will move toward it mainly by sliding along its glide plane. The movement of this half-loop section increases the area of the crystal, which is relaxed by the defect. It eventually will reach the interface where it will form a straight segment, aligned alongside either the [110] or the $[1\bar{1}0]$ direction. For this reason, that section of the half-loop is usually called the "misfit segment." The remaining two segments of the half-loop will tend to align in a favorable line direction. Because of symmetry in the diamond/zinc-blende structure, they are the $\langle 110 \rangle$ lines. Energetically speaking, the most convenient line direction is the one aligned with the Burgers vector. Such sections of the half-loop will present a screw character because of that. They will move in opposite directions in the glide plane

of the loop under the action of the PK force. It's important to note that they play an indirect role in the strain release. Indeed, a screw dislocation does not have any (edge) component able to relax the compressive strain, but by moving in their glide plane, they will increase the length of the loop's misfit segment at the interface. It actually plays an active role in the strain release. Notably, either the [110] or the [1$\bar{1}$0] direction can form the glide plane of a screw segment together with the dislocation Burgers vector. It enables screw dislocation to change their glide plane. The ability to change their glide plane, it's known as the possibility of having a cross-slip of the dislocation line. For the purposes of strain release, the ability of the threading arm to cross-slip does not influence too much either the global strain release.[150]*

In Figure 4.1 we reported the snapshots of molecular dynamics simulation of a dislocation loop evolving in an epitaxially strained germanium film at 600K.

Using the procedure introduced in the Section 2.3.3 we prepared simulation cells as follows:

- A silicon substrate: it is represented by 18 ML of atoms placed as prescribed by the ideal perfect crystal lattice.
- The epitaxial Ge film: it is represented by 64 ML of atoms placed coherently with the silicon substrate lattice parameter.

1920 atoms make up each ML, and this number corresponds to the replication of 24 unit cells along the x direction and 20 unit cells along the y direction.

Simulation cells have their axis oriented along the crystallographic directions as described on page 62 (x = [1$\bar{1}$0], y = [110] and z = [001]) and periodic boundary conditions are applied along x and y. The loop has been inserted in a Ge film where a straight dislocation line at the interface is present. It is perpendicular to the misfit segment direction of the loop (see Figure 4.1 (**a**)). The Burgers vector of the inserted loop is $\vec{b}$ = [011], and its misfit segment is aligned with the [110] direction. The epi-layer is dislocated by the presence of a straight dislocation line in the $\vec{\xi}$ = [1$\bar{1}$0], and the two defects have the same Burgers vector.

*Cross slip enables the possibility of two threading arms to annihilate even if their loop glide plane are not intersecting but on a minimal spatial scale.

The presence of the dislocation line is needed to prevent the cross-slip of the threading arms of the loop. With the perpendicular dislocation line present, the loop opens, expanding in its glide plane. Initially, the section of the loop close to the free surface is expelled, transforming the dislocation loop into a half-loop (see Figure 4.1 (**b**)). After that, the lower section of the half-loop reaches the dislocation line at the interface, forming a characteristic intersection which is visible in Figure 4.1 (**c**). The loop will further extend, and it will reach the periodic boundaries where its left threading arm will encounter the right one as shown in Figure 4.1 (**d**). If we take the same line direction, the two threading arms have an opposite Burgers vector, and therefore they annihilate. An infinite dislocation line is now formed (Figure 4.1 (**e**)), and it gradually migrates to the silicon interface. In the end, a perfect crossing of two perpendicular dislocation lines appears, as shown in panel (**f**).

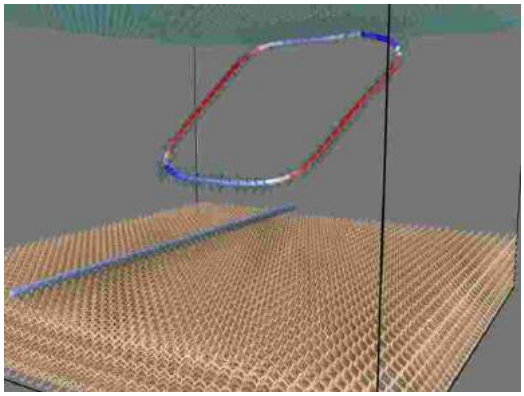

(a) Initial configuration.

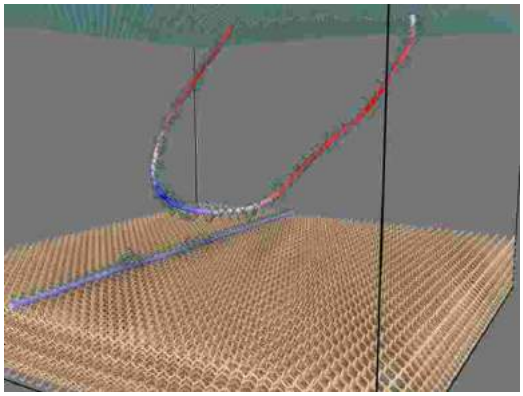

(b) Snapshot after 100 ps.

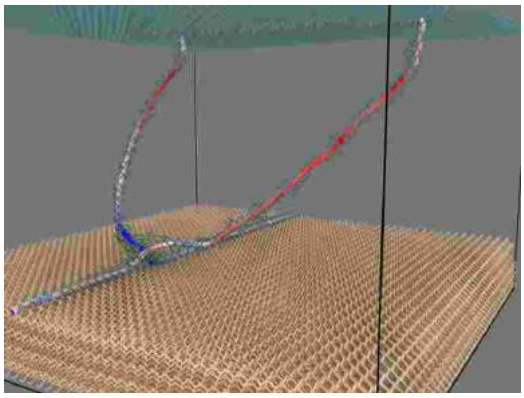

(c) Snapshot after 200 ps.

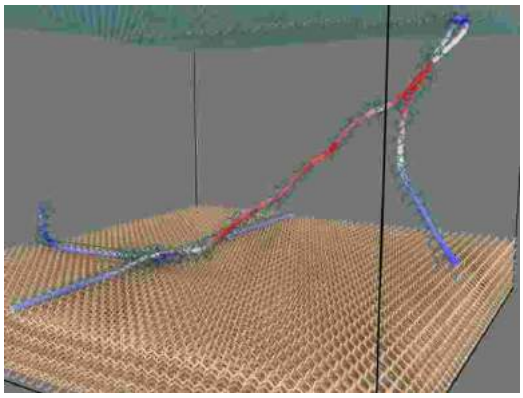

(d) Snapshot after 400 ps.

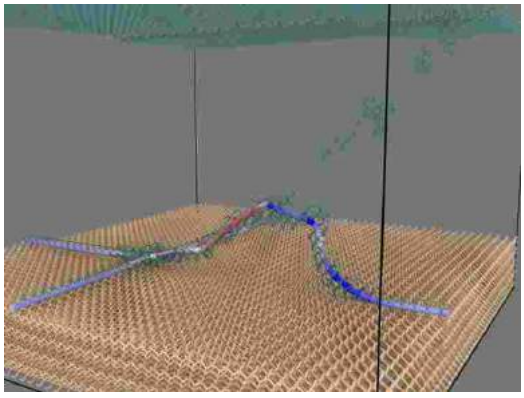

(e) Snapshot after 500 ps.

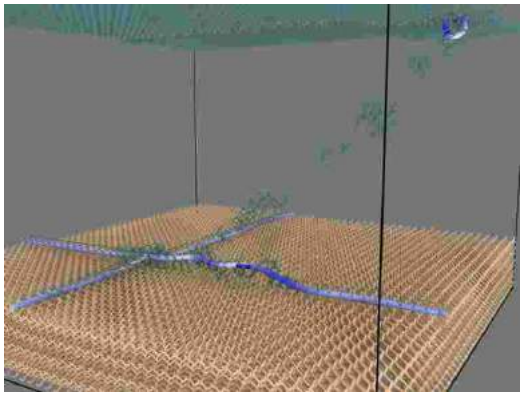

(f) Snapshot after 600 ps.

Figure 4.1: Several snapshots of the simulation via MD of a dislocation loop, inserted in a virtual epitaxial Ge film strained on a silicon substrate at 600K. Ocra sticks represent Si atoms and bonds, green ones Ge atoms and bonds. Atoms of the film that are in the ideal diamond structure are hidden to show the dislocation segments which are depicted by a colored line. Line colors indicate the character of each dislocation segment, i.e. red means screw, blue means edge.

4.2 Misfit segment glide and climb

In the previous section, we verified that classic MD simulations are a valid tool to study dislocation evolution in epitaxial Ge films grown on Si (001) substrates. In this section, we will use them to comprehend experimental evidence about a still unclear mechanism. Indeed, it is an open question why, during growths characterized by low temperatures (low-T) or high deposition rates followed by high-temperature (high-T) annealing, misfit dislocations are prevalently 90° ones in ordered arrays, whereas isolated 60° are less abundant. Let's recall one of the most promising growth techniques for pure Ge films. It is the depositing of a low-T Ge layer (which is usually called *seed layer*), often followed by the deposition of a high-temperature Ge layer (which is generally called *cap layer*) followed by subsequent annealing. The result is a high-quality, relaxed, epitaxial Ge film on a Si(001) substrate grown using an ultra-high vacuum chemical vapor deposition system. As described in the preceding section, in Ge/Si(001) epitaxial heterostructures, plastic relaxation occurs mainly through the nucleation at the surface of dislocation (semi-)loops,[151] with Burgers vectors $\vec{b} = a/2\langle 011\rangle$ - a being the epilayer lattice parameter - gliding in {111} planes. As the loop radius increases, the dislocation progressively releases the epi-layer lattice compression, eventually creating a 60° misfit dislocation segment at the hetero-interface. Edge misfit dislocations (often called Lomer dislocations) are characterized by Burgers vectors $\vec{b} = \pm a/2[1\bar{1}0]$ or $\vec{b} = \pm a/2[110]$ lying in the interface plane. Two different questions are still under discussion: (i) How are 90° dislocations formed? (ii) How is lateral ordering of dislocation at the interface reached?

A partial answer to the first question was supplied as different possible mechanisms leading to the formation of edge dislocations at the interface were proposed.[27] Experiments and theoretical calculations[25,26,152] have highlighted the importance of one of them, i.e., preferential nucleation of a "complementary"[28] 60° dislocation: the stress field induced in the proximity of the free surface by the presence of a 60° dislocation at the Ge/Si interface lowers the barrier for nucleation of a second (the "complementary one") 60° dislocation with Burgers vector such that the superimposition of the two generates a 90° dislocation. For this reaction to occur through simple dislocation gliding, however, the original dislocation must lay on the glide plane of the complementary one. While this can happen in some cases, the most probable configuration leads to close pairs of 60°

dislocations, clearly observed in low-T experiments.[25] How such pairs evolve into a 90° dislocation upon annealing is not yet clarified. Similarly, no clear answer to question (ii) - regarding annealing-induced ordering - is present in the literature. The possible role of vacancies in influencing gliding/climbing and lateral ordering was invoked[13] but only at the speculative level. As reaching defect uniformity is an important requirement for applications, we find it of utmost importance to provide a solid atomic-scale explanation.

In this section, we shall clarify both the mechanism of 90° dislocation formation from pairs of complementary 60° dislocations and of lateral ordering at the Ge/Si interface by suitable molecular dynamics (MD) simulations, highlighting the key role played by vacancies in influencing defects motion and the importance of the growth/post-growth conditions.

4.2.1 Methods

All simulation results presented in this Section were obtained in the framework of classical molecular dynamics using LAMMPS.[38] The Tersoff potential[46,47,55] was used to describe interatomic interactions. While obviously not exact, such approach has been widely exploited to model defects in Ge/Si systems,[25,153–155] yielding results compatible with experimental evidences. Simulations presented in the present article were run in the canonical ensemble, using a Nose–Hoover thermostat[105] and setting the time step to 1fs. The latter was calibrated in a set of dedicated microcanonical simulations where relative fluctuations in total energy lower than 1^{-5} were observed even at the highest ($T = 1400K$) sampled temperature.

Orthogonal simulation cells, oriented along the directions determined by the vectors $x = [\bar{1}10]$, $y = [110]$, $z = [001]$ were used, and periodic boundary conditions (PBCs) were applied in the x and y directions. To model a strained epitaxial layer we created a simulation cell composed of 32 monolayers of Ge atoms on top of other 32 mono-layers of silicon atoms along the $z = [001]$ direction. The lattice parameter was set as the one of pure silicon. In this way germanium atoms were strained in the x, y directions $\varepsilon_{xx} = \varepsilon_{yy} \approx 4\%$. To simulate the effect of a thick bulk substrate below the Ge layer, the bottom three layers of silicon atoms in the simulation cell were kept fixed to bulk positions. The top Ge surface was reconstructed 2×1 upon forming dimers accordingly. We performed simulations of

dislocation arrays by using three different cell dimensions ($9.987/14.980/19.973 \times 1.536 \times 8.530\ \mathrm{nm}^3$) depending on the explored strain conditions. The cell size along x corresponds respectively to a complete relaxation (L_x =9.987 nm), 75% relaxation (L_x =14.980 nm), and half the relaxation (L_x =19.973 nm), when a 90° edge dislocation is placed at the interface. At this, we assume that the film is actually completely relaxed by such a dislocation array. Specific experimental conditions during a real Ge film growth may not correspond to a complete relaxation of a film with the effective thickness we use in our simulations, as for example theoretically predicted in Ref. [156]. Nevertheless, for the mechanisms we will investigate in this Section we assume that such thermodynamic aspects can be neglected. Furthermore, the main result of this Section are minimally related to the lateral size of the simulation cell being, instead, related to the presence of vacancies. Atomic trajectories were analyzed using OVITO.[40]

Dislocation modeling

For the sake of simplicity, dislocations were introduced in the system as straight segments running along the y direction. Starting from a more realistic (half)loop configuration would have required a larger cell in the y direction, making it impossible to reach the remarkable time scales simulated when describing climb (see the next subsection). Instead, we could set the cell length along y as rather small (1.536nm). Shortening the dislocation line further would be critical as it would preclude the formation of kinks and jogs, allowing for the natural motion of dislocations. On the other hand we verified that, despite being minimal, the simulation cell was indeed large enough along y: we repeated a subset of the simulations using a three time larger cell along y without observing any significant dependence of the results on the dimensions.

Dislocation lines were inserted in the simulation cell by shifting each atom by the displacement field vectors calculated by dislocation modeling in the framework of the linear elasticity theory,[2] as described in Section 2.3.3. The obtained configurations were geometrically optimized using a conjugated gradient minimization algorithm.

Simulation of vacancy-induced dislocation motion

Dislocation climbing requires vacancies to migrate to the dislocation core along the whole dislocation line.[2] Brute-force runs where both typical experimental temperatures and physically-sound vacancy concentrations are considered do not show any sigificant evolution due to the timescale limitations imposed by MD. Even if one disregards experimental conditions, observing climbing along the full dislocation line with MD is not trivial. One can attempt speeding-up the motion by increasing the simulation temperature, therefore raising the diffusion coefficient of the vacancies. However, there exists a limit beyond which excessive disorder is introduced in the system (we used up to T=1400K, well below the Tersoff-potential Ge melting temperature of around 2400K[157]). Instead of manipulating the diffusion coefficient one can attempt reducing the path which a vacancy must travel to reach the dislocation core. A possible way to achieve this is to consider very high vacancy densities. If vacancies are placed too close one to each other, however, the formation of slowly-diffusing vacancy complexes precludes observation of migration to the dislocation core. After attempting several strategies along the lines traced here-above, we came up with a procedure which we find as particularly appealing since the system is left sufficiently free to evolve and climbing of the entire dislocation line can be observed. The procedure is the following one: we start by introducing a dislocation (an extension to two dislocations is also exploited in Section 4.2.4) in the simulation cell. We then remove one atom of the crystal randomly. We start the MD simulation and we track the vacancy motion on the fly by performing a Wigner Seitz Defect Analysis using the OVITO software. If the vacancy ends up at the dislocation core or at the top free surface we then randomly insert a second vacancy and start tracking its motion, otherwise we keep on simulating the system dynamics. The procedure is iterated until the desired number of vacancies are inserted. As demonstrated in the Results section, the procedure works and allows to observe vacancy-induced motion of a full dislocation line.

In principle we could have randomly created vacancies within the full simulation cell. In order to decrease the time needed for the vacancy to reach the dislocation core, however, we defined a smaller "vacancy-spawn" region -where the point defect was created- composed of the atoms distant less than 3nm from the dislocation core. In addition, such region was restricted to be at a distance from the upper free surface larger than the one of

the dislocation core as vacancies created between the dislocation core and the free surface where observed to irreversibly annihilate at the latter.

4.2.2 Gliding of pairs of 60° misfit dislocation

As already stressed above, induced nucleation of a second, complementary 60° dislocation by a first 60° dislocation at the Ge/Si interface has been recognized as the primary cause for the creation of 90° dislocation and of 60° dislocation pairs.[25,158] As no atomic-scale description of further evolution under annealing is present in the literature, we shall start our analysis precisely from these pairs. Following Ref. [25], the typical initial condition leading to their formation is given by having one 60° dislocation – called "A" in Figure 4.2 – at the Ge/Si interface and a second one – "B" in Figure 4.2 – nucleated close to the free surface. If the position of the core of dislocation "A" belongs to the glide plane of dislocation "B" (this glide plane is often called *mirror-like* (ML) glide plane and is indicated by a red dashed line in Figure 4.2) then simple gliding of "B" towards "A" can lead to the formation of a 90° dislocation. For this case, annealing is not needed to promote the existence of such a defect. A close pair of 60° dislocations is formed when, instead, dislocation "B" glide plane intersects dislocation "A" glide plane not at the interface. Three representative initial configurations are displayed in Figure 4.2, together with the evolution predicted by molecular dynamics simulations at 1000 K. Dislocation "A", with Burgers vector $\vec{b} = [011]$ is placed at the interface (the dislocation core is highlighted in green), dislocation "B", with Burgers vector $\vec{b} = [\bar{1}0\bar{1}]$, is placed 1.5nm below the free surface (the dislocation core is highlighted in red). The glide planes of the two dislocations are misaligned; therefore, they cannot form a 90° dislocation at the interface. The distance d_{ML}, between the glide plane of the second dislocation (at the interface) and the mirror-like glide plane, is used as a parameter. Three cell sizes along the x direction were used to simulate different relaxation of the Ge film: ≈10 nm - corresponding to full relaxation of the ~ 4% Ge/Si lattice mismatch in the presence of a 90° edge dislocation at the interface per cell, ≈15 nm - i.e., 75% relaxation with a 90° edge dislocation at the interface, ≈20 nm - i.e., half relaxation with a 90° edge dislocation at the interface.

A wide range of relative arrangements of two complementary dislocations are possible and was observed in low-T experiments. Still, the results of their evolution can be grouped

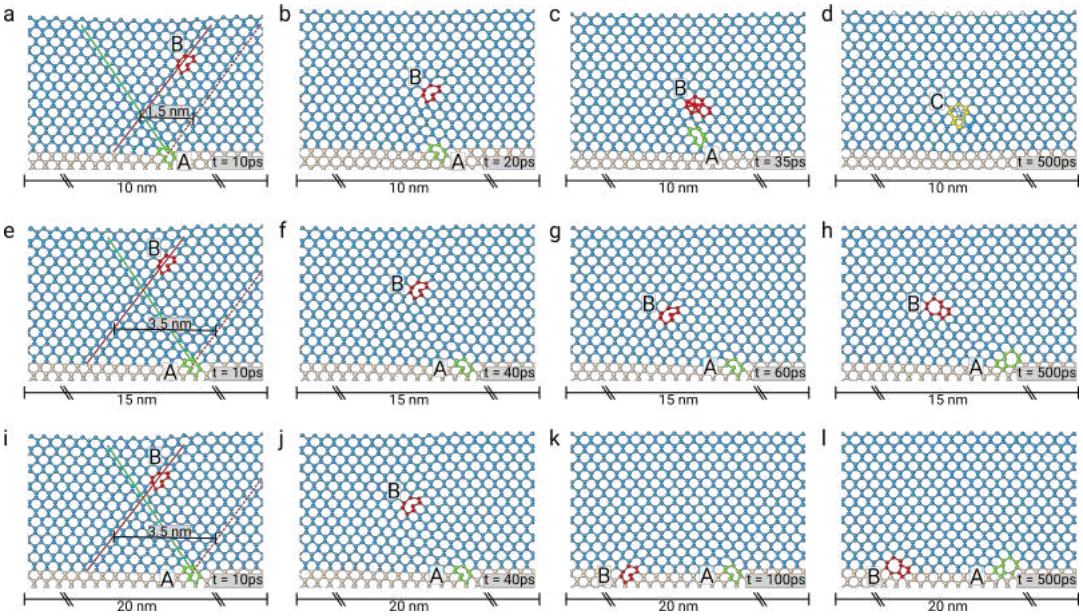

Figure 4.2: Evolution of complementary dislocations pairs. Each row corresponds to a different simulation performed using different cell sizes to simulate different degrees of relaxation. Light blue spheres represent Ge atoms, pink spheres Si atoms, green spheres highlight the core of the dislocation "A," which start at the interface (Burgers vector $\vec{b} = [011]$), red spheres highlight the core of the complementary dislocation "B" 1.5nm below the free surface (Burgers vector $\vec{b} = [\bar{1}0\bar{1}]$). The glide planes of the dislocations are shown in the first row by colored solid lines; the mirror-like glide plane is shown as a dashed line. (**a**)-(**d**): Complementary 60° dislocations joining above the interface forming the pure edge 90° dislocation "C"; the glide plane of the second dislocation is 1.5nm away from the mirror-like glide plane, and the dimension of the simulated cell is 10nm in the direction perpendicular to dislocation lines. (**e**)-(**h**): Complementary 60° dislocation blocked above the interface; the glide plane of the second dislocation is 3.5nm away from the mirror-like glide plane, and the dimension of the simulated cell is 15nm in the direction perpendicular to dislocation lines. (**i**)-(**l**): Complementary 60° dislocations both at the interface; the glide plane of the second dislocation is 3.5nm away from the mirror-like glide plane, and the dimension of the simulated cell is 20nm in the direction perpendicular to dislocation lines.

in a few categories only: an edge dislocation at the Si/Ge interface (see Brunetto et al.[25]), an edge dislocation few nanometers above the Si/Ge interface, a 60° dislocation "floating" few nm above the Si/Ge interface in the vicinity of its complementary counterpart, and two complementary 60° dislocations both at the interface. MD simulations were able to fully capture all these behavior, as seen in Figure 4.2. Indeed, different initial position of the complementary dislocation placed at the surface and different stress in the cell (i.e., different cell size) lead to the configurations experimentally observed. The evolution reported in panels Figure 4.2 (**a**)-(**d**) ends with a 90° dislocation above the interface, the ones in Figure 4.2 (**e**)-(**h**) with the stopping of the complementary dislocation within the layer, and that in Figure 4.2 (**i**)-(**l**) with both the dislocation at the interface.

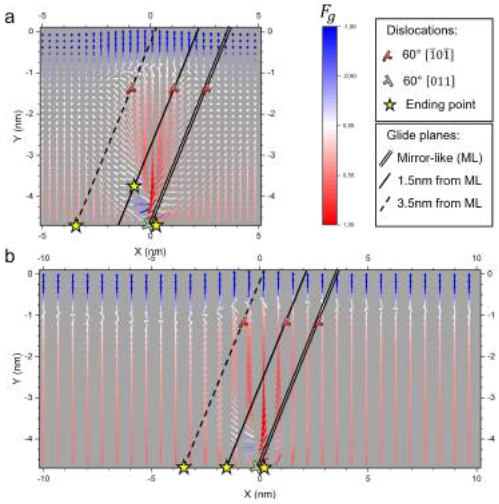

Figure 4.3: Map of the Peach and Koehler force acting on dislocation "B" with Burgers vector $\vec{b} = [\bar{1}0\bar{1}]$ as a function of its position in a Ge film. The complementary dislocation "A" with Burgers vector $\vec{b} = [011]$ is fixed at the interface in $x = 0$. The force vectors are colored in blue-red scale to represent the projection of the Peach and Koehler force along the glide plane. Black lines are inserted to show some possible glide planes of dislocation "B": double line - mirror-like glide plane, solid line - glide plane at $d_{\mathrm{ML}} = 1.5\,\mathrm{nm}$, dashed line - glide plane at $d_{\mathrm{ML}} = 3.5\,\mathrm{nm}$. For each glide plane, a star indicates the position where the dislocation will stop following the force gradient. Panel (**a**) cell size 10nm, panel (**b**) cell size 20 nm.

To explain the results of the here-above reported molecular dynamics simulations, we find it helpful to report, in Figure 4.3, the force field experienced by dislocation "B" placed in different positions while keeping dislocation "A" at the Ge/Si interface. Such force field can be conveniently computed based on elasticity theory,[159] including periodic boundary conditions and the effect of the top free surface. Figure 4.3 allows for an immediate interpretation of the various configurations obtained at the end of the molecular dynamics simulations of Figure 4.2. Note that, differently from molecular dynamics, the analytical calculation assumes[159] an isotropic medium. However, it is evident from the comparison between Figure 4.3 and the final configurations of Figure 4.2 that the qualitative behavior found by MD and predicted by the analytical model corresponds.

The force field displayed in Figure 4.3 (**a**) is computed for an array of dislocations with periodicity of 10nm (ideal periodicity of 90° dislocations to relax pure Ge on Si). The one shown in Figure 4.3 (**b**), instead, corresponds to a 20nm periodicity. The force vectors are colored in red/blue to show the intensity and the orientation of the glide component of the force in a specific position. A saturated red means a strong glide force towards the Si/Ge interface, saturated blue means a strong glide force towards the free surface, pale/white

hues indicate a small/zero force. In Figure 4.3 a star indicates where dislocation "B" will stop its glide for some selected glide planes. The formation of an edge dislocation at the Si/Ge interface is achieved when dislocation "B" nucleates and glide along a plane which is exactly the mirror-like glide plane (double solid line in Figure 4.3). In this case, the force acting on the dislocation is almost aligned to the glide plane resulting in an easy glide. An edge dislocation above the Si/Ge interface can be formed when dislocation "B" nucleates slightly apart from the mirror-like glide plane. Consider for reference the single solid line in Figure 4.3, in this case of dislocation "B" can move on a glide plane which is 1.5nm away from the mirror-like glide plane. The projection of the force acting on dislocation "B" on its glide plane (i.e., the glide component of the force) changes in sign a few nanometers above the Si/Ge interface (see red/blue color-changing). Therefore the dislocation, in this case, will glide towards the Si but will stop in the vicinity of its complementary dislocation (a star indicates the position where the dislocation will stop in Figure 4.3). It clearly corresponds to what happen in the molecular dynamics simulation of Figure 4.2 (**a**)-(**d**). At that height dislocation "B" can attract dislocation "A", making it gliding upward to merge and form a 90° dislocation at their junction (Figure 4.2 (**d**)).

A qualitatively different result is obtained by placing dislocation "B" further away from the mirror-like glide plane. Indeed, when the distance between the glide plane of "B" and the mirror-like glide plane (d_{ML}) is 3.5 nm (dashed black line in the Figure 4.3 (**a**)) we can notice that at a certain height the force acting on the dislocation is directed for the most outside its glide plane. This can result in an evolution which is that reproduced via molecular dynamics and shown in Figure 4.2 (**e**)-(**h**): dislocation "B" migrate from the free surface towards the Si/Ge interface, but in the middle of the film it transforms from a shuffle-set 60° to a glide-set 60° under the action of a strong climb component of the Peach and Koehler force. It freezes there, and dislocation "B" remains floating in the Ge film, too far away from dislocation "A" to make it glide towards it.

This behavior can be expected to change in the case of a much higher strain. Indeed using a periodicity of 20nm instead of 10nm (or 15nm), as shown in Figure 4.3 (**b**), the glide component of the Peach and Koehler force is much higher, and dislocation "B" is pushed towards the Si/Ge interface with almost the same force intensity throughout all the Ge film. In this latter case dislocation "B" will reach the interface, exactly as reproduced via

the molecular dynamics simulations illustrated in Figure 4.2 (**i**)-(**l**)

In many low-T growth experiments, proofs of the presence of these particular arrangements of complementary dislocations are commonly observed,[25] but when the successive annealing at high temperature is performed, most of the defects are found at the interface, they are ordered, and most of them are 90° edge dislocations.[13] The pure glide motion of 60° misfit dislocations cannot explain either the formation of 90° misfit dislocation to a large extent or the ordering of the 90° dislocation arrays. Climbing processes are often evoked to explain that experimental evidence, but no atomic-scale description based on simulations was given. Here we present our analysis filling the gap.

4.2.3 Climbing of 90° misfit dislocation

We analyzed the role of the climbing mechanism in the formation and ordering of 90° edge dislocations starting from the configuration found as the final state reached by glide motion. In particular, we considered the configuration of dislocations in Figure 4.2 (**d**) - i.e. a 90° Lomer dislocation formed above the Si/Ge interface. Climbing of an edge dislocation is the simplest case of dislocation climbing motion and is often used in the literature as a prototypical example.[2] We have already described in Section 4.2.1 how we triggered climbing by inserting vacancies one at the time, removing atoms of the crystal randomly within a "vacancy spawn region," before simulating the system evolution at T=1400 K and checking whether the conditions to insert a new vacancy are met. Here we shall illustrate the procedure further by analyzing the actual simulation where climbing of the 90° edge dislocation is tackled (Figure 4.4). As shown in Figure 4.4 (**e**), the first vacancy, which is represented by the large blue sphere, is observed to diffuse through the Ge film (blue trajectory in the same Figure) while the edge dislocation stays immobile. After few hundreds ps, the vacancy reaches the dislocation core. At this point another vacancy is inserted (red sphere in Figure 4.4 (**e**)) and the system is evolved until also the second vacancy reaches the dislocation core (see Figure 4.4 (**f**), this time its trajectory is highlighted in red). The simulation is iterated, and a new vacancy is created in the "vacancy spawn" region every time there are no vacancies in that region, i.e., the vacancy has reached the dislocation core or is lost towards the free surface. The third vacancy (green sphere) reaches in turn the dislocation core (Figure 4.4 (**g**)), and thereafter, in few hundreds of ps, is followed by

the fourth vacancy (yellow sphere, Figure 4.4 (**h**)). With four vacancies, there is a section of the dislocation line that is one layer below its original position, i.e., a jog has formed. A fifth vacancy is inserted and it migrate to the dislocation core (tile sphere, Figure 4.4 (**i**)). The successive vacancy is the sixth one, and it also reaches the dislocation core that now is almost completely one glide plane below its starting position (purple sphere, Figure 4.4 (**j**)). The seventh vacancy (gray sphere, Figure 4.4 (**k**)) does the same, and finally the last vacancy migrates to the dislocation core, achieving the complete climb of the dislocation (orange sphere, Figure 4.4 (**l**)). The starting and final configuration are shown them Figure 4.4 (**a**) and (**c**), respectively. A black arrow show the displacement of the dislocation core from its starting position. The top views of the dislocation core with and without vacancies are shown in Figure 4.4 (**d**) and Figure 4.4 (**b**), respectively. Notice that, occasionally, we observed the newly inserted vacancy migrate to the free surface. In such cases, not reported in Figure 4.4, we re-insert a new point defect randomly in the vacancy spawn region

The analysis of vacancy trajectories clearly shows that the motion of a single vacancy is random-like at the beginning, while in the proximity of the dislocation core, the attraction between the point and the linear defect leads to the irreversible capture of the former at the core of the latter. It is also evident that vacancies are attracted by the compressive deformation below the dislocation core. A relevant trend, which can be easily observed by considering trajectory lines, is that once vacancies are close to the dislocation core, they start to move towards the dislocation preferentially along {111} planes. Such behavior can be ascribed to the attraction of the vacancies by the compressive region below the Lomer dislocation, which is characterized by having two compressive lobes aligned along {111} planes.

4.2.4 Climbing motion involving pairs of 60° misfit dislocation

After having demonstrated that the introduction of one vacancy at a time in the simulation cell allows one to conveniently simulate climbing of an edge dislocation, we extended the same procedure for investigating vacancy-induced motion of 60° pairs. In particular, we started by investigating the evolution of a 60° dislocation blocked a few nanometers above its complementary pair at the interface. Dislocations are positioned as shown in Figure

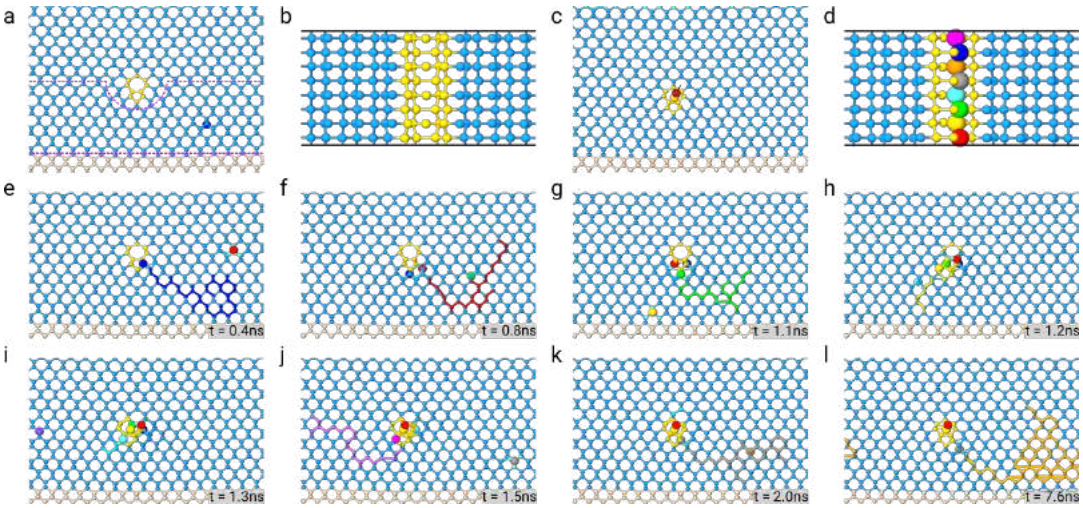

Figure 4.4: Simulation of edge dislocation climb. The first row shows the initial and final state, while the second and third rows show the relevant snapshot of the evolution. Light blue spheres represent Ge atoms, pink spheres Si atoms, yellow spheres highlight the core of an edge dislocation 2.0 nm above the interface (Burgers vector $\vec{b} = [\bar{1}10]$). Larger spheres show the position of the vacancies as identified by Wigner-Seitz defect analysis in OVITO. A trajectory is provided for each vacancy by a colored line. (**a**) Starting configuration: a Lomer dislocation 2.0 nm above the Si/Ge interface, the "vacancy spawn" region is shown by the dashed purple line. (**b**) top view of the dislocation core. (**c**) final snapshot after eight vacancies has been inserted in the cell (a black arrow shows the displacement of the dislocation), with the corresponding top view (**d**). Simulation snapshots are provided in sequence; the corresponding simulation time is shown in the inset (**e**-**l**).

4.2 (**h**), and we will refer to dislocation "A" and "B" in the same way.

Considering Figure 4.3 (**a**) it is clear that dislocation "B" was immobile, but the glide component of the Peach and Koehler was not zero. It was frozen in its position above the other dislocation because it transformed from a shuffle 60° dislocation to a glide 60° dislocation. This can be ascribed to the strong climb component of the Peach and Koehler force that wanted to make it move towards its complementary counterpart (see Figure 4.3 (**a**)). MD simulations (not reported here) show that dislocation "B" remains immobile until enough vacancies make it climb by a single glide plane. After that, the glide core of the dislocation is destroyed, the dislocation can glide again, and it eventually reaches the interface. Notably, the response of a 60° misfit dislocation, which is glissile, to the interaction with vacancies is not a pure climb motion. Indeed, it resulted that instead of climbing all the way towards its complementary pair, dislocation "B" interacts only with few vacancies and then glides towards the interface.

The formation of a 90° Lomer at the interface can still be achieved by the motion of two complementary 60° dislocations alongside the Si/Ge interface. The situation where

two complementary 60° misfit dislocations are located nearby at the interface has been revealed in many experiments, in particular before annealing.[158,160] Annealing can cause vacancy migration towards dislocations, making them climb one towards the other, eventually leading to dislocation joining, forming an edge dislocation. To check this hypothesis, we studied the interaction of vacancies with two complementary 60° dislocations already at the Si/Ge interface as in Figure 4.2 (**k**), separated by a distance of 3 nm. We inserted a vacancy at a time, randomly deleting an atom in a region below the dislocation cores, excluding the cores themselves by the region (excluding a cylindrical region with axis along the y direction, a radius equal to 7 nm, centered in the middle point of the two dislocations).

In Figure 4.5 we show snapshots of MD simulations of the evolution of vacancies in the presence of the two complementary 60° dislocations. In particular, in Figure 4.5 (**a**) the initial position of the two dislocations is shown. The simulated time and the total number of vacancies inserted so far in the cell are shown in the inset of each panel. Each dislocation core is highlighted in a different color, we will refer to them following the same convention used in Figure 4.2, dislocation "A" for the one with Burgers vector $\vec{b} = [011]$ (colored in green) and dislocation "B" for the one with Burgers vector $\vec{b} = [\bar{1}0\bar{1}]$ (colored in red). Dashed lines, colored accordingly, also show their glide planes.

After 13 vacancies have been inserted in the cell and a simulated time of more than 14 ns, dislocation "A" climbs, moving outside its original glide plane (the dotted green line) towards the next glide plane (dashed green line), see Figure 4.5 (**b**). Now dislocation "A" has climbed inside the Si/Ge interface, and therefore it glides along its glide planes back to the Ge film, moving towards dislocation "B" (Figure 4.5 (**c**)). After that, in the successive two ns, dislocation "A" climbs and glide again, as displayed by the arrows in Figure 4.5 (**d**). The former glide planes are shown for reference as dotted green lines, with the thinner being the original one. Also dislocation "B" climbs, as shown in Figure 4.5 (**e**), reducing the distance between the two dislocations. Actually, at such limited distance, the attraction between the two dislocations becomes so strong that dislocation "B" glides along its glide plane and reaches the same height above the interface of dislocation "A." Still, some more vacancies are needed to make the two dislocations climb and react. Enough vacancies eventually arrive at the dislocation cores after 41.2 ns, as shown in Figure 4.5 (**g**) (old glide

planes are shown by dotted lines for reference). The glide plane of the newly formed 90° edge dislocation is 2 mono-layers above the Si/Ge interface (see Figure 4.5 (**h**)). Additional migration of the newly formed 90° edge dislocation (which core is highlighted in yellow) happens. It climbs to the Si/Ge interface adding more vacancies in the cell, as shown in the last snapshot (Figure 4.5 (**i**)). The new glide plane is shown by a dashed yellow line, and the former one by a dotted yellow line, an arrow shows the displacement of the edge dislocation.

In Figure 4.5 we have chosen to present a section of the whole-cell taken by slicing the cell perpendicularly to the dislocation lines to ease the view. In effect, at every step of the present simulation, there is some disorder because we are simulating the evolution of 60° dislocations that are not sessile, as in the case of an edge dislocation. Therefore dislocation segments move easily and not as a whole (i.e., kinks of the dislocation line are present). Anyway, we were able to obtain a final configuration of a perfect edge dislocation at the interface long as the whole simulation cell. It was achieved by continuing the presented simulation, increasing the time left to the system to equilibrate itself before a new vacancy insertion, and annealing the system for other 50 ns.

While not the main aim of this work, we notice how the present simulations, see Figure 4.5 (**i**), naturally predict the presence of Ge and Si intermixing around dislocation cores and in the surrounding areas, as observed in experiments and explained theoretically.[160,161] Mixing is produced by the motion of the vacancies that allow for Ge/Si exchanges without involving bulk diffusion.

Our simulations also partially reproduced this mixing of Ge atoms in the substrate and vice-versa (note Ge atoms colored in blue in the Si region and vice-versa in Figure 4.5 (**f**)-(**i**).

4.2.5 Glide of 90° misfit dislocation

In the former two sections, we investigated the role of vacancies in dislocation climb. As expected, simulations showed that vacancies are attracted by dislocations, eventually producing their climbing motion. As a result, edge dislocations from the Ge film can migrate to the Si/Ge interface, and pairs of complementary 60° dislocations can migrate alongside

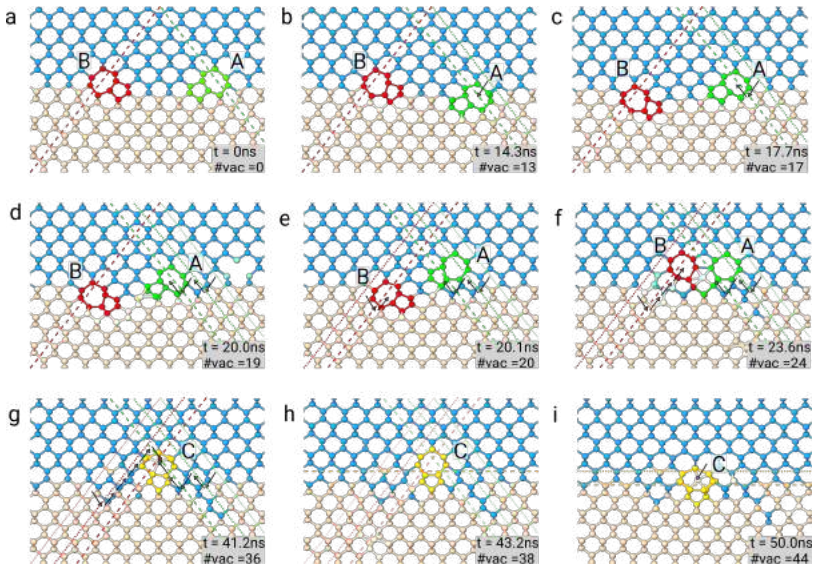

Figure 4.5: Simulation of a pair of 60° dislocations climb. Along all three rows, relevant snapshots of the evolution are shown. Light blue spheres represent Ge atoms, pink spheres Si atoms, green spheres highlight the core of the dislocation "A" (Burgers vector $\vec{b} = [011]$), red spheres highlight the core of the complementary dislocation "B" (Burgers vector $\vec{b} = [\bar{1}0\bar{1}]$). The glide planes of the dislocations are shown by dashed lines colored accordingly to which dislocation they belong. Simulation snapshots are provided in sequence (**a**-**i**), the number of vacancies inserted in the cell and the corresponding simulation time are shown in the inset. Black arrows show the displacement of the dislocations.

the interface and there join to form edge dislocations. Based on our results, we can therefore provide the following explanation of the experimental findings:[13,25] during low-T growth, a large density of vacancies is introduced in the system as a direct consequence of out-of-equilibrium growth. However, their mobility is limited once again due to the low temperature. The situation changes when a second stage involving either annealing or high-temperature growth follows. Vacancies can now quickly diffuse, enabling the interaction of complementary 60° misfit dislocation, grouped initially into pairs, eventually forming edge dislocations.

Having provided an answer to the first open question regarding the annealing-induced abundance of 90° vs 60° dislocations, we can now address the second, i.e., how such edge dislocations can move laterally, producing an ordered distribution.

To answer, we considered the situation where an array of non-equidistant 90° is present at the Si/Ge interface. Indeed, we considered a simulation cell 20nm wide. We inserted two edge dislocations distanced by only 3nm (as we use PBCs, this actually corresponds to an array of dislocations where each defect has a distance of 3nm with the closest defect and of 17nm with the next one) checking whether mechanism leading to an increase of

such distance towards the 10nm ideal value was occurring.

We ran an MD simulation at 1400K, and we observed a single gliding event (i.e., lateral motion leading to an increase in lateral distance) after an extremely long simulation time (~ 90ns). At a lower temperature of 1200K, no events at all were witnessed in as long as 100 ns, the maximum time we reached with our simulations. We conclude that lateral motion can occur but on quite long time scales. Interestingly, however, we noticed that a single vacancy could lead to a noticeable increase in gliding velocity. In Figure 4.6, indeed, we show the results of a simulation where a single vacancy is inserted a few lattice sites to the right of Lomer dislocation "*C*", in Figure 4.6 (**a**). The vacancy, represented by a purple sphere, is attracted by the dislocation and reaches its core in a relatively short timescale (Figure 4.6 (**b**)). No vacancy is present near the other edge dislocation "D." The presence of a vacancy in the dislocation "C" core enables the formation of a kink as shown in Figure 4.6 (**c**) (the top view of the defect, together with the corresponding dislocation line, is provided).

Once the kink has formed, the completion of the glide step is relatively fast; indeed, only ≈ 100 ps are needed to move the whole dislocation line (see Figure 4.6 (**d**), (**e**)). The vacancy is still around the dislocation core so that it can enhance the glide motion of dislocation "C" again. Indeed, after ≈ 50 ns dislocation "C" glides on the right again as shown in Figure 4.6 (**f**) (the black arrows are inserted for reference). A third and a fourth glide jumps to the right are observed in the next ≈ 30 ns (Figure 4.6 (**g**), (**h**)). Notably, we also observe dislocation "D" glide on the left, but after 92.3 ns of simulation time.

In the presence of the vacancy, a single glide step was also observed in a simulation run at 1200 K.

4.2.6 Conclusions on vacancy-dislocation interaction

In this last section, we exploited molecular dynamics simulations to shed light on the atomic-scale mechanisms leading to the experimentally observed formation of a laterally-ordered array of 90° dislocations at the interface of Ge/Si(001) films.[13,160,162] Importantly, such arrays are typically obtained in experiments where a first low-T deposition stage is followed by a raise in temperature.[13] In the former pairs of 60° dislocations are formed by pure gliding motion, which can occur even in the absence of fast-moving vacancies.

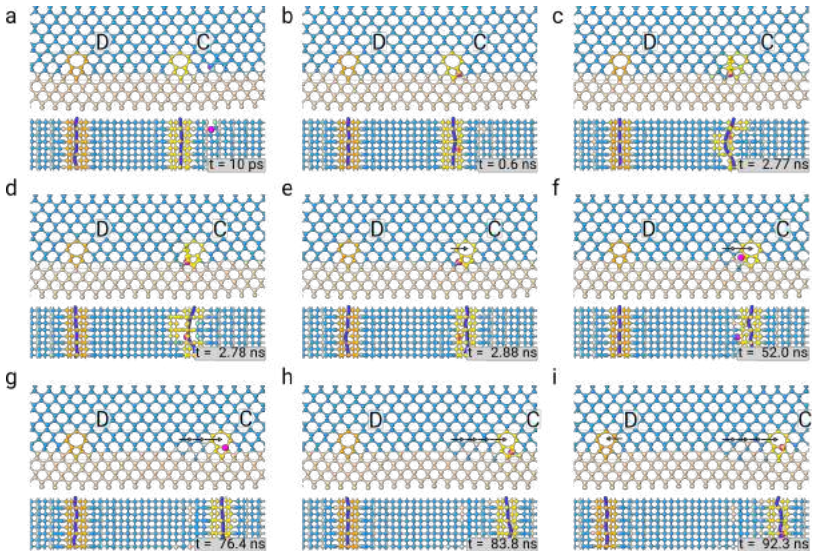

Figure 4.6: Simulation of 90° edge dislocation vacancy-assisted glide. Relevant snapshots of the evolution are shown. Light blue spheres represent Ge atoms, pink spheres Si atoms, yellow spheres highlight the core of the dislocation "C" on the right (Burgers vector $\vec{b} = [\bar{1}10]$), orange spheres highlight the core of the identical dislocation "D" on the left (Burgers vector $\vec{b} = [\bar{1}10]$). The vacancy, as identified by Wigner-Seitz defect analysis in Ovito, is depicted as a big purple sphere. For each configuration, a top view of a slice around the defects is provided below each snapshot. Thin black lines indicate the sliced region of each snapshot. Simulation snapshots are provided in sequence (**a**-**i**), and the corresponding simulation time is shown in the inset. Black arrows show the displacement of the dislocations.

And, indeed, we could observe the formation of such pairs in MD simulations where no point defects at all were present. Explaining the full transition of the pairs into 90° dislocations required climbing motion to be activated at the higher temperature following the low-T stage. After having introduced a convenient procedure to introduce vacancies in the simulation cell, we were able to observe full vacancy-induced dislocation climbing leading to the transformation of the 60° pairs into 90° dislocations and/or climbing of 90° dislocations at the Ge/Si(001) interface. At this point, we tackled lateral ordering of 90° dislocations at the interface. While lateral gliding motion was also observed in the absence of point defects, our simulations revealed how even the presence of a single vacancy could significantly speed up the process, ultimately leading to an ordered array. With this respect, we find it interesting to point out that the final stage of lateral ordering can also be reached without imaging an excess of vacancies in the system, at variance with the transformation of 60° into 90° in the likely situation where nucleation of the second 60° dislocation does not occur on the mirror glide plane.

In conclusion, our simulations reproduced experimental findings and, in doing so,

helped in understanding the different phases needed to achieve the limit of a unimodal distribution of laterally-ordered dislocations in Ge/Si(001), highlighting when the role played by vacancies is crucial and when it is not. This can help to devise new growth strategies where alternating close-to-equilibrium and far-from-equilibrium conditions are exploited to influence the dislocation distribution.

4.3 Conclusions

In this Chapter, we have discussed different aspects of dislocation modeling via molecular dynamics simulation considering Germanium. The compressive strain implies that most of the defects are perfect 60° or 90° dislocations whereas the observation of stacking faults in Ge is much rarer. We have considered Ge films on Si (001), and we studied strain release mechanisms via the motion of extended defects. It has represented a perfect case to investigate the modeling of perfect dislocation glide and climb via classical molecular dynamics simulations. In this Chapter, we studied the glide of perfect misfit dislocation loops in all their three-dimensional extension and the glide and climb of straight dislocation lines. We started our analysis by considering the evolution of misfit dislocation loops. Our molecular dynamics simulations provided the atomic detail of the well-known mechanism of a 60° dislocation loop opening to relax the compressive epitaxial stress. The analysis of the evolution of the whole dislocation line showed the dynamics of both threading arms and misfit dislocation segments. Such simulations help in the comprehension of the real mechanics happening in an epitaxial Ge film in a full three-dimensional view. We then restricted our focus to a simplified -almost two-dimensional- case of a straight dislocation line in a narrow simulation cell. This approach allowed us to focus on an open question that remained open for many years: how ordered arrays of edge misfit dislocation lines are formed. The presence of vacancies has been often invoked to explain such experimental evidence, but only in a speculative form. Vacancies can play an active role in dislocation motion activating the climb motion of dislocation. The modeling of such a way dislocation move is not simple to achieve in the classical molecular dynamics framework. Nevertheless, we were able to set up a complex set of simulation tools to model such a complex mechanism. By studying the climb of 60° and 90° misfit dislocation lines we, first, provided a detailed description of the atomic details of such mechanisms, but we also understand

an important mechanism that can indeed explain the formation of ordered arrays of 90° misfit dislocation lines in Ge films grown at low temperature or high deposition rate when a thermal anneal follows the initial deposition. By considering our results, it resulted indeed that climb of misfit dislocation require a high number of vacancy, but such a large number of vacancy can be explained in low T / high deposition rate and therefore the higher abundance of 90° dislocations at the expenses of 60° ones can be explained. Notably, it also resulted that only a few vacancies, in the successive thermal treatment, can activate the lateral gliding of 90° dislocation by favoring the formation of dislocation kinks along the dislocation line. In conclusion, we highlighted the role played by vacancies in the lateral-ordering of dislocations in Ge/Si(001) also reproducing experimental findings. Our result can help to devise new growth strategies by considering close-to-equilibrium and far-from-equilibrium conditions to influence the dislocation lines distribution and therefore the strain uniformity.

Chapter 5

Perspectives: Metadynamics

In this Thesis, we have encountered atomic mechanisms spanning over different time scales. Some of them are not conveniently studied with conventional molecular dynamics. Such events, indeed, are characterized by too large activation barriers to be observed in reasonable time scales (and at reasonable temperatures) regardless of the available computational power.

Therefore, we have looked at the possibility of using alternative methods to observe rare events. In particular, we considered using metadynamics, which is a method introduced some 20 years ago,[163] and which quickly became popular among a broad community of computational researchers.

To learn the method from an expert in the field, I spent my six-months mandatory Ph.D. period abroad within the group of Prof. F. Pietrucci at the Sorbonne University in Paris. The idea was to learn one of the most used software for metadynamics simulations, PLUMED,[164] and to apply it to the study of extended defects dynamics. Unfortunately, after only one month, the COVID-19 pandemic exploded, and the original plan had to be reviewed. The collaboration with Professor Pietrucci during that period continued remotely with some obvious difficulties. Even if we obtained only partial results in the limited time the pandemic gave us, they clearly suggest that many mechanisms regarding defects in semiconductor crystals can be understood using metadynamics. We will present them in the following, after a brief description of the method.

5.1 Metadynamics simulations

In this section, we will present some key aspects of metadynamics and how it works in general. Metadynamics is a method that artificially changes a system's evolution to explore new configurations, allowing the estimation of free energy profiles.[163] It is achieved by changing the real potential energy landscape, adding a fictitious external potential.

Let us consider a simple case: a particle in a double-well potential. The particle cannot escape from a local minimum only by thermal fluctuations because the energy barrier is too high. See for example the Figure 5.1 (**a**).

In the general situation, a metadynamics simulation proceeds as follows. One or more collective variables $\vec{s}$ are defined to describe the system's configuration at any given time t_0. A series of Kernels are added to the potential energy discouraging the system from coming back and visiting the previous points (in the collective variables space). These Kernels are typically multi-dimensional Gaussian functions centered in $s = s_t$, i.e., the position in the collective variable space of the system at $t = t_0$.

At a given time the total bias $V_{\text{bias}}(\vec{s})$ is:

$$V_{\text{bias}}(\vec{s}) = V_{\text{bias}}^{\text{old}}(\vec{s}) + \tau\omega e^{-\frac{1}{2}\left|\frac{\vec{s}-\vec{s}_t}{\vec{\sigma}}\right|^2} \tag{5.1}$$

where $V_{\text{bias}}^{\text{old}}(\vec{s})$ is the bias at $t < t_0$, τ and ω are fixed parameters determined by the Gaussians' deposition rate and bias height, and $\vec{\sigma}$ is the Gaussians' width.

The forces acting on a particle i will be given by the sum of the forces acting on it plus the forces $\vec{F}_{\text{bias},i}$ added by the bias potential:

$$\vec{F}_i = -\frac{\partial V(\{\vec{r}\})}{\partial \vec{r}_i} \overbrace{-\frac{\partial V_{\text{bias}}(\vec{s})}{\partial \vec{s}}\bigg|_{\vec{s}_t} \frac{\partial \vec{s}(\{\vec{r}\})}{\partial \vec{r}_i}}^{\vec{F}_{\text{bias},i}} \tag{5.2}$$

where $\{\vec{r}\}$ are the positions in the real space, s is the actual position of the system in the collective variable space, and $\vec{r}_i$ is the position of the particle. The system is let free to evolve as in a conventional MD simulation where the added Gaussians have modified the potential landscape. Then the procedure is iterated, gradually preventing the system from visiting points where it have already been. The frequency at which the Gaussians are added, their height and their width can be fixed or not.[163,165,166]

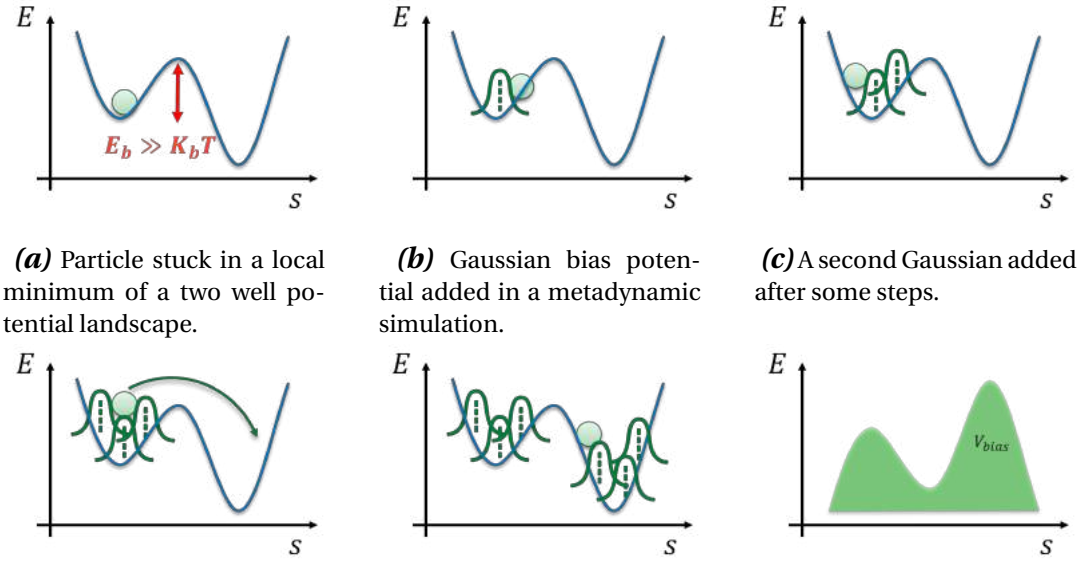

(a) Particle stuck in a local minimum of a two well potential landscape.

(b) Gaussian bias potential added in a metadynamic simulation.

(c) A second Gaussian added after some steps.

(d) Reduced barrier height.

(e) Filling of the second well.

(f) Converged bias potential, i.e., the inverse of the free energy.

Figure 5.1: Bias potential and estimation of energy barriers. Example of a metadynamics simulation for a single particle in a double well. The blue line is the Free Energy; the green sphere represents the particle position in the collective variable space; the green bells are the added Gaussians; V_{bias} is the total bias potential added.

As shown in Figure 5.1, the added Gaussians will gradually fill the potential well in which the system is stacked. If a good collective variable has been chosen, the system will be able to explore new regions of the configurational space as displayed schematically in Figure 5.1 (**d**). The accumulated bias potential can converge to free energy with opposite signs after long simulations. An indicator of convergence is that the system starts to diffuse freely, and the bias potential oscillates around a mean value.

5.2 Application: vacancy diffusion

As a first example, we start from a mechanism that has the advantage of being a rare event with an energy barrier that is high but not so high that it cannot be overcome using prolonged high-temperature annealing: the diffusion of vacancies in germanium. The system interested us for many aspects, presented in Chapter 4. In particular, we want to study how vacancies interact with misfit dislocations in strained germanium films grown by epitaxy on Si(001) substrates. In Section 4.2 we have shown the evolution of single vacancies, and we know that (at least at high temperature) vacancies are attracted by misfit dislocations

allowing their climb and ordering. We can hence test if the same behavior is found at low temperature via metadynamics simulations, gaining at the same time information on an interesting process, and do a first test of this approach applied to defects in the systems of our interest.

5.2.1 Collective variable: PIV

As a first step, we need to find a good collective variable to use. The most trivial solution that one can imagine is to use the actual position of a vacancy to make it move at a low temperature. But in reality, the definition of a continuous position of the lack of one atom as a function of the position of the real atoms is not easy at all. We decided to employ a collective variable related to the coordination concept: the so-called Permutation Invariant Vector (PIV). It is a vector made up of the entries in descending order of the contact matrix of all the system atoms. The contact matrix is a matrix that expresses the property of two particles of being neighbors or equivalently to be "in contact." It is done by defining a value between zero and one, which is a function of their distance: one means that they are in contact; zero means no contact at all. We can easily obtain the coordination of each atom by counting the number of entries of the contact matrix associated with a specific atom i that are above a threshold (close to one) that we define as the one needed to be neighbors. Alternatively, we can define an atomic coordination, which is the sum of the entries of the contact matrix for each atom*. To produce the PIV of a system configuration, we proceed as follows.

We define the contact using a switching function $S(d_{ij}) : \mathbb{R}^+ \rightarrow [0;1]$ that has the distance d_{ij} between two atoms i and j as input:

$$S(d_{ij}) = \frac{1-\left(\frac{d_{ij}-D_0}{R_0}\right)^n}{1-\left(\frac{d_{ij}-D_0}{R_0}\right)^m} \tag{5.3}$$

For $d_{ij} <= D_0$ the function is $S(d_{ij}) = 1$, for $d_{ij} > D_0$ the function $S(d_{ij})$ decays smoothly to zero depending on the parameters $R_0 \in \mathbb{R}^+$; n, $m \in \mathbb{N}$ (with $m > n$). For a system of N atoms the function S is computed for all the $1/2N(N-1)$ pairs of atoms†. The entries which are below a cut-off are ignored and replaced by zeros. The matrix entries are sorted

*in this way we can have a definition of the coordination that is continuos

†A subsystem of the atoms in a simulation can be considered to reduce the computational cost.

in descending order and made up the entries of a vector V which is the PIV. The zero entries can be ignored, reducing the size of the V vector, which can be very high. Alternatively is also possible to not sort the entries of the vector V, but in this case, the vector must also contain all the null entries. We consider two collective variables s, z that map the position of the actual configuration $\mathbb{X}_t$ into a two-dimensional space (s, z) of the configurations of the system. To do so, an initial configuration $\mathbb{A}$ and a target configuration $\mathbb{B}$ are needed. The Euclidean distance between the actual structure and the two references are computed:

$$d_{\mathbb{A}}^2 = \sum^{i} (V_i^{\mathbb{X}_t} - V_i^{\mathbb{A}}) \tag{5.4}$$

$$d_{\mathbb{B}}^2 = \sum^{i} (V_i^{\mathbb{X}_t} - V_i^{\mathbb{B}})^2 \tag{5.5}$$

The two collective variables are defined as follow. The first one, s, defines the position of the configuration along the path that connects the two references in the configurational space.

$$s(t) = \frac{1 \cdot e^{-\lambda d_{\mathbb{A}}} + 2 \cdot e^{-\lambda d_{\mathbb{B}}}}{e^{-\lambda d_{\mathbb{A}}} + e^{-\lambda d_{\mathbb{B}}}} \tag{5.6a}$$

The second one, z, measures the (perpendicular) distance of the actual configuration from the ideal path.

$$z(t) = -\frac{1}{\lambda} ln(e^{-\lambda d_{\mathbb{A}}} + e^{-\lambda d_{\mathbb{B}}}) \tag{5.6b}$$

where λ is a parameter which is use to fine tune the resolution of the configuration mapping. Its easy to demonstrate that the first variable $s \in [1;2]$, where 1 is the initial configuration $\mathbb{A}$, and 2 corresponds to the target configuration $\mathbb{B}$. We provide an example of a trivial transition path for a system made up by five particles in Figure 5.2.

These two collective variables have been successfully applied to perform metadynamics simulations on phase transitions in ice.[167]

5.2.2 Vacancy diffusion enhancement

Our first test was to prove the effectiveness of the collective variables in accelerating the motion of vacancies at low temperature (600 K). Initially, we considered only an unstrained germanium cell, and we inserted two vacancies as shown in Figure 5.3 (**a**).

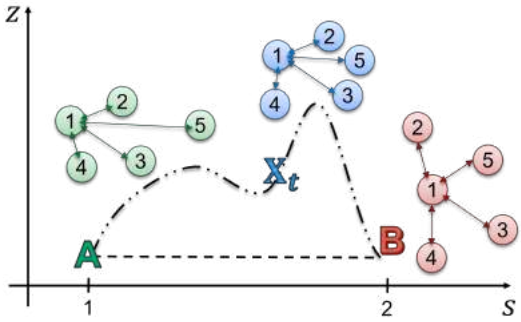

Figure 5.2: Example of a transition path for a simple system made up by five atoms. In green the initial configuration; in red the target reference, and in blue the actual configuration. The dashed line show the ideal path between configurations $\mathbb{A}$ and $\mathbb{B}$; the dot-dashed line show a more complex path that represents a lower energy path.

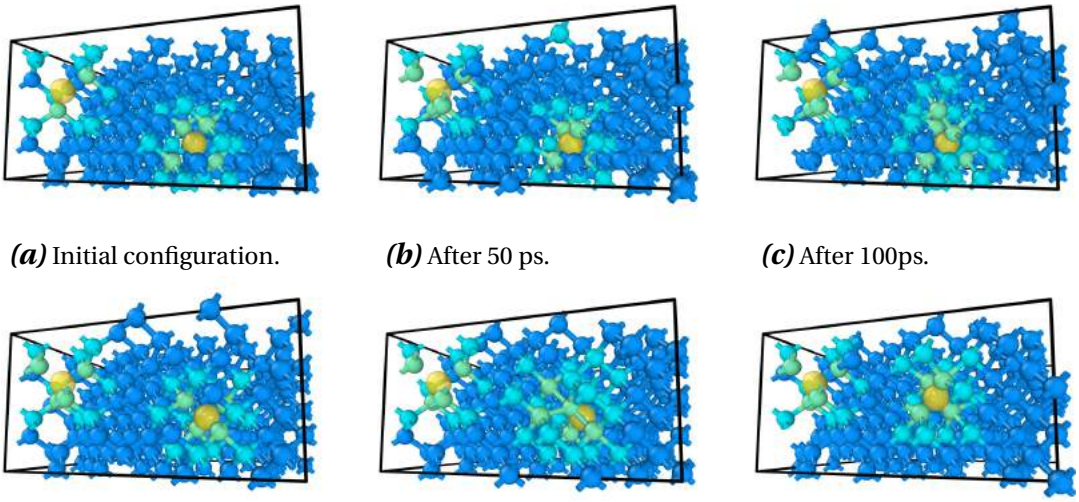

(a) Initial configuration. ***(b)*** After 50 ps. ***(c)*** After 100ps.

(d) After 150ps. ***(e)*** After 350ps. ***(f)*** After 400ps.

Figure 5.3: Metadynamics simulation of the diffusion of two vacancies. The yellow spheres are the vacancies, identified by the WS modifier in OVITO. The blue spheres are Ge atoms, the pale blue atoms are Ge atoms which are not identified as in the perfect diamond structure. Colored sticks represent bond between atoms and are colored accordingly.

The simulation was performed in the canonical ensemble (NVT) using the Tersoff potential. The molecular dynamics was performed using LAMMPS integrated with PLUMED. The simulation cell is a box of Ge atoms with edges $4 \cdot a \times 4 \cdot a \times 2 \cdot a$ oriented along the conventional [100], [010], and [001] directions. The thermostat temperature is set to 300K. We performed a metadynamics simulation by adding Gaussian bias potential in the (s, z) space determined by the two collective variables s and z. The initial reference configuration is shown in Figure 5.3 (**a**), the target configuration has a bi-vacancy on the left top corner of the simulation cell. The switching function used to build the PIV is plotted in blue

in Figure 5.4. It has been chosen considering the radial distribution of the Ge atoms. Our idea is that a switching function that is zero beyond the first neighbors should distinguish in a good manner configuration where particles change their first neighbors, particularly if we turn off the sorting of the PIV. If the sorting is left on, a smoother switching function should be used, for example, the one plotted in orange in Figure 5.4.

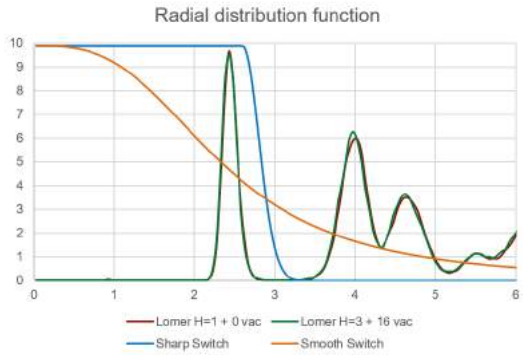

Figure 5.4: Example of two switching functions to build the PIVs. The blue line is a sharp switch which is zero beyond the first neighbors ($m = 2n = 16$; $D_0 = 2.7$; $R_0 = 0.3$). The orange line is a smooth switching function ($m = 2n = 4$; $D_0 = 0$; $R_0 = 2.7$). The radial distribution functions of two configurations of Ge atoms in a dislocated film are plotted to identify the distribution of neighbors in Ge. The units on the vertical scale have been arbitrarily set to be equal, with a maximum equal to ten for a better illustration.

The snapshots of the results of the metadynamics simulations are displayed in sequence in Figure 5.3. A migration of the vacancy on the right is observed in a few tenths of ps (see Figure 5.3 (**d**)). Note the motion of the atom above the vacancy in Figure 5.3 (**c**) that takes the place of the vacancy in Figure 5.3 (**d**). A similar trend is observed after other 200 ps in Figure 5.3 (**e**) and (**f**). Two jumps of one vacancy are observed in less than 500 ps. The result is a clear enhance on the vacancy motion, consider indeed that we are at a temperature that is more than 1000K below the temperature used in our simulation of vacancy motion in Section 4.2.

5.2.3 Vacancy diffusion and interaction with climb

The exciting results obtained applying metadynamics to the process of diffusion led us to try an additional test. As a first tentative simulation, we tried to simulate the migration of sixteen vacancies toward a 90° Lomer dislocation in an epitaxial film. The simulation cell is the one used in Section 4.2 to study the climb of a misfit Lomer dislocation. We performed the metadynamics simulation at a thermostat temperature of 300K. This time

the best results were obtained using a smooth switching function. The preliminary results are shown in Figure 5.5.

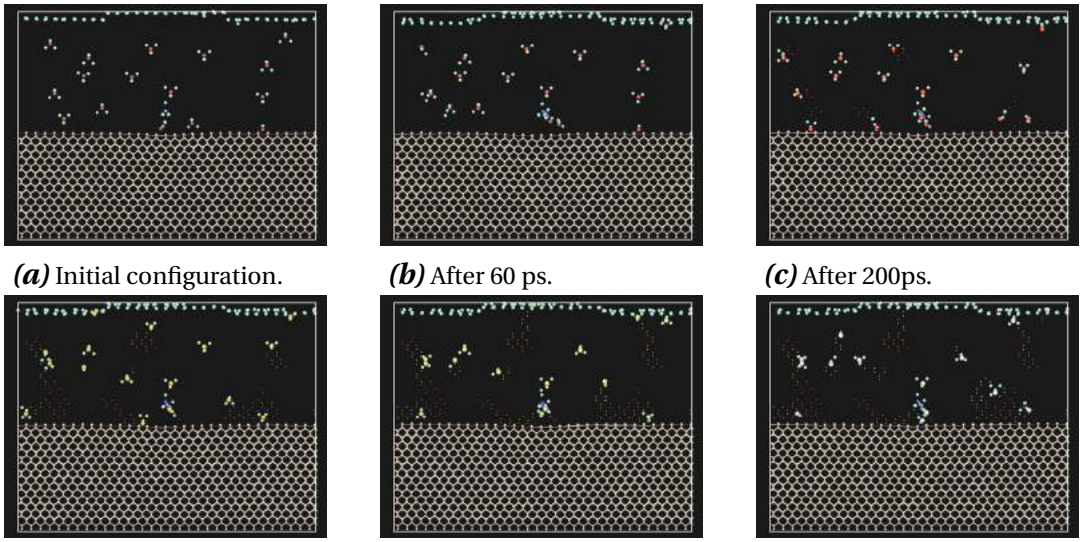

(a) Initial configuration. ***(b)*** After 60 ps. ***(c)*** After 200ps.

(d) After 350ps. ***(e)*** After 450ps. ***(f)*** After 600ps.

Figure 5.5: Metadynamics simulation of the diffusion of sixteen vacancies near a 90° Lomer dislocation in a Ge film on Si (001). The big spheres are the vacancies, identified by the WS modifier in OVITO and colored with time from red to pale yellow. The silicon substrate is shown by pink spheres and sticks, the pale blue spheres are Ge atoms near defects, Ge atoms which are identified as in the perfect diamond structure are not displayed. Colored small point represent the position of the vacancies in the preceding steps.

Our idea was to simulate the Lomer dislocation climb via the interaction with the sixteen vacancies in the cell. The initial configuration used to construct the collective variable is, therefore, the one in Figure 5.5 (**a**). The target one now is a configuration with no vacancies and the Lomer dislocation two glide planes below where it started. The two configurations have the same number of atoms. In theory, the application of a bias in the (s,z) space may make the vacancy move toward the dislocation core to transform the initial configuration into the one where the Lomer has climbed. Note that the radial distribution functions in Figure 5.4 are obtained from these two configurations. The radial distribution function of the initial configuration is the green line "Lomer H=3 + 16 vac"; the distribution of the target one is the brown line "Lomer H=1 + 0 vac."

In the presented simulation, vacancies move randomly initially, but some are attracted by the dislocation core and absorbed by it. The first vacancy arrives at the dislocation core in less than 60 ps, as the second one does (see Figure 5.5 (**b**) and (**c**)). A third one arrives after 450 ps (see Figure 5.5 (**e**)). The metadynamics provides vacancy motion at

300K, which is a good result but unfortunately, only three vacancies effectively reach the dislocation core. Note that the presented simulation is much more shorted in terms of simulated time than those presented in Chapter 4. Indeed, using the same amount of computational power, a simulation where we are performing metadynamics takes much more time than a standard MD simulation.

To conclude, metadynamics can be used to enhance and study vacancy diffusion and climb of misfit dislocation at low temperatures. Still, many technical and theoretical aspects require further investigation and understanding. In particular, we believe that the present investigation would strongly benefit from a refinement of the switching function. As of today, we see the use of metadynamics as an exciting perspective to speed up simulations of the evolution of defects, and we hope that further collaboration with the group in Paris will soon lead to new interesting results.

Conclusions

In this Thesis, we have studied extended defects in epitaxial film grown on silicon substrates in the framework of classical molecular dynamics. We considered two prototypical cases of semiconductor epitaxy: the cubic silicon carbide and the germanium. Their epitaxy on silicon represents the ideal test case for extended defect modeling via classical molecular dynamics simulations. Classical molecular dynamics simulation resulted in being an appropriate instrument for modeling the evolution of extended defects in both cases as we found them to be reflected by experimental observations. The obtained results gave us essential information that can practically be used to reduce the appearance of those defects in the epitaxial systems. Most of the work presented in this Thesis is represented by the study on extended defects and, in particular stacking faults, in the cubic silicon carbide. Our analysis on the molecular dynamics potential functions that can be used to model stacking fault evolution in 3C-SiC provided the technical details about the reliability of the different potentials on the description of defects. They were used through the whole part of the Thesis that focused on SiC. Then we addressed the lack of theoretical understanding of the mechanisms regarding stacking fault aggregation into multiplane stacking faults characterized of being composed specially by two or three defected planes. Ad hoc simulations allowed us to understand a crucial point in the composition of these structures: only specific configurations of stacking faults are possible. Stable configurations are determined by the partial dislocations that bound each stacking fault with the perfect crystal. Some prescriptions on the choice of potential partial dislocations that generated the stacking fault exist. Their Burgers vector should be different for each one of the stacking fault planes. An important implication arises from that: multiplane stacking faults (that are the most abundant ones) are generated by defects that can evolve under very different strain conditions. The latter point determined how we proceeded in the investigation of stacking fault evolution thereon: we needed to reconsider carefully the

growth conditions experienced by the 3C-SiC film. We indeed found that a change in the strain sign is achieved after the first stages of the growth, after the so-called carbonization process. The former high tensile strain becomes a slight compressive strain thanks to the formation of an array of Lomer dislocation at the SiC/Si interface. We, therefore, draw a novel picture of stacking fault evolution and formation: stacking faults are formed in the initial phase, which is tensile, so the partial dislocations present are well known. We identify them in being either 90° partial dislocations leading stacking fault extension from the surface to the interface, or either 30° partial ones leading stacking fault expansion from the interface toward the free surface. We hence analyzed an unexplained experimental observation that leads to stacking fault annihilation when they migrate from the interface toward the free surface. We identified the dislocations leading the stacking fault expansion in being 30° partial ones. We thereafter identified the annihilation mechanism in being the formation of a Lomer-Cottrell lock at the junction of two crossing stacking faults. We, in the end, demonstrated, with molecular dynamics simulations, that the change of the strain sign also determines an enhancement in the probability of having double or even more frequently triple stacking faults with a common boundary of partial dislocations. We were able to explain the observed and not completely understood shape of stacking faults in 3C-SiC. We found that the Δ and V shape of stacking faults are determined by the evolution of individual stacking faults in the initial tensile strain. They successively transform into multiple stacking faults when a compressive strain arises in the film. In the end, with a synergic approach of molecular dynamics and density functional theory calculations, we identified in the complex of bounding partial dislocations the defect that can be charged with being the source of leakage currents in 3C-SiC devices (the latter calculations were performed by other research group members).

Different aspects of dislocation modeling with molecular dynamics simulation were addressed in the study of the second material considered. Germanium is indeed, for many aspects, on the completely opposite side of the defect behavior spectrum with respect to SiC. First, it experiences a compressive strain, does not present polytypism, and is completely miscible with Si (whereas SiC is stochiometric). The compressive strain implies that the observation of stacking faults in Ge is much rarer than in SiC, and most of the

defects in the material are perfect 60° or 90° dislocations. We consider Ge films on Si (001), and we studied strain release mechanisms via the motion of extended defects. It has represented a perfect case to investigate the modeling of perfect dislocation glide and climb via classical molecular dynamics simulations. The glide of perfect dislocations was studied in detail both for misfit dislocation loops in all their three-dimensional extension and for straight dislocation lines. It provided exactly the expected results in terms of dislocation evolution and strain release. The climb was studied in the simplified case of a straight dislocation line. Many issues regarding the timescale of this process have been addressed, and we successfully achieved the result of modeling misfit dislocation climb via a molecular dynamics computational approach. This latter result led us to the comprehension of the formation of ordered arrays of edge dislocation in germanium films grown at low temperature or high deposition rates.

In conclusion, we used molecular dynamics to model extended defect evolution in epitaxial systems focusing on open problems about defect evolution in SiGe and cubic SiC. Inside collaborations that involved experimental measures, ab-initio calculation, and the use of the elastic theory, we showed that our results had an essential role in providing an interpretative picture of extended defect evolution. The ability to set up virtual experiments to understand the evolution of dislocations and stacking faults provides an incredibly powerful tool to have important insight on the atomic scale processes governing their evolution. At this, the development of new powerful modeling instruments in the framework of molecular dynamics, such as new machine learning potentials or innovating simulation techniques, is a unique perspective.

Publications

Publications related to the thesis work

- Sarikov, A., Marzegalli, A., Barbisan, L., Montalenti, F., & Miglio, L. (2019). Structure and Stability of Partial Dislocation Complexes in 3C-SiC by Molecular Dynamics Simulations. MATERIALS, 12(18 - Sept 2019) [10.3390/ma12183027].

- Sarikov, A., Marzegalli, A., Barbisan, L., Scalise, E., Montalenti, F., & Miglio, L. (2019). Molecular dynamics simulations of extended defects and their evolution in 3C-SiC by different potentials. MODELLING AND SIMULATION IN MATERIALS SCIENCE AND ENGINEERING, 28(1) [10.1088/1361-651X/ab50c7].

- Scalise, E., Barbisan, L., Sarikov, A., Montalenti, F., Miglio, L., & Marzegalli, A. (2020). The origin and nature of killer defects in 3C-SiC for power electronic applications by a multiscale atomistic approach. JOURNAL OF MATERIALS CHEMISTRY. C, 8(25), 8380-8392 [10.1039/d0tc00909a].

- Barbisan, L., Sarikov, A., Marzegalli, A., Montalenti, F., & Miglio, L. (2021). Nature and Shape of Stacking Faults in 3C-SiC by Molecular Dynamics Simulations. PHYSICA STATUS SOLIDI B-BASIC RESEARCH [10.1002/pssb.202000598].

- Sarikov, A., Marzegalli, A., Barbisan, L., Zimbone, M., Bongiorno, C., Mauceri, M., et al. (2021). Mechanism of stacking fault annihilation in 3C-SiC epitaxially grown on Si(001) by molecular dynamics simulations. CRYSTENGCOMM, 23(7), 1566-1571 [10.1039/d0ce01613f].

Other publications

- Scalise, E., Sarikov, A., Barbisan, L., Marzegalli, A., Migas, D., Montalenti, F., et al. (2021). Thermodynamic driving force in the formation of hexagonal-diamond Si

and Ge nanowires. APPLIED SURFACE SCIENCE, 545 (15 April 2021).

Alphabetical Index

Bibliography

[1] G. E. Moore. “Cramming more components onto integrated circuits, Reprinted from Electronics, volume 38, number 8, April 19, 1965, pp.114 ff.” In: *IEEE Solid-State Circuits Society Newsletter* 11.3 (Sept. 2006), pp. 33–35. ISSN: 1098-4232. DOI: 10.1109/N-SSC.2006.4785860.

[2] J.P. Hirth and J. Lothe. *Theory of Dislocations*. Krieger Publishing Company, 1982.

[3] R.J. Asaro and W.A. Tiller. “Interface morphology development during stress corrosion cracking: Part I. Via surface diffusion”. English. In: *Metallurgical Transactions* 3.7 (1972), pp. 1789–1796.

[4] “The stress driven instability in elastic crystals: Mathematical models and physical manifestations”. English. In: *Journal of Nonlinear Science* 3.1 (1993), pp. 35–83.

[5] D.J. Srolovitz. “On the stability of surfaces of stressed solids”. In: *Acta Metallurgica* 37.2 (1989), pp. 621–625.

[6] Yaoyu Pang and Rui Huang. “Nonlinear effect of stress and wetting on surface evolution of epitaxial thin films”. In: *Physical Review B* 74 (7 Aug. 2006), p. 075413.

[7] Jean-Noël Aqua and Xianbin Xu. “Directed self-organization of quantum dots”. In: *Physical Review E* 90.3 (2014), 030402–030406(R).

[8] J.W. Matthews and A.E. Blakeslee. “Defects in epitaxial multilayers: I. Misfit dislocations”. In: *Journal of Crystal Growth* 27 (1974), pp. 118–125.

[9] J.W. Matthews and A.E. Blakeslee. “Defects in epitaxial multilayers: II. Dislocation pile-ups, threading dislocations, slip lines and cracks”. In: *Journal of Crystal Growth* 29.3 (1975), pp. 273–280.

[10] J. W. Matthews and A. E. Blakeslee. “Defects in epitaxial multilaters: III. Preparation of Almost Perfect Multilayers”. In: *Journal of Crystal Growth* 32 (1976), pp. 265–273.

[11] R. People and J. C. Bean. “Calculation of critical layer thickness versus lattice mismatch for GexSi1-x/Si strained-layer heterostructures”. In: *Applied Physics Letters* 47.3 (1985), pp. 322–324.

[12] J. W. P. Hsu et al. “Surface morphology of related GexSi1-x films”. In: *Applied Physics Letters* 61.11 (1992), pp. 1293–1295.

[13] Akira Sakai et al. “Pure-edge dislocation network for strain-relaxed SiGe/Si(001) systems”. In: *Applied Physics Letters* 86.22 (2005), p. 221916. DOI: 10.1063/1.1943493. eprint: https://doi.org/10.1063/1.1943493. URL: https://doi.org/10.1063/1.1943493.

[14] J. Weertman and J.R. Weertman. *Elementary dislocation theory*. Macmillan series in materials science. Macmillan, 1964.

[15] F.C. Frank. “LXXXIII. Crystal dislocations.—Elementary concepts and definitions”. In: *The London, Edinburgh, and Dublin Philosophical Magazine and Journal of Science* 42.331 (1951), pp. 809–819.

[16] W. Cai et al. “A non-singular continuum theory of dislocations”. In: *Journal of Mechanics Physics of Solids* 54 (Mar. 2006), pp. 561–587.

[17] A K Head. “Edge Dislocation in Inhomogeneous Media”. In: *Proceedings of the Physical Society. Section B* 66 (Dec. 2002), p. 793.

[18] J. Hornstra. “Dislocations in the diamond lattice”. In: *Journal of Physics and Chemistry of Solids* 5.1 (1958), pp. 129 –141.

[19] F. C. Frank and J. H. van der Merwe. “One-dimensional dislocations - III. Influence of the second harmonic term in the potential representation, on the properties of the model”. In: *Proceedings of the Royal Society of London. Series A. Mathematical and Physical Sciences* 200 (1060 Dec. 1949), pp. 125–134. ISSN: 0080-4630. DOI: 10.1098/rspa.1949.0163. URL: https://royalsocietypublishing.org/doi/10.1098/rspa.1949.0163.

[20] Vasily Bulatov and Wei Cai. *Computer Simulations of Dislocations*. Oxford University Press, Nov. 2006. ISBN: 9780198526148. DOI: 10.1093/oso/9780198526148.001.0001.

[21] Anna Marzegalli. “Modeling of dislocations in heteroepitaxial SiGe films and nanometric islands”. PhD thesis. Università degli studi di Milano-Bicocca, 2005.

[22] M. Peach and J. S. Koehler. “The Forces Exerted on Dislocations and the Stress Fields Produced by Them”. In: *Phys. Rev.* 80 (3 Nov. 1950), pp. 436–439.

[23] D. Hull and D.J. Bacon. *Introduction to Dislocations*. Elsevier Science, 2001.

[24] J. W. Matthews. “Defects associated with the accommodation of misfit between crystals”. In: *Journal of Vacuum Science and Technology* 12.1 (1975), pp. 126–133.

[25] Anna Marzegalli et al. “Onset of plastic relaxation in the growth of Ge on Si(001) at low temperatures: Atomic-scale microscopy and dislocation modeling”. In: *Physical Review B* 88 (Oct. 2013), p. 165418. DOI: 10.1103/PhysRevB.88.165418.

[26] O Trushin et al. “Minimum energy path for the nucleation of misfit dislocations in Ge/Si(0 0 1) heteroepitaxy”. In: *Modelling and Simulation in Materials Science and Engineering* 24.3 (Feb. 2016), p. 035007. DOI: 10.1088/0965-0393/24/3/035007. URL: https://doi.org/10.1088/0965-0393/24/3/035007.

[27] Yu B Bolkhovityanov et al. “Mechanisms of edge-dislocation formation in strained films of zinc blende and diamond cubic semiconductors epitaxially grown on (001)-oriented substrates”. In: *J. Appl. Phys* 109 (2011), p. 123519. DOI: 10.1063/1.3597903. URL: https://doi.org/10.1063/1.3597903.

[28] E. P. Kvam, D. M. Maher, and C. J. Humphreys. “Variation of dislocation morphology with strain in Ge_xSi_{1-x} epilayers on (100)Si”. In: *Journal of Materials Research* 5.9 (1990), 1900–1907. DOI: 10.1557/JMR.1990.1900.

[29] P. Pirouz and J.W. Yang. “Polytypic transformations in SiC: the role of TEM”. In: *Ultramicroscopy* 51 (1-4 June 1993), pp. 189–214. ISSN: 03043991. DOI: 10.1016/0304-3991(93)90146-O. URL: https://linkinghub.elsevier.com/retrieve/pii/0304399193901460.

[30] Lewis S. RAMSDELL. “STUDIES ON SILICON CARBIDE”. In: *American Mineralogist* 32 (64 1947).

[31] P. Pirouz, C. M. Chorey, and J. A. Powell. “Antiphase boundaries in epitaxially grown β-SiC”. In: *Applied Physics Letters* 50 (4 Jan. 1987), pp. 221–223. ISSN: 0003-6951. DOI: 10.1063/1.97667.

[32] P. Pirouz et al. “Lattice Defects in β-Sic Grown Epitaxially On Silicon Substrates”. In: *MRS Proceedings* 91 (Feb. 1987). ISSN: 0272-9172. DOI: 10.1557/PROC-91-399.

[33] G. L. Harris. *Properties of Silicon Carbide*. INSPEC, 1995.

[34] Massimo Pappalardo et al. *Micromachined Ultrasonic Transducers*. Springer US, 2008. DOI: 10.1007/978-0-387-76540-2_22.

[35] Charles E. Wooddell. “Method of Comparing the Hardness of Electric Furnace Products and Natural Abrasives”. In: *Transactions of The Electrochemical Society* 68 (1 1935). ISSN: 00964743. DOI: 10.1149/1.3493860.

[36] Emilio Scalise et al. “Temperature-Dependent Stability of Polytypes and Stacking Faults in <math display="inline" overflow="scroll"> <mrow> <mi>Si</mi> <mi mathvariant="normal">C</mi> </mrow> </math> : Reconciling Theory and Experiments”. In: *Physical Review Applied* 12 (2 Aug. 2019). ISSN: 2331-7019. DOI: 10.1103/PhysRevApplied.12.021002.

[37] Daan Frenkel and Berend Smit. *Understanding molecular simulation : from algorithms to applications. 2nd ed.* Vol. 50. Jan. 1996.

[38] Steve Plimpton. “Fast Parallel Algorithms for Short-Range Molecular Dynamics”. In: *Journal of Computational Physics* 117.1 (1995), pp. 1 –19. URL: http://lammps.sandia.gov.

[39] Chaofeng Hou et al. “Petascale molecular dynamics simulation of crystalline silicon on Tianhe-1A”. In: *The International Journal of High Performance Computing Applications* 27.3 (2013), pp. 307–317.

[40] Alexander Stukowski. “Visualization and analysis of atomistic simulation data with OVITO–the Open Visualization Tool”. In: *Modelling and Simulation in Materials Science and Engineering* 18.1 (2010), p. 015012. URL: http://ovito.sourceforge.net/.

[41] A Stukowski and A Arsenlis. “On the elastic–plastic decomposition of crystal deformation at the atomic scale”. In: *Modelling and Simulation in Materials Science and Engineering* 20 (3 Apr. 2012), p. 035012. ISSN: 0965-0393. DOI: 10.1088/0965-0393/20/3/035012. URL: https://iopscience.iop.org/article/10.1088/0965-0393/20/3/035012.

[42] Alexander Stukowski and Karsten Albe. "Extracting dislocations and non-dislocation crystal defects from atomistic simulation data". In: *Modelling and Simulation in Materials Science and Engineering* 18.8 (2010), p. 085001.

[43] Alexander Stukowski, Vasily V Bulatov, and Athanasios Arsenlis. "Automated identification and indexing of dislocations in crystal interfaces". In: *Modelling and Simulation in Materials Science and Engineering* 20.8 (2012), p. 085007.

[44] Michael P. Allen and Dominic J. Tildesley. *Computer Simulation of Liquids*. Vol. 1. Oxford University Press, Nov. 2017. ISBN: 9780198803195. DOI: 10.1093/oso/9780198803195.001.0001. URL: https://oxford.universitypressscholarship.com/view/10.1093/oso/9780198803195.001.0001/oso-9780198803195.

[45] Frank H. Stillinger and Thomas A. Weber. "Computer simulation of local order in condensed phases of silicon". In: *Phys. Rev. B* 31 (8 Apr. 1985), pp. 5262–5271.

[46] J. Tersoff. "New empirical approach for the structure and energy of covalent systems". In: *Phys. Rev. B* 37 (12 Apr. 1988), pp. 6991–7000.

[47] J. Tersoff. "Modeling solid-state chemistry: Interatomic potentials for multicomponent systems". In: *Phys. Rev. B* 39 (8 Mar. 1989), pp. 5566–5568.

[48] Paul Erhart and Karsten Albe. "Analytical potential for atomistic simulations of silicon, carbon, and silicon carbide". In: *Physical Review B* 71 (3 Jan. 2005), p. 035211. ISSN: 1098-0121. DOI: 10.1103/PhysRevB.71.035211. URL: https://link.aps.org/doi/10.1103/PhysRevB.71.035211.

[49] Priya Vashishta et al. "Interaction potential for silicon carbide: A molecular dynamics study of elastic constants and vibrational density of states for crystalline and amorphous silicon carbide". In: *Journal of Applied Physics* 101 (10 May 2007), p. 103515. ISSN: 0021-8979. DOI: 10.1063/1.2724570. URL: http://aip.scitation.org/doi/10.1063/1.2724570.

[50] Karsten Albe et al. "Modeling of compound semiconductors: Analytical bond-order potential for Ga, As, and GaAs". In: *Physical Review B* 66 (3 July 2002), p. 035205. ISSN: 0163-1829. DOI: 10.1103/PhysRevB.66.035205. URL: https://link.aps.org/doi/10.1103/PhysRevB.66.035205.

[51] J Nord et al. “Modelling of compound semiconductors: analytical bond-order potential for gallium, nitrogen and gallium nitride”. In: *Journal of Physics: Condensed Matter* 15 (32 Aug. 2003), pp. 5649–5662. ISSN: 0953-8984. DOI: 10.1088/0953-8984/15/32/324. URL: https://iopscience.iop.org/article/10.1088/0953-8984/15/32/324.

[52] G. C. Abell. “Empirical chemical pseudopotential theory of molecular and metallic bonding”. In: *Physical Review B* 31 (10 May 1985). ISSN: 0163-1829. DOI: 10.1103/PhysRevB.31.6184.

[53] Donald W. Brenner. “Relationship between the embedded-atom method and Tersoff potentials”. In: *Physical Review Letters* 63 (9 Aug. 1989), pp. 1022–1022. ISSN: 0031-9007. DOI: 10.1103/PhysRevLett.63.1022. URL: https://link.aps.org/doi/10.1103/PhysRevLett.63.1022.

[54] M. C. Payne et al. “Iterative minimization techniques for ab initio total-energy calculations: molecular dynamics and conjugate gradients”. In: *Reviews of Modern Physics* 64 (4 Oct. 1992). ISSN: 0034-6861. DOI: 10.1103/RevModPhys.64.1045.

[55] J. Tersoff. “New empirical approach for the structure and energy of covalent systems”. In: *Physical Review B* 37 (12 Apr. 1988). ISSN: 0163-1829. DOI: 10.1103/PhysRevB.37.6991.

[56] João F. Justo et al. “Interatomic potential for silicon defects and disordered phases”. In: *Physical Review B* 58 (5 Aug. 1998). ISSN: 0163-1829. DOI: 10.1103/PhysRevB.58.2539.

[57] *Pattern Recognition & Machine Learning*. Elsevier, 1992. ISBN: 9780120588305. DOI: 10.1016/C2009-0-22409-3. URL: https://linkinghub.elsevier.com/retrieve/pii/C20090224093.

[58] Albert P. Bartok et al. “Machine Learning a General-Purpose Interatomic Potential for Silicon”. In: *Physical Review X* 8 (4 Dec. 2018). ISSN: 2160-3308. DOI: 10.1103/PhysRevX.8.041048.

[59] Albert Bartok-Partay. *The Gaussian Approximation Potential*. Springer Berlin Heidelberg, 2010. ISBN: 978-3-642-14066-2. DOI: 10.1007/978-3-642-14067-9.

[60] A. Fissel, B. Schröter, and W. Richter. “Low-temperature growth of SiC thin films on Si and 6H–SiC by solid-source molecular beam epitaxy”. In: *Applied Physics Letters* 66 (23 June 1995). ISSN: 0003-6951. DOI: 10.1063/1.113716.

[61] W. Kleber. “Verma, Ajit Ram and P. KrishnaPolymorphism and polytypism in crystals. John Wiley and Sons, Inc. New York-London-Sydney 1966. XIX+3415”. In: *Kristall und Technik* 1 (4 1966). ISSN: 00234753. DOI: 10.1002/crat.19660010415.

[62] G. R. Fisher and P. Barnes. “Towards a unified view of polytypism in silicon carbide”. In: *Philosophical Magazine B* 61 (2 Feb. 1990). ISSN: 1364-2812. DOI: 10.1080/13642819008205522.

[63] H. Okumura et al. “Growth and characterization of cubic GaN”. In: *Journal of Crystal Growth* 178 (1-2 June 1997). ISSN: 00220248. DOI: 10.1016/S0022-0248(97)00084-5.

[64] P. B. Mirkarimi et al. “Growth of cubic BN films on β-SiC by ion-assisted pulsed laser deposition”. In: *Applied Physics Letters* 66 (21 May 1995). ISSN: 0003-6951. DOI: 10.1063/1.113484.

[65] T. Ohno et al. “Direct observation of dislocations propagated from 4H–SiC substrate to epitaxial layer by X-ray topography”. In: *Journal of Crystal Growth* 260 (1-2 Jan. 2004). ISSN: 00220248. DOI: 10.1016/j.jcrysgro.2003.08.065.

[66] Michael E. Levinshtein, Sergey L. Rumyantsev, and Michael S. Shur. *Properties of Advanced Semiconductor Materials: GaN, AIN, InN, BN, SiC, SiGe*. Wiley, 2001.

[67] Yuuki Ishida et al. “Investigation of the Relationship between Defects and Electrical Properties of 3C-SiC Epilayers”. In: *Materials Science Forum* 389-393 (Apr. 2002). ISSN: 1662-9752. DOI: 10.4028/www.scientific.net/MSF.389-393.459.

[68] H. Nagasawa et al. “Hetero- and homo-epitaxial growth of 3C-SiC for MOS-FETs”. In: *Microelectronic Engineering* 83 (1 Jan. 2006). ISSN: 01679317. DOI: 10.1016/j.mee.2005.10.046.

[69] Hiroyuki Nagasawa et al. “High Quality 3C-SiC Substrate for MOSFET Fabrication”. In: *Materials Science Forum* 711 (Jan. 2012). ISSN: 1662-9752. DOI: 10.4028/www.scientific.net/MSF.711.91.

[70] Jens Eriksson et al. “Toward an ideal Schottky barrier on 3C-SiC”. In: *Applied Physics Letters* 95 (8 Aug. 2009). ISSN: 0003-6951. DOI: 10.1063/1.3211965.

[71] Takamitsu Kawahara et al. “Correlation between Leakage Current and Stacking Fault Density of p-n Diodes Fabricated on 3C-SiC”. In: *Materials Science Forum* 645-648 (Apr. 2010). ISSN: 1662-9752. DOI: 10.4028/www.scientific.net/MSF.645-648.339.

[72] Michael A. Capano et al. “Structural Defects and Critical Electric Field in 3C-SiC”. In: *Materials Science Forum* 527-529 (Oct. 2006). ISSN: 1662-9752. DOI: 10.4028/www.scientific.net/MSF.527-529.431.

[73] Tsunenobu Kimoto and James A. Cooper. *Fundamentals of Silicon Carbide Technology*. John Wiley & Sons Singapore Pte. Ltd, Sept. 2014. ISBN: 9781118313534. DOI: 10.1002/9781118313534. URL: http://doi.wiley.com/10.1002/9781118313534.

[74] Fuyuki Shimojo et al. “Molecular Dynamics Simulation of Structural Transformation in Silicon Carbide under Pressure”. In: *Physical Review Letters* 84 (15 Apr. 2000). ISSN: 0031-9007. DOI: 10.1103/PhysRevLett.84.3338.

[75] Wanghui Li, Xiaohu Yao, and Xiaoqing Zhang. “Planar impacts on nanocrystalline SiC: a comparison of different potentials”. In: *Journal of Materials Science* 53 (9 May 2018). ISSN: 0022-2461. DOI: 10.1007/s10853-018-1985-1.

[76] Wanghui Li et al. “Shock induced damage and fracture in SiC at elevated temperature and high strain rate”. In: *Acta Materialia* 167 (Apr. 2019). ISSN: 13596454. DOI: 10.1016/j.actamat.2018.12.035.

[77] Saeed Zare Chavoshi and Xichun Luo. “Molecular dynamics simulation study of deformation mechanisms in 3C–SiC during nanometric cutting at elevated temperatures”. In: *Materials Science and Engineering: A* 654 (Jan. 2016). ISSN: 09215093. DOI: 10.1016/j.msea.2015.11.100.

[78] Saurav Goel et al. “Anisotropy of single-crystal 3C–SiC during nanometric cutting”. In: *Modelling and Simulation in Materials Science and Engineering* 21 (6 Sept. 2013). ISSN: 0965-0393. DOI: 10.1088/0965-0393/21/6/065004.

[79] Andrey Sarikov et al. “Structure and Stability of Partial Dislocation Complexes in 3C-SiC by Molecular Dynamics Simulations”. In: *Materials* 12 (18 Sept. 2019). ISSN: 1996-1944. DOI: 10.3390/ma12183027.

[80] Andrey Sarikov et al. “Mechanism of stacking fault annihilation in 3C-SiC epitaxially grown on Si(001) by molecular dynamics simulations”. In: *CrystEngComm* 23 (7 2021), pp. 1566–1571. ISSN: 1466-8033. DOI: 10.1039/D0CE01613F. URL: http://xlink.rsc.org/?DOI=D0CE01613F.

[81] Emilio Scalise et al. “The origin and nature of killer defects in 3C-SiC for power electronic applications by a multiscale atomistic approach”. In: *Journal of Materials Chemistry C* 8 (25 2020), pp. 8380–8392. ISSN: 20507526. DOI: 10.1039/d0tc00909a.

[82] Andrey Sarikov et al. “Molecular dynamics simulations of extended defects and their evolution in 3C–SiC by different potentials”. In: *Modelling and Simulation in Materials Science and Engineering* 28 (1 Jan. 2020), p. 015002. ISSN: 0965-0393. DOI: 10.1088/1361-651X/ab50c7. URL: https://iopscience.iop.org/article/10.1088/1361-651X/ab50c7.

[83] WanJun Yan et al. “Melting kinetics of bulk SiC using molecular dynamics simulation”. In: *Science China Physics, Mechanics and Astronomy* 56 (9 Sept. 2013). ISSN: 1674-7348. DOI: 10.1007/s11433-013-5184-4.

[84] B Grazman. “Handbook of Chemistry and Physics: A Ready-Reference Book of Chemical and Physical Data”. In: *TrAC Trends in Analytical Chemistry* 10 (2 Feb. 1991), pp. ix–x. ISSN: 01659936. DOI: 10.1016/0165-9936(91)85111-4. URL: https://linkinghub.elsevier.com/retrieve/pii/0165993691851114.

[85] G Dearnaley. “Electronic Structure and Properties of Solids: The Physics of the Chemical Bond”. In: *Physics Bulletin* 31 (10 Dec. 1980). ISSN: 0031-9112. DOI: 10.1088/0031-9112/31/10/051.

[86] Robert F. Adamsky and Kenneth M. Merz. “Synthesis and crystallography of the wurtzite form of silicon carbide”. In: *Zeitschrift für Kristallographie* 111 (1-6 Jan. 1959). ISSN: 0044-2968. DOI: 10.1524/zkri.1959.111.1-6.350.

[87] X G Ning and H Q Ye. “Experimental determination of the intrinsic stacking-fault energy of SiC crystals”. In: *Journal of Physics: Condensed Matter* 2 (50 Dec. 1990). ISSN: 0953-8984. DOI: 10.1088/0953-8984/2/50/028.

[88] Alexander Thorsten Blumenau. “The modelling of dislocations in semiconductor crystals”. PhD thesis. University of Padeborn, 2002.

[89] M. H. Hong A. V. Samant P. Pirouz. “Stacking fault energy of 6H-SiC and 4H-SiC single crystals”. In: *Philosophical Magazine A* 80 (4 Apr. 2000). ISSN: 0141-8610. DOI: 10.1080/014186100250615.

[90] A. T. Blumenau et al. “Structure and motion of basal dislocations in silicon carbide”. In: *Physical Review B* 68 (17 Nov. 2003). ISSN: 0163-1829. DOI: 10.1103/PhysRevB.68.174108.

[91] U. Kaiser and I. I. Khodos. “On the determination of partial dislocation Burgers vectors in fcc lattices and its application to cubic SiC films”. In: *Philosophical Magazine A* 82 (3 Feb. 2002). ISSN: 0141-8610. DOI: 10.1080/01418610110075500.

[92] C. Wen et al. “Nature of interfacial defects and their roles in strain relaxation at highly lattice mismatched 3C-SiC/Si (001) interface”. In: *Journal of Applied Physics* 106 (7 Oct. 2009). ISSN: 0021-8979. DOI: 10.1063/1.3234380.

[93] M. Skowronski. “Degradation of Hexagonal Silicon Carbide-based Bipolar Devices”. In: IEEE, pp. 138–138. ISBN: 1-4244-0083-X. DOI: 10.1109/ISDRS.2005.1596018. URL: http://ieeexplore.ieee.org/document/1596018/.

[94] X. Song et al. “Evidence of electrical activity of extended defects in 3C–SiC grown on Si”. In: *Applied Physics Letters* 96 (14 Apr. 2010). ISSN: 0003-6951. DOI: 10.1063/1.3383233.

[95] Alexander A. Lebedev et al. “Influence of the defect density (twins boundaries) on electrical parameters of 3C-SiC epitaxial films”. In: *Physica B: Condensed Matter* 404 (23-24 Dec. 2009). ISSN: 09214526. DOI: 10.1016/j.physb.2009.08.183.

[96] Hiroyoki Nagasawa, Ramya Gurunathan, and Maki Suemitsu. “Controlling Planar Defects in 3C-SiC: Ways to Wake it up as a Practical Semiconductor”. In: *Materials Science Forum* 821-823 (June 2015). ISSN: 1662-9752. DOI: 10.4028/www.scientific.net/MSF.821-823.108.

[97] Kenji Tanaka, Masanori Kohyama, and Mikio Iwasa. "The Variety of Structures of the Σ=3 Incoherent Twin Boundary in β-SiC". In: *Materials Science Forum* 294-296 (Nov. 1998). ISSN: 1662-9752. DOI: 10.4028/www.scientific.net/MSF.294-296.187.

[98] Koji Tanaka and Masanori Kohyama. "Experimental and theoretical study of Σ = 3 incoherent twin boundary in β-SiC". In: *Philosophical Magazine A* 82 (2 Jan. 2002). ISSN: 0141-8610. DOI: 10.1080/01418610208239595.

[99] M. Lancin, C. Ragaru, and C. Godon. "Atomic structure and core composition of partial dislocations and dislocation fronts in β-SiC by high-resolution transmission electron microscopy". In: *Philosophical Magazine B* 81 (11 Nov. 2001). ISSN: 1364-2812. DOI: 10.1080/13642810108223108.

[100] R. Vasiliauskas et al. "Polytype transformation and structural characteristics of 3C-SiC on 6H-SiC substrates". In: *Journal of Crystal Growth* 395 (June 2014). ISSN: 00220248. DOI: 10.1016/j.jcrysgro.2014.03.021.

[101] Hiroyuki Nagasawa et al. "Fabrication of high performance 3C-SiC vertical MOSFETs by reducing planar defects". In: *physica status solidi (b)* 245 (7 July 2008). ISSN: 03701972. DOI: 10.1002/pssb.200844053.

[102] Luca Barbisan et al. "Nature and Shape of Stacking Faults in 3C-SiC by Molecular Dynamics Simulations". In: (2021). DOI: 10.1002/pssb.202000598. URL: https://doi.org/10.1002/pssb.202000598..

[103] Sha Sun et al. "Molecular dynamics simulation in single crystal 3C-SiC under nanoindentation: Formation of prismatic loops". In: *Ceram. Int.* 43.18 (2017), pp. 16313 – 16318. ISSN: 0272-8842. DOI: https://doi.org/10.1016/j.ceramint.2017.09.003. URL: http://www.sciencedirect.com/science/article/pii/S0272884217319193.

[104] Izabela Szlufarska et al. "Atomistic mechanisms of amorphization during nanoindentation of SiC: A molecular dynamics study". In: *Phys. Rev. B* 71 (17 May 2005), p. 174113. DOI: 10.1103/PhysRevB.71.174113. URL: https://link.aps.org/doi/10.1103/PhysRevB.71.174113.

[105] Wataru Shinoda, Motoyuki Shiga, and Masuhiro Mikami. "Rapid estimation of elastic constants by molecular dynamics simulation under constant stress". In: *Phys. Rev. B* 69 (13 Apr. 2004), p. 134103. DOI: 10.1103/PhysRevB.69.134103. URL: https://link.aps.org/doi/10.1103/PhysRevB.69.134103.

[106] Shigehiro Nishino et al. "Chemical Vapor Deposition of Single Crystalline β-SiC Films on Silicon Substrate with Sputtered SiC Intermediate Layer". In: *Journal of The Electrochemical Society* 127 (12 Dec. 1980). ISSN: 0013-4651. DOI: 10.1149/1.2129570.

[107] Bin Chen et al. "Electrical activities of stacking faults and partial dislocations in 4H-SiC homoepitaxial films". In: *Superlattices and Microstructures* 45 (4-5 Apr. 2009). ISSN: 07496036. DOI: 10.1016/j.spmi.2008.10.021.

[108] S. Ha, M. Skowronski, and H. Lendenmann. "Nucleation sites of recombination-enhanced stacking fault formation in silicon carbide p-i-n diodes". In: *Journal of Applied Physics* 96 (1 July 2004). ISSN: 0021-8979. DOI: 10.1063/1.1756218.

[109] S. I. Maximenko and T. S. Sudarshan. "Stacking fault nucleation sites in diffused 4H-SiC p-i-n diodes." In: *Journal of Applied Physics* 97 (7 Apr. 2005). ISSN: 0021-8979. DOI: 10.1063/1.1872196.

[110] Yu Sun et al. "Core element effects on dislocation nucleation in 3C–SiC: Reaction pathway analysis". In: *Computational Materials Science* 79 (Nov. 2013). ISSN: 09270256. DOI: 10.1016/j.commatsci.2013.05.055.

[111] Giuseppe Fisicaro et al. "Genesis and evolution of extended defects: The role of evolving interface instabilities in cubic SiC". In: *Applied Physics Reviews* 7 (2 June 2020). ISSN: 1931-9401. DOI: 10.1063/1.5132300.

[112] Massimo Zimbone et al. "Generation and Termination of Stacking Faults by Inverted Domain Boundaries in 3C-SiC". In: *Crystal Growth & Design* 20 (5 May 2020). ISSN: 1528-7483. DOI: 10.1021/acs.cgd.9b01708.

[113] F. La Via et al. "From thin film to bulk 3C-SiC growth: Understanding the mechanism of defects reduction". In: *Materials Science in Semiconductor Processing* 78 (May 2018). ISSN: 13698001. DOI: 10.1016/j.mssp.2017.12.012.

[114] Yu Sun et al. "Origin of the Warpage of 3C-SiC Wafer: Effect of Nonuniform Intrinsic Stress". In: *Materials Science Forum* 717-720 (May 2012). ISSN: 1662-9752. DOI: 10.4028/www.scientific.net/MSF.717-720.501.

[115] Giuseppe D'Arrigo et al. "3C-SiC Heteroepitaxial Growth on Inverted Silicon Pyramids (ISP)". In: *Materials Science Forum* 645-648 (Apr. 2010). ISSN: 1662-9752. DOI: 10.4028/www.scientific.net/MSF.645-648.135.

[116] Massimo Zimbone et al. "3C-SiC Growth on Inverted Silicon Pyramids Patterned Substrate". In: *Materials* 12 (20 Oct. 2019). ISSN: 1996-1944. DOI: 10.3390/ma12203407.

[117] H. von Känel et al. "Defect reduction in epitaxial 3C-SiC on Si(001) and Si(111) by deep substrate patterning". In: *Mater. Sci. Forum* 821-823 (2015), p. 193.

[118] M. Meduňa et al. "Stacking Fault Analysis of Epitaxial 3C-SiC on Si(001) Ridges". In: *Mater. Sci. Forum* 858 (2016), p. 147.

[119] V. Papaioannou et al. "Topology of twin junctions in epitaxial β-SiC". In: *Diamond and Related Materials* 6 (10 Aug. 1997). ISSN: 09259635. DOI: 10.1016/S0925-9635(97)00093-9.

[120] J Yamasaki et al. "Atomic structure analysis of stacking faults and misfit dislocations at 3C-SiC/Si(0 0 1) interfaces by aberration-corrected transmission electron microscopy". In: *Journal of Physics D: Applied Physics* 45 (49 Dec. 2012). ISSN: 0022-3727. DOI: 10.1088/0022-3727/45/49/494002.

[121] Wei Cai et al. "Periodic image effects in dislocation modelling". In: *Philosophical Magazine* 83 (5 Jan. 2003). ISSN: 1478-6435. DOI: 10.1080/0141861021000051109.

[122] D. Méndez et al. "Defect morphology and strain of CVD grown 3C-SiC layers: effect of the carbonization process". In: *physica status solidi (a)* 202 (4 Mar. 2005). ISSN: 18626300. DOI: 10.1002/pssa.200460421.

[123] J.R. O'Connor, J. Smiltens, and Air Force Cambridge Research Laboratories (U.S.). Electronics Research Directorate. *Silicon Carbide, a High Temperature Semiconductor*. Pergamon Press, 1960. URL: https://books.google.it/books?id=huANAQAAIAAJ.

[124] W. M. Yim and R. J. Paff. “Thermal expansion of AlN, sapphire, and silicon”. In: *Journal of Applied Physics* 45 (3 Mar. 1974). ISSN: 0021-8979. DOI: 10.1063/1.1663432.

[125] Bing Yang et al. “Defect-induced strain relaxation in 3C-SiC films grown on a (100) Si substrate at low temperature in one step”. In: *CrystEngComm* 18 (36 2016). ISSN: 1466-8033. DOI: 10.1039/C6CE01409G.

[126] Werner Wegscheider. “Effect of compressive and tensile strain on misfit dislocation injection in SiGe epitaxial layers”. In: *Journal of Vacuum Science & Technology B: Microelectronics and Nanometer Structures* 11 (3 May 1993). ISSN: 0734211X. DOI: 10.1116/1.587007.

[127] HANNES JÓNSSON, GREG MILLS, and KARSTEN W. JACOBSEN. “Nudged elastic band method for finding minimum energy paths of transitions”. In: WORLD SCIENTIFIC, June 1998. ISBN: 978-981-02-3498-0. DOI: 10.1142/9789812839664_0016.

[128] M. Skowronski and S. Ha. “Degradation of hexagonal silicon-carbide-based bipolar devices”. In: *Journal of Applied Physics* 99 (1 Jan. 2006). ISSN: 0021-8979. DOI: 10.1063/1.2159578.

[129] A. Boulle et al. “Quantitative analysis of diffuse X-ray scattering in partially transformed 3C-SiC single crystals”. In: *Journal of Applied Crystallography* 43 (4 Aug. 2010), pp. 867–875. ISSN: 0021-8898. DOI: 10.1107/S0021889810019412. URL: http://scripts.iucr.org/cgi-bin/paper?S0021889810019412.

[130] Thomas Kreiliger et al. “3C-SiC Epitaxy on Deeply Patterned Si(111) Substrates”. In: *Materials Science Forum* 858 (May 2016). ISSN: 1662-9752. DOI: 10.4028/www.scientific.net/MSF.858.151.

[131] Francesco La Via et al. “Patterned substrate with inverted silicon pyramids for 3C–SiC epitaxial growth: A comparison with conventional (001) Si substrate”. In: *Journal of Materials Research* 28 (1 Jan. 2013). ISSN: 0884-2914. DOI: 10.1557/jmr.2012.268.

[132] Naoki Hatta et al. “Reliable Method for Eliminating Stacking Fault on 3C-SiC(001)”. In: *Materials Science Forum* 717-720 (May 2012). ISSN: 1662-9752. DOI: 10.4028/www.scientific.net/MSF.717-720.173.

[133] C. Long, S. A. Ustin, and W. Ho. “Structural defects in 3C–SiC grown on Si by supersonic jet epitaxy”. In: *Journal of Applied Physics* 86 (5 Sept. 1999). ISSN: 0021-8979. DOI: 10.1063/1.371085.

[134] Makoto Kitabatake. “SiC/Si heteroepitaxial growth”. In: *Thin Solid Films* 369 (1-2 July 2000), pp. 257–264. ISSN: 00406090. DOI: 10.1016/S0040-6090(00)00819-1. URL: https://linkinghub.elsevier.com/retrieve/pii/S0040609000008191.

[135] A. Severino et al. “High-quality 6inch (111) 3C-SiC films grown on off-axis (111) Si substrates”. In: *Thin Solid Films* 518 (6 Jan. 2010). ISSN: 00406090. DOI: 10.1016/j.tsf.2009.10.080.

[136] C. W. Liu and J. C. Sturm. “Low temperature chemical vapor deposition growth of β-SiC on (100) Si using methylsilane and device characteristics”. In: *Journal of Applied Physics* 82 (9 Nov. 1997). ISSN: 0021-8979. DOI: 10.1063/1.366192.

[137] Ulf Lindefelt et al. “Stacking faults in <math display="inline"> <mn>3</mn> <mi>C</mi> <mo>-</mo> <mo>,</mo> <mi> </mi> <mn>4</mn> <mi>H</mi> <mo>-</mo> <mo>,</mo> </math> and <math display="inline"> <mn>6</mn> <mi>H</mi> <mo>-</mo> <mi mathvariant="normal">SiC</mi> </math> polytypes investigated by an ab initio supercell method”. In: *Physical Review B* 67 (15 Apr. 2003), p. 155204. ISSN: 0163-1829. DOI: 10.1103/PhysRevB.67.155204. URL: https://link.aps.org/doi/10.1103/PhysRevB.67.155204.

[138] I. Deretzis et al. “Electron backscattering from stacking faults in SiC by means of ab initio quantum transport calculations”. In: *Physical Review B* 85 (23 June 2012). ISSN: 1098-0121. DOI: 10.1103/PhysRevB.85.235310.

[139] J. Zou and D. J. H. Cockayne. “Theoretical consideration of equilibrium dissociation geometries of 60° misfit dislocations in single semiconductor heterostructures”. In: *Journal of Applied Physics* 77 (6 Mar. 1995). ISSN: 0021-8979. DOI: 10.1063/1.358772.

[140] A. M. Sanchez et al. “Stable Defects in Semiconductor Nanowires”. In: *Nano Letters* 18 (5 May 2018). ISSN: 1530-6984. DOI: 10.1021/acs.nanolett.8b00620.

[141] P. Käckell, J. Furthmüller, and F. Bechstedt. “Polytypic transformations in SiC: An ab initio study”. In: *Physical Review B* 60 (19 Nov. 1999). ISSN: 0163-1829. DOI: 10.1103/PhysRevB.60.13261.

[142] Fabio Bernardini and Luciano Colombo. “Interaction of doping impurities with the 30° partial dislocations in SiC: An ab initio investigation”. In: *Physical Review B* 72 (8 Aug. 2005). ISSN: 1098-0121. DOI: 10.1103/PhysRevB.72.085215.

[143] Philip Tanner et al. “Excellent Rectifying Properties of the n-3C-SiC/p-Si Heterojunction Subjected to High Temperature Annealing for Electronics, MEMS, and LED Applications”. In: *Scientific Reports* 7 (1 Dec. 2017). ISSN: 2045-2322. DOI: 10.1038/s41598-017-17985-9.

[144] Filippo Giannazzo et al. “Impact of Stacking Faults and Domain Boundaries on the Electronic Transport in Cubic Silicon Carbide Probed by Conductive Atomic Force Microscopy”. In: *Advanced Electronic Materials* 6 (2 Feb. 2020). ISSN: 2199-160X. DOI: 10.1002/aelm.201901171.

[145] J.W. Matthews and A.E. Blakeslee. “Defects in epitaxial multilayers”. In: *Journal of Crystal Growth* 27 (Dec. 1974). ISSN: 00220248. DOI: 10.1016/S0022-0248(74)80055-2.

[146] J.W. Matthews and A.E. Blakeslee. “Defects in epitaxial multilayers”. In: *Journal of Crystal Growth* 29 (3 July 1975). ISSN: 00220248. DOI: 10.1016/0022-0248(75)90171-2.

[147] J.W. Matthews and A.E. Blakeslee. “Defects in epitaxial multilayers”. In: *Journal of Crystal Growth* 32 (2 Feb. 1976). ISSN: 00220248. DOI: 10.1016/0022-0248(76)90041-5.

[148] J. W. Matthews. “Defects associated with the accommodation of misfit between crystals”. In: *Journal of Vacuum Science and Technology* 12 (1 Jan. 1975). ISSN: 0022-5355. DOI: 10.1116/1.568741.

[149] O Trushin et al. “Minimum energy path for the nucleation of misfit dislocations in Ge/Si(0 0 1) heteroepitaxy”. In: *Modelling and Simulation in Materials Science and Engineering* 24 (3 Mar. 2016), p. 035007. ISSN: 0965-0393. DOI: 10.1088/0965-0393/24/3/035007. URL: https://iopscience.iop.org/article/10.1088/0965-0393/24/3/035007.

[150] K. W. Schwarz. “Discrete Dislocation Dynamics Study of Strained-Layer Relaxation”. In: *Physical Review Letters* 91 (14 Oct. 2003). ISSN: 0031-9007. DOI: 10.1103/PhysRevLett.91.145503.

[151] E. Kasper and K. Lyutovich. *Properties of Silicon Germanium and SiGe:Carbon*. INSPEC, 2000.

[152] T. J. Gosling. “Mechanism for the formation of 90°dislocations in high-mismatch (100) semiconductor strained-layer systems”. In: *Journal of Applied Physics* 74 (9 1993), pp. 5415–5420. ISSN: 00218979. DOI: 10.1063/1.354247.

[153] Anna Marzegalli, Francesco Montalenti, and Leo Miglio. “Stability of shuffle and glide dislocation segments with increasing misfit in Si1-xGex/Si(001) epitaxial layers”. In: *Applied Physics Letters* 86 (4 2005), p. 041912. DOI: 10.1063/1.1856145. URL: https://doi.org/10.1063/1.1856145.

[154] Song Hu et al. “Screw dislocation induced phonon transport suppression in SiGe superlattices”. In: *Physical Review B* 100 (7 Aug. 2019). ISSN: 24699969. DOI: 10.1103/PhysRevB.100.075432.

[155] Sweta Kumari and Amlan Dutta. “Vacancy-mediated diffusion of atoms at Ge/Si interfaces: An atomistic perspective”. In: *Materialia* 11 (June 2020). ISSN: 25891529. DOI: 10.1016/j.mtla.2020.100666.

[156] Vlado A. Lubarda. “Dislocation Arrays at the Interface between an Epitaxial Layer and Its Substrate”. In: *Mathematics and Mechanics of Solids* 3 (4 Dec. 1998), pp. 411–431. ISSN: 1081-2865. DOI: 10.1177/108128659800300403.

[157] Pedro López et al. “Molecular dynamics simulations of damage production by thermal spikes in Ge”. In: *Journal of Applied Physics* 111 (3 Feb. 2012). ISSN: 0021-8979. DOI: 10.1063/1.3682108.

[158] Chunwang Zhao et al. “Strain status of epitaxial Ge film on a Si (001) substrate”. In: *Journal of Physics and Chemistry of Solids* 90 (Mar. 2016), pp. 87–92. ISSN: 00223697. DOI: 10.1016/j.jpcs.2015.11.019.

[159] Daniele Lanzoni, Fabrizio Rovaris, and Francesco Montalenti. “Computational Analysis of Low-Energy Dislocation Configurations in Graded Layers”. In: *Crystals* 10.8 (2020). ISSN: 2073-4352. DOI: 10.3390/cryst10080661. URL: https://www.mdpi.com/2073-4352/10/8/661.

[160] Rojas Dasilva Arroyo et al. “Effect of thermal annealing on the interface quality of Ge/Si heterostructures”. In: *Scripta Materialia* 170 (Sept. 2019), pp. 52–56. ISSN: 1359-6462. DOI: 10.1016/J.SCRIPTAMAT.2019.05.025.

[161] Lucio Martinelli et al. “Formation of strain-induced Si-rich and Ge-rich nanowires at misfit dislocations in SiGe: A model supported by photoluminescence data”. In: *Applied Physics Letters* 84 (15 Apr. 2004), pp. 2895–2897. DOI: 10.1063/1.1705727.

[162] G. Capellini et al. “Strain relaxation in high Ge content SiGe layers deposited on Si”. In: *Journal of Applied Physics* 107 (6 Mar. 2010), p. 063504. ISSN: 0021-8979. DOI: 10.1063/1.3327435. URL: https://aip.scitation.org/doi/abs/10.1063/1.3327435.

[163] A. Laio and M. Parrinello. “Escaping free-energy minima”. In: *Proceedings of the National Academy of Sciences* 99 (20 Oct. 2002). ISSN: 0027-8424. DOI: 10.1073/pnas.202427399.

[164] The PLUMED consortium. “Promoting transparency and reproducibility in enhanced molecular simulations”. In: *Nature Methods* 16 (8 Aug. 2019), pp. 670–673. ISSN: 1548-7091. DOI: 10.1038/s41592-019-0506-8. URL: http://www.nature.com/articles/s41592-019-0506-8.

[165] Alessandro Barducci, Giovanni Bussi, and Michele Parrinello. “Well-Tempered Metadynamics: A Smoothly Converging and Tunable Free-Energy Method”. In: *Physical Review Letters* 100 (2 Jan. 2008). ISSN: 0031-9007. DOI: 10.1103/PhysRevLett.100.020603.

[166] Davide Branduardi, Giovanni Bussi, and Michele Parrinello. “Metadynamics with Adaptive Gaussians”. In: *Journal of Chemical Theory and Computation* 8 (7 July 2012). ISSN: 1549-9618. DOI: 10.1021/ct3002464.

[167] S. Pipolo et al. “Navigating at Will on the Water Phase Diagram”. In: *Physical Review Letters* 119 (24 2017), pp. 1–5. ISSN: 10797114. DOI: 10.1103/PhysRevLett.119.245701.